MODIFIED METAL ORGANIC-FRAMEWORKS: MULTI-CORE-SHELL COMPOSITES AS ADSORBENTS AND PHOTOCATALYSTS

Ph.D. THESIS

by

RAMESH CHANDRA

DEPARTMENT OF CHEMISTRY
INDIAN INSTITUTE OF TECHNOLOGY ROORKEE
ROORKEE - 247667 (INDIA)
MAY, 2019

MODIFIED METAL ORGANIC-FRAMEWORKS: MULTI-CORE-SHELL COMPOSITES AS ADSORBENTS AND PHOTOCATALYSTS

A THESIS

Submitted in partial fulfilment of the requirements for the award of the degree

of

DOCTOR OF PHILOSOPHY

in

CHEMISTRY

by

RAMESH CHANDRA

DEPARTMENT OF CHEMISTRY
INDIAN INSTITUTE OF TECHNOLOGY ROORKEE
ROORKEE - 247667 (INDIA)
MAY, 2019

INDIAN INSTITUTE OF TECHNOLOGY ROORKEE
ROORKEE

CANDIDATE'S DECLARATION

I hereby certify that the work which is being presented in the thesis entitled **"MODIFIED METAL ORGANIC-FRAMEWORKS: MULTI-CORE-SHELL COMPOSITES AS ADSORBENTS AND PHOTOCATALYSTS"** in partial fulfilment of the requirements for the award of the Degree of Doctor of Philosophy and submitted in the Department of Chemistry of the Indian Institute of Technology Roorkee, Roorkee is an authentic record of my own work carried out during a period from August, 2014 to May, 2019 under the supervision of Dr. (Mrs.) Mala Nath, Professor, Department of Chemistry, Indian Institute of Technology Roorkee, Roorkee.

The matter presented in this thesis has not been submitted by me for the award of any other degree of this or any other Institution.

(RAMESH CHANDRA)

This is to certify that the above statement made by the candidate is correct to the best of my knowledge.

(Mala Nath)
Supervisor

The Ph.D. Viva-Voce examination of **Mr. Ramesh Chandra**, Research Scholar, has been held on 13th September 2019.

Chairman, SRC **Signature of External Examiner**

This is to certify that the student has made all the corrections in the thesis.

Signature of Supervisor **Head of the Department**
Dated:

Dedicated

to

My Dear Parents

ABSTRACT

The sustainable strategies/methods for degradation of colouring materials, particularly for the organic dyes, are the prime concern worldwide because the discharge of such dye containing effluents into water bodies makes them polluted to such an extent that aquatic lives are in danger due to decrease oxygen contents. Organic pollutants, *for instance*, methylene blue (MB), rhodamine-B (RB), congo red (CR) and 4-nitrophenol (4-NP) are the main contaminates in the effluents of textile and some other industries. They have been recognized as toxic, carcinogenic and mutagenic along with a very minimal biodegradability in ecosystems. Prior to discharge of these organic pollutants into water bodies, the adequate removal of pollutants must be ensured. Various methods have been employed for the waste water treatment such as physio-chemical and biological methods but they are inefficient.

In last few decades, much efforts have been dedicated for degradation of dyes by using novel metal nanoparticles (Au, Ag and Pt etc.,) and semiconducting nanomaterials such as ZnO, SnO_2, Fe_2O_3, and TiO_2 having small band gap and chemical stability but there are the drawback of fast recombination rate of electron (e^-) and hole (h^+), and agglomeration of NPs reduces their efficiency which can be partially solved by their immobilization. Several efforts have been made to immobilize them by encapsulation into porous materials such as zeolite. Recently, core@shell nanoparticles or composites, involving metal organic frameworks as shell/host, have been reported to reduce the recombination rate of e^- and h^+, thereby, enhancing their photocatalytic efficiency.

Metal organic frameworks (MOFs) have emerged as a hybrid inorganic-organic materials which are constructed through covalent bonding of metal ions with organic linker molecules. These materials have high porosity, tunable shapes and pore sizes, high surface area, and a wide range of applications such as heterogeneous catalysts, gas storage and chemical sensing. Besides, MOFs are very useful in drug release application on account of their fascinating hydrophilic-hydrophobic internal microenvironments. Zeolitic imidazole frameworks (ZIFs) are a kind of metal organic frameworks which consist of mainly transition metal ions (*e.g.* Co and Zn) and imidazole or its derivatives as linkers. In ZIFs, the metal centers are tetrahedrally coordinated with N-atom of imidazole ring. The topology of ZIFs resemble zeolite as metal-imidazole-metal (M-Im-M) bond angles are retained to be 145° as aluminosilicate zeolite (Si-O-Si bond angle =145°). Myriad numbers of ZIFs have been reported on account of their constitutional unit and porosity. Among them, ZIF-8 was found to be more chemically and thermally stable. ZIF-8 has larger pores 11.6 Å connected with small

apertures 3.4 Å. Owing to its highly porous, chemical and thermal stability, ZIF-8 is considered to be very useful for various applications such as gas storage, adsorbent, drug delivery and host of catalyst in heterogeneous catalysis. Fabrication of ZIFs with metal oxides, novel metal nanoparticles and molecules has been an emerging challenge. And so, ZIF-8 has been selected for fabrication of metal oxides and novel metal nanoparticles. The present study describes the synthesis of metal oxides (MOx) and novel metal nanoparticles (MNPs) encapsulated within ZIFs. Further, MOx@ZIFs and MNPs@ZIFs have been used as photocatalysts for the waste water treatment and biomedical applications which are described in the successive six chapters.

First Chapter presents a brief literature on ZIF-8 and its composites with novel metal nanoparticles (Au, Ag, Pd and Pt), metal oxides (ZnO, TiO_2, SnO_2 and Fe_3O_4) and molecules. The synthetic methods and probable applications of some important reported composites have also been presented.

Second Chapter describes the make and purity of chemicals used in the present study. This chapter also highlights the specifications of various sophisticated instruments and details of procedures/methods used in all the chapters.

Third Chapter includes the synthesis of multi-core-shell TiO_2NPs@ZIF-8 composites by *in situ* encapsulation of different amounts of TiO_2NPs *i.e.* 150, 300 and 500 µL suspension of TiO_2NPs in methanol within ZIF-8 at ambient temperature. Encapsulation of TiO_2NPs in ZIF-8 was confirmed by transmission electron microscopy and X-ray photoelectron spectroscopy. ZIF-8 and its core-shell composites have identical crystal structure and morphology as confirmed by powder X-ray diffraction analysis and scanning electron microscopy. The detailed photocatalytic degradation and adsorption studies of MB and RB were investigated by analyzing various factors, *viz.*, loading amount of TiO_2NPs in ZIF-8, amount of photocatalyst, pH and initial concentration of the dye. At higher pH (11.5−12.6), TiO_2NPs@ZIF-8 composite exhibited higher (*ca.* 8 times) photocatalytic activity as compared to TiO_2NPs and the optimum amount of TiO_2NPs@ZIF-8 composite was 10 mg for the maximum photodegradation of 3.19 mg L^{-1} (93%) and 2.4 mg L^{-1} (57%) of MB and RB, respectively. After the degradation of both dyes (MB and RB), the degraded by-products were analyzed by GC-MS and the degradation path has also been proposed.

Chapter four describes the synthesis of multi-functional and thermally stable SnO_2NPs@ZIF-8 composites (NC1, NC2 and NC3) by a facile and sustainable approach involving *in situ* encapsulation of SnO_2NPs (150, 300 and 500 µL suspension in methanol) within zeolitic imidazole framework at ambient temperature. The morphology and crystallinity of ZIF-8 remained unchanged upon the proper encapsulation of SnO_2NPs in its matrix. Herein,

for the first time, the antiviral potential of ZIF-8 and SnO_2NPs@ZIF-8 composite was explored against chikungunya virus by investigating their cytotoxicity against *Vero* cell line employing MTT ((3-(4,5-dimethylthiazol-2-yl)-2, 5-diphenyltetrazolium bromide)) assay. The maximum non-toxic dose was found to be 0.04 mg mL^{-1} for ZIF-8 and SnO_2NPs@ZIF-8, and 0.1 mg mL^{-1} for SnO_2NPs. Further, NC1 exhibited (based on plaque assay) reduction in viral load/titers up to >80% during post-treatment and >50% during pre-treatment, greater than that of ZIF-8 and SnO_2NPs due to synergistic effect. Further, NC1 (10 mg) exhibited enhanced photocatalytic efficiency (≥96%) for degradation of MB (0.5×10^{-5} M) at pH >7.0. The probable mechanism for their anti-viral activity and photocatalytic activity has been discussed.

Chapter five contains two sections. **Section-A** consists of synthesis of novel multi-core-shell AgNPs@ZIF-11 (AZ1, AZ2 and AZ3) composites by *in situ* encapsulation of Ag nanoparticles (150, 300 and 500 μL suspension in methanol) in ZIF-11 (Zeolitic Imidazole Framework) at ambient temperature using binary solvent mixture (methanol and toluene). The lowering of band gap of ZIF-11 from 4.36 to 4.21 eV indicates the micro-environment of AgNPs within ZIF-11 framework. Particle size of encapsulated AgNPs within the matrix of ZIF-11 was found to be 11.76 ± 2.3 nm. ZIF-11 and AgNPs@ZIF-11 composites are highly thermally stable up to 500 °C under both air and nitrogen environments. Application of AgNPs@ZIF-11 (AZ1, AZ2 and AZ3) composites towards photodegradation of MB dye has been investigated by varying the amount of catalyst (5, 10 and 15 mg) and dye concentration (1.6, 3.19 and 6.38 mg L^{-1}). AZ1 (10 mg) exhibits excellent photocatalytic activity; degrades 100% MB (1.6 mgL^{-1}) at pH ≥ 7. AZ1 also exhibits potential efficiency (86%) for the conversion of 4-nitrophenol into 4-aminophenol. Further, AZ1 can be reutilized up to three cycles with 100% efficiency while under fourth and fifth cycle it can degrade 92.12% and 72.75% MB, respectively. The degraded by-products of MB dye have also been analyzed by GC-MS followed by the brief discussion of the mechanism.

Section-B describes an auspicious approach towards the heterogeneous photocatalytic degradation of MB and CR using AgNPs@ZIF-8 composites. The facile synthesis of AgNPs encapsulated ZIF-8 via *in situ* synthesis of AgNPs and ZIF-8 has been demonstrated. AgNPs@ZIF-8 composite has been synthesized by incorporation of pre-synthesized ZIF-8 *in situ* synthesis of AgNPs and named as SZ while pre-synthesized AgNPs have been encapsulated within ZIF-8 in different amounts such as 150, 300 and 500 μL methanol suspensions *in situ* synthesis of ZIF-8 and named as SZ1 SZ2 and SZ3, respectively. All four synthesized SZ, SZ1 SZ2 and SZ3 composites have been characterized by various spectroscopic techniques. Owing to highly porous and unique properties of AgNPs@ZIF-8

composites, they exhibit remarkable photocatalytic activity for the degradation of MB and CR as compared to ZIF-8. Further, the degradation mechanism and degradation path way of both the dyes have been discussed.

Chapter six comprises of two sections. **Section-A** describes the synthesis of ZnO-SnO_2 nanocomposites in the various molar ratio *i.e.*1:1, 2:8, 4:6, 6:4 and 8:2 of Zn and Sn using sol-gel (ZS-11, ZS-28, ZS-46, ZS-64 and ZS-82) and grinding (ZS-A, ZS-B, ZS-C, ZS-D and ZS-E) method and detailed characterization using various instrumental techniques. The synthesized ZnONPs looks like flower structure while SnO_2NPs and ZnO-SnO_2 nanocomposites have spherical morphology confirmed by SEM analysis. In addition, the formation ZnO-SnO_2 was investigated by HR-TEM analysis. Further, the elemental composition and the close fitting of Zn 2p, Sn 3d, and O 1s of ZnO-SnO_2 have been ensured by XPS analysis. In order to explore photocatalytic application, adsorption and photodegradation efficiency have been examined using a model dye, *for instance*, MB. It has been found that ZS-E (8:2 molar ratio of Zn:Sn synthesized by grinding method) nanocomposite exhibits maximum photodegradation efficiency which can degrade off 58.68% [MB] = 1.6 mg L^{-1} dye solution. Further, ZS-E nanocomposite has been optimized for its encapsulation within ZIF-8 due to its maximum photocatalytic response at pH ≥ 7 which is described in Section-B.

In Section-B, ZnO-SnO_2 nanocomposite (ZS-E) has been anchored (ZS@Z) and encapsulated (ZS@Z1;150 µL/ZS@Z2;300 µL/ZS@Z3;500 µL) within ZIF-8 framework successfully by employing solvothermal and bench method, respectively. The synthesized composites were also exploited as photocatalysts for the removal of MB. Further, it has been found that ZnO-SnO_2 nanocomposite anchored on ZIF-8 composite (ZS@Z) exhibits 100% degradation of [MB] = 1.6 mg L^{-1} dye solution at pH ≥ 7 while ZS@Z1, ZS@Z2 and ZS@Z3 composites can degrade off 93.43, 97.43 and 91.93%, respectively. The possible mechanism has also been described.

Chapter seven highlights the conclusions and future prospect of synthesized composites.

ACKNOWLEDGEMENTS

First of all, I would like to offer my excessive admiration to the omniscient and omnipotent almighty God who kept his blessings on me in any circumstances, and strengthen me to accomplish this herculean task.

"ज्ञानं परमं बलम्"

"Knowledge is the supreme power"

I would like to express my sincere gratitude to my benign supervisor **Prof. (Mrs.) Mala Nath** (Professor, Department of Chemistry, IIT Roorkee) for giving me the opportunity to do research and providing invaluable guidance throughout my research work. Her dynamism, vision, sincerity and motivation have deeply inspired me. She has taught me the methodology to carry out the research and to present the research works as clearly as possible. She has contributed a great deal to my understanding in research through valuable discussions, ideas and useful comments, which were a great source of my inspiration. It was a great privilege and honor to work and study under her guidance. I am extremely grateful for her support because this monumental work could not be accomplished without her guidance.

"श्रमम् विना न किमपि साध्यम्"

"Without effort nothing is possible"

I am highly grateful to **Prof. K. R. Justin Thomas** *Head,* **Prof. M. R. Maurya,** and **Prof. Anil Kumar**, *Ex-Head,* Department of Chemistry, IIT Roorkee, Roorkee for providing me all sophisticated instruments facilities and support to carry out my research work.

I express my sincere thanks to my Student Research Committee (SRC) members **Prof. Anil Kumar (SRC Chairman), Prof. Bina Gupta (Internal Expert),** and **Prof. Partha Roy (External Expert)** for their constructive suggestions, rational comments and candid opinions during the SRC meetings.

I am thankful to the Ministry of Human Resource Development (MHRD), New Delhi, India, for providing financial assistance in the form of Junior Research Fellowship (JRF) and Senior Research Fellowship (SRF) which is reinforced me to perform my work comfortably.

I am thankful to **Dr. Shailly Tomar** (Associate Professor Department of Biotechnology, IIT Roorkee) and her research scholar **Vedita Singh** for their valuable contribution in my research work.

I am thankful to all other teachers, technical and non-technical staff (Mr. D. C. Meena, Mr. B. Ram, Mr. Madan Pal, Mr. Pankaj, Mr. Tilak Ram, Mr. Anshu and Mr. Ankur Sharma) of the Department of Chemistry, IIT Roorkee for their cooperation and support.

I am profoundly indebted to my seniors' fellows **Dr. P. K. Saini, Dr. Nagamani Kompalli, Dr. Maridula, Dr. Sundeep Kumar** and **Dr. Ranjana Kumari** for their cooperation, motivational support and encouragement throughout my research work. I truly appreciate my other companions **Ankur, Pooja, Subham, Vinod** and **Praveen** who not only have inspired but also morally supported me. I wish to evince my special thanks to my elder brother **Dr. Sundeep Kumar** for all short of occasional help, and his exuberance and diligence are truly appreciated at the proofreading stage to emend the manuscript.

I am extending my thanks to my near and dear friends Neeraj, Dr. M. Waheed, Dr. P. J. S. Rana, Saurabh Singh, Ram Nayan, Prabhat, Manish Tripathi, Virat Agnihotri, S. M. Ezaz, Satwant Rao, Yashwant, Alok Singh and R. N. Mishra to stay beside me whenever I needed.

No words are enough to articulate my feelings for my adorable parents **Smt. Usha Devi** and **Sh. Deepchandra Ram** for their unconditional love, prayers, caring and sacrifices for educating and preparing me for my future. Also, I express my thanks to my sisters, **Bina and Reema** and brothers **Rakesh, Pramesh and Rohit** and my lovely **niece & nephew.**

Last but not least, I am thankful to almighty God once again for his mercy and grace upon me.

IIT, Roorkee — Ramesh Chandra

May, 2019

LIST OF ABBREVIATIONS

Å	Angstrom
4-AP	4-aminopnenol
BET	Brunauer-Emmett-Teller
BSA	Bovine serum albumin protein
BASF	Badische Anilin and Soda Fabrik
BCT	
BQ	Benzequenone
°C	Degree centigrade
ca.	Circa
CB	Conduction Band
CR	Congo red
cm^{-1}	Centimetre inverse
CHIKV	Chikungunya Virus
CPE	Cytopathic effect
CMC	Carboxy methylcellulose
COD	1,5-cyclooctadiene
cc/g	Cubic centimeter per gram
CVD	Chemical vapor deposition
DMEM	Dulbecco's modified eagle's medium
DMSO	Dimethyl sulphoxide
EDTA	Ethylenediaminetetraacetic acid
EDX	Energy dispersive X-ray
e.g.	For example (*exempli gratia*)
eV	Electron bolt
Eq.	Equation
FBS	Fetal bovine serum
FE-SEM	Field emission scanning electron microscopy
Fig.	Figure
FT-IR	Fourier transform infrared microscopy
FWHM	Full width half maxima
g	Gram
$g\ cm^{-3}$	Gram per centimeter cube
GC-MS	Gas chromatography - mass spectrometry
h	hour
Hz	Hertz
HKUST	Hong Kong University of Science and Technology
HOMO	Highest occupied molecular orbital
HRTEM	High resolution transmission electron microscopy
IRMOF	Isoreticular metal-organic framework
IUPAC	International Union of Pure Applied Chemistry
i.e.	That is (*id est.*)
LUMO	Lowest unoccupied molecular orbital
M	Molar

m	Mass
MB	Methylene Blue
Me	Methyl
min	Minute
MIL	Material of Institute Lavoisier
mL	Milliliter
mJ/Kg	Millijule per kilogramm
mL/min	Milliliter per minute
µL	Microliter
mM	Millimole
MEM	Minimum essential media
MeCP	Methylcyclopentadienyl
MOFs	Metal organic frameworks
MO_x	Metal oxides
MNPs	Metal nanoparticles
MSS	Mesoporous silica spheres
MTT	3-(4,5-dimethylthiazol-2-yl)-2,5-diphenyltetrazolium bromide
MOI	Multiplicity of infection
MNTD	Maximum non-toxic dose
nm	Nanometer
NPs	Nanoparticles
4-NP	4-nitrophenol
P	Pressure
ppm	Parts per million
PL	Photoluminescence
PFU	Plaque forming unit
PSS	Poly styrenesulfonate sodiumsulphate
PTA	Phosphotungastic acid
PVP	Polyvinylpyrrolidone
PU	Polyurethane
QCMB	Quartz crystal micro-balance
q_t	Adsorption capacity
RNA	Ribonucleic acid
ROS	Reactive oxidizing species
SALE	Solvent assistant linker exchange
SC	Super capacitor
SEAD	Selected area electron diffraction
SPR	Surface plasmon resonance
SOD	
t	Time
TGA	Thermogravimetric Analysis
t-BuOH	*tertiary*-butyl alcohol
UV	Ultraviolet
UV-DRS	Ultraviolet diffuse reflectance spectroscopy
V	Volume

VB	Valence bond
viz.	*Videlicet*
Wt.	Weight
XPS	X-ray photoelectron spectroscopy
ZIFs	Zeolitic imidazole frameworks

LIST FIGURES

Fig. 3.10. (a, b) TGA analysis of TiO_2NPs, ZIF-8 their TiO_2NPs@ZIF-8 composites in air and N_2 atmosphere, respectively.

Fig. 3.11. The effect of amount of TiO_2NPs encapsulated in ZIF-8 for adsorption and photodegradation of [MB] = 1.64 mg L^{-1}; pH 8.5; photocatalyst amount 10 mg.

Fig. 3.12. The effect of photocatalyst's amount for adsorption and photodegradation of [MB] = 1.64 mg L^{-1} at pH 8.5 (a); and [RB] = 1.64 mg L^{-1} at pH 8.6 (b).

Fig. 3.13. The effect of pH for adsorption and photodegradation of [MB] = 1.64 mg L^{-1} at pH = 3.1, 8.5 and 11.5, represented as (a), (b) and (c), respectively, and [RB] = 2.4 mg L^{-1}at pH = 3.3, 8.6 and 12.6 represented as (d), (e) and (f), respectively.

Fig. 3.14. The effect of initial concentration of MB and RB for adsorption and photodegradation of [MB] = 3.19 mg L^{-1} (a) and [MB] = 6.38 (b), at pH = 11.5; [RB] = 4.79 (c) and [RB] = 9.58 (d) at pH = 12.6; photocatalyst's amount 10 mg.

Fig. 3.15. Fluorescence spectral changes (excitation at 315 nm; under UV-visible light) of terephthalic acid (0.5 mM; NaOH 2 mM) (a); in presence of ZIF-8 (10 mg) (b); in presence of TiO_2NPs@ZIF-8 composite (10 mg) (c); in presence of TiO_2NPs (equivalent amount present in 150 µL encapsulated TiO_2NPs@ZIF-8 composite) (d).

Fig. 3.16. Fluorescence spectral changes (excitation at 315 nm; under dark) of terephthalic acid (0.5 mM; NaOH 2 mM) (a); in presence of ZIF-8 (10 mg) (b); in presence of TiO_2NPs@ZIF-8 composite (10 mg) (c); in presence of TiO_2NPs (equivalent amount present in 150 µL suspension) (d).

Fig. 3.17. Mechanism of photocatalytic activity of TiO_2NPs@ZIF-8 composite. The dashed lines indicate VB and CB of TiO_2NPs, whereas E'_g represents decreased band gap of TiO_2NPs after encapsulation. The solid lines indicate VB and CB of TiO_2NPs@ZIF-8 composite and E_g represents band gap of TiO_2NPs.

Fig. 3.18. The GC-MS spectra of identified intermediates structure (Proposed in Scheme 3.2) after the degradation of MB are shown (a-c), respectively.

Fig. 3.19. The GC-MS spectra of identified intermediates structure (Proposed in Scheme 3.3) after degradation of RB are shown (a-e), respectively.

Fig. 3.20. (a, b) Kinetic plots of MB and RB dye are shown, respectively.

Fig. 4.1. (a) PXRD patterns of SnO_2NPs calcined at various temperatures; (b) PXRD patterns of ZIF-8 and its composites NC1, NC2 and NC3; (c) PXRD patterns of used and unused composite NC1; (d) IR spectra of SnO_2NPs, ZIF-8 and composites NC1, NC2 and NC3.

Fig. 4.2. SEM images of SnO_2NPs at (a) 100 Kx; (b) 200 Kx; (c) SEM image of ZIF-8 at 50 Kx and (d) SEM image of composite NC1 at 100 Kx.

Fig. 5A.5 (a, b) FE-SEM images of ZIF-11 and AZ1 composite, respectively. Fig. 5A.5(c-e) represents the mapping of C, N and Zn elemental composition, respectively, of ZIF-11.

Fig. 5A.6. (a-e) The EDX spectra of ZIF-11, AZ1, AZ2, AZ3 and AgNPs, respectively.

Fig. 5A.7. TEM image of (a) AgNPs, (b) ZIF-11, (c, d) AZ1 composite in order of increasing magnification, SEAD pattern of (e) AgNPs and (f) AZ1 composite, respectively.

Fig. 5A.8. (a, b) Particle size distribution plots of AgNPs as synthesized and after encapsulation within ZIF-11, respectively.

Fig. 5A.9. (a, b) Combined DRS spectra of ZIF-11, AZ1, AZ2 and AZ3 composites by direct and indirect transition method, respectively, and (c) UV-visible absorbance spectra of ZIF-11 and composites AZ1, AZ2 AZ3. Fig. 5A.9(d) UV-visible absorbance spectra of synthesized AgNPs suspension.

Fig. 5A.10. (a-d) BET adsorption-desorption isotherm indexed with pore size distribution plot of ZIF-11 and its composite AZ1, AZ2 and AZ3, respectively.

Fig. 5A.11. (a, b) Survey scan and expanded XPS spectra of Ag 3d of AgNPs.

Fig. 5A.12. (a-d) Survey scan and expanded XPS spectra of Zn 2p, C 1s and N 1s of ZIF-11 are shown as (a), (b), (c) and (d), respectively.

Fig. 5A.13. (a-e) Survey scan and expanded XPS spectra of Zn 2p, C 1s, N 1s and Ag 3d of AZ1 are shown as (a), (b), (c), (d) and (e), respectively.

Fig. 5A.14. (a-e) Survey scan and expanded XPS spectra of Zn 2p, C 1s, N 1s and Ag 3d of AZ2 are shown as (a), (b), (c), (d) and (e), respectively.

Fig. 5A.15. (a-e) Survey scan and expanded XPS spectra of Zn 2p, C 1s, N 1s and Ag 3d of AZ3 are shown as (a), (b), (c), (d) and (e), respectively.

Fig. 5A.16. (a, b) TGA analysis of ZIF-11 and AgNPs@ZIF-11 composites (AZ1, AZ2 and AZ3) under air and N_2 atmosphere, respectively.

Fig. 5A.17. Effect of encapsulation amount of AgNPs suspensions within ZIF-11 framework for adsorption and photodegradation of [MB] = 1.64 mg L^{-1}; pH = 8.35; photocatalyst's amount = 10 mg (0.5 g L^{-1}).

Fig. 5A.18. Effect of photocatalyst's amount for adosrption and photodegradation of [MB] = 1.6 mg L^{-1} at pH = 8.35.

Fig. 5A.19. Effect of initial dye concentration for adsorption and photodegradation of [MB] (a) 1.6 mg L^{-1}; (b) 3.19 mg L^{-1}; (c) 6.38 mg L^{-1} at pH = 8.35; Photocatalyst's amount = 10 mg.

Fig. 5A.20. (a, b) UV-visible absorbance spectra under UV-visible irradiation of MB with AZ1 and pictorial graph for its recyclability test are illustrated respectively.

LIST OF SCHEMES

LIST OF TABLES

LIST OF PUBLICATIONS

1. **R. Chandra**, S. Mukhopadhyay and M. Nath, "TiO_2@ZIF-8: A novel approach of modifying micro-environment for enhanced photo-catalytic dye degradation and high usability of TiO_2 nanoparticles" *Mater. Lett.* 164 (2016) 571-574.
2. **R. Chandra** and M. Nath, "Multi-Core–shell TiO_2NPs@ZIF-8 Composite for Enhanced Photocatalytic Degradation and Adsorption of Methylene Blue and Rhodamine-B" *ChemistrySelect* 2 (2017) 7711-7722.
3. **R. Chandra**, V. Singh, S. Tomar and M. Nath, "Multi-core–shell Composite SnO_2NPs@ZIF-8: Potential Antiviral Agent and effective Photocatalyst for Waste-water Treatment" *Environ. Sci. Pollut. R.* 26 (2019) 23346–23358.
4. **R. Chandra** and M. Nath, "Toluene Assisted Synthesis of ZIF-11 and Multi-Core-Shell AgNPs@ZIF-11 composite: As an Effective Photocatalyst for Industrial Pollutants" under review.
5. **R. Chandra** and M. Nath "Controlled Synthesis of AgNPs@ZIF-8 Composite for Enhanced Photocatalytic degradation of Methylene Blue and Congo Red" under review.

CONFERENCES

1. **R. Chandra** and M. Nath, "Synthesis of TiO_2@ZIF-8 Composite and its Photocatalytic Activity for Degradation of Methylene Blue" (ICAM 2016): International Conference on Advanced Materials for Energy, Environment and Health, March 4-7, 2016, at IIT Roorkee.
2. **R. Chandra** and M. Nath, "Novel Multi-Core-Shell SnO_2NPs@ZIF-8 Composite: A Potential Antiviral Inhibitor for Chikungunya Virus" (Su-Chem2018): International Conference on Sustainable Chemistry for Health, Environmental and Materials at CSIR, August 5-8, 2018, IICT Hyderabad.
3. M. Nath and **R. Chandra**, "Core-Shell Based Composite SnO_2NPs@ZIF-8 as an Effective Photo-catalyst for Degradation of Methylene" (ICMAT): 9th International conference on materials for advanced technologies, June 18-23, 2017 Suntec organized by Material Research Society Singapore.
4. M. Nath and **R. Chandra** "Toluene Assisted Synthesis of ZIF-11 and Multi-Core-Shell AgNPs@ZIF-11 composite: As an Effective Photocatalyst for Industrial Pollutants" 17^{th} International Conference on Emerging Materials and Nanotechnolgy held at Berlin, Germany, on March 7-8, 2019.

* Underlined author presented the paper in the conference.

TABLE OF CONTENTS

Chapter One

Introduction

"Education is the kindling of a flame, not the filling of a vessel."

Socrates

1.1. INTRODUCTION

To design and develop an easily executable heterogeneous photocatalytic method or material employed for the degradation of organic industrial effluents has been the most challenging concern. Organic pollutants in the wastewater effluents are specifically referred to organic dyes which are used as coloring materials, *for instance*, methylene blue (MB), rhodamine-B (RB), congo red (CR), and 4-nitrophenol (4-NP). They have been recognized as toxic, carcinogenic and mutagenic along with a very minimal biodegradability in ecosystems [1]. Additionally, the excessive discharge of these dye-enriched effluents into the water bodies may disturb the aquatic ecosystem by preventing the penetration of sunlight through them, which in turn may adversely affect the dissolved oxygen content [2]. The adequate removal of organic pollutants must be ensured prior to the discharge of waste effluents into the water bodies. Commonly employed physio-chemical and biological methods are seemed to appear inefficient as they are considerably slow and unable to destroy the pollutants completely, and sometimes may trigger off production of harmful secondary pollutants as by-products [2]. In order to improve the methodology for the mineralization of organic pollutants, advanced oxidation process (AOPs) has been employed. In AOPs, organic pollutants undergo mineralization due to oxidation *in situ* generation of reactive oxidizing species (ROS) such $^{\bullet}OH$ and $O_2^{\bullet-}$ under photo-irradiation of suitable photocatalyst. In spite of that, AOPs contains chemical oxidation, photochemical oxidation and heterogeneous photocatalysis but among them, photocatalysis is an efficient and excellent process for the degradation of organic pollutants without using any harmful chemicals. The heterogeneous photocatalysis is illustrated in Scheme 1.1 which describes the degradation of organic pollutants followed by generation of electron (e^-) and hole (h^+). In the first step, the semiconducting (SC) materials (TiO_2, ZnO, WO_3 and SnO_2) become activated by absorbing a photon with equivalent energy of their band gap. As a consequence, electron (e^-) and hole (h^+) are generated by promotion of e^- from valence band to conduction band [3]. Photo-induced e^- and h^+ react with O_2 and H_2O molecules to produce ROS according to the following equations.

$$SC + h\nu \rightarrow SC\ (e^- \text{ and } h^+) \quad (1.1)$$

$$h^+ + H_2O \rightarrow {}^{\bullet}OH + H^+ \quad (1.2)$$

$$h^+ + OH^- \rightarrow {}^{\bullet}OH \quad (1.3)$$

$$e^- + O_2 \rightarrow O_2^{\bullet-} \quad (1.4)$$

$$O_2^{\bullet} + H_2O \rightarrow HO_2^{\bullet} + OH^- \quad (1.5)$$

$$HO_2^{\bullet} + H_2O \rightarrow {}^{\bullet}OH + H_2O_2 \quad (1.6)$$

$$H_2O_2 \rightarrow 2{}^{\bullet}OH \quad (1.7)$$

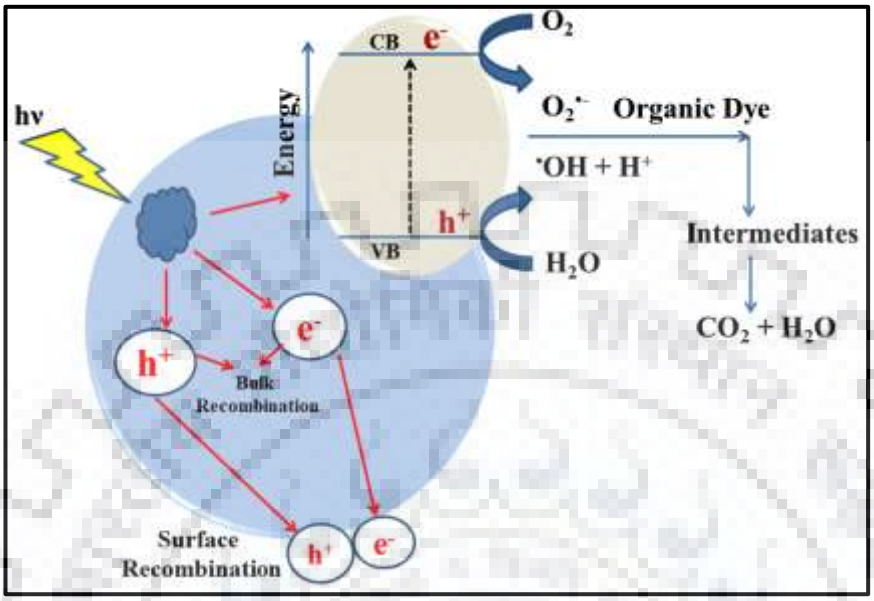

Scheme 1.1. Schematic illustration of heterogeneous photocatalysis of organic pollutants/dye (Wherein VB and CB refer valence band and conduction band, respectively, of a photocatalyst material).

There are several semiconductors such as TiO_2, ZnO, CdS, MoS_2, WO_3 and SnO_2 used for waste water treatment. Among them, TiO_2 nanoparticles are found to be the promising photocatalyst. TiO_2 exhibits three crystalline phases *i.e.* anatase, rutile and brookite as shown in Fig.1.1 [4]. Interestingly, anatase phase is non-toxic, crystalline and the most active phase associated with a broad band gap *ca.* 3.35 eV, and has been utilized as heterogeneous photocatalyst in waste water treatment [5]. Similarly, SnO_2 nanoparticles are chemically stable, less toxic, and exhibit a suitable band gap (*ca.* 3.62 eV) which accounts for their wide applications as an anode in the lithium ion batteries, sensors, and photocatalyst for the degradation of MB dye [6, 7]. Additionally, SnO_2 is an *n*-type semiconductor which is mostly used as electron acceptor in mixed metal oxides such as SnO_2-TiO_2, SnO_2-ZnO and SnO_2-ZnO-TiO_2 nanocomposites. SnO_2 exists predominantly into rutile phase which can be invariably transformed into another one upon increasing pressure according to the following sequence; rutile, $CaCl_2$-type, α-PbO_2-type, pyrite, ZrO_2-type, cotunnite and fluorite [8]. Moreover, polymorphic SnO_2 has been reported to transform sequentially into rutile→$CaCl_2$-type→α-PbO_2-type→fluorite at increasing pressure of 11.35, 14.69 and 58.22 GPa, respectively, as

depicted in Fig.1.2 [9]. ZnO nanoparticles, a unique class of semiconducting materials, generally adopt either a hexagonal wurtzite or cubic zinc blende structure (Fig. 1.3) [10]. ZnO nanoparticles possess a wide band gap *ca.* 3.37 eV and have been exploited in the various fields such as biomedical science, optoelectronics, sensors, transducer and photocatalysis [11].

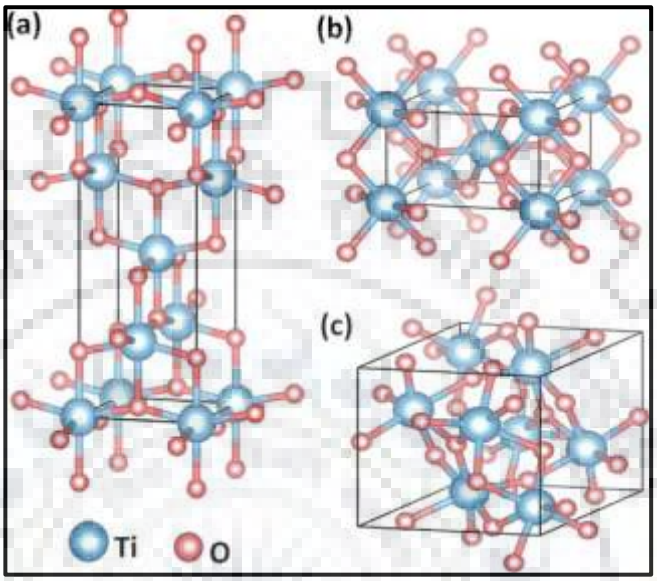

Fig. 1.1. Crystal structures of (a) anatase, (b) rutile and (c) brookite phase of TiO_2 [4].

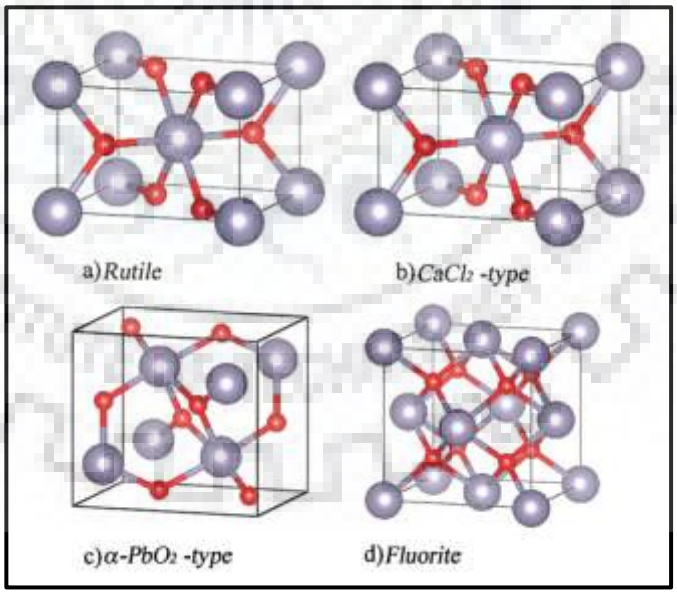

Fig. 1.2. Crystal structures of (a) rutile (b) $CaCl_2$-type (c) α-PbO_2-type and (d) fluorite phases of SnO_2 [9].

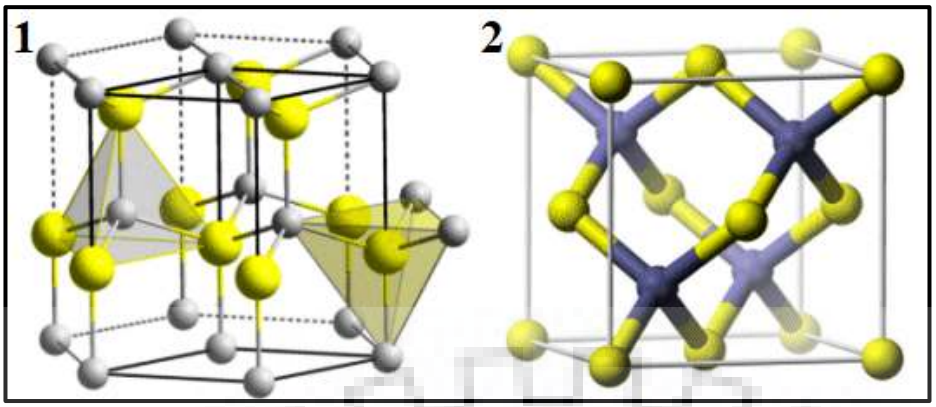

Fig. 1.3. ZnO nanocrystal structures of (1) wurtzite (hexagonal) (2) zinc blende (cubic) phase [10].

In the last few decades, much efforts have been dedicated for degradation of dyes and deposition of toxic heavy metals by using novel metal nanoparticles (Au, Ag and Pt), bimetallic and semiconducting nanomaterials such as ZnO, SnO_2, Fe_2O_3, and TiO_2 [12-16] having small band gap and chemical stability but there are some drawbacks, which are mentioned in following points.

1) Fast recombination rate of e^- and h^+ pairs.
2) Agglomeration of nanoparticles.
3) Stability of nanoparticles.
4) Recyclability or reusability

For consideration of above points, several efforts have been made to immobilize nanoparticles for enhancing their efficiency by their encapsulation into different substrates or porous materials such as zeolite, clay and carbon nanotubes [17]. Recently, core@shell composites, involving metal organic frameworks as shell/host, have been reported to reduce the agglomeration of bare nanoparticles and recombination rate of e^- and h^+ pairs, thereby, enhancing their photocatalytic efficiency [18]. Further, shell materials provided the stability to core materials and can be utilized for several cycles.

1.1.1. About MOFs

Metal organic frameworks (MOFs) are constituted by metal ions or metal cluster ions occupy at nodal positions held by bi/or multipodal organic linkers [19] as shown in Scheme 1.2. The crystal structure defines empty spaces in the range of nanometre scales [20]. After detailed discussion of world famous scientist related to material science on the coordination polymer and metal organic framework terminology in IUPAC (*International Union of Pure and*

Applied Chemistry) forum, it has been suggested that "***Metal Organic Framework (MOF) is a coordination network with organic ligands containing potential voids***" [21].

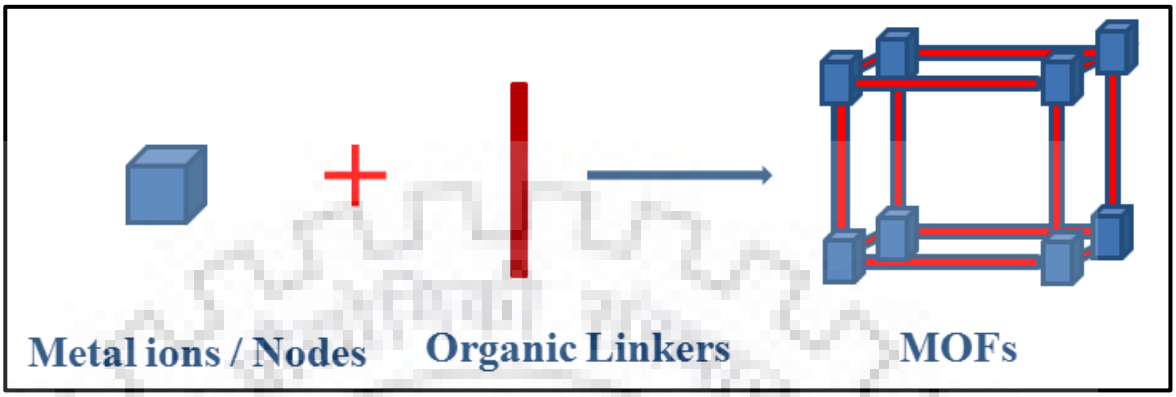

Scheme 1.2. General representation of MOFs structure.

Metal organic frameworks have emerged as an extensive class of crystalline materials with ultra-porosity (up to 90% free volume) and enormous internal surface area. Zeolites and activated carbon exhibit maximum surface area *ca.* 1000 m^2/g and 3500 m^2/g, respectively, while MOFs exhibit 10000 m^2/g which is outmost apparent surface area and porosity are reported so far [22, 23]. Other important features of MOFs are their chemical composition such as the diversity of transition metal ions and variety of organic linkers. Owing to high surface area, tunable shape and size and diversity of chemical compositions, MOFs can be used in the various applications such as gas storage, gas sensing, catalysis, CO_2 capturing, drug delivery and imaging [24-38].

1.1.2. Synthesis of MOFs

Various methods have been reported for the synthesis of MOFs as illustrated in Scheme 1.3. Liquid-phase synthesis methods are exclusively preferred wherein a metal salt and ligand solutions are mixed together in a narrow reaction vial without disturbing the liquid-liquid interface. In the liquid-phase synthesis, solvents play an important role for determining the different aspects such as reactivity, solubility, redox potential, thermodynamics of reaction, activation energy and stability constant etc. Apart from this, solid-phase synthesis methods have been utilized, which are easier and rapid but have some drawbacks, *for instance*, development of a single crystal. Further, there are broad categories of synthesis methods such as solvothermal, hydrothermal, microwave assisted synthesis, sonochemical synthesis, slow

evaporation, mechanochemical synthesis and electrochemical synthesis methods have been employed to synthesize MOFs.

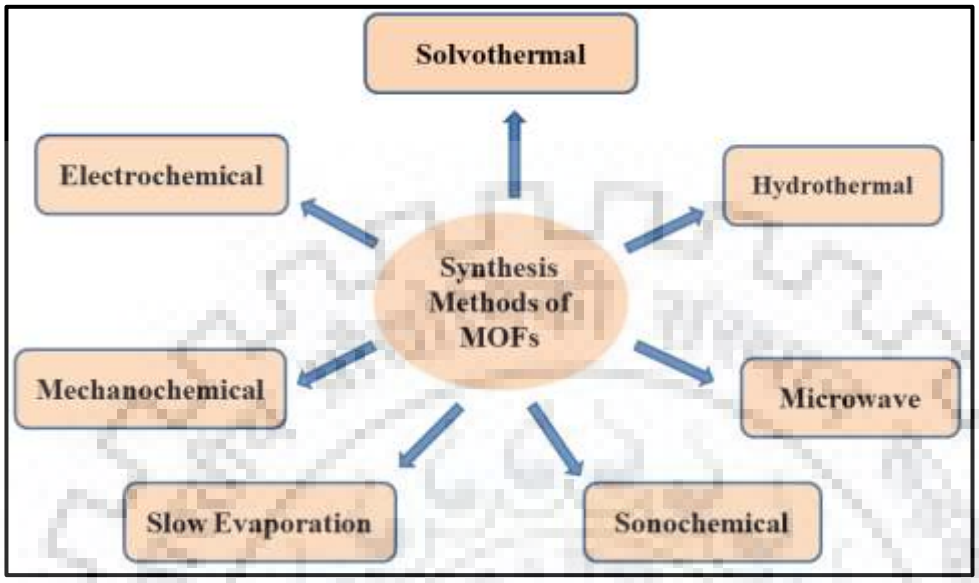

Scheme 1.3. Methods of synthesis of MOFs.

1.1.2.1. Solvothermal Method

In this method, the reactions are carried out in closed vessels under autogenous pressure above the boiling point of non-aqueous solvent for *e.g.* dimethylformamide, acetonitrile, acetone, ethanol, methanol, etc. To avoid the solubility problems of different starting materials, a mixture of solvents is preferred. Temperature is also one of the important parameters for the synthesis of hybrid materials. This method permits the modification in controlling shape, size and crystallinity of the materials [39]. ZIF-8 has been synthesized by this method [40] using $ZnCl_2$, 2-methyleimidazole and $NaHCO_2$ in 1:2:2 molar ratios in methanol. The resultant solution was placed in a sealed glass tube under homogeneous heating at 130 °C for 4 h in a conventional oven. The rhombic dodecahedral crystal of ZIF-8 has been obtained as shown in Fig. 1.4.

1.1.2.2. Hydrothermal Method

Hydrothermal synthesis method is similar to solvothermal method but there is a principal difference of solvent, and materials can be crystallized from aqueous solution at high vapour pressure in closed vessels. In 1995, Cu metal based 3D MOF has been synthesized by using a mixture of copper nitrate pentahydrate (0.74 mmol), 4,4-bipyridine (1.11 mmol) and 1,3,5-triazine (0.49 mmol) in 15 mL deionized water (DI H_2O) which was placed in

programmable furnace at 140 °C for 12 h. A rectangular orange crystal of Cu(4,4-bpy)$_{1.5}$.NO$_3$(H$_2$O)$_{1.25}$ has been obtained [41].

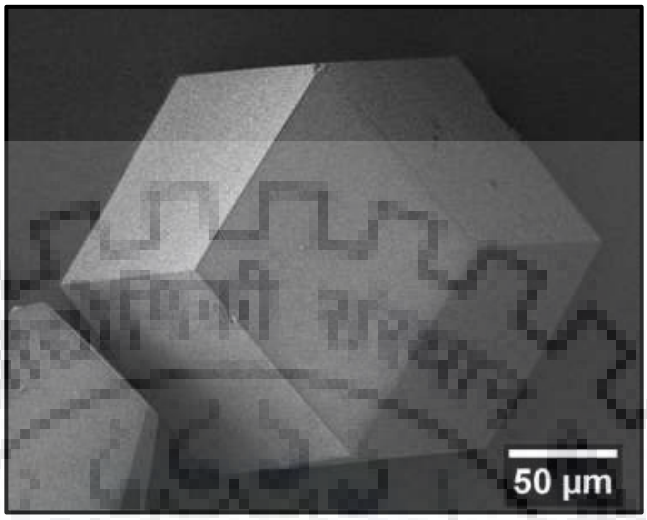

Fig. 1.4. SEM image of ZIF-8 crystal synthesized by solvothermal method [40].

1.1.2.3. Microwave-Assisted Synthesis

It provides a rapid synthesis of MOFs. A mixture of metal and ligand solution is allowed to react in a microwave reactor for an hour to produce nano-sized crystals. This method provides uniformity in the quality of crystals of MOFs as compared to solvothermal method [42]. Isoreticular metal organic framework (IRMOF) has been synthesized by employing this method. The clear solution of Zn(NO$_3$)$_2$.6H$_2$O (0.67 mmol) and 1,4-benzenedicarboxylic acid (0.50 mmol) in 10 mL of N,N-diethylformamide (DEF) was placed in a 4 mL Pyrex sample vial for microwave heating at 150 W. Finally, cubic crystals of IRMOF-1 (shown in Fig. 1.5) having average particle size 4 ± 1 µm have been obtained [43].

1.1.2.4. Sonochemical Synthesis

Sonochemistry is a phenomenon in which molecules undergo chemical change owing to intense ultrasonic radiation (20-10 kHz). In this method, a cavitation process involves the formation, growth and instant collapse of bubbles in liquid due to chemical and physical changes which create local hot spots of a short lifetime at high temperature and pressure [44]. By employing this method, MOF-5 has been synthesized using Zn(NO$_3$)$_2$.6H$_2$O and terephthalic acid as organic linker. The mixture of reactants were dissolved in 40 mL of NMP (1-methyl-2-pyrrolidone) and transferred into 50 mL tube reactor and allowed to ultrasonication for 10-75 min at 20 kHz. MOF-5 has also been synthesized by convective

heating at 129-164 °C by using same reactants and compared the crystalline texture and morphology as illustrated in Fig. 1.6, which indicates that both have similar cubic morphology [45].

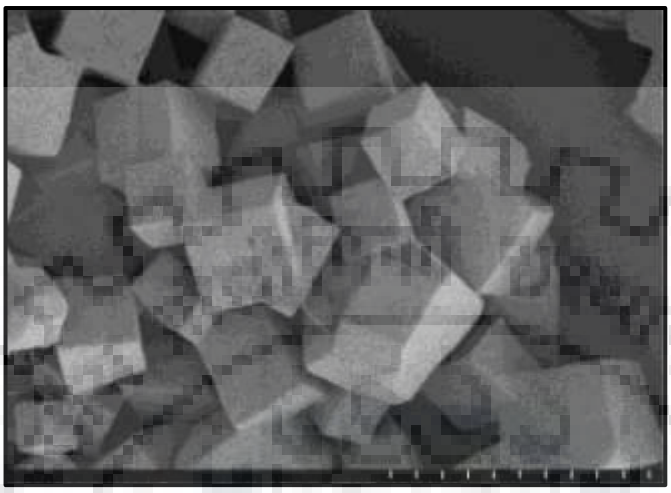

Fig. 1.5. SEM image of IRMOF-1 synthesized by microwave-assisted synthesis method [43].

1.1.2.5. Slow Evaporation Synthesis

It is conventional method for the synthesis of MOFs and co-ordination polymers without involving any additional energy. According to this method, solution of a mixture of starting material undergoes slow evaporation at ambient temperature; sometimes a mixture of solvents is used to increase the evaporation process. This method is slow and requires longer time period as compared to other methods [46]. A flexible building of co-ordination polymer $[Cu(pya)_2(H_2O)_2]_n$ has been synthesized by using this method; a methanol solution of 4-pyridylacetic acid was placed in a straight glass tube and maintained pH *ca.* 6 using aqueous solution of 0.1M KOH, followed by the addition of methanol solution of $Cu(ClO_4)_2.6H_2O$ and the reaction mixture was allowed for slow evaporation for several days. Blue prism crystal of $[Cu(pya)_2(H_2O)_2]_n$ co-ordination polymer has been obtained [46].

1.1.2.6. Mechanochemical Synthesis

This is a solvent free synthesis method in which a chemical reaction takes place by employing the mechanical force. Recently, Beldon *et al.* have synthesized MOFs using ligand-assisted grinding method [47]. This synthetic route was also applied for the synthesis of zeolitic imidazole frameworks. The reaction was carried out by grinding of 1:2 molar ratio of ZnO and

imidazole into 10 mL stainless steel jar along with 7 mm diameter stainless steel balls for 5-60 min continuously at ambient temperature [47]. Friscic *et al.* have investigated the effect of mixture of solvent in ligand-assisted grinding method and isolated successfully one-dimensional, two-dimensional and three dimensional co-ordination polymers from same reaction mixture [48].

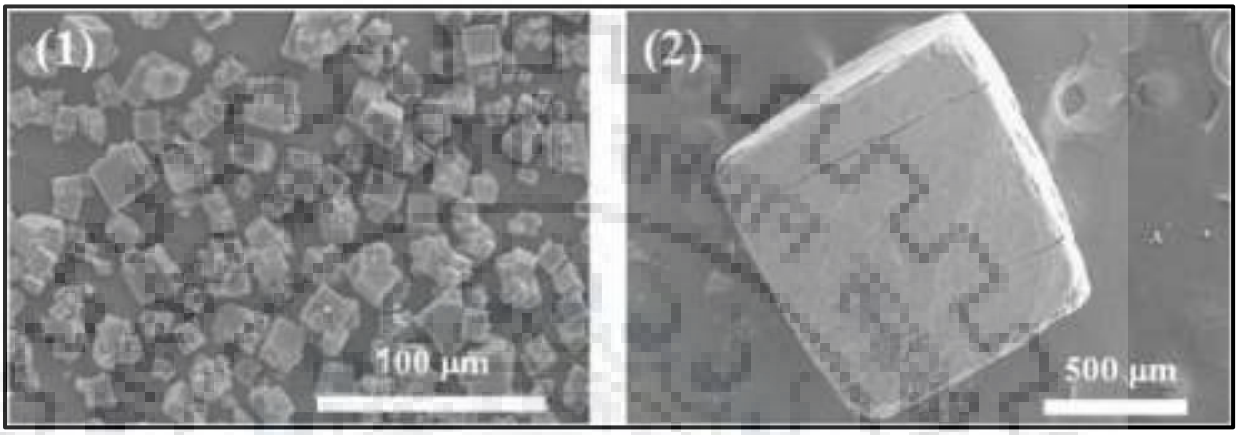

Fig. 1.6. SEM images of MOF-5 synthesized by (1) sonochemical method and (2) convective heating [45].

1.1.2.7. Electrochemical Method

Electrochemical method has been reported for the first time by BASF (Badische Anilin and Soda Fabrik) research group in 2005 [49]. The prime objective of this method was exclusion of anions, such as nitrate, perchlorate, or chloride during the reaction to produce the MOFs at large-scale. During synthesis of MOFs, metal ions instead of metal salts are introduced through anodic dissolution into the reaction medium which contains the dissolved organic linker molecules and a conducting salt. The depositions of metal ions are avoided by using protic solvents [50]. Several MOFs having various topology *viz.*, HKUST-1(HKUST = Hong Kong University of Science and Technology), ZIF-8 (ZIF-8 = Zeolitic imidazole framework-8), MIL-100(Al) (MIL = Material of Institute Lavoisier), MIL-53(Al) and NH2-MIL-53(Al) have been synthesized by this method. Among them, for the first time HKUST-1 metal organic framework has been synthesized by electrochemical method. A clear solution of 1,3,5-benzenetricarboxylic acid (15 mmol) and tributylmethylammonium methyl sulfate (MTBS, 33 mmol) in 100 mL ethanol were prepared [50]. The resultant solution was heated up to 40 °C in the electrochemical cell with two copper electrodes and passed 50 mA current

through the system for 1 h. Finally, HKUST-1 was electrochemically deposited on copper electrode as shown in Fig. 1.7.

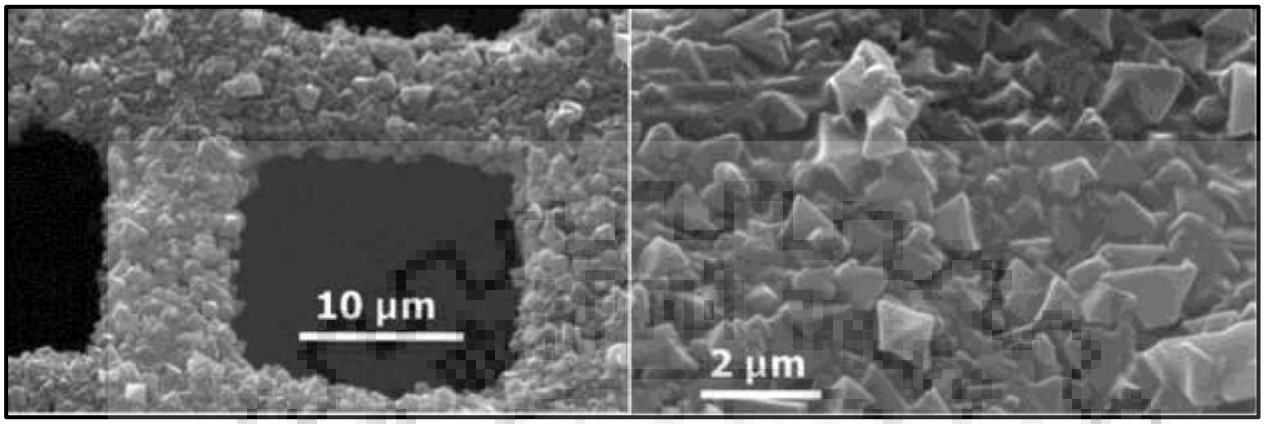

Fig. 1.7. SEM micrograph of HKUST-1 layered deposition on copper electrode [50].

1.1.3. Applications of MOFs

The combination of high porosity with tunable chemistry from metal ions and ligand functional groups leads to potential applications of MOFs in gas sorption, gas separation, drug delivery and catalysis [51] as illustrated in Scheme 1.4. Recently, main group IIA metal based MOFs are reported to exhibit lighter weight as compared to transition metal based MOFs, *for instance,* [mmen-Mg_2(dobpdc)] (mmen = N,N'-dimethylethylenediamine and dobpdc^{4-} = 4,4'-dioxido-3,3'-biphenyldicarboxylate) and it display an exceptional capacity for CO_2 adsorption at low pressure [52]. Undoubtedly, hydrogen has been using an alternative fuel because of its high energy content (120 MJ/Kg to 44 MJ/Kg for gasoline) and clean exhaust products (water vapor without CO_2 or NO_x). Eventually, eco-friendly hydrogen driven car were envisioned. In this regard, the hydrogen storage capacity of copper metal based MOFs named HKUST-1 was evaluated and the study revealed that this material can store 0.47 %wt of H_2 at 303K and 35 bar [53]. There are useful active sites within MOFs which are capable of binding molecules or ions. Recently, [Fe_2(dobdc)] (dobdc^{4-} = 2,5-dioxido-1,4-benzenedicarboxylate) metal organic framework has been reported to feature channels lined with very high concentration of Fe^{2+} cation sites and found to exhibit excellent performance characteristics for the separation of ethylene/ethane and propylene/propane mixture at 318 K [54]. In 2015, researcher at CSIRO (Commonwealth scientific and industrial research organisation) proved that biomolecules such as protein, enzyme and nucleic acid can be encapsulated within MOFs during the crystallization process and encapsulated enzymes have been found to be stable and active even after being treated rigorously in harsh conditions [55]. ZIF-8, MIL-88A, HKUST-1 and several

luminescent MOFs comprising of lanthanide metals have been utilized for the biomimetic mineralization process [55]. Regarding their use as heterogeneous catalysts, MOFs offer at least three different possibilities derived from their porous structure. The most widely explored strategy has been the exchange of the coordination number among the metal ions that will act as active sites. Recently, the importance of structural defects around the metal nodes and their implication in catalysis has been revealed [56]. The second methodology is based on the use of the ligands as active sites [57]. The third approach that derives from the large pore volume available in MOFs includes the incorporation of guest species in the internal void space that will act as a catalytic site [58].

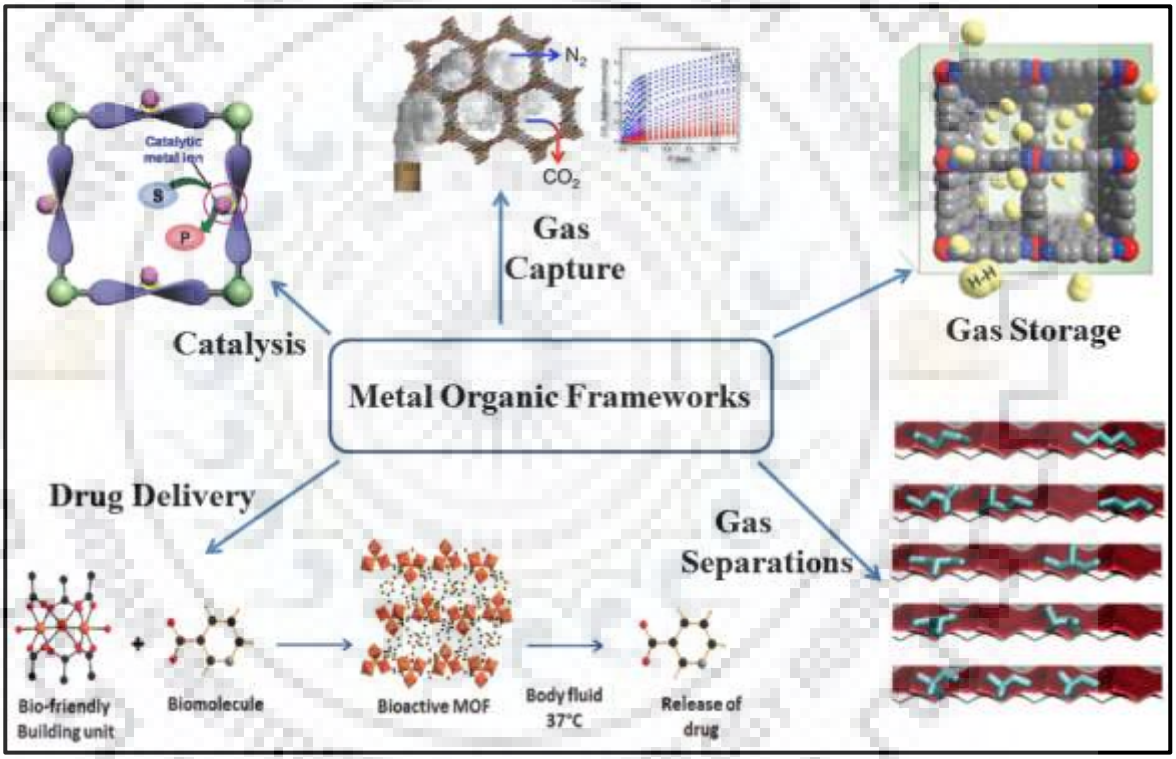

Scheme 1.4. Applications of MOFs in various fields [51].

1.2. LITERATURE REVIEW

The available literature of the last one decade pertaining to the synthesis, characterization and applications of ZIF-8 has been compiled in the following subsections. Metal oxides (MOx), metal nanoparticles (MNPs) and molecules encapsulated ZIF-8 (MO_x@ZIF-8, MNPs@ZIFs and molecules@ZIF-8) and their probable applications have also been incorporated.

1.2.1. Zeolitic Imidazole Frameworks (ZIFs)

Zeolitic imidazole frameworks (ZIFs) are a kind of metal organic framework which consists of mainly transition metal ions (*i.e.* Co and Zn) and imidazole or its derivatives as linkers. In ZIFs, metal centers are tetrahedrally-coordinated with N-atom of imidazole ring. The topology of ZIFs are identical to zeolite because metal-imidazole-metal (M-Im-M) bond angle is retained 145° (Scheme 1.5) as mentioned in aluminosilicate zeolite (Si-O-Si bond angle =145°).

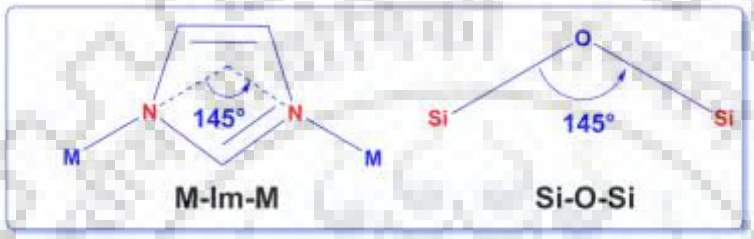

Scheme 1.5. The similar bond angle of M-Im-M and Si-O-Si are found to be 145° [59].

Yaghi *et al.* have reported numerous ZIFs associated with various interesting topology [59] which are tabulated in Table 1.1 and their single crystal structures are illustrated in Scheme 1.6. Among them, ZIF-8 and ZIF-11 are chemically and thermally stable. ZIF-8 and ZIF-11 have large pores 11.6 Å and 14.6 Å connected with small apertures 3.4 Å, and 3.0 Å, respectively [59]. ZIF-8 has been synthesized by solvothermal method. A mixture of $Zn(NO_3)_2.4H_2O$ (0.803 mmol) and 2-methylimidazole (0.731 mmol) was dissolved in dimethylformamide (DMF) and placed in 20 mL stainless steel vial. The capped vial was heated at 140 °C with increasing rate of 5 °C per min for 24 h and then cooled it at 4 °C per min to room temperature. After that colourless polyhedral crystals of ZIF-8 has been obtained. Sorption analysis and apparent surface area of ZIF-8 (1810 m^2 g^{-1} for Langmuir model and 1630 m^2 g^{-1} for Brunauer-Emmett-Teller model) surpass the highest value for zeolite and mesoporous materials [60-62]. Owing to their enormous porosity and tremendous chemical and thermal stability, they have been utilized preferentially in many applications like gas storage, adsorbent, drug delivery and host of catalyst in heterogeneous catalysis.

Table 1.1. Composition, structure and textural properties of ZIFs [59].

ZIFs	Compositions	Net	Zeolite	T/V (nm^{-3})	d(Å)	N
ZIF-1	$Zn(Im)_2$	crb	BCT	3.64	6.94	12
ZIF-2	$Zn(Im)_2$	crb	BCT	2.80	6.00	12
ZIF-3	$Zn(Im)_2$	dft	DFT	2.66	8.02	16
ZIF-4	$Zn(Im)_2$	cag	-	3.68	2.04	20
ZIF-5	$In_2Zn_3(Im)_{12}$	gar	-	3.80	3.03	20
ZIF-6	$Zn(Im)_2$	gis	GIS	2.31	8.80	20
ZIF-7	$Zn(PhIm)_2$	sod	SOD	2.50	4.31	24
ZIF-8	$Zn(MeIm)_2$	sod	SOD	2.47	11.60	24
ZIF-9	$Co(PhIm)_2$	sod	SOD	2.51	4.31	24
ZIF-10	$Zn(Im)_2$	mer	MER	2.25	12.12	24
ZIF-11	$Zn(PhIm)_2$	rho	RHO	2.01	14.64	48
ZIF-12	$Co(PhIm)_2$	rho	RHO	2.01	14.64	48

* Im = Imidazole, MeIm = 2-methyleimidazole, PhIm = benzimidazole, T/V = density of metal atom per unit volume and N = number of vertices of largest cage. Net and zeolite topology of three letters abbreviation come from reticular chemistry structure source [59].

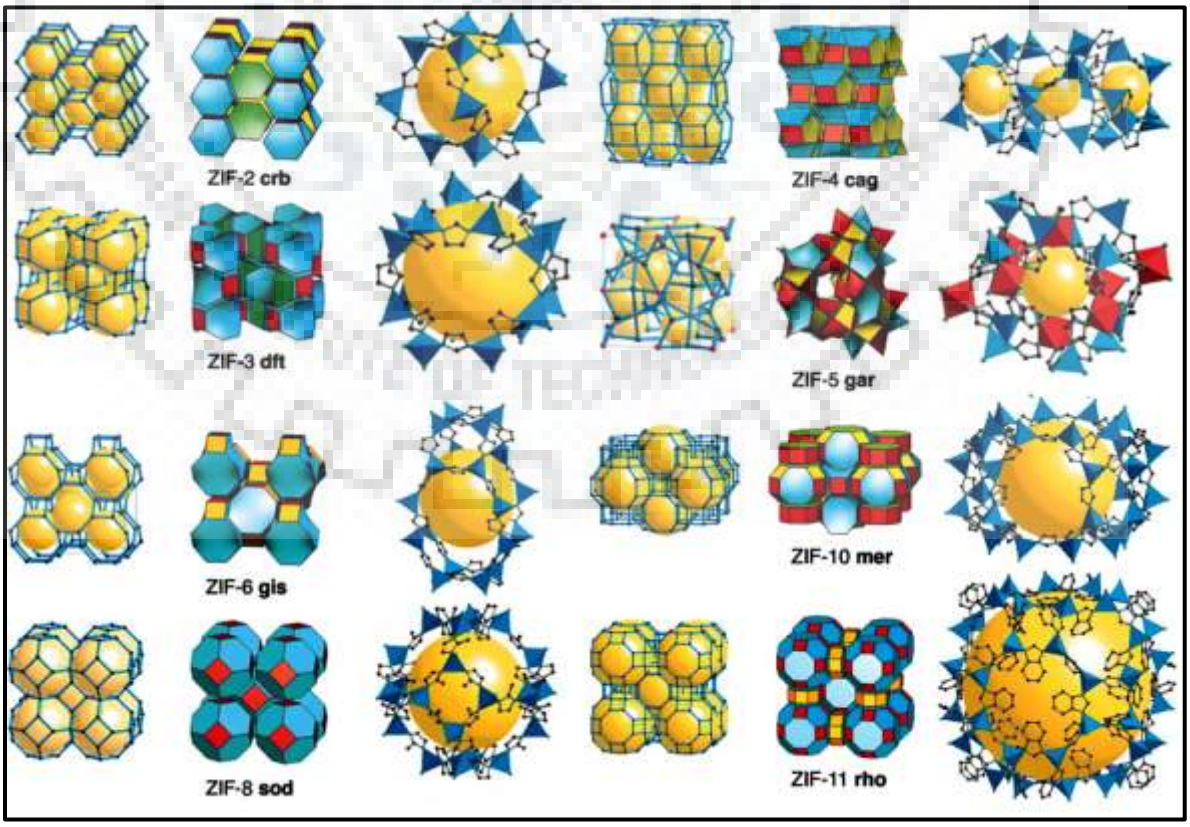

Scheme 1.6. The single crystal X-ray structure and largest cage in each ZIFs [59].

Yaghi *et al.* have evaluated the CO_2 capturing efficiency of various ZIFs [63]. In order to optimize the synthetic conditions and extend the applications of ZIF-8, Carreon *et al.* have synthesized ZIF-8 membranes (*ca.* 5-9 μm thickness) by employing "*secondary seeded growth*" on tubular α-Al_2O_3 porous support and exploited them for the separation of CO_2/CH_4 [64]. Additionally, a silicon substrate was employed to obtain ZIF-8 film which was utilized as a selective sensor for the chemical vapors and gases [65].

Wang *et al.* have reported the "*contra-diffusion*" synthesis of ZIF-8 film on a polymer substrate such as nylon [66]. Contra-diffusion is a facile synthesis method wherein ZIF-8 can be grown conveniently on a flexible polymer substrate as illustrated in Scheme 1.7. Similar method has been adopted for the *in situ* synthesis of thin membrane of ZIF-8 for the separation of propylene and propane hydrocarbons [67]. In continuation, ZIF-8 membranes have been developed on a porous α-alumina disc via "hydrothermal seeded growth" method [68] and utilized for the effective separation of a mixture of hydrocarbons such as ethane/propane, ethylene/propylene and ethylene/propane, etc.

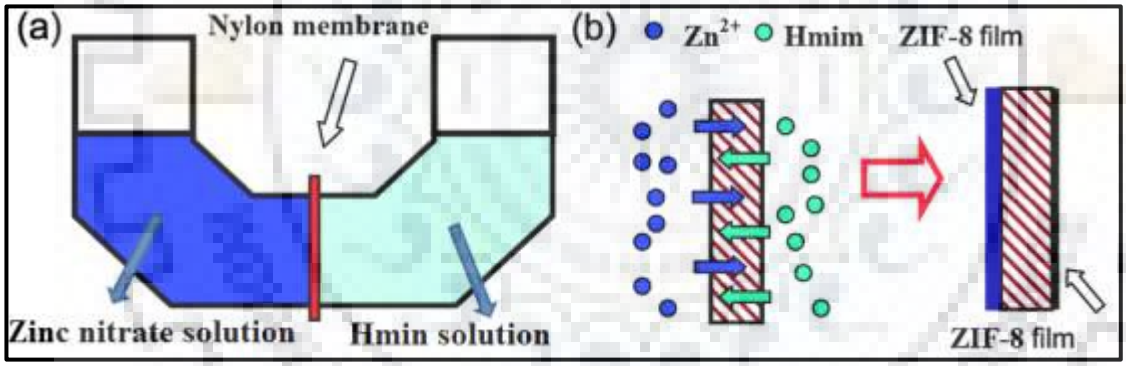

Scheme 1.7. (a) Diffusion cell and (b) schematic representation of ZIF-8 film formation on both sides of nylon support [66].

Hump *et al.* reported ZIF-8 opening into zeolitic imidazole framework (ZIF) material of SOD topology having primarily unsubstituted imidazole linker by "*Solvent Assistant Linker Exchange*" method (SALE) [69] which is illustrated in Scheme 1.8. It has been reported that ZIF materials exhibit the Bronsted base catalysis which cannot be accomplished by ZIF-8.

Yamauchi *et al.* have synthesized nanoporous carbon particles by employing a simple *"carbonization"* method of mono-dispersed ZIF-8 crystal which is confirmed by quartz crystal micro-balance studies (QCMB). The small sized nanoporous carbon particles were utilized as good adsorbent and fast sensor for the detection of toluene molecule [70].

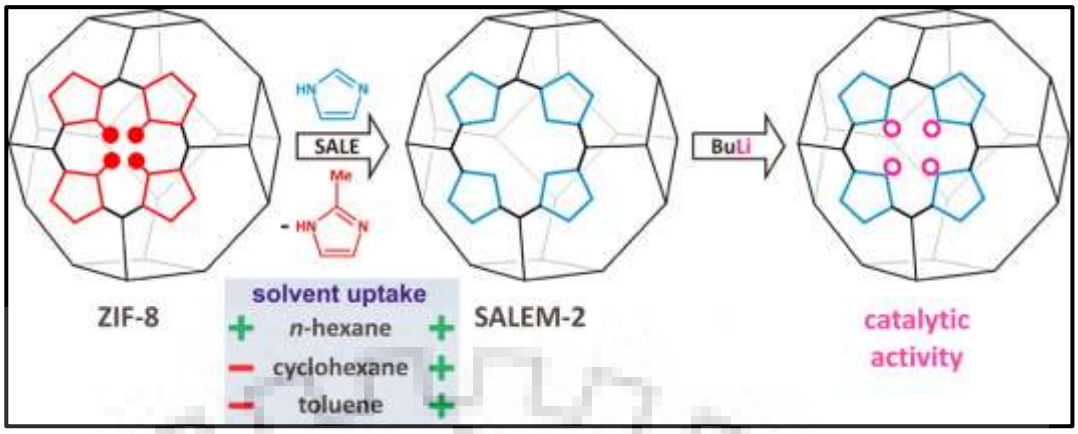

Scheme 1.8. ZIF-8 exchange into ZIF having primarily unsubstituted imidazole linker by SALE method [69].

Wang *et al.* have reported "slow evaporation" method for the synthesis of ZIF-8 and exploited ZIF-8 as a photocatalyst for photocatalytic degradation of methylene blue (MB) under UV light irradiation. The plausible mechanism and degradation path of MB have also been discussed [71].

The synthesis of multi-facets hollow oxide composites using ZIF-8 was reported by Chen *et al.* [72] (Scheme 1.9). The hollow oxide composites ZnO/SiO_2 and ZnO/TiO_2 were synthesized using ZIF-8 by employing sol-gel coating of metal oxide precursor of SiO_2 and TiO_2 nanoparticles, respectively.

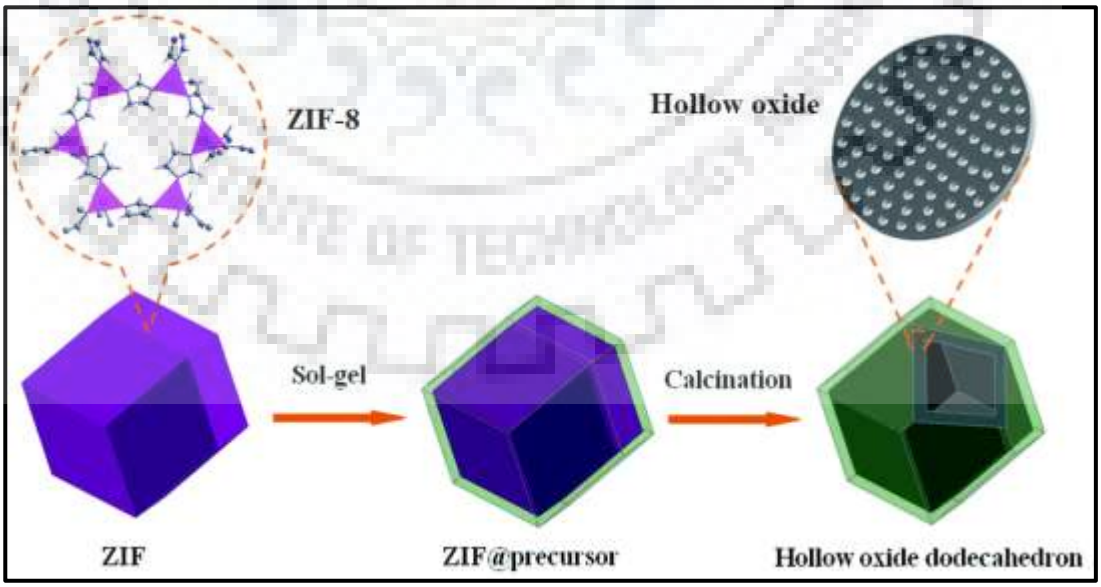

Scheme 1.9. Schematic illustration of synthesis of hollow oxide composites using ZIF-8 [72].

1.2.2. Metal Nanoparticles (MNPs) Encapsulated Zeolitic Imidazole Framework-8: MNPs@ZIF-8

Fabrication of ZIFs with metal oxide, novel metal nanoparticle and drug molecule has been an emerging challenge among the scientific community. So far, only a few publications pertaining to the metal nanoparticles encapsulated ZIF-8 have been reported which are compiled in Table 1.2.

Xu *et al.* have reported the hydrogen generation from hydrolysis of ammonia borane by employing Ni nanoparticle encapsulated composite (Ni@ZIF-8) synthesized by the *"chemical deposition"* method [73]. The highly dispersed Ni NPs were successfully immobilized within ZIF-8 matrix yielding water stable composite which exhibits the excellent catalytic activity for the hydrolysis of ammonia borane.

Iridium nanoparticles were stabilized and immobilized within ZIF-8 [74]. IrNPs@ZIF-8 composite was synthesized by sublimation of gas phase loading of Ir(COD)(MeCp) into activated ZIF-8 followed by the hydrolysis of Ir(COD)(MeCp)@ZIF-8 compound at 300 °C (COD = 1,5-cyclooctadiene and MeCp = methylcyclopentadienyl). IrNPs@ZIF-8 composite was utilized for the hydrogenation of cyclohexene and phenylacetylene under very mild conditions as shown in Scheme 1.10. Further, the stability, selectivity, and reusability of IrNPs@ZIF-8 composite have also been analyzed.

Scheme 1.10. (a) Hydrogenation of cyclohexene and (b) phenylacetylene using IrNPs@ZIF-8 composite [74].

Various metal nanoparticles associated with different particle sizes and modified with polyvinylpyrrolidone (PVP) were encapsulated within ZIF-8 as illustrated in Scheme 1.11 [75]. The controlled synthesis method was adopted to yield Pt@ZIF-8, Fe_3O_4/ZIF-8, $NaYF_4$/ZIF-8 and CdTe/ZIF-8 and their catalytic, magnetic and photoluminescence properties have been studied. Pt@ZIF-8 composite has been applied for the size selective hydrogenation of *n*-hexene and *cis*-cyclooctene and field dependent magnetization curve of Fe_3O_4/ZIF-8 composite exhibits the supermagnetic behavior while $NaYF_4$/ZIF-8 and CdTe/ZIF-8 were used as luminescent material.

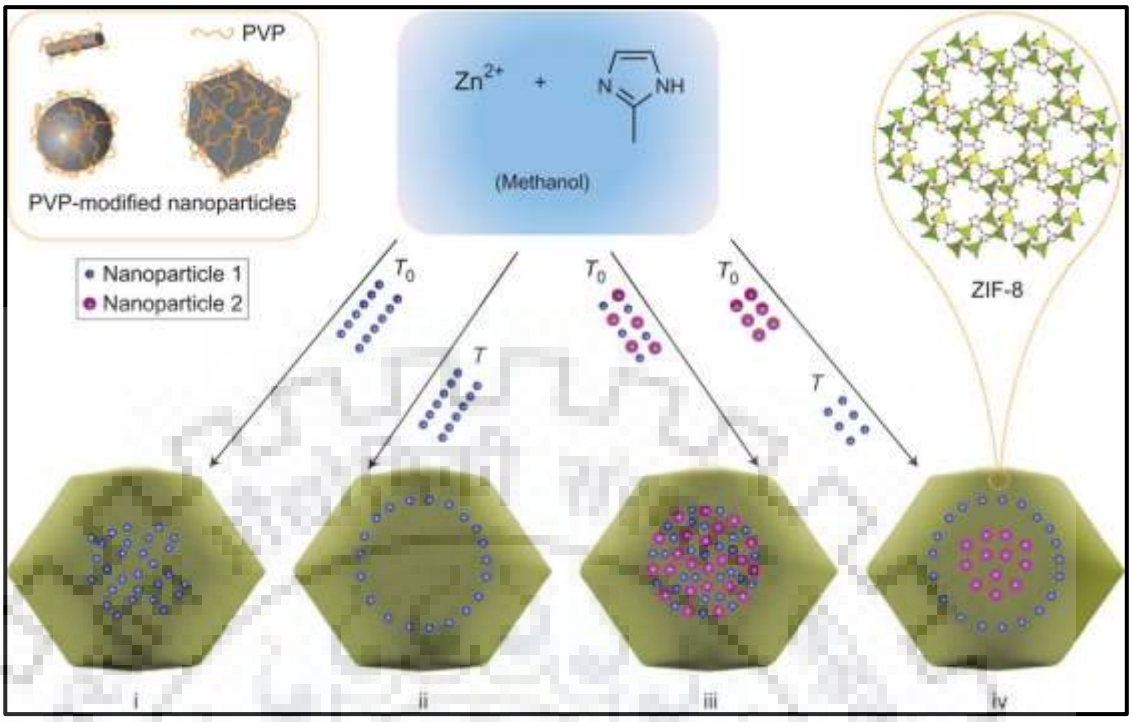

Scheme 1.11. Schematic illustration of nanoparticle distribution within MOFs (i) in the central area (ii) off the central area (iii) mixture of various sizes of nanoparticle in the central area (iv) and bigger nanoparticle in the central while smaller particle shown off the central area [75] (T_0 represents the encapsulation of nanoparticle at the beginning of reaction while T represents the encapsulation of nanoparticle at certain time during the synthesis of MOF).

Duan *et al.* have reported the synthesis of single and multi-core shell structure of Au encapsulated Au@ZIF-8 composite and utilized it as a catalyst [76]. The polyvinylpyrrolidone (PVP) modified Au NPs were encapsulated *in situ* synthesis of ZIF-8 by incubation at 50 °C for 2 h (Scheme 1.12). As a consequence, single and multi-core shell AuNPs@ZIF-8 composites have been obtained. Due to synergic effect of Au NPs and ZIF-8, AuNPs@ZIF-8 composite has been exploited as a good catalyst for the oxidation of benzyl alcohol. Subsequently, the bimetallic nanoparticles were also encapsulated within ZIF-8. The PVP modified Pd/Au nanoparticles were encapsulated during the synthesis of ZIF-8 and resulting Pd/Au@ZIF-8 composite has also been used as catalyst for the liquid phase aerobic alcohol oxidation [77].

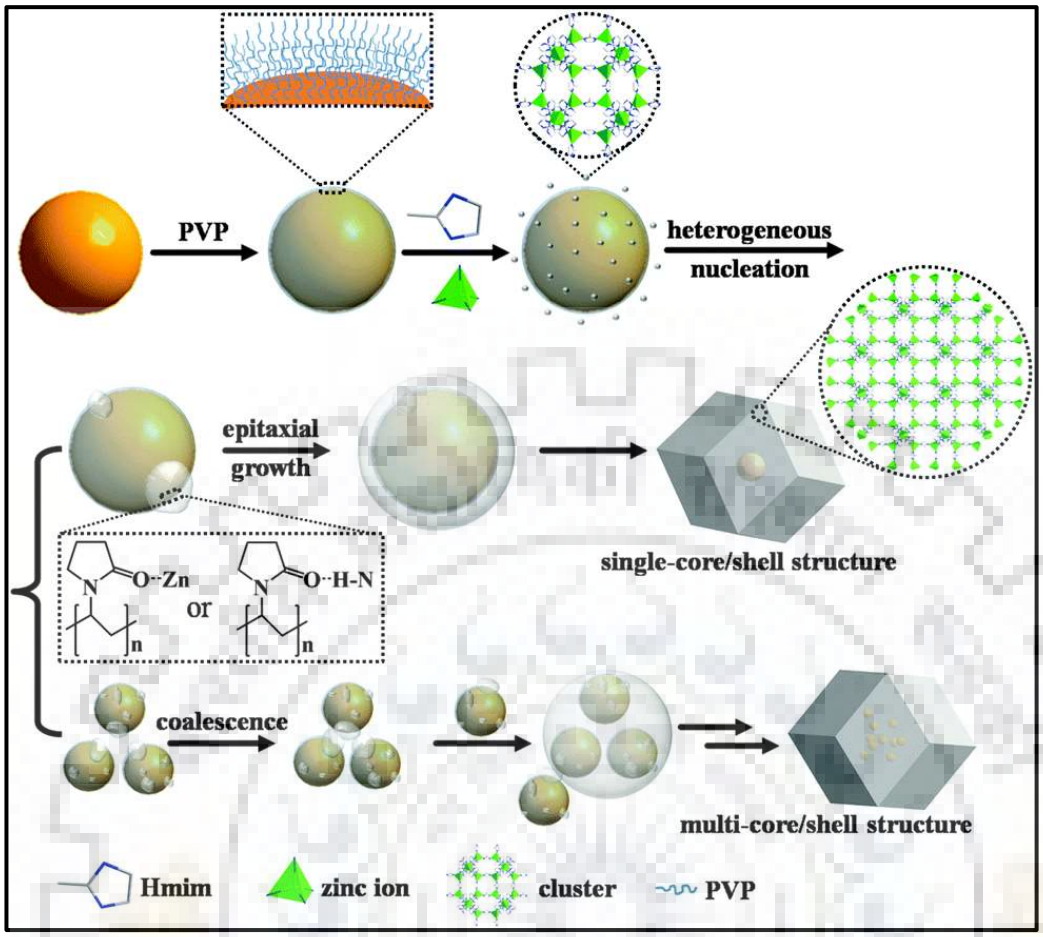

Scheme 1.12. Schematic illustration of Au NPs encapsulation and synthesis of single or multi-core-shell AuNPs@ZIF-8 composite [76].

Yeung *et al.* have reported the hierarchically core-shell structure of Pd decorated mesoporous silica sphere (MSS) and ZIF-8 [78]. Pd/MSS@ZIF-8 composite has been synthesized in two steps as shown in Scheme 1.13. In the first step, Pd nanoparticles were decorated on the uniform sized mesoporous silica spheres (MSS) and subsequently ZIF-8 was grown on the surface of Pd/MSS. Further, the synthesized Pd/MSS@ZIF-8 composite was used for the hydrogenation of 1-hexene and cyclohexene. For the first time, Pt decorated ZIF-8 was loaded within TiO_2 nanotubes which have been utilized for the degradation of phenol [79]. The specific architecture of composite material was developed by fabrication of Pt, ZIF-8 and TiO_2 nanotubes. The Pt/ZIF-8 loaded TiO_2 nanotubes degraded off 18.6% phenol under visible light irradiation. The path way for the photocatalytic degradation of phenol is vividly shown in Scheme 1.14.

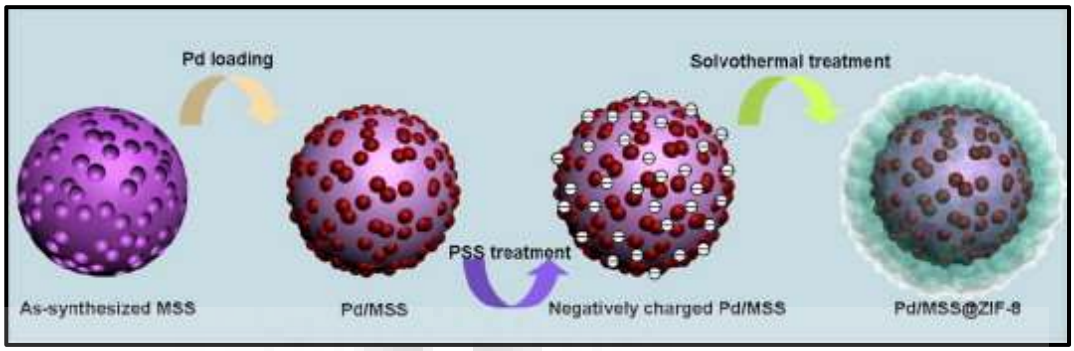

Scheme 1.13. Synthesis of core-shell Pd/MSS@ZIF-8 composite [78].

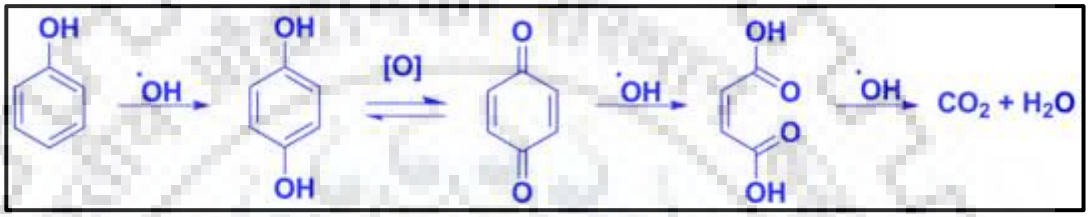

Scheme 1.14. The degradation path way of phenol using Pt/ZIF-8 loaded TiO_2 nanotube [79].

ZIF-8 was grown on Ag nanowires to synthesize Ag@ZIF-8 heterostructure nanowires for the biological application [80]. The pre-synthesized Ag nanowires were sonicated with imidazole ligand and stirred with zinc metal salt for 2 h at room temperature. Ag@ZIF-8 heterostructure was investigated for antibacterial activity against Gram-positive (*Bacillus subtilis*) and Gram negative (*Escherichia coli BL21*) bacteria which exhibits 100% inhibition of *B. subtilis* bacteria with 200 µg/mL after 8 h incubation while 300 µg/mL concentration was used for *E. coli*.

Tsung *et al.* have reported the synthesis of yolk-shell nanocrystal@ZIF-8 nanostructures using CuO_2 as sacrificial template [81]. New strategy has been adopted for the synthesis of Pd nanocrystal@ZIF-8 composite wherein yolk-shell nanostructure possess core (Pd), microporous shell (ZIF-8) and a cavity in between core-shell which is shown in Fig. 1.8. Nanocrystal@ZIF-8 nanostructures have been applied as catalysts for the hydrogenation of alkene. Interestingly, core (Pd nanocrystal), shell (microporous ZIF-8) and cavity between them provide new strategy/tool for efficient and selective heterogeneous catalysis [81]. Fe-ZIF-8 composite has been synthesized by doping of Fe(II) *in situ* synthesis of ZIF-8 and utilized as a sunlight driven photocatalyst for the degradation of remadazole deep black (RDB) [82].

For the first time, Wang *et al.* [83] have synthesized Ag/AgCl@ZIF-8 composite using pre-synthesized ZIF-8 and $AgNO_3$. ZIF-8 (0.1 g) was dispersed into 7 mL of $AgNO_3$ solution

(1:6 volume ratio of water and ethanol) and stirred at room temperature. The resultant suspension was injected drop wise into 49 mL NaCl solution (10.48 mmol in to 1:6 volume ratio of water and ethanol) yielding Ag/AgCl@ZIF-8 composite (Scheme 1.15) which is utilized as photocatalyst for the degradation of rhodamine-B under visible light irradiation.

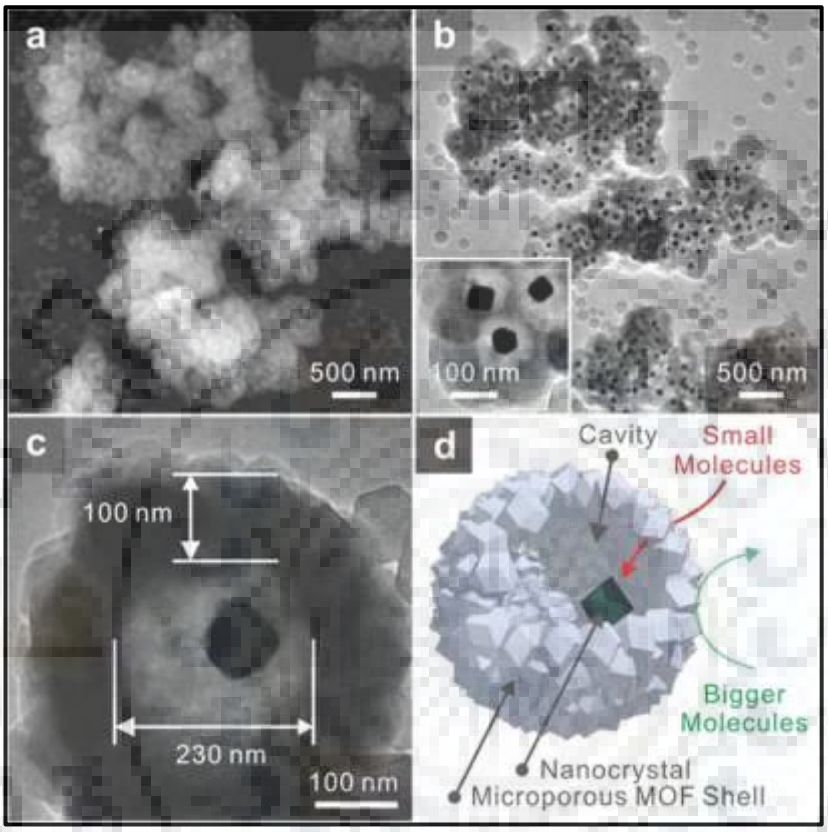

Fig. 1.8. (a) SEM and (b, c) TEM images indicate the formation of yolk-shell nanocrystal@ZIF-8 nanostructures. (d) schematic illustration of yolk-shell nanostrucutre [81].

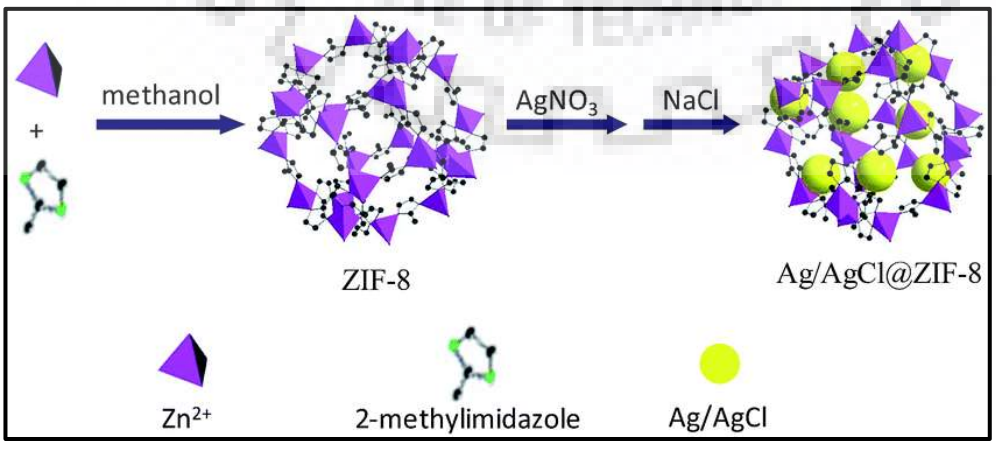

Scheme 1.15. Schematic illustration of synthesis of Ag/AgCl@ZIF-8 composite [83].

Similarly, Ag/AgCl/ZIF-8 composites have been synthesized and exploited as photocatalyst for the degradation of rhodamine-B [84] and acetaminophen [85]. Further, Ag@AgCl nanofilm was grown on the ZIF-8 surface [86]. 0.1 g ZIF-8 was dispersed into $AgNO_3$ solution and kept on constant stirring and the suspension was irradiated with UV-visible light for 30 min resulting Ag@AgCl nanofilm/ZIF-8 composite. Ag@AgCl nanofilm/ZIF-8 composite was employed as visible light driven photocatalyst for the degradation of methylene blue.

Table 1.2. Metal nanoparticles encapsulated ZIF-8 and their applications [73-86].

S.N.	Materials	Encapsulated Nanoparticle	Application	Ref.
1	Ni@ZIF-8	Ni Nanoparticle	Hydrolysis of Ammonia borane	73
2.	IrNPs@ZIF-8	IrNPs	Hydrogenation of Cyclohexene	74
3	Au@ZIF-8, Pt@ZIF-8, T-Pt@ZIF-8, Fe_3O_4/ZIF-8, $NaYF_4$/ZIF-8 and CdTe/ZIF-8	Au, Pt, Fe_3O_4, $NaYF_4$ and CdTe	Catalytic, Magnetic and Photoluminescence Studies	75
4	Au@ZIF-8	Au	Oxidation of benzyl alcohol	76
5	Pd/Au@ZIF-8	Pd and Au	Liquid Phase Aerobic Alcohol Oxidation	77
6.	Pd/MSS@ZIF-8	Pd/MSS	Hydrogenation of Alkenes	78
7	Pt/ZIF-8/TiO_2	Pt and TiO_2	Photodegradation of Phenol	79
8.	Ag@ZIF-8	Ag nanowire	Anti-bacterial Activity	80
9.	Nanocrystal@ZIF-8	Pd	Hydrogenation of Alkene	81
10	Fe-ZIF-8	Fe	Photodegradation of remadazole deep black (RDB)	82
11	Ag/AgCl/ZIF-8	Ag/AgCl	Photodegradation of rhodamine-B (RB) and acetaminophen	83-85
12	Ag@AgCl nanofilm/ZIF-8	Ag@AgCl nanofilm	Photodegradation of methylene blue (MB)	86

1.2.3. Metal Oxides Nanoparticles Encapsulated Zeolitic Imidazole Framework-8: MO_xNPs@ZIF-8

Some metal oxides *viz.*, ZnO, Fe_3O_4, SnO_2, and TiO_2 have also been encapsulated within zeolitic imidazole framework for various applications as compiled in Table 1.3. For the first time, Quantum confined ZnO nanoparticles were stabilized within ZIF-8 [87]. ZnO@ZIF-8 was synthesized using *"chemical vapor deposition infiltration"* method followed by oxidative annealing, and the composite was utilized for the CO_2 adsorption. In addition, ZIF-8 has been grown on the surface of ZnO nanorod and obtained the core-shell ZnO@ZIF-8 heterostructures wherein ZnO nanorod acts as core material and ZIF-8 acts as shell material [88]. ZnO@ZIF-8 heterostructure has been synthesized by hydrothermal synthesis method wherein ZnO used as template also provides Zn^{2+} ion for the synthesis of ZIF-8 as illustrated in Scheme 1.16. The synthesized ZnO@ZIF-8 heterostructure has been analyzed for photocurrent response toward H_2O_2 in the presence of serous buffer.

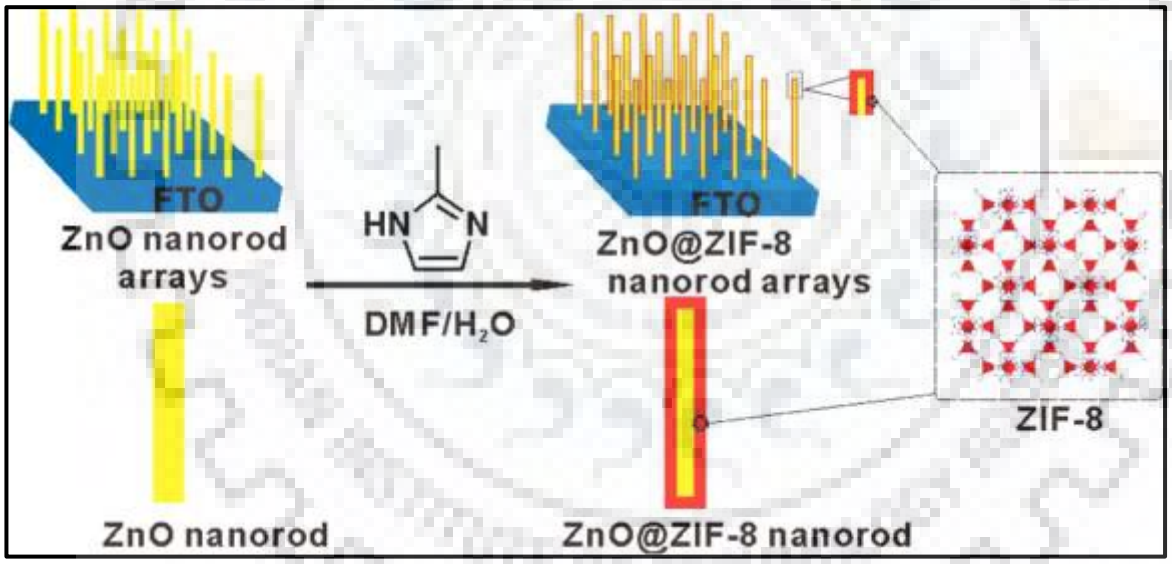

Scheme 1.16. Synthesis of core-shell ZnO@ZIF-8 heterostructure [88].

Wee *et al.* have reported the synthesis of ZnO nanorod@ZIF-8 composite which is used as a photocatalyst for the photocatalytic degradation of methylene blue under UV light irradiation [89]. Similarly, core-shell ZnO@ZIF-8 nanospheres were synthesized by using ZnO as self-template and utilized for the photocatalytic degradation of methylene blue under UV light irradiation [90].

Wang *et al.* have reported the rapid construction of ZnO@ZIF-8 heterostructures [91]. ZnO colloidal spheres were employed as template and Zn^{2+} source for the synthesis of ZIF-8,

and ZnO@ZIF-8 heterostructures were utilized for size selective reduction of Cr(VI) and methylene blue as shown in Scheme 1.17.

Recently, Luo *et al.* have reported the synthesis of ZnO/ZIF-8 hybrid material using $AgNO_3$ [92]. The synthesized ZnO/ZIF-8 hybrid material has been employed as catalyst for the degradation of rhodamine-B under UV light (300 Watt UV lamp at $\lambda = 400$ nm). ZnO nano rod was recently induced by $AgNO_3$ and embedded on the ZIF-8 surface. Further, synthesized ZnO@ZIF-8 material has been evaluated as antimicrobial catheters [93].

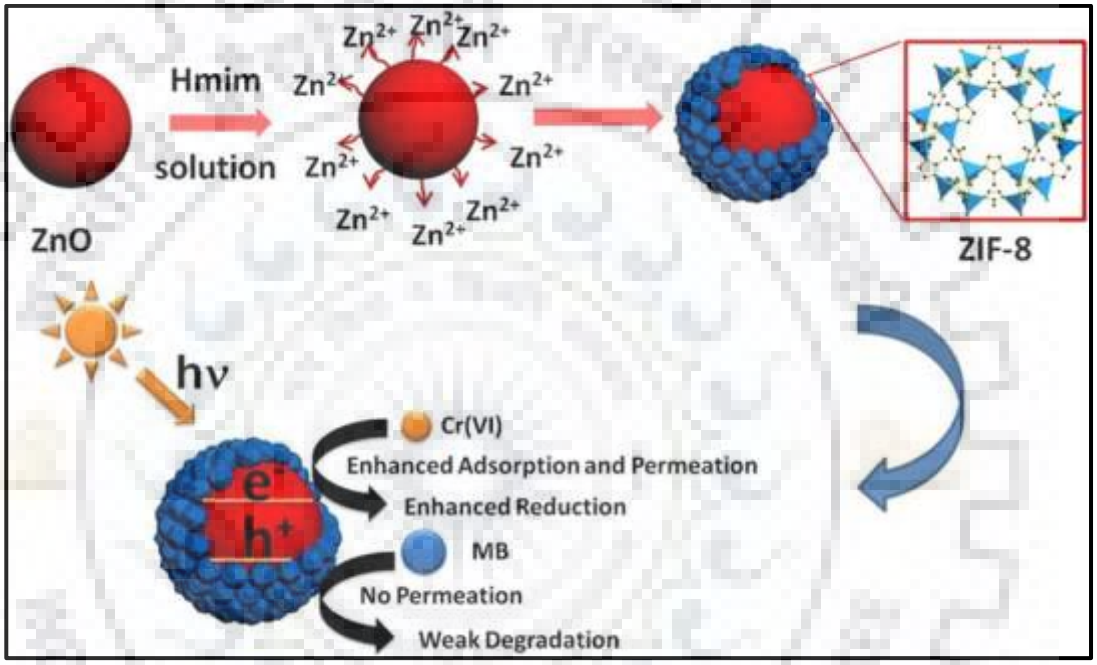

Scheme 1.17. Schematic illustration of synthesis and photocatalysis of ZnO@ZIF-8 [91].

PSS (Poly styrenesulfonate sodium sulphate) modified Fe_3O_4 microsphere has been encapsulated successfully within ZIF-8 matrix by stirring of starting materials (Fe_3O_4 microsphere, 2-methyleimidazole and zinc nitrate hexahydrate) at 323 K for 3 h [94] while Gei *et al.* reported the aqueous synthesis of Fe_3O_4@ZIF-8 composite at ambient temperature [95] which was exploited for the Knoevenagel condensation reaction. Fe_3O_4@ZIF-8 composite can be separated very easily and reused for several cycles on account of its magnetic behaviour. Further, core-shell Fe_3O_4@ZIF-8 heterostructure was synthesized by encapsulation of Fe_3O_4 without any modification and was utilized as an efficient adsorbent for the methylene blue [96], selective separation of UO_2^{2+}/Ln^{3+} [97] and As(III) removal from water [98].

For the first time, Tang *et al.* have synthesized SnO_2 quantum dot@ZIF-8 and explored its electrochemical performance [99]. The specific capacitance (SC) of synthesized SnO_2

quantum dot@ZIF-8 composite has been examined and compared with ZIF-8 and bare SnO_2 quantum dot. The SnO_2 quantum dot@ZIF-8 composite was observed to exhibit higher SC value *i.e.* 931 F g^{-1} while ZIF-8 and SnO_2 quantum dot exhibited 99 and 241 F g^{-1} at 5 mV scan rate.

Lei *et al.* have reported the synthesis of a novel catalyst NiO-PTA/ZIF-8 using NiO, phosphotunastic acid (PTA) and ZIF-8 by impregnation method which is shown in Scheme 1.18 [100]. The synthesized NiO-PTA/ZIF-8 catalyst was observed to exhibit the selectivity of C15-C18 hydrocarbon *ca.* 67.31% for hydrocracking of Jatropha oil, and was also compared with NiO-PTA/Al_2O_3 catalyst, it has been observed that the efficiency of NiO-PTA/ZIF-8 catalyst was found to be 10 times better as compared to NiO-PTA/Al_2O_3 due to its huge surface area [100].

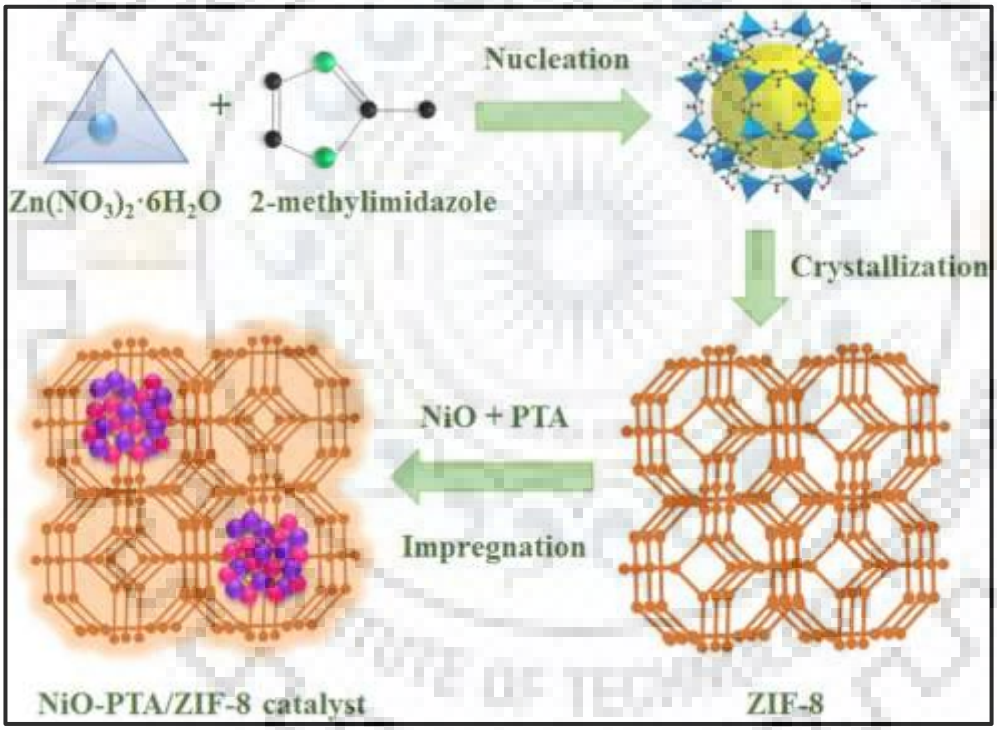

Scheme 1.18. Synthesis of NiO-PTA/ZIF-8 catalyst by impregnation method [100].

ZIF-8 was successfully decorated on TiO_2 nanofibers without any surfactant (Scheme 1.19) using sonochemical method [101] and TiO_2/ZIF-8 nanofibers were exploited for the photocatalytic application which was found to be better photocatalyst for the degradation of Rhodamine-B as compared to commercial P25. Additionally, TiO_2/ZIF-8 hybrid material has been synthesized by deposition on the surface of mesoporous TiO_2 nanobeads of ZIF-8 nano sized material [102]. Further, TiO_2/ZIF-8 hybrid has been used for the photocatalytic reduction

of Cr(VI) and it was found to exhibit an enhanced photocatalytic activity as compared to pristine TiO_2 bead. Very recently, ZIF-8 has been decorated hollow TiO_2 nanosphere and synthesized double–shell TiO_2@ZIF-8 nanospheres by using *"sonocrystallization"* method which has been utilized for the hydrogen evaluation [103].

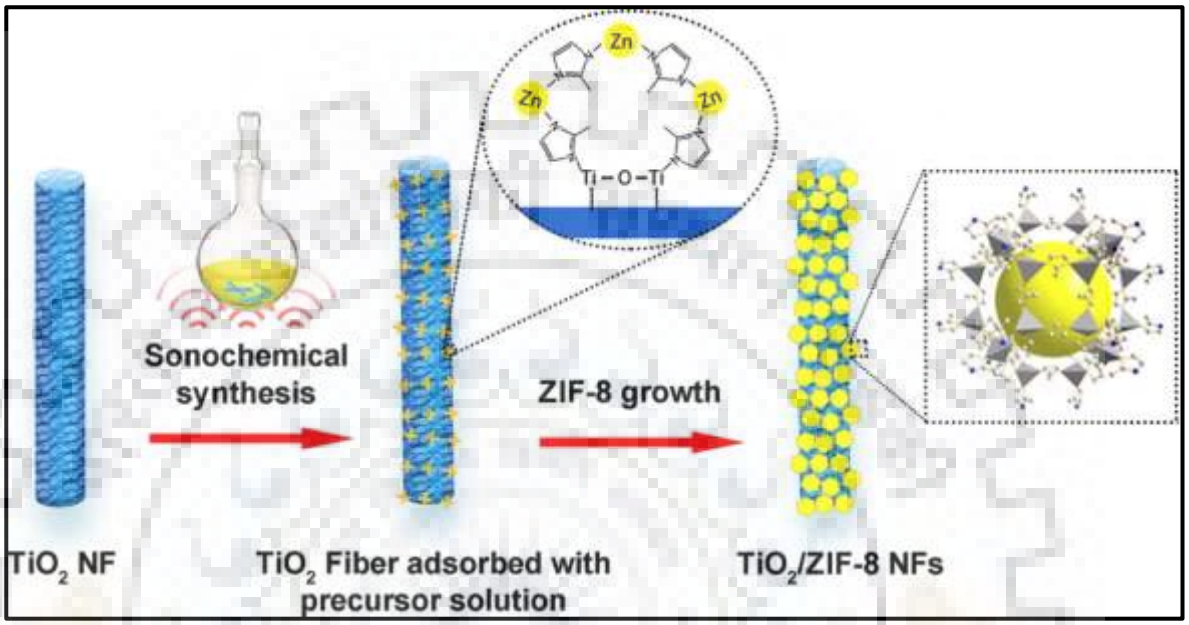

Scheme 1.19. Synthesis of TiO_2/ZIF-8 nanofibers *via* sonochemical method [101].

Li *et al.* have reported the sol-gel synthesis of TiO_2@ZIF-8 composite [104]. Pre-synthesized ZIF-8 (10 mg in 5 mL methanol) were dispersed in 4 mL $Ti(OBu)_4$ and obtained sol-gel hydrolyzed by acetic acid. Titanium sol-gel/ZIF-8 was aged for 24 h after that the resultant powder was calcined at 300 °C for 3 h. Synthesized TiO_2@ZIF-8 composite was applied for the removal of As(III) toxicity from water.

Table 1.3. Metal oxides encapsulated ZIF-8 and their applications [87-104].

S.N.	Materials	Encapsulated Materials	Application	Ref.
1.	ZnO@ZIF-8	ZnO nanopaticle	CO_2 Adsorption	87
2	ZnO@ZIF-8	ZnO nanorod	Photoelectrochemical Response	88
3.	ZnO nanorod@ZIF-8	ZnO nanorod	Degradation of methylene blue	89
4	ZnO@ZIF-8 nanospheres	ZnO nanospheres	Degradation of methylene blue	90
5	ZnO@ZIF-8 heterostructures	ZnO colliodal	Reduction of Cr(VI) and methylene blue	91
6	ZnO/ZIF-8 hybrid	ZnO nanopaticle	Degradation of Rhodamine-B	92
7	ZnO@ZIF-8	ZnO nanorod	Antimicrobial properties	93
8.	Fe_3O_4@ZIF-8	Fe_3O_4 Microspheres	Knoevenagel condensation	94,95
9	Core-shell Fe_3O_4@ZIF-8	Fe_3O_4 nanopaticle	Adsorption of Methylene blue	96
10.	Core-shell Fe_3O_4@ZIF-8	Fe_3O_4 nanopaticle	Separation of UO_2^{2+}/Ln^{3+} and As(III) removal	97,98
11.	SnO_2quantum dots@ZIF-8	SnO_2 quantum dots	Supercapacitors	99
12.	NiO-PTA/ZIF-8	NiO-PTA	Hydrocracking of Jatropha oil.	100
13.	TiO_2@ZIF-8	TiO_2 nanofibers	Degradation of Rhodamine-B	101
14.	TiO_2/ZIF-8	TiO_2 bead	Reduction of Cr(VI)	102
15.	Double-shell TiO_2@ZIF-8	TiO_2 hallow sphere	Hydrogen evaluation	103
16.	TiO_2@ZIF-8	TiO_2	As(III) removal	104

1.2.4. Molecules Encapsulated Zeolitic Imidazole Framework-8: Molecules@ZIF-8

The molecule or drug encapsulated ZIF-8 composite materials have been scarcely reported so far. One step encapsulation of caffeine *in situ* synthesis of ZIF-8 has been reported by Coronas *et al.* [105]. ZIF-8 has been demonstrated as a good host and loaded *ca.* 28 wt% of caffeine. Further, control release of guest molecule has also been discussed and it has been found to be *ca.* 27 days for 100% release out of caffeine molecule form the host material (ZIF-8). Tan *et al.* has reported polymer-MOF nanocomposite [106]. Polyurethane (PU) polymer has been fabricated with ZIF-8 for the studies of thermo-mechanical and viscoelastic properties of polymer materials.

ZIF-8 has been demonstrated as good carrier of biomolecules. Recently, carbohydrates (CHs) have been encapsulated within ZIF-8 for biomimetic mineralization [107]. The functional groups of carbohydrate (COO-) help in encapsulation within ZIF-8 due to coulombic attraction of Zn^{2+} and functional groups. CHs@ZIF-8 has been synthesized by addition of aqueous solution of carbohydrates into aqueous solution of 2-methyleimidazole (2-mIM; 160 mM) and zinc acetate (40 mmol) at ambient temperature (Scheme 1.20). Further, 100% control encapsulation and release of molecule have been investigated by chelation of fluorescein isothiocynate (FITC) tagged carboxymethyl dextran and ethyelendiaminetetraacetic acid (EDTA).

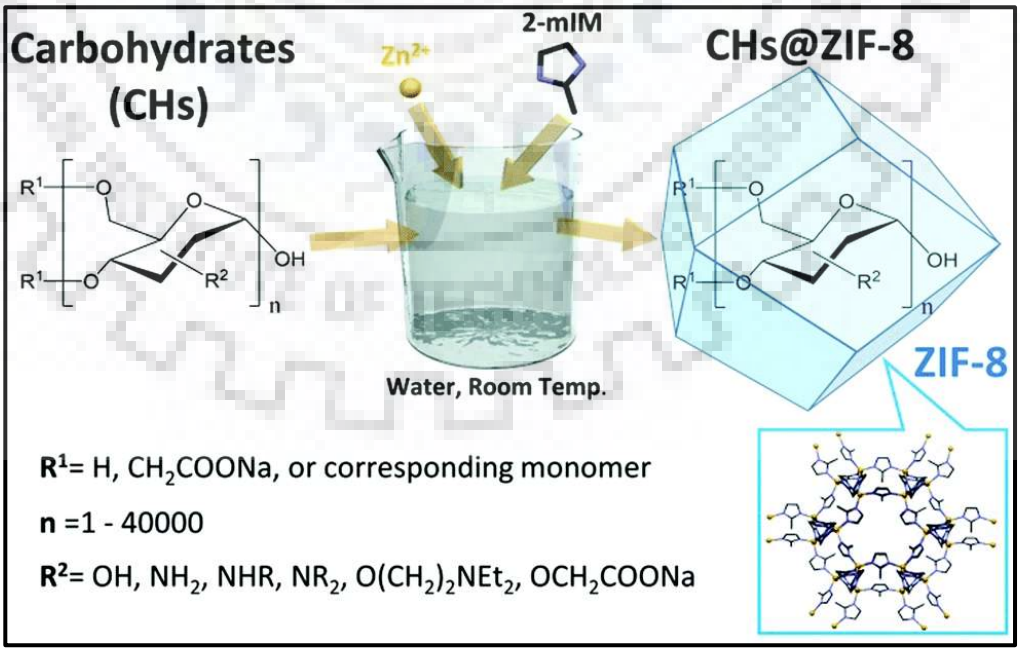

Scheme 1.20. Schematic illustration of synthesis of CHs@ZIF-8 [107].

Highly biocampatible, biodegradable and natural chemotherapeutic agent, *for instance*, Curcumin has been succesfully loaded within nano-sized ZIF-8 and CCM@ZIF-8 composites have been applied for the treatment of cervical cancer against human epithelial carcinoma cell (HeLa cells line) [108] as shown in Scheme 1.21. CCM@ZIF-8 composites seem to have a very good efficiency (*ca.* 88.2%), stabilty and rapid drug release at target (tumor cell) in acidic environment. Nano-sized ZIF-8 carriers promote the uptake of curcumin as ensured by the confocal laser scanning microscopy and cytotoxity experimets.

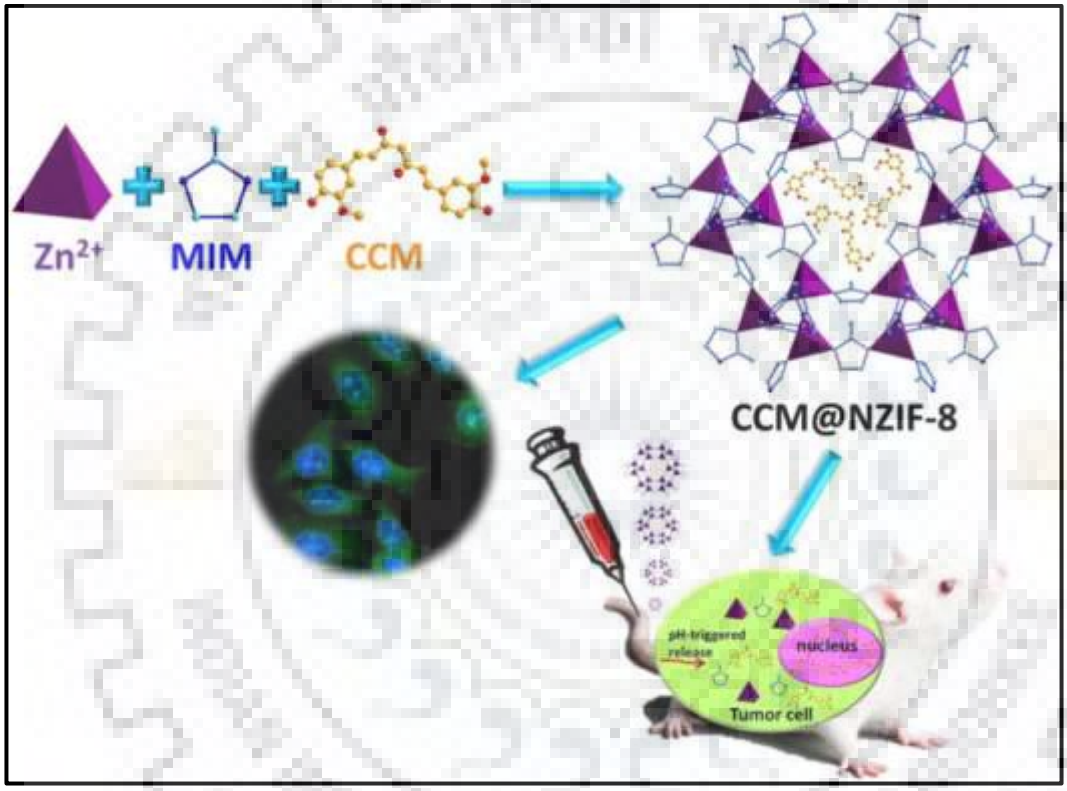

Scheme 1.21. Schematic illustration of synthesis of CCM@ZIF-8 and its application *in vitro* bioimaging and *in vivo* anticancer therapy [108].

Das *et al.* have reported the encapsulation of polyoxometalate (POM) within zeolitic imidazole framework matrix [109]. A keggin type of POM such as $K_6[CoW_{12}O_{40}]$ has been encapsulated within ZIF-8 and applied for the water oxidation at neatral pH. Efficiency of POM@ZIF-8 composite for water oxidation has been determined by O_2 evolved in a costant-current coulometry observation which is found to be 95.7%. Turnover frquency (12.5 s^{-1}) has also been evaluated which also supports the robust efficiency of POM@ZIF-8 composite for water oxidation.

Table 1.4. Molecules encapsulated ZIF-8 and their probable applications [105-109].

S.N.	Materials	Encapsulated molecule	Application	Ref.
1	Caffeine@ZIF-8	Caffeine	Drug delivery	105
2.	Polymer-MOF nanocomposite	Polyurethane (PU)	Thermo-mechanical and viscoelastic properties	106
3.	CHs@ZIF-8	Carbohydrates (CHs)	Biomimetic mineralization	107
4.	CCM@ZIF-8	Curcumin (CCM)	Treatment for cervical cancer	108
5.	POM@ZIF-8	Polyoxometalate (POM)	Water oxidation	109

1.3. FORMULATION OF PROBLEM

A careful inspection of the available literature survey implies that following imperative points need to be discussed.

- TiO_2 nanoparticles or nanowires have been fabricated successfully within ZIF-8 and applied for various applications such as Cr(VI) reduction, removal of As(III), hydrogen evaluation and photocatalytic degradation of rhodamine-B but not explored for degradation of other dyes.
- SnO_2 quantum dots have been encapsulated within ZIF-8 (SnO_2quantum dots@ZIF-8) and employed for the electrochemical performance but SnO_2 nanoparticles were not encapsulated within ZIF-8 matrix so far. Further, the application of SnO_2@ZIF-8 as photocatalyst has not been reported. Moreover, SnO_2quantum dots@ZIF-8 or SnO_2NPs@ZIF-8 may be anticipated role as anti-viral, anti-bacterial, anti-fungal and photocatalysts, etc.
- Metal nanoparticles and metal oxides nanoparticles have been fabricated within ZIF-8 *via* sophisticated and high energy involving synthesis methods but the easily executable/sustainable methods are not reported though out the literature review.
- Ag/AgCl/ZIF-8 nanocomposite and Ag@AgCl/Ag nanofilm/ZIF-8 have been employed for the photocatalytic degradation of rhodamine-B, acetaminophen and methylene blue, respectively, but bare Ag nanoparticles (NPs) encapsulated ZIFs composites have not been reported for the photocatalytic degradation of organic dyes. AgNPs allows the extension of light absorption of wide band gap ZIFs due to *Surface Plasmon Resonance* and enhanced the photo conversion yield.

- Metal oxides (MO_x) nanoparticles encapsulated ZIF-8 (MO_x@ZIF-8) composites have not been explored for the biological applications such as anti-bacterial, anti-viral and anti-fungal activity so far.
- Mixed metal oxides nanoparticles such as ZnO-SnO_2, ZnO-TiO_2, ZnO-Fe_3O_4, TiO-SnO_2 and TiO_2-Fe_3O_4 nanocomposite encapsulated ZIF-8 composite materials have not been synthesized so far.

1.4. ORGANIZATION OF WORK

The present work is organized in order to achieve the desired objectives which are incorporated in the following chapters of thesis.

- Multi-core-shell TiO_2NPs@ZIF-8 composites have been synthesized by *in situ* encapsulation of TiO_2NPs within ZIF-8 matrix at room temperature and studied the adsorption and photodegradation of methylene blue and rhodamine-B by considering the various factors such as dosing amount of TiO_2NPs, amount of catalysts, pH and concentration of dye solutions.
- SnO_2NPs, ZIF-8 and multi-core-shell SnO_2NPs@ZIF-8 composites have been synthesized by sustainable method at room temperature and utilized as photocatalyst for the photodegradation of methylene blue. Further, SnO_2NPs, ZIF-8 and SnO_2NPs@ZIF-8 composites were analyzed for anti-viral activity against *Chikungunya virus*.
- Novel metal nanoparticles, *for instance*, AgNPs have been synthesized and encapsulated within ZIF-11 through different reaction conditions and optimized the best reaction condition. The photodegradation of methylene blue and reduction of 4-nitrophenol were studied using AgNPs@ZIF-11 composite. Similarly, AgNPs@ZIF-8 has also been synthesized by a sustainable method and used as photocatalyst for the photodegradation of methylene blue and congo red.
- Mixed metal oxides such as ZnO-SnO_2 nanocomposites have been synthesized using different molar ratio of Zn and Sn (1:1, 2:8, 4:6, 6:4 and 8:2) by employing sol-gel and grinding method. The synthesized ZnO-SnO_2 nanocomposites were optimized as an efficient photocatalyst for degradation of methylene blue. For the first time, ZnO-SnO_2 nanocomposite has been encapsulated within ZIF-8 and resulting ZnO-SnO_2@ZIF-8 composites exhibit enhanced photocatalytic activity.

1.5. REFERENCES

(1) (a) Martínez-Huitle, C. A.; Brillas, E. Decontamination of Wastewaters Containing Synthetic Organic Dyes by Electrochemical Methods: A General Review. *Appl. Catal. B: Environ.* **2009**, *87* (3-4), 105-145. (b) Xie, Y.; Chen, F.; He, J.; Zhao, J.; Wang, H. Photoassisted Degradation of Dyes in the Presence of Fe^{3+} and H_2O_2 Under Visible Irradiation. *J. Photochem. Photobiol. A-Chem.* **2000**, *136* (3), 235-240.

(2) (a) Chen, K. C.; Wu, J. Y.; Liou, D. J.; Hwang, S. C. J. Decolorization of the Textile Dyes by Newly Isolated Bacterial Strains. *J. Biotechnol.* **2003**, *101* (1), 57-68. (b) Stock, N. L.; Peller, J.; Vinodgopal, K.; Kamat, P. V. Combinative Sonolysis and Photocatalysis for Textile Dye Degradation. *Environ. Sci. Technol.* **2000**, *34* (9), 1747-1750.

(3) Hoffmann, M. R.; Martin, S. T.; Choi, W.; Bahnemann, D. W. Environmental Applications of Semiconductor Photocatalysis. *Chem. Rev.* **1995**, *95*, 69-96.

(4) Dambournet, D.; Belharouak, I.; Amine, K. Tailored Preparation Methods of TiO_2 Anatase, Rutile, Brookite: Mechanism of Formation and Electrochemical Properties. *Chem. Mater.* **2010**, *22*, 1173-1179.

(5) Schneider, J.; Matsuoka, M.; Takeuchi, M.; Zhang, J.; Horiuchi, Y.; Anpo, M.; Bahnemann, D. W. Understanding TiO_2 Photocatalysis: Mechanisms and Materials. *Chem. Rev.* **2014**, *114*, 9919-9986.

(6) Shi, L.; Lin, H. Preparation of Band Gap Tunable SnO_2 Nanotubes and Their Ethanol Sensing Properties. *Langmuir* **2011**, *27*, 3977-3981.

(7) Kim, S. P.; Choi, M. Y.; Choi, H. C. Photocatalytic Activity of SnO_2 Nanoparticles in Methylene Blue Degradation. *Mater. Res. Bull.* **2016**, *74*, 85-89.

(8) Erdem, I.; Kart, H. H.; Cagin, T. High Pressure Phase Transitions in SnO_2 Polymorphs by First-principles Calculations. *J. Alloys Comp.* **2014**, *587*, 638-645.

(9) Das, P. K.; Chowdhury, A.; Mandal, N.; Arya, A. First-principles Characterization of the Pressure-dependent Elastic Anisotropy of SnO_2 Polymorphs. *Philos. Mag.* **2016**, *96* (18), 1861-1882.

(10) Fu, Y. Q.; Luo, J. K.; Du, X. Y.; Flewitt, A. J.: Li, Y.; Markx, G. H.; Walton, A. J.; Milne, W. I. Recent Developments on ZnO Films for Acoustic Wave Based Bio-Sensing and Microfluidic Applications: A Review. *Sens. Actuator B* **2010**, *143*, 606-619.

(11) Ma, H.; Williams, P. L.; Diamond, S. A. Ecotoxicity of Manufactured ZnO Nanoparticles-A Review. *Environ. Pollut.* **2013**, *172*, 76-85.

(12) Raj, S.; Kumar, S.; Srivastava, S. K.; Kar, P.; Roy, P. Deposition of Tin Oxide Thin Films by Successive Ionic Layer Adsorption Reaction Method and Its Characterization. *J. Nanosci. Nanotechnol.* **2018**, *18*, 2569-2575.

(13) Shankar, R.; Singla, N.; Asija, M.; Kociok-Köhn, G.; Molloy, K. C. Synthesis and Structural Studies of Diorganotin(IV)-Based Coordination Polymers Bearing Silaalkylphosphonate Ligands and Their Transformation into Colloidal Domains. *Inorg. Chem.* **2014**, *53*, 6195-6203.

(14) Pandey, P. C.; Pandey. G. One-Pot Two-Step Rapid Synthesis of 3-Aminopropyltrimethoxysilane-Mediated Highly Catalytic Ag@(PdAu) Trimetallic Nanoparticles. *Catal. Sci. Technol.* **2016**, *6*, 3911-3917.

(15) Srivastava, K.; Panda, A.; Sharma, S.; Singh, H. B. Telluroxanes: Synthesis, Sructure and Applications. *J. Organomet. Chem.* **2018**, *861*, 174-206.

(16) Singh, J. D.; Maheshwari, M.; Khan, S.; Butcher R. J. Sterically Encumbered Hexakis(Alkylseleno)Benzenes: Conformational Behavior of Hexakis(iso-propylselenomethyl)-Benzene Toward Hg^{2+} Ions on Selective Recognition. *Tetrahedron Lett.* **2008**, *49*, 117-121.

(17) Dhakshinamoorthy, A.; Garcia, H. Catalysis by Metal Nanoparticles Embedded on Metal-Organic Frameworks. *Chem. Soc. Rev.* **2012**, *41*, 5262-5284.

(18) Zhu, Q. L.; Xu, Q. Metal-Organic Framework Composites. *Chem. Soc. Rev.* **2014**, *43*, 5468-5512.

(19) Li, H.; Eddaoudi, M.; O'Keeffe, M.; Yaghi, O. M. Design and Synthesis of an Exceptionally Stable and Highly Porous Metal-Organic Framework. *Nature* **1999**, *402* (6759), 276.

(20) Yaghi, O. M.; O'keeffe, M.; Ockwig, N. W.; Chae, H. K.; Eddaoudi, M.; Kim, J. Reticular Synthesis and the Design of New Materials. *Nature* **2003,** *423* (6941), 705.

(21) Batten, S. R.; Champness, N. R.; Chen, X. M.; Garcia-Martinez, J.; Kitagawa, S.; Öhrström, L.; O'Keeffe, M.; Suh, M. P.; Reedijk, J. Coordination Polymers, Metal-Organic Frameworks and the Need for Terminology Guidelines. *CrystEngComm.* **2012**, *14* (9), 3001-3004.

(22) Farha, O. K.; Eryazici, I.; Jeong, N. C.; Hauser, B. G.; Wilmer, C. E.; Sarjeant, A. A.; Snurr, R. Q.; Nguyen, S. T.; Yazaydın, A. Ö.; Hupp, J. T. Metal-Organic Framework

Materials with Ultrahigh Surface Areas: Is the Sky the Limit? *J. Am. Chem. Soc.* **2012**, *134*, 15016-15021.

(23) Gómez-Gualdrón, D. A.; Moghadam, P. Z.; Hupp, J. T.; Farha, O.K.; Snurr, R. Q. Application of Consistency Criteria to Calculate BET Areas of Micro- and Mesoporous Metal-Organic Frameworks. *J. Am. Chem. Soc.* **2016**, *138*, 215-224.

(24) Gomez-Gualdron, D. A.; Colon, Y. J.; Zhang, X.; Wang, T. C.; Chen, Y.-S.; Hupp, J. T.; Yildirim, T.; Farha, O. K.; Zhang, J.; Snurr, R. Q. Evaluating Topologically Diverse Metal-Organic Frameworks for Cryoadsorbed Hydrogen Storage. *Energy Environ. Sci.* **2016**, *9*, 3279-3289.

(25) Mason, J. A.; Oktawiec, J.; Taylor, M. K.; Hudson, M. R.; Rodriguez, J.; Bachman, J. E.; Gonzalez, M. I.; Cervellino, A.; Guagliardi, A.; Brown, C. M.; Llewellyn, P. L.; Masciocchi, N.; Long, J. R. Methane Storage in Flexible Metal-Organic Frameworks with Intrinsic Thermal Management. *Nature* **2015**, *527*, 357-361.

(26) Holcroft, J. M.; Hartlieb, K. J.; Moghadam, P. Z.; Bell, J. G.; Barin, G.; Ferris, D. P.; Bloch, E. D.; Algaradah, M. M.; Nassar, M. S.; Botros, Y. Y.; Thomas, K. M.; Long, J. R.; Snurr, R. Q.; Stoddart, J. F. Carbohydrate-Mediated Purification of Petrochemicals. *J. Am. Chem. Soc.* **2015**, *137*, 5706-5719.

(27) Li, J. R.; Kuppler, R. J.; Zhou, H. C. Selective Gas Adsorption and Separation in Metal-Organic Frameworks. *Chem. Soc. Rev.* **2009**, *38*, 1477-1504.

(28) DeCoste, J. B.; Peterson, G. W. Metal-Organic Frameworks for Air Purification of Toxic Chemicals. *Chem. Rev.* **2014**, *114*, 5695-5727.

(29) Liu, J.; Chen, L.; Cui, H.; Zhang, J.; Zhang, L.; Su, C. Y. Applications of Metal-Organic Frameworks in Heterogeneous Supramolecular Catalysis. *Chem. Soc. Rev.* **2014**, *43*, 6011-6061.

(30) Corma, A.; García, H.; Llabrés i Xamena, F. X. Engineering Metal Organic Frameworks for Heterogeneous Catalysis. *Chem. Rev.* **2010**, *110*, 4606-4655.

(31) McDonald, T. M.; Mason, J. A.; Kong, X.; Bloch, E. D.; Gygi, D.; Dani, A.; Crocella, V.; Giordanino, F.; Odoh, S. O.; Drisdell, W. S.; Vlaisavljevich, B.; Dzubak, A. L.; Poloni, R.; Schnell, S. K.; Planas, N.; Lee, K.; Pascal, T.; Wan, L. F.; Prendergast, D.; Neaton, J. B.; Smit, B.; Kortright, J. B.; Gagliardi, L.; Bordiga, S.; Reimer, J. A.; Long, J. R. Cooperative Insertion of CO_2 in Diamine-Appended Metal-Organic Frameworks. *Nature* **2015**, *519*, 303-308.

(32) Sumida, K.; Rogow, D. L.; Mason, J. A.; McDonald, T. M.; Bloch, E. D.; Herm, Z. R.; Bae, T. H.; Long, J. R. Carbon Dioxide Capture in Metal-Organic Frameworks. *Chem. Rev*. **2012**, *112*, 724-781.

(33) Yazaydın, A. Ö.; Snurr, R. Q.; Park, T. H.; Koh, K.; Liu, J.; LeVan, M. D.; Benin, A. I.; Jakubczak, P.; Lanuza, M.; Galloway, D. B.; Low, J. J.; Willis, R. R. Screening of Metal-Organic Frameworks for Carbon Dioxide Capture from Flue Gas Using a Combined Experimental and Modeling Approach. *J. Am. Chem. Soc.* **2009**, *131*, 18198-18199.

(34) Li, P.; Modica, J. A.; Howarth, A. J.; Vargas L., E.; Moghadam, P. Z.; Snurr, R. Q.; Mrksich, M.; Hupp, J. T.; Farha, O. K. Toward Design Rules for Enzyme Immobilization in Hierarchical Mesoporous Metal-Organic Frameworks. *Chem.* **2016**, *1*, 154-169.

(35) Faust, T. Nanomedicine: MOFs Deliver. *Nat. Chem.* **2015**, *7*, 270-271.

(36) Bernini, M. C.; Fairen-Jimenez, D.; Pasinetti, M.; Ramirez-Pastor, A. J.; Snurr, R. Q. Screening of Bio-Compatible Metal-Organic Frameworks as Potential Drug Carriers Using Monte Carlo Simulations. *J. Mater. Chem. B* **2014**, *2*, 766-774.

(37) Orellana-Tavra, C.; Baxter, E. F.; Tian, T.; Bennett, T. D.; Slater, N. K. H.; Cheetham, A. K.; Fairen-Jimenez, D. Amorphous Metalorganic Frameworks for Drug Delivery. *Chem. Commun.* **2015**, *51*, 13878-13881.

(38) Miller, S. E.; Teplensky, M. H.; Moghadam, P. Z.; Fairen-Jimenez, D. Metal-Organic Frameworks as Biosensors for Luminescence Based Detection and Imaging. *Interface Focus* **2016**, *6*, 20160027.

(39) Wang, C. C.; Ying, J. Y. Sol-Gel Synthesis and Hydrothermal Processing of Anatase and Rutile Titania Nanocrystals. *Chem. Mater.* **1999**, *11* (11), 3113-3120.

(40) Cravillon, J.; Schroder, C.A.; Bux, H.; Rothkirch, A.; Caro, J.; Wiebcke, M. Formate Modulated Solvothermal Synthesis of ZIF-8 Investigated Using Time-Resolved *in situ* X-ray Diffraction and Scanning Electron Microscopy. *CrystEngComm.* **2012**, *14*, 492-498.

(41) Yaghi, O. M.; Li, H. Hydrothermal Synthesis of a Metal-Organic Framework Containing Large Rectangular Channels. *J. Am. Chem. Soc.* **1995**, *117*, 10401-10402.

(42) Bux, H.; Liang, F.; Li, Y.; Cravillon, J.; Wiebcke, M.; Caro, J. R. Zeolitic Imidazolate Framework Membrane with Molecular Sieving Properties by Microwave-Assisted Solvothermal Synthesis. *J. Am. Chem. Soc.* **2009**, *131* (44), 16000-16001.

(43) Ni, Z.; Masel, R. I. Rapid Production of Metal-Organic Frameworks via Microwave-Assisted Solvothermal Synthesis. *J. Am. Chem. Soc.* **2006**, *128*, 12394-12395.

(44) Mason, T. J.; Peters, D. Practical Sonochemistry: Uses and Applications of Ultrasound; Woodhead, **2002**.

(45) Son, W. J.; Kim, J.; Kim, J.; Ahn, W. S. Sonochemical Synthesis of MOF-5. *Chem. Commun.* **2008**, 6336-6338.

(46) (a) Du, M.; Li, C. P.; Zhao, X. J. Metal-Controlled Assembly of Coordination Polymers with the Flexible Building Block 4-pyridylacetic Acid (Hpya). *Cryst. Growth Des.* **2006**, *6* (1), 335-341. (b) Halper, S. R.; Do, L.; Stork, J. R.; Cohen, S. M. Topological Control in Heterometallic Metal−Organic Frameworks by Anion Templating and Metalloligand Design. *J. Am. Chem. Soc.* **2006**, *128* (47), 15255-15268. (c) Ohi, H.; Tachi, Y.; Itoh, S. Supramolecular and Coordination Polymer Complexes Supported by a Tripodal Tripyridine Ligand Containing a 1, 3, 5-triethylbenzene Spacer. *Inorg. Chem.* **2004**, *43* (15), 4561-4563.

(47) Beldon, P. J.; Fábián, L.; Stein, R. S.; Thirumurugan, A.; Cheetham, A. K.; Friščid, T. Rapid Room-Temperature Synthesis of Zeolitic Imidazolate Frameworks by Using Mechanochemistry. *Angew Chem Int Ed.* **2010**, *49* (50), 9640-9643.

(48) Friščid, T.; Halasz, I.; Beldon, P. J.; Belenguer, A. M.; Adams, F.; Kimber, S. A.; Honkimäki, V.; Dinnebier, R. E. Real-time and *in situ* Monitoring of Mechanochemical Milling Reactions. *Nat. Che.* **2013**, *5* (1), 66.

(49) Mueller, U.; Puetter, H.; Hesse, M.; Wessel, H. WO 2005/049892 German Patent.

(50) Martinez Joaristi, A.; Juan-Alcañiz, J.; Serra-Crespo, P.; Kapteijn, F.; Gascon, J. Electrochemical Synthesis of Some Archetypical Zn^{2+}, Cu^{2+}, and Al^{3+} Metal Organic Frameworks. *Cryst. Growth Des.* **2012**, *12* (7), 3489-3498.

(51) MacGillivay, L. R. New: Metal-Organic Frameworks: Design and Application; John Wiley & Sons, Inc. **2010**.

(52) McDonald, T. M.; Lee, W. R.; Mason, J. A.; Wiers, B. M.; Hong, C. S.; Long, J. R. Capture of Carbon Dioxide from air and Flue Gas in the Alkylamine-Appended Metal-Organic Framework mmen-Mg_2(dobpdc). *J. Am. Chem. Soc.* **2012**, *134* (16), 7056-7065.

(53) Sumida, K.; Stuck, D.; Mino, L.; Chai, J. D.; Bloch, E. D.; Zavorotynska, O.; Murray, L. J.; Dinc, M.; Chavan, S.; Bordiga, S.; Head-Gordon, M.; Long, J. R. Impact of Metal and Anion Substitutions on the Hydrogen Storage Properties of M-BTT Metal–Organic Frameworks. *J. Am. Chem. Soc.* **2013**, *135* (3), 1083-1091.

(54) Geier, S. J.; Mason, J. A.; Bloch, E. D.; Queen, W. L.; Hudson, M. R.; Brown, C. M.; Long, J. R. Selective Adsorption of Ethylene over Ethane and Propylene over Propane in the Metal-Organic Frameworks M_2(dobdc) (M=Mg, Mn, Fe, Co, Ni, Zn). *Chem. Sci.* **2013**, *4*(5), 2054-2061.

(55) Liang, K.; Ricco, R.; Doherty, C. M.; Styles, M. J.; Bell, S.; Kirby, N.; Mudie, S.; Haylock, D.; Hill, A. J.; Doonan, C. J. Biomimetic Mineralization of Metal-Organic Frameworks as Protective Coatings for Biomacromolecules. *Nat. Commun.* **2015**, *6*, 7240.

(56) Vermoortele, F.; Ameloot, R.; Alaerts, L.; Matthessen, R.; Carlier, B.; Fernandez, E. V. R.; Gascon, J.; Kapteijn, F.; De Vos, D. E. Tuning the Catalytic Performance of Metal–Organic Frameworks in Fine Chemistry by Active Site Engineering. *J. Mater. Chem.* **2012**, *22* (20), 10313-10321.

(57) Lescouet, T.; Kockrick, E.; Bergeret, G.; Pera-Titus, M.; Farrusseng, D. Engineering MIL-53(Al) Flexibility by Controlling Amino Tags. *Dalton Trans.* **2011**, *40* (43), 11359-11361.

(58) Juan-Alcañiz, J.; Gascon, J.; Kapteijn, F. Metal-Organic Frameworks as Scaffolds for the Encapsulation of Active Species: State of the art and Future Perspectives. *J. Mater. Chem.* **2012**, *22* (20), 10102-10118.

(59) (a) Park, K. S.; Ni, Z.; Côté, A. P.; Choi, J. Y.; Huang, R.; Uribe-Romo, F. J.; Chae, H. K.; O'Keeffe, M.; Yaghi, O. M. Exceptional Chemical and Thermal Stability of Zeolitic Imidazolate Frameworks. *Proc. Natl. Acad. Sci.* **2006**, *103* (27), 10186-10191. (b) Tan, J. C.; Bennett, T. D.; Cheetham A. K. Chemical Structure, Network Topology, and Porosity Effects on the Mechanical Properties of Zeolitic Imidazolate Frameworks. *Proc. Natl. Acad. Sci.* **2010**, *107*, 9938-9943.

(60) Breck, D. W. Zeolite Molecular Sieves; Wiley New York, **1974**, 593-724.

(61) Kruk, M.; Jaroniec, M.; Sayari, A. Adsorption Study of Surface and Structural Properties of MCM-41 Materials Of Different Pore Sizes. *J. Phys. Chem. B* **1997**, *101* (4), 583-589.

(62) Zhao, D.; Huo, Q.; Feng, J.; Chmelka, B. F.; Stucky, G. D. Nonionic Triblock and Star Diblock Copolymer and Oligomeric Surfactant Syntheses of Highly Ordered, Hydrothermally Stable, Mesoporous Silica Structures. *J. Am. Chem. Soc.* **1998**, *120* (24), 6024-6036.

(63) Banerjee, R.; Phan, A.; Wang, B.; Knobler, C.; Furukawa, H.; O'keeffe, M.; Yaghi, O. M. High-Throughput Synthesis of Zeolitic Imidazolate Frameworks and Application to CO_2 Capture. *Science* **2008**, *319* (5865), 939-943.

(64) (a) Venna, S. R.; Carreon, M. A., Highly Permeable Zeolite Imidazolate Framework-8 Membranes for CO_2/CH_4 Separation. *J. Am. Chem. Soc.* **2009**, *132* (1), 76-78. (b) Ordonez, M. J. C.; Balkus Jr, K. J.; Ferraris, J. P.; Musselman, I. H. Molecular Sieving Realized with ZIF-8/Matrimid® Mixed-Matrix Membranes. *J. Membr. Sci.* **2010**, *361*, 28-37.

(65) Lu, G.; Hupp, J. T. Metal-Organic Frameworks as Sensors: A ZIF-8 Based Fabry-Pérot Device as a Selective Sensor for Chemical Vapors and Gases. *J. Am. Chem. Soc.* **2010**, *132* (23), 7832-7833.

(66) Yao, J.; Dong, D.; Li, D.; He, L.; Xu, G.; Wang, H. Contra-Diffusion Synthesis of ZIF-8 Films on a Polymer Substrate. *Chem. Commun.* **2011**, *47* (9), 2559-2561.

(67) Kwon, H. T.; Jeong, H. K. *In situ* Synthesis of thin Zeolitic-Imidazolate Framework ZIF-8 Membranes Exhibiting Exceptionally High Propylene/Propane Separation. *J. Am. Chem. Soc.* **2013**, *135* (29), 10763-10768.

(68) Pan, Y.; Lai, Z. Sharp Separation of C2/C3 Hydrocarbon Mixtures by Zeolitic Imidazolate Framework-8 (ZIF-8) Membranes Synthesized in Aqueous Solutions. *Chem. Commun.* **2011**, *47* (37), 10275-10277.

(69) Karagiaridi, O.; Lalonde, M. B.; Bury, W.; Sarjeant, A. A.; Farha, O. K.; Hupp, J. T. Opening ZIF-8 a Catalytically Active Zeolitic Imidazolate Framework of Sodalite Topology with Unsubstituted Linkers. *J. Am. Chem. Soc.* **2012,** *134* (45), 18790-18796.

(70) Torad, N. L.; Hu, M.; Kamachi, Y.; Takai, K.; Imura, M.; Naito, M.; Yamauchi, Y. Facile Synthesis of Nanoporous Carbons with Controlled Particle Sizes by Direct Carbonization of Monodispersed ZIF-8 Crystals. *Chem. Commun.* **2013,** *49* (25), 2521-2523.

(71) Jing, H. P.; Wang, C. C.; Zhang, Y. W.; Wang, P.; Li, R. Photocatalytic Degradation of Methylene Blue in ZIF-8. *RSC Adv.* **2014**, *4* (97), 54454-54462.

(72) Wu, R.; Wang, D. P.; Han, J.; Liu, H.; Zhou, K.; Huang, Y.; Xu, R.; Wei, J.; Chen, X.; Chen, Z. A General Approach towards Multi-Faceted Hollow Oxide Composites Using Zeolitic Imidazolate Frameworks. *Nanoscale* **2015**, *7* (3), 965-974.

(73) Li, P. Z.; Aranishi, K.; Xu, Q. ZIF-8 Immobilized Nickel Nanoparticles: Highly Effective Catalysts for Hydrogen Generation from Hydrolysis of Ammonia Borane. *Chem. Comm.* **2012**, *48* (26), 3173-3175.

(74) Zahmakiran, M. Iridium Nanoparticles Stabilized by Metal Organic Frameworks (IrNPs@ ZIF-8): Synthesis, Structural Properties and Catalytic Performance. *Dalton Trans.* **2012**, *41* (41), 12690-12696.

(75) Lu, G.; Li, S.; Guo, Z.; Farha, O. K.; Hauser, B. G.; Qi, X.; Wang, Y.; Wang, X.; Han, S.; Liu, X. Imparting Functionality to a Metal-Organic Framework Material by Controlled Nanoparticle Encapsulation. *Nat. Chem.* **2012**, *4* (4), 310.

(76) Chen, L.; Peng, Y.; Wang, H.; Gu, Z.; Duan, C. Synthesis of Au@ZIF-8 Single-or Multi-Core-Shell Structures for Photocatalysis. *Chem. Commun.* **2014**, *50* (63), 8651-8654.

(77) Rösler, C.; Esken, D.; Wiktor, C.; Kobayashi, H.; Yamamoto, T.; Matsumura, S.; Kitagawa, H.; Fischer, R. A. Encapsulation of Bimetallic Nanoparticles into a Metal-Organic Framework: Preparation and Microstructure Characterization of Pd/Au@ZIF-8. *Eur. J. Inorg. Chem.* **2014**, *2014* (32), 5514-5521.

(78) Zhang, T.; Li, B.; Zhang, X.; Qiu, J.; Han, W.; Yeung, K. L. Pd Nanoparticles Immobilized in a Microporous/Mesoporous Composite ZIF-8/MSS: A Multifunctional Catalyst for the Hydrogenation of Alkenes. *Micropor Mesopor Mat.* **2014**, *197*, 324-330.

(79) Isimjan, T. T.; Kazemian, H.; Rohani, S.; Ray, A. K. Photocatalytic Activities of Pt/ZIF-8 loaded Highly Ordered TiO_2 Nanotubes. *J. Mater. Chem.* **2010**, *20* (45), 10241-10245.

(80) Guo, Y. F.; Fang, W. J.; Fu, J. R.; Wu, Y.; Zheng, J.; Gao, G. Q.; Chen, C.; Yan, R. W.; Huang, S. G.; Wang, C. C. Facile Synthesis of Ag@ZIF-8 Core-Shell Heterostructure Nanowires for Improved Antibacterial Activities. *Appl. Surf. Sci.* **2018**, *435*, 149-155.

(81) Kuo, C. H.; Tang, Y.; Chou, L. Y.; Sneed, B. T.; Brodsky, C. N.; Zhao, Z.; Tsung, C. K. Yolk–Shell Nanocrystal@ZIF-8 Nanostructures for Gas-Phase Heterogeneous Catalysis with Selectivity Control. *J. Am. Chem. Soc.* **2012**, *134* (35), 14345-14348.

(82) Thanh, M. T.; Thien, T. V.; Du, P. D.; Hung, N. P.; Khieu, D. Q. Iron Doped Zeolitic Imidazolate Framework (Fe-ZIF-8): Synthesis and Photocatalytic Degradation of RDB Dye in Fe-ZIF-8. *J. Porous Mater.* **2018**, *25*, 857-869.

(83) Gao, S. T.; Liu, W. H.; Shang, N. Z.; Feng, C.; Wu, Q. H.; Wang, Z.; Wang, C. Integration of a Plasmonic Semiconductor with a Metal-Organic Framework: a Case of Ag/AgCl@ZIF-8 with Enhanced Visible Light Photocatalytic Activity. *RSC Adv.* **2014**, *4*, 61736-61742.

(84) Liu, J.; Li, R.; Wang, Y.; Wang, Y.; Zhang, X.; Fan C. The Active Roles of ZIF-8 on the Enhanced Visible Photocatalytic Activity of Ag/AgCl: Generation of Superoxide Radical and Adsorption. *J. Alloy Compd*. **2017**, *693*, 543-549.

(85) Fan, G.; Zheng, X.; Luo, J.; Peng, H.; Lin, H.; Bao, M.; Hong, L.; Zhou, J. Rapid Synthesis of Ag/AgCl@ZIF-8 as a Highly Efficient Photocatalyst for Degradation of Acetaminophen Under Visible Light. *Chem. Eng.* **2018**, *351*, 782-790.

(86) Liu, J.; Li, R.; Hu, Y.; Li, T.; Jia, Z.; Wang, Y.; Wang, Y.; Zhang, X.; Fan, C. Harnessing Ag Nanofilm as an Electrons Transfer Mediator for Enhanced Visible Light Photocatalytic Performance of Ag@AgCl/Agnanofilm/ZIF-8 Photocatalyst. *Applied Catal. B: Environ.* **2017**, *202*, 64-71.

(87) Esken, D.; Noei, H.; Wang, Y.; Wiktor, C.; Turner, S.; Van Tendeloo, G.; Fischer, R. A., ZnO@ZIF-8: Stabilization of Quantum Confined ZnO Nanoparticles by a Zinc Methylimidazolate Framework and their Surface Structural Characterization Probed by CO_2 Adsorption. *J. Mater. Chem.* **2011**, *21* (16), 5907-5915.

(88) Zhan, W. W.; Kuang, Q.; Zhou, J. Z.; Kong, X. J.; Xie, Z. X.; Zheng, L. S. Semiconductor@Metal-Organic Framework Core-Shell Heterostructures: a Case of ZnO@ ZIF-8 Nanorods with Selective Photoelectrochemical Response. *J. Am. Chem. Soc.* **2013**, *135* (5), 1926-1933.

(89) Wee, L. H.; Janssens, N.; Sree, S. P.; Wiktor, C.; Gobechiya, E.; Fischer, R. A.; Kirschhock, C. E.; Martens, J. A. Local Transformation of ZIF-8 Powders and Coatings into ZnO Nanorods for Photocatalytic Application. *Nanoscale* **2014**, *6* (4), 2056-2060.

(90) Yu, B.; Wang, F.; Dong, W.; Hou, J.; Lu, P.; Gong, J. Self-Template Synthesis of Core-Shell ZnO@ZIF-8 Nanospheres and the Photocatalysis under UV Irradiation. *Mater. Lett.* **2015**, *156*, 50-53.

(91) Wang, X.; Liu, J.; Leong, S.; Lin, X.; Wei, J.; Kong, B.; Xu, Y.; Low, Z. X.; Yao, J.; Wang, H. Rapid Construction of ZnO@ZIF-8 Heterostructures with Size-Selective Photocatalysis Properties. *ACS Appl. Mater. Interfaces* **2016**, *8* (14), 9080-9087.

(92) Yang, X.; Wen, Z.; Wu, Z.; Luo, X. Synthesis of ZnO/ZIF-8 Hybrid Photocatalysts Derived from ZIF-8 with Enhanced Photocatalytic Activity. *Inorg. Chem. Front.* **2018**, *5* (3), 687-693.

(93) Redfern, J.; Geerts, L.; Seo, J. W.; Verran, J.; Tosheva, L.; Wee, L. H. Toxicity and Antimicrobial Properties of ZnO@ZIF-8 Embedded Silicone Against Planktonic and

Biofilm Catheter-Associated Pathogens. *ACS Appl. Nano Mater.* **2018**, *1* (4), 1657-1665.

(94) Zhang, T.; Zhang, X.; Yan, X.; Kong, L.; Zhang, G.; Liu, H.; Qiu, J.; Yeung, K. L. Synthesis of Fe_3O_4@ZIF-8 Magnetic Core-Shell Microspheres and their Potential Application in a Capillary Microreactor. *Chem. Eng.* **2013**, *228*, 398-404.

(95) Pang, F.; He, M.; Ge, J. Controlled Synthesis of Fe_3O_4/ZIF-8 Nanoparticles for Magnetically Separable Nanocatalysts. *Chem.: Eur. J.* **2015**, *21* (18), 6879-6887.

(96) Zheng, J.; Cheng, C.; Fang, W. J.; Chen, C.; Yan, R. W.; Huai, H. X.; Wang, C. C. Surfactant-Free Synthesis of a Fe_3O_4@ZIF-8 Core-Shell Heterostructure for Adsorption of Methylene Blue. *CrystEngComm.* **2014**, *16* (19), 3960-3964.

(97) Min, X.; Yang, W.; Hui, Y. F.; Gao, C. Y.; Dang, S.; Sun, Z. M. Fe_3O_4@ ZIF-8: A Magnetic Nanocomposite for Highly Efficient UO_2^{2+} Adsorption and Selective UO_2^{2+}/Ln^{3+} Separation. *Chem. Commun.* **2017**, *53* (30), 4199-4202.

(98) Huo, J. B.; Xu, L.; Yang, J. C. E.; Cui, H. J.; Yuan, B.; Fu, M. L. Magnetic Responsive Fe_3O_4@ZIF-8 Core-Shell Composites for Efficient Removal of As (III) from Water. *Colloids Surf. A* **2018**, *539*, 59-68.

(99) Gao, Y.; Wu, J.; Zhang, W.; Tan, Y.; Zhao, J.; Tang, B. The Electrochemical Performance of SnO_2 quantum dots@zeolitic Imidazolate Frameworks-8 (ZIF-8) Composite Material for Supercapacitors. *Mater. Lett.* **2014**, *128*, 208-211.

(100) Liu, J.; He, J.; Wang, L.; Li, R.; Chen, P.; Rao, X.; Deng, L.; Rong, L.; Lei, J. NiO-PTA Supported on ZIF-8 as a Highly Effective Catalyst for Hydrocracking of Jatropha Oil. *Sci. Rep.* **2016**, *6*, 23667.

(101) Zeng, X.; Huang, L.; Wang, C.; Wang, J.; Li, J.; Luo, X. Sonocrystallization of ZIF-8 on Electrostatic Spinning TiO_2 Nanofibers Surface with Enhanced Photocatalysis Property through Synergistic Effect. *ACS Appl. Mater. Interfaces* **2016**, *8* (31), 20274-20282.

(102) Liu, Q.; Zhou, B.; Xu, M.; Mao, G. Integration of Nanosized ZIF-8 Particles onto Mesoporous TiO_2 Nanobeads for Enhanced Photocatalytic Activity. *RSC Adv.* **2017**, *7* (13), 8004-8010.

(103) Zhang, M.; Shang, Q.; Wan, Y.; Cheng, Q.; Liao, G.; Pan, Z. Self-Template Synthesis of Double-Shell TiO_2@ZIF-8 Hollow Nanospheres *via* Sonocrystallization with Enhanced Photocatalytic Activities in Hydrogen Generation. *Appl Catal B: Environ.* **2019**, *241*, 149-158.

(104) Li, G.; Jiang, H.; Li, D.; Liao, T.; Yuan, L.; Geng, W. Preparation of TiO_2@ZIF-8 for the Removal of As(III) in Water. *Water Sci. Technol.* **2017**, *17*(6), 1730-1739.

(105) Liédana, N.; Galve, A.; ubio, C. S.; Téllez, C.; Coronas, J. CAF@ ZIF-8: One-Step Encapsulation of Caffeine in MOF. *ACS Appl. Mater. Interfaces* **2012**, *4* (9), 5016-5021.

(106) Mahdi, E.; Tan, J. C. Dynamic Molecular Interactions between Polyurethane and ZIF-8 in a Polymer-MOF Nanocomposite: Microstructural, Thermo-Mechanical and Viscoelastic Effects. *Polymer* **2016**, *97*, 31-43.

(107) Astria, E.; Thonhofer, M.; Ricco, R.; Liang, W.; Chemelli, A.; Tarzia, A.; Alt, K.; Hagemeyer, C. E.; Rattenberger, J.; Schroettner, H.; Wrodnigg, T.; Amenitsch, H.; Huang, D. M.; Doonan, C. J.; Falcaro, P. Carbohydrates@MOFs. *Mater. Horiz.* **2019**.

(108) Zheng, M.; Liu, S.; Guan, X.; Xie, Z. One-Step Synthesis of Nanoscale Zeolitic Imidazolate Frameworks with High Curcumin Loading for Treatment of Cervical Cancer. *ACS Appl. Mater. Interfaces* **2015**, *7*, 22181-22187.

(109) Mukhopadhyay, S.; Debgupta, J.; Singh, C.; Kar, A.; Das, S. K. A Keggin Polyoxometalate Shows Water Oxidation Activity at Neutral pH: POM@ZIF-8, an Efficient and Robust Electrocatalyst. *Angew. Chem. Int. Ed.* **2018**, *57*, 1918-1923.

Chapter Two

Materials and Methods

"Learning process gives creativity, creativity leads to thinking, thinking provides knowledge, knowledge makes you great".

Dr. A. P. J. Abdul Kalam

2.1. MATERIALS

2.1.1. Metal Salts

Zinc acetate dihydrate ($Zn(CH_3COO)_2.2H_2O$, 98% Merck), zinc nitrate hexahydrate ($Zn(NO_3)_2.6H_2O$, 98% Merck), anhydrous zinc chloride ($ZnCl_2$, 98% Merck), tin tetrachloride pentahydrate ($SnCl_4.5H_2O$, 98% Sigma), silver nitrate ($AgNO_3$, Extra pure Merck) and potassium chloride (KCl, Rankem) were used without further purification.

2.1.2. Ligands

2-Methylimidazole ($C_4H_6N_2$, 99% Sigma Aldrich) and benzimidazole ($C_7H_6N_2$, 98% Sigma Aldrich) were used as ligands for the synthesis of zeolitic imidazole frameworks.

2.1.3. Solvents and other Chemicals

The organic solvents of AR grade *viz.*, methanol (CH_3OH, Rankem), acetone ($(CH_3)_2CO$, Merck), toluene (C_7H_8, Merck), chloroform ($CHCl_3$, Qualigens), dichloromethane (CH_2Cl_2, Merck) and ethanol (C_2H_5OH, Emsure Merck) were used as received. Ammonia solution (NH_4OH, 25% Merck), potassium hydroxide (KOH, Rankem), sodium hydroxide (NaOH, Rankem), trisodium citrate dihydrate ($HOC(COONa)(CH_2COONa)_2.2H_2O$, 99% Hi-Media), methylene blue ($C_{16}H_{18}ClN_3S.xH_2O$, Sigma Aldrich), rhodamine-B ($C_{28}H_{31}ClN_2O_3$, Sigma Aldrich), congo red ($C_{32}H_{22}N_6Na_2O_6S_2$, Merck), terephthalic acid ($C_8H_6O_4$, 98% Himedia), 4-nitrophenol ($C_6H_5NO_3$, Sigma Aldrich), sodium borohydride ($NaBH_4$, Merck), barium sulphate ($BaSO_4$, Himedia) ethylenediaminetetraacetic acid (EDTA) ($C_{10}H_{16}N_2O_8$, Merck), p-benzoquinone (BQ) ($C_6H_4O_2$, 98% LOBA Chem) and *t*-butyl alcohol (*t*-BuOH) ($(CH_3)_3COH$, 99.5% Merck) were also used as received.

2.2. TECHNIQUES

Zeolitic Imidazole Frameworks (ZIFs), nanoparticles (NPs) and their NPs@ZIFs composites were characterized by employing various sophisticated instrumental techniques, *viz.*, Powder X-ray Diffraction (PXRD), X-ray Photoelectron Spectroscopy (XPS), Field Emission Scanning Electron Microscopy (FE-SEM), High Resolution Transmission Electron Microscopy (HR-TEM) and Thermal Gravimetric Analysis (TGA) available at ***Institute Instrumentation Center (IIC), Indian Institute of Technology (IIT) Roorkee***, ***India,*** and others (Fourier Transform Infra-red spectroscopy (FT-IR), Ultra-violet Diffuse Reflectance

Spectroscopy (UV-DRS), Gas Chromatograph equipped with Mass Spectroscopy (GC-MS), Brunauer-Emmett-Teller (BET) surface area analyzer, Zeta Potential, Fluorescence and UV-visible absorbance Spectroscopy) available at the ***Department of Chemistry, IIT Roorkee***, ***India***, as described below.

2.2.1. Powder X-ray Diffraction (PXRD) Analysis

PXRD pattern of synthesized materials were recorded on a Bruker D8 Advance with Cu-Kα (λ_{max}=1.54056 Å) between 2θ values of 5° and 100° with a typical goniometer speed of 1° per minute.

2.2.2. Fourier Transform Infra-red Spectroscopy (FT-IR)

FT-IR spectra were recorded in the range of 400 to 4000 cm^{-1} on a FT-IR Nicolet 6700 Nexus spectrometer using KBr pellets. The pellets were prepared by mixing of KBr with the samples using manual hydraulic press machine.

2.2.3. Field Emission Scanning Electron Microscopy (FE-SEM)

The samples were prepared by sonicating a very small amount of materials in ethanol for 1 h. The prepared suspension of materials was taken (*ca.* 20 µL) on a well cleaned glass slide. The glass slide was dried in *vacuum* for 30 min at 50°C. The FE-SEM analysis of the thin layer coated of the materials was analyzed on FEI-QUANTA 200F (resolution < 2 nm, magnification: 12X-1000kX) and Carl Zeiss Ultra Plus (resolution up to 0.8 nm, magnification: 12- 100,000X (SE); 100-100,000X (BSE)) equipped with energy dispersive X-ray (EDX) analysis.

2.2.4. High Resolution Transmission Electron Microscopy (HR-TEM)

TEM analysis was carried out on a FEI TECNAI G2 electron microscope operating at 200 kV an acceleration voltage, at the ***IIC, IIT Roorkee, India,*** while high resolution TEM analysis was accomplished on JEM 3200FS electron microscope equipped with a field emission gun of 300 kV accelerating voltage, at the ***Department of Metallurgical and Materials Engineering, IIT Roorkee, India***. A very small amount of sample was taken in ethanol and sonicated for 30 min for better dispersion. A couple of drops of this suspension are placed on a TEM grid, which is a copper grid coated with a layer of amorphous carbon. The grid is dried and used for TEM analysis.

2.2.5. Brunauer-Emmett-Teller (BET) Surface Area Analyzer

The BET (Brunauer-Emmett-Teller) surface area of the samples was analyzed by "Quantachrome Nova Station A" instrument at 77 K using liquid N_2 as the coolant. The BET adsorption/desorption isotherms of samples were also used to determine their surface areas.

2.2.6. Ultra-violet Diffuse Reflectance Spectroscopy (UV-DRS) Analysis

The UV-DRS analysis was performed on a Shimadzu UV-2450 UV-visible spectrophotometer in the range of 200-800 nm (λ) with powder samples. The barium sulphate ($BaSO_4$) was employed as the reference throughout the UV-DRS analysis of all samples.

2.2.7. X-ray Photoelectron Spectroscopy (XPS) Analysis

The surface composition of synthesized materials was examined by XPS analysis with the help of PHI5000 Versa Probe-III spectrometer (Physical Electronic) using Al Kα radiation (1486.6 eV).

2.2.8. Thermal Analysis

The thermal behavior of synthesized materials was studied on a Perkin Elmer Pyris Diamond TGA/DTA 6300 Instrument. The sample *ca.* 5-10 mg were taken for each analysis under air/N_2 atmosphere with the flow rate of 200 mL per min, in the temperature range of 10 $^{\circ}$C to 1000 $^{\circ}$C with a temperature rate at 10 $^{\circ}$C per minute.

2.2.9. Zeta Potential Analysis

Zeta potential analysis was performed on Malvern Zeta Sizer (Model No. ZEN3690). The samples were prepared in deionized water (DI H_2O). 1 mg of each sample was dispersed in 3 mL DI H_2O and sonicated for 30 min before the analysis.

2.2.10. UV-visible Absorbance Spectroscopy

For the adsorption, photocatalytic degradation of dye and scavenger analysis, the absorbance spectra were recorded on a Shimadzu 2450 UV-visible spectrophotometer in a quartz cell (1 mL) having 1 cm path length, in the range of 200 nm to 800 nm.

2.2.11. Gas Chromatograph Equipped with Mass Spectroscopy (GC-MS)

For the analysis of small fragments of degraded dye or intermediates of dye molecules were analyzed on GC-MS Perkin-Elmer instrument (Model Clarus500) equipped with TR-5MS capillary column (30 m × 0.25 mm × 0.25 µm) by injecting of 5 µL of samples with the help of micro syringe.

2.2.12. Fluorescence Spectrophotometric Analysis

Fluorescence spectra were recorded in a quartz cell of 1 cm path length on Horiba Scientific Fluoromax-4 fluorescence spectrophotometer (200-800 nm) equipped with Xenon lamp.

2.3. Adsorption and Photodegradation Studies

To investigate the adsorption and photodegradation of dye, identical glass capped tubes preferably of 50 mL were taken which are transparent to UV-visible ray and having no marks on its wall. Four sets of test tubes having following compositions were prepared for the adsorption/photodegradation studies.

1. 20 mL of 0.5×10^{-5} M dye solution.
2. 20 mL of 0.5×10^{-5} M dye solution and 10 mg of MOFs materials (ZIF-8/ZIF-11).
3. 20 mL of 0.5×10^{-5} M dye solution and 10 mg of composite materials (TiO_2NPs@ZIF-8/SnO_2NPsZIF-8/AgNPs@ZIF-8/AgNPs@ZIF-11/ZnO-SnO_2@ZIF-8).
4. 20 mL of 0.5×10^{-5} M dye solution and equivalent amount of nanoparticles (TiO_2/SnO_2/AgNPs/ZnO-SnO_2) present in 10 mg of composites materials.

The dye solutions were prepared in de-ionized water (DI H_2O). For the adsorption study, dye solutions were sonicated for 30 min and kept under dark for 2 h. After the centrifugation, the UV-visible absorbance spectra were recorded at certain time interval. Further, photo degradation was investigated under UV-visible irradiation as the energy source (50 W halogen lamp) for 2 h. Before exposure to the UV-visible irradiation each solution was sonicated under dark for 30 min for maintaining the adsorption-desorption equilibrium. Further, UV-visible absorbance spectrum of each solution was recorded in the same time interval.

Chapter Three

Synthesis and Characterization of ZIF-8 and Multi-core-shell TiO_2NPs@ZIF-8 Composite: Potential Photocatalysts for MB and RB Degradation

"Education should be known as process of development into enjoyable, rational, harmoniously, balanced, useful and natural life"

Jean-Jacques Rousseau

3.1. INTRODUCTION

In the recent years, several metal oxides nanoparticles (NPs) (e.g., ZnO, Fe_2O_3, TiO_2, etc.) have been extensively used for their photocatalytic degradation and among them, TiO_2NPs were observed to be more efficient and safe because of its low toxicity, remarkable band gap (*ca.* 3.35 eV) and a very low production cost [1-3]. Interestingly, the natural efficiency of NPs was found to be remarkably enhanced upon their immobilization into porous materials such as *zeolite.*

Recently, a myriad number of methods including the utilization of TiO_2NPs for photocatalysis either with coating agents or encapsulation of TiO_2NPs within zeolites have been extensively tried so far. However, many of them possess certain limitations, e.g. coating of TiO_2NPs eventually leads to a partial loss of activity ascribed to its inaccessibility to dissolved organic dyes, and encapsulation of TiO_2NPs in zeolites invariably attain stability problems [4-7]. In order to achieve effective inorganic immobilization and encapsulation of TiO_2NPs into the porous materials, ZIF-8 was chosen to encapsulate TiO_2NPs. TiO_2NPs having less-toxicity and high thermal stability are chosen for encapsulation as core within ZIF-8 cavity [8, 4]. Out of three phases (rutile, brookite and anatase), anatase TiO_2NPs exhibits good photocatalytic activity [9, 10]. Thus, it is envisioned to synthesize a core-shell based composite material employing semiconducting TiO_2NPs in macromolecular frameworks such as ZIF-8 for photodegradation of organic dyes.

This chapter enumerates the synthesis of ZIF-8 and its respective multi-core-shell TiO_2NPs@ZIF-8 composites obtained by encapsulation of 150 µL, 300 µL and 500 µL suspensions of TiO_2NPs in methanol, and detailed characterization by employing various spectroscopic and analytical techniques. The detailed study of various parameters on adsorption and photocatalytic activity of composites such as pH, initial concentration of dye, loading amount of TiO_2NPs and the amount of photocatalyst has been included. The proposed plausible mechanisms for photodegradation have also been discussed.

3.2. EXPERIMENTAL SECTION

3.2.1. Synthesis of ZIF-8

Zeolitic imidazole framework-8 was synthesized by employing bench method. Anhydrous $ZnCl_2$ (0.341 g; 2.5 mmol in 20 mL methanol) and 2-methylimidazole (1.642 g; 20 mmol in 25 mL methanol) solutions were prepared separately and mixed slowly by maintaining

the interface undisturbed as much as possible in a small reaction vial at room temperature (*ca*. 22 °C), and kept for 24 h. After mixing the both solutions, turbidity persists within 5-30 min which continued to increase. After 24 h, reaction mixture was centrifuged and properly washed several times with methanol, and the desired product so obtained was vacuum dried at 70 °C for 6 h, and was stored in desiccator for further study.

3.2.2. Synthesis of TiO_2NPs@ZIF-8 Composites

TiO_2NPs@ZIF-8 composites were prepared *in situ* by encapsulation of 150 µL suspension of TiO_2NPs during the synthesis of ZIF-8 which is vividly illustrated in Scheme 3.1. 20 mg TiO_2NPs were sonicated in 10 mL of methanol for 1 h, and 150 µL of this suspension was dropwise added into the reaction mixture of ZIF-8 at certain time intervals in smaller volume. The solution became turbid instantly. After keeping the reaction mixture undisturbed for 24 h, the solution was centrifuged and washed with methanol several times. After complete washing the composite was kept for vacuum drying at 70 °C for 6 h. At last the composite was collected and stored in desiccator for further study. Similar procedure was adopted for the encapsulation of different amounts of TiO_2NPs using 300 µL and 500 µL suspension of TiO_2NPs.

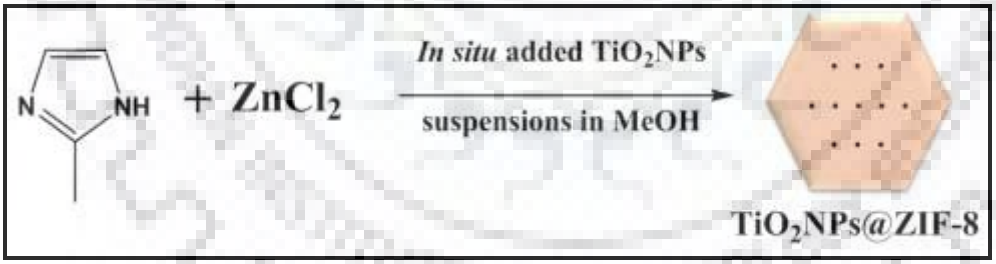

Scheme 3.1. Schematic representation of synthesis of TiO_2NPs@ZIF-8 composite by *in situ* incorporation of TiO_2NPs.

3.2.3. Adsorption and Photodegradation Studies

To study the adsorption and photodegradation of methylene blue/rhodamine-B (20 mL; 0.5×10^{-5} M), 10 mg of ZIF-8 or TiO_2NPs@ZIF-8 composite was added to the dye solution and first kept in dark for 1 h for adsorption study, then exposed to constant UV-visible radiations emitted from a halogen lamp of 50 W under room temperature (after sonication for 30 min in dark in order to stabilize the adsorption-desorption equilibrium). During photodegradation reaction, the stirring was continued to keep the catalyst in suspension. At

regular intervals, a small aliquot of solution was analyzed spectrophotometrically. The amount of dye remaining in the solution was calculated from the absorbance at 663 and 553 nm for MB and RB, respectively. To investigate the effects of various parameters such as encapsulation amount of TiO_2NPs suspension, photcatalyst's amount, initial pH, and initial concentration of dye, only one parameter was varied at a time in the experiments while keeping others constant. %Photodegradation of dye and adsorption capacity (qt)) were calculated using equations (3.1) and (3.2), and %dye removal is also calculated using Eq. (3.1).

$$\%\text{Photodegradation} = [(C_o - C_t) \div C_o] \times 100 \qquad \text{(Eq. 3.1)}$$

$$\text{Adsorption Capacity } (q_t) = [(C_o - C_t) \times V] \div (m \times 1000) \qquad \text{(Eq. 3.2)}$$

Where C_o and C_t = concentrations of dye (mg L^{-1}) at initial and given time 't', V = volume of dye solution (mL) and m = weight of photocatalyst (g), q_t = amount of adsorption (in mg g^{-1}).

3.2.4. Fluorescence Studies

Hydroxyl radicals ($^{\bullet}$OH) are the crucial active species during photocatalytic process [11] and its high generation rate usually results in rapid degradation of dyes in short reaction time. Terephthalic acid traps $^{\bullet}$OH effectively and selectively yielding 2-hydroxy terephthalic acid (yield 35%), which emits fluorescence at 425 nm when excited at 315 nm. The yield of $^{\bullet}$OH can be quantified by fluorescence spectroscopic measurements of the generated 2-hydroxy terephthalic acid [12]. Therefore, $^{\bullet}$OH mediated by photocatalysts was detected by fluorescence method using terephthalic acid as a probe molecule [13]. Similar photocatalytic experimental procedures were adopted except the aqueous solution of MB or RB was replaced by an aqueous solution of 0.5 mM terephthalic acid and 2 mM NaOH. A small aliquot was extracted every 20 min, and fluorescence spectra were recorded at 315 nm of excitation wavelength.

3.3. RESULTS AND DISCUSSION

Multi-core-shell composites TiO_2NPs@ZIF-8 were synthesized by *in situ* encapsulation of 150, 300 and 500 μL suspension of TiO_2NPs in ZIF-8 at room temperature. The yield was about 60%. White crystalline solid was stable in air (> 8 months) and chemically also as well. All the three composites were characterized by using Powder X-Ray Diffraction (PXRD), Field Emission Scanning Electron Microscopy (FE-SEM), High Resolution Transmission Electron

Microscopy (HR-TEM), Fourier-Transform Infra-Red Spectroscopy (FT-IR), Zeta potential, Ultra-violet Diffuse Reflectance Spectroscopy (UV-DRS) and Spectrofluorometric techniques. Since the composite prepared by encapsulating 150 μL suspension of TiO_2NPs in ZIF-8 has maximum photodegradation efficiency for the studied dyes, therefore, XPS of that composite was recorded and described.

3.3.1. PXRD Analysis

The crystal structure of the zeolitic imidazole framework (*i.e.*, ZIF-8) and the synthesized TiO_2NPs@ZIF-8 composites were confirmed by PXRD analysis. Encapsulation of TiO_2NPs in different amounts in ZIF-8 does not affect PXRD pattern and also the crystalline order of ZIF-8 host matrix (Fig. 3.1(a)) ensuring proper encapsulation of TiO_2NPs in ZIF-8. The characteristic diffractions of TiO_2 (Fig. 3.1(b)) are not observed in PXRD of TiO_2NPs@ZIF-8 composite indicating uniform dispersion of TiO_2NPs. Chemical stability of ZIF-8 and TiO_2NPs@ZIF-8 composite was ensured by PXRD pattern (Fig. 3.1(c)) that's indicates no change in their peak pattern after 8 months. Further, after using ZIF-8 and TiO_2NPs@ZIF-8 composite for photodegradation of dyes (after 10 cycles), and keeping them in aqueous medium for three months, their PXRD patterns remain unchanged with slight reduction in intensity of the peaks, which indicate their remarkable chemical stability and reusability (Fig. 3.1(d)).

3.3.2 FT-IR Spectroscopic Studies

FT-IR spectra of ZIF-8 and TiO_2NPs@ZIF-8 composite are depicted in Fig. 3.2. Almost similar stretching frequencies appear due to characteristics of the imidazole ring [14]. The obvious reason of not finding any strong stretching frequencies of Ti−O bond may be because of very low concentration of TiO_2NPs and its perfect encapsulation without much affect in the bonding of ZIF-8 itself. Thus, it did not shift any of the ZIF-8 peaks in notable extent from its position. The probable coupling of Ti–O bond stretching frequency (very weak) with the stretching frequencies of ZIF-8 may be assumed to be another important reason behind its non-existence in the spectrum [15]. Further, the bending frequency [16] of Ti–O bond (very weak) at1115 cm^{-1} is clearly observed in TiO_2NPs@ZIF-8 composites (1095 cm^{-1}) with reduction in its intensity as the amount of loading of TiO_2NPs is decreased.

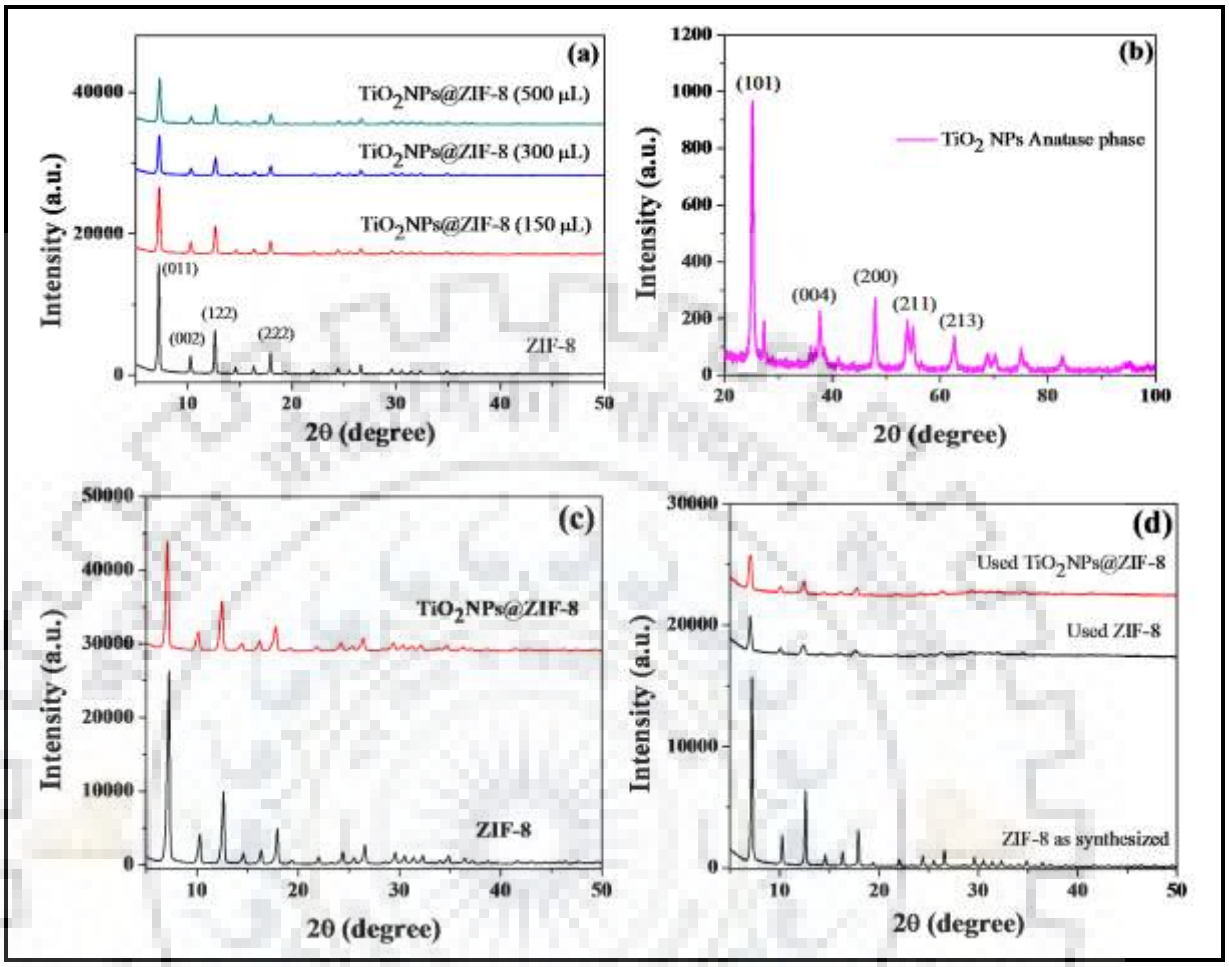

Fig. 3.1. (a) PXRD pattern of ZIF-8 and TiO_2NPs@ZIF-8 composites; (b): PXRD pattern of TiO_2 NPs Anatase phase; (c) PXRD pattern of ZIF-8 and TiO_2NPs@ZIF-8 composite after 8 months; (d) PXRD pattern of ZIF-8 (before use and after use) and TiO_2NPs@ZIF-8 composite (used) after photodegradation study.

3.3.3 FE-SEM and HR-TEM Analysis

A further investigation of the morphology of ZIF-8 and TiO_2NPs@ZIF-8 composite (prepared by using 150 µL suspensions of TiO_2NPs) has been examined by FE-SEM and HR-TEM. ZIF-8 has hexagonal morphology (Fig. 3.3(a)) and there is no change in morphology of ZIF-8 after encapsulation of TiO_2NPs as ensured by FE-SEM (Fig. 3.3(b)) and HR-TEM (Fig. 3.4) images. Encapsulation of TiO_2NPs is clearly evidenced as spots in ZIF-8 cages in HR-TEM images (Fig. 3.4(b-d)) while in the ZIF-8 there is no any such kind of spot. From HR-TEM images of composite, the size distribution of encapsulated TiO_2NPs in ZIF-8 was calculated with the help of *ImageJ* software and the plot of particle size distribution is shown in

Fig. 3.5. It has been found that the average particle size of encapsulated TiO_2NPs is 9.37 ± 2.35 nm. The elemental composition of ZIF-8 and three TiO_2NPs@ ZIF-8 composites (prepared by using 150, 300 and 500 µL suspensions of TiO_2NPs) were estimated by using energy dispersive X-ray (EDX) analysis. EDX results are given in Table 3.1 and EDX spectrum is shown in Fig. 3.6. The EDX analysis also ensured the TiO_2NPs encapsulation with in ZIF-8

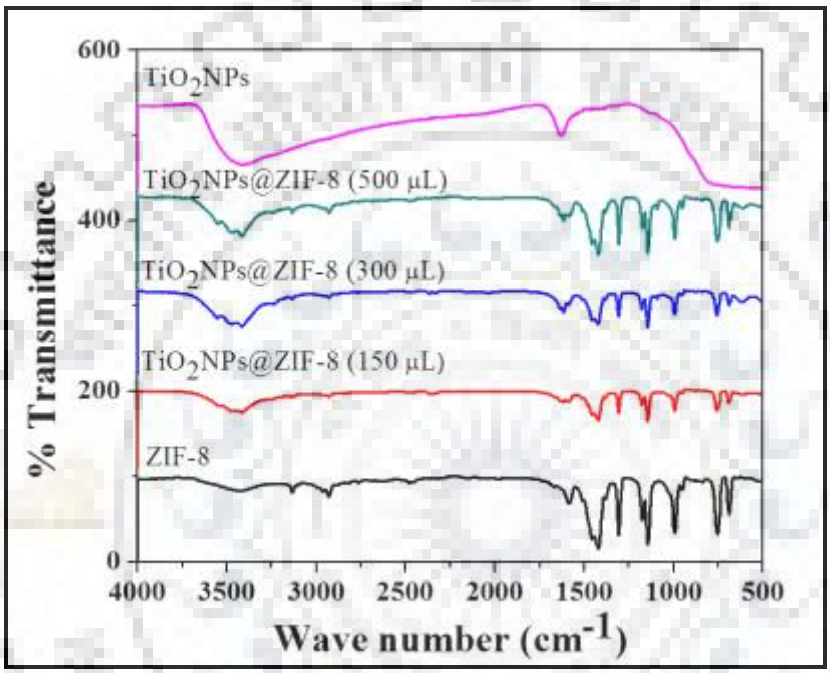

Fig. 3.2. FT-IR spectra of TiO_2NPs, ZIF-8 and their TiO_2NPs@ZIF-8 composites.

.

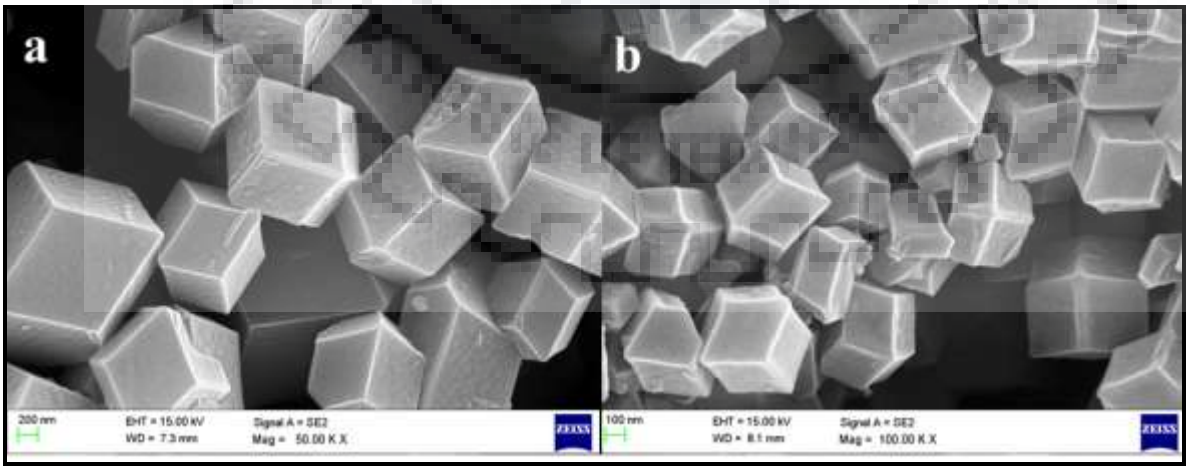

Fig. 3.3. FE–SEM images of (a) ZIF-8 and (b) TiO_2NPs@ZIF-8 composite.

Table 3.1. Elemental composition of ZIF-8 and its TiO_2NPs@ZIF-8 composites.

S.N.	Samples	Atomic %				
		C	N	O	Zn	Ti
1.	ZIF-8	55.5	37.5	-	6.9	-
2.	TiO_2NPs@ZIF-8 (150 µL)	36	17.5	39	5.1	0.04
3.	TiO_2NPs@ZIF-8 (300 µL)	43.7	22.4	30	5.0	0.13
4.	TiO_2NPs@ZIF-8 (500 µL)	33.2	12.1	49.2	5.2	0.26

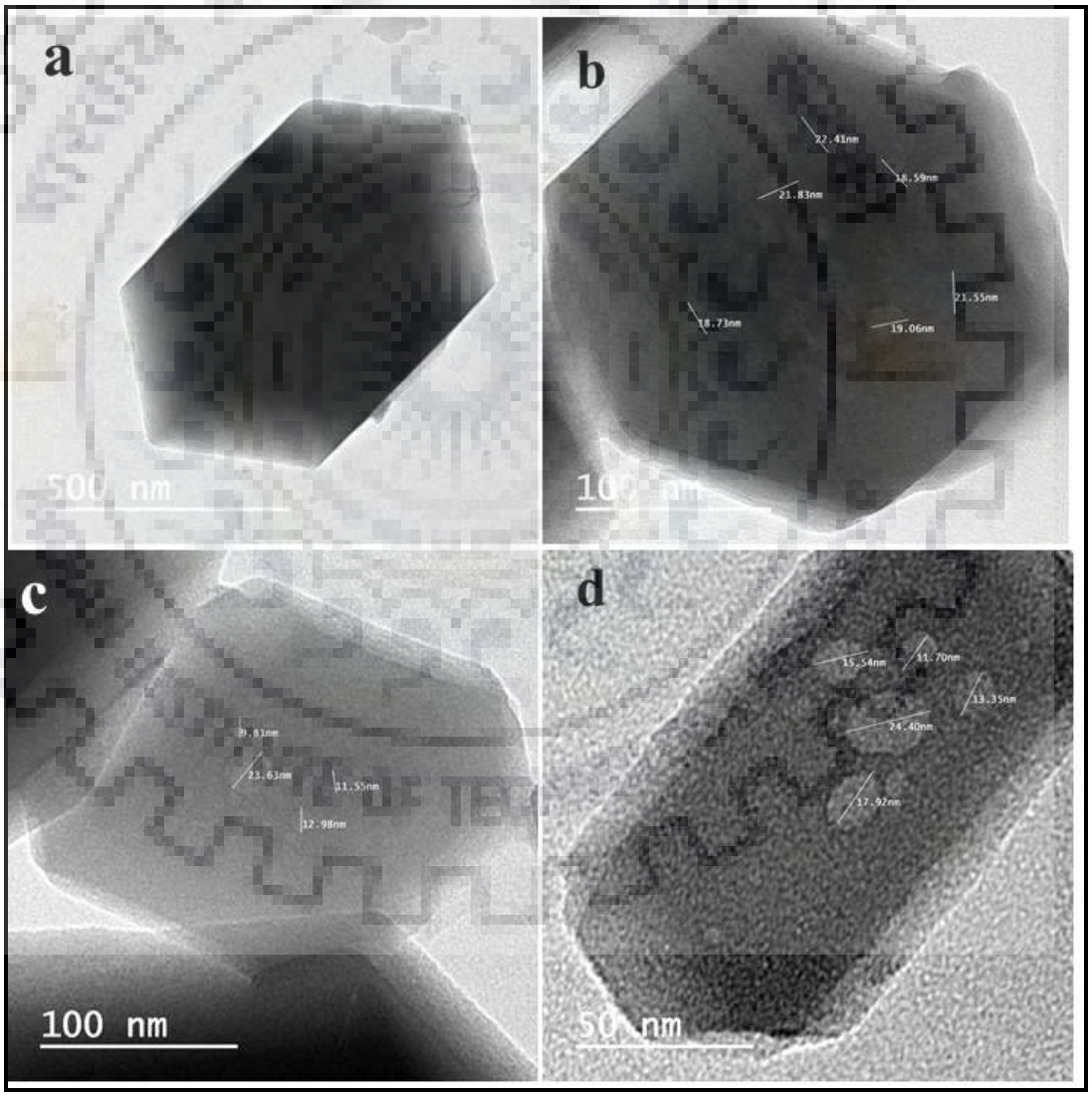

Fig. 3.4. TEM images of ZIF-8 (a) and TiO_2NPs@ZIF-8 composite (b–d) in increasing order of magnification.

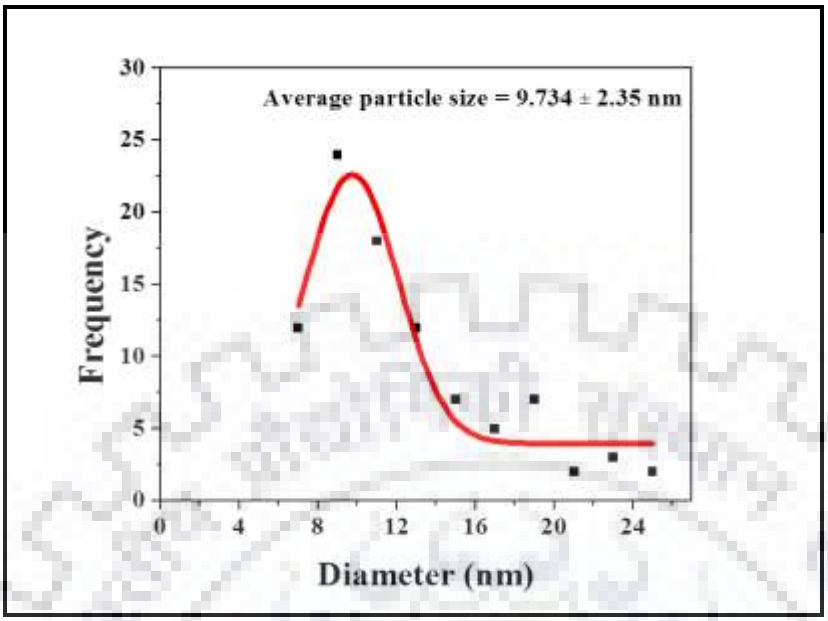

Fig. 3.5. Particle size distributopn plot of encapsulated TiO_2NPs in TiO_2NPs@ZIF-8 composite.

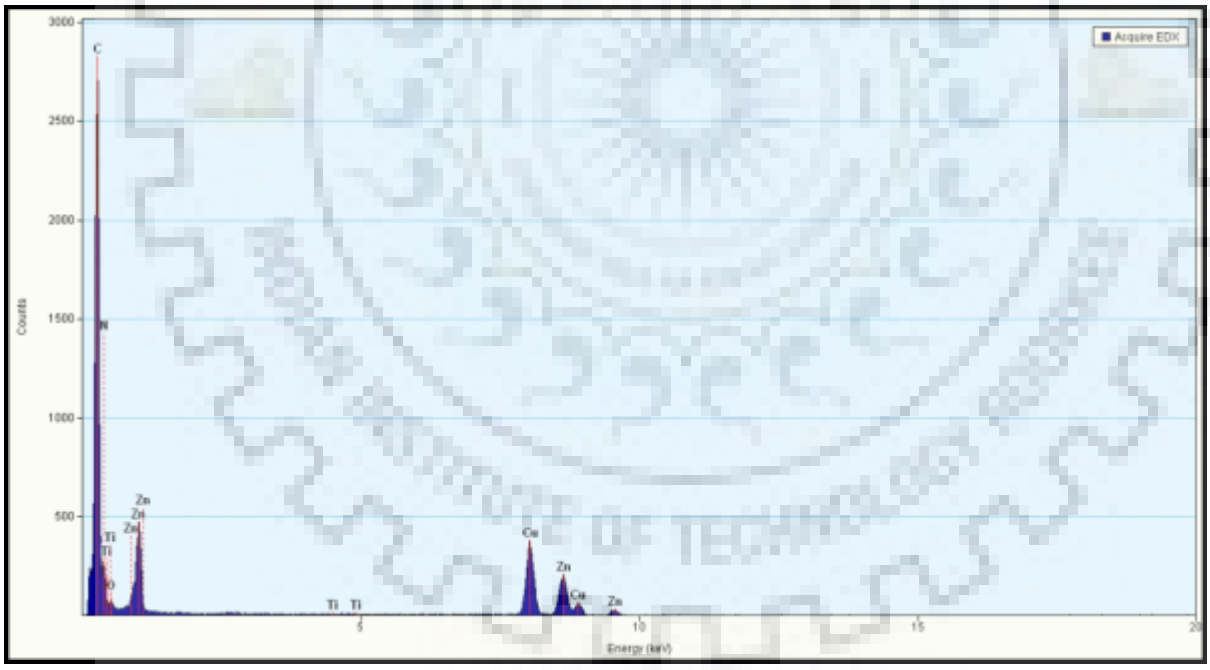

Fig. 3.6. EDX spectrum of TiO_2NPs@ZIF-8 composite using 150 µL suspension of TiO_2NPs.

3.3.4. UV-DRS Studies

UV-DRS spectra of all three composites prepared by encapsulation of different amounts of TiO_2NPs in ZIF-8 and that of ZIF-8 and TiO_2NPs indicate the flat band structure. The band

gaps have been calculated using Tauc method by plotting $(\alpha h\nu)^2$ *versus* hν and $(\alpha h\nu)^{1/2}$ *versus* hν for the direct and indirect transitions, respectively [17], and the typical Tauc plots are shown in Fig. 3.7. Band gap in all the three synthesized composites is almost similar (3.43-3.44 eV) for the direct transitions. Further, the observed band gap (5.16 eV) in ZIF-8 for the direct transitions is also in good agreement with the reported value [11]. For the direct transitions the band gaps of 3.49, 5.25 and 3.43 eV are obtained for TiO_2NPs, ZIF-8 and TiO_2NPs@ZIF-8 composite, respectively, while the values of 3.14, 5.14 and 3.09 eV, respectively, are obtained for the indirect transitions. This may be attributed to the definite shift in the micro-environment of the NPs with in ZIF-8 frameworks. The band gap value in general depends on crystallite size, structural parameter, loading amount of NPs, lattice strain and impurities [18].

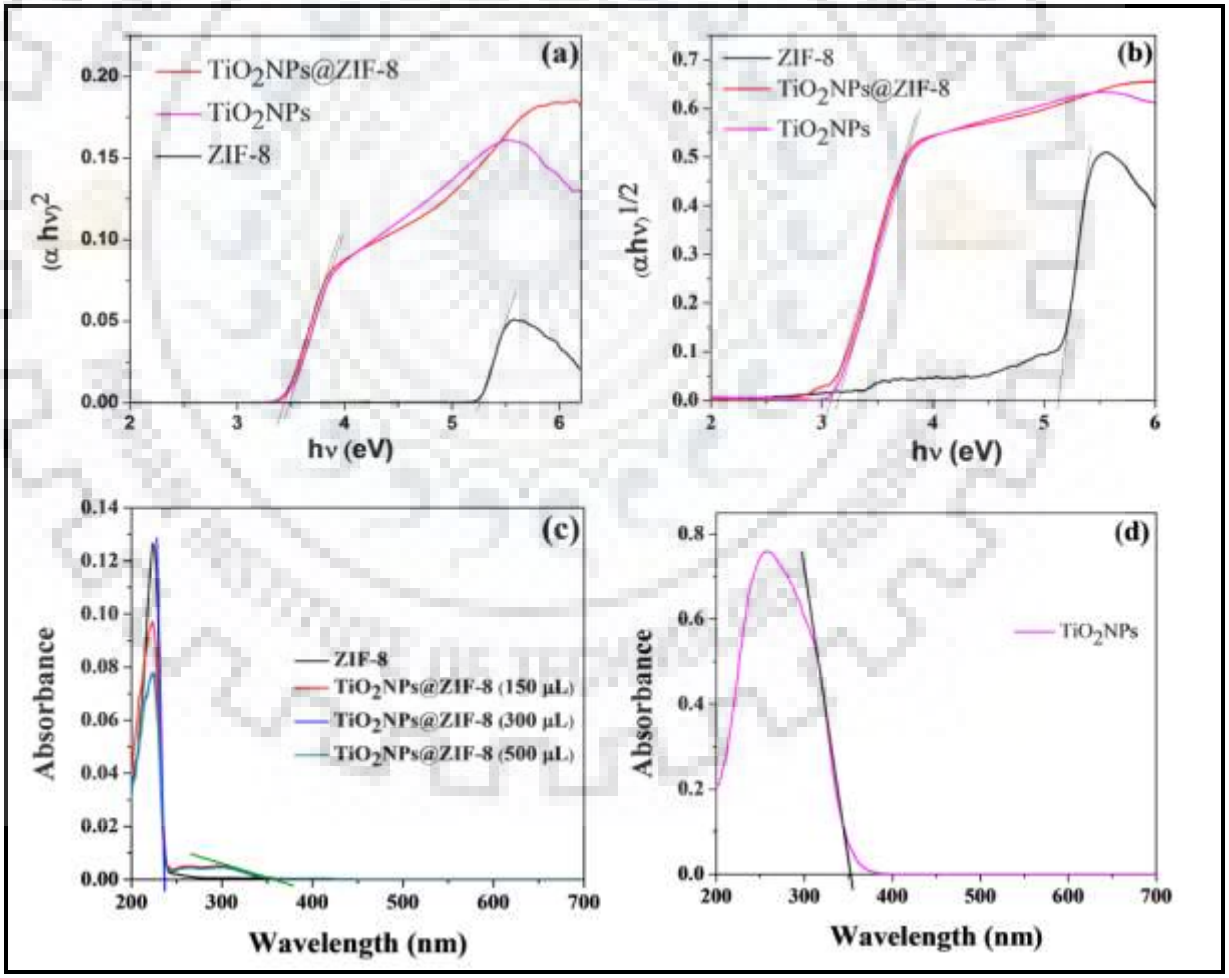

Fig. 3.7. (a, b) Typical Tauc plots of ZIF-8, TiO_2NPs and TiO_2NPs@ZIF-8 composite by direct and indirect method, respectively. (c, d) UV-visible absorbance spectra of ZIF-8, TiO_2NPs@ZIF-8 composite and TiO_2NPs, respectively.

3.3.5. BET Surface Area Analysis

Porosity is unique properties of ZIF-8 and its TiO_2NPs@ZIF-8 composite which is determined by Brunauer-Emmet-Teller (BET) adsorption studies. It has been observed that a lowering of the surface area from ≈ 1357 $m^2 g^{-1}$ to 1318 $m^2 g^{-1}$ occurs when the nitrogen gas adsorption-desorption isotherms of ZIF-8 and TiO_2NPs@ZIF-8 composite (prepared by 150 µL suspension of TiO_2NPs) are compared (Fig. 3.8). This is due to the encapsulation of TiO_2NPs in ZIF-8 framework which resulted in lowering of accessible voids space for N_2 gas adsorption.

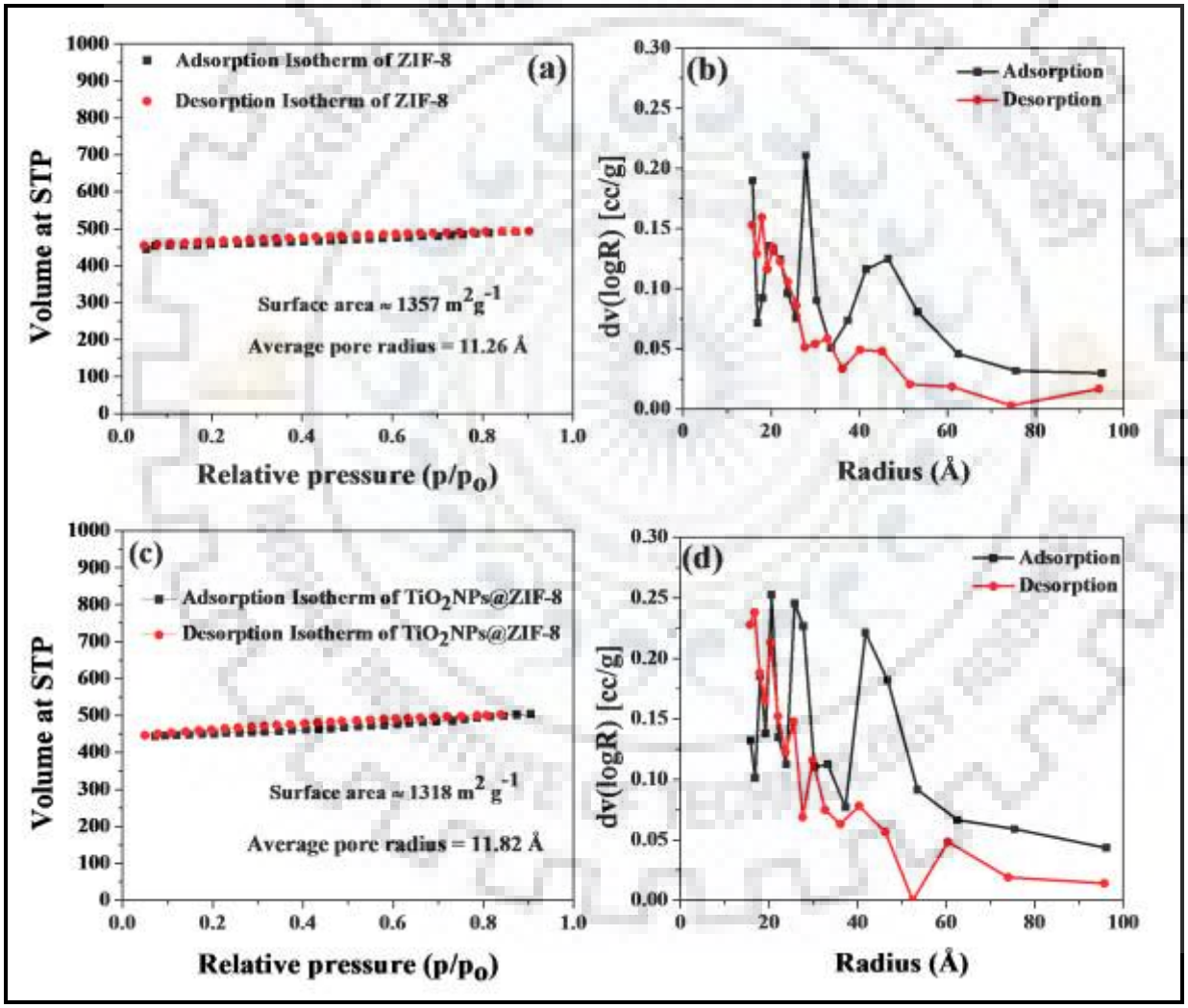

Fig. 3.8. (a-d) BET adsorption-desorption isotherms and pore size distribution of ZIF-8 and TiO_2NPs@ZIF-8 composite, respectively.

3.3.6. XPS Analysis

XPS analysis of TiO_2NPs@ZIF-8 composite (prepared by using 150 µL suspensions of TiO_2 NPs) indicates the presence of electronic states of constituents and their atomic percentages. XPS survey scan of TiO_2NPs@ZIF-8 composite is shown in Fig. 3.9(a). The extended XPS spectra for Zn 2p; N 1s, C1s, O1s and Ti 2p are shown in Fig. 3.9(b-f) and binding energy of various electronic states are also tabulated in Table 3.2. Ti 2p XPS peak in TiO_2NPs@ZIF-8 is less intense, broad and has binding energy 458.6 eV attributed to Ti^{+4} state while pure TiO_2 shows more intense and narrow peak with binding energy 458.7 eV [19]. The XPS peaks of metal compounds become broad and weakly intense upon their encapsulation [20]. The XPS peaks of Zn $2p_{3/2}$ and Zn $2p_{1/2}$ are very intense and narrow, having binding energy 1020.78 eV and 1043.95 eV, respectively, whereas Zn 3s and Zn 3d peaks are less intense and narrow, having low binding energy 88.08 and 9.62 eV, respectively. The C 1s, N 1s and O 1s XPS peaks correspond to binding energy 283.99, 397.62 and 531.24 eV, respectively.

Table 3.2. XPS data of Ti^{+4}, Zn^{+2} ions and 1s state of C, N and O elements.

S.N.	Elements/Ions	Term/State	Binding Energy (eV)	FWHM (eV)
1.	Ti^{+4}	2p	458.44	0.815
2.		2s	584.75	2.109
3.		3p	38.32	0.595
4.		3s	79.32	0.59
5.	Zn^{+2}	$2p_{1/2}$	1043.95	2.38
6.		$2p_{3/2}$	1020.78	2.22
7.		3s	88.08	3.79
8.		3d	9.62	2.7
9.	C	1s	283.99	2.797
10.	N	1s	397.62	2.785
11.	O	1s	531.24	0.825

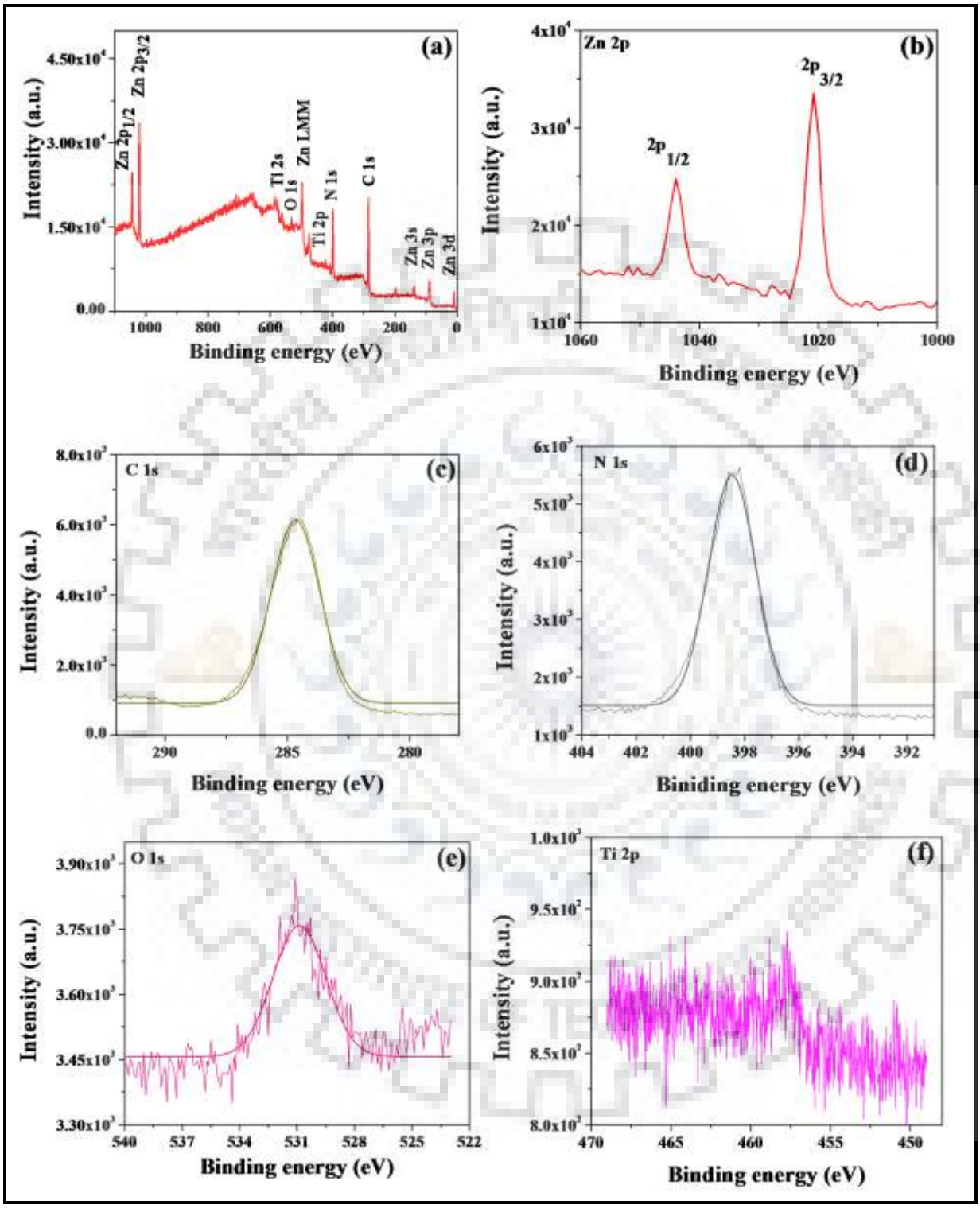

Fig. 3.9. (a) Survey XPS spectra of TiO_2NPs@ZIF-8 composite. (b-f) Expanded XPS spectra of Zn 2p, C 1s, N 1s, O 1s and Ti 2p are shown, respectively.

3.3.7. Thermal Analysis

The thermal gravimetric analysis (TGA) plot of ZIF-8 and its TiO_2NPs@ZIF-8 composites are shown in Fig. 3.10(a-b) under air and nitrogen atmosphere, respectively. By thermal gravimetric analysis, the ZIF-8 and TiO_2NPs@ZIF-8 composites were found to be highly stable up to 250 ºC in aerial and N_2 atmosphere. Beyond this temperature the framework slowly started to decompose and a flat valley was obtained till *ca.* 670 ºC.

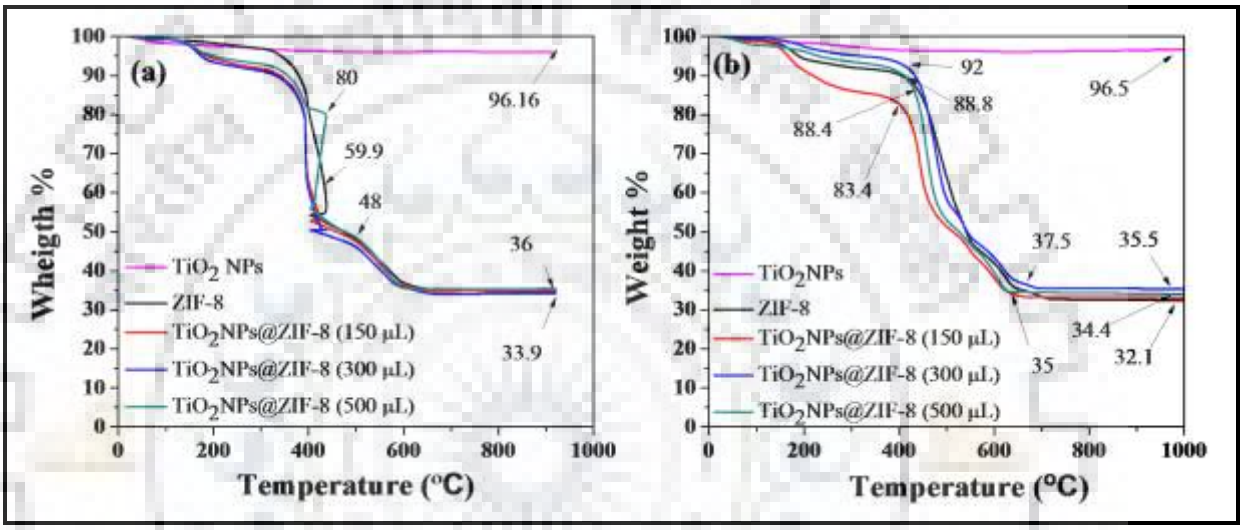

Fig. 3.10. (a, b) TGA analysis of TiO_2NPs, ZIF-8 their TiO_2NPs@ZIF-8 composites in air and N_2 atmosphere, respectively.

3.3.8. Adsorption and Photodegradation Studies

3.3.8.1. Effect of Encapsulation Amount of TiO_2NPs

Effect of different amounts of encapsulation of TiO_2NPs in ZIF-8 for the photodegradation and adsorption of methylene blue (MB) has been investigated spectrophotometrically using all three TiO_2NPs@ZIF-8 composites (10 mg) prepared by *in situ* encapsulation of 150, 300 and 500 µL suspension of TiO_2NPs in ZIF-8 for MB (1.64 mg L^{-1}; 0.5×10^{-5} M) at pH 8.5 and the results (q_t and %dye removal for time length: 60 min and % photodegradation after 120 min) are given in Table 3.3 and plot between concentration (C/C_o) vs time is shown in Fig. 3.11. There is not major difference in %photodegradation of MB using three different composites, which indicates that the amount of loading of TiO_2NPs in ZIF-8 has negligible effect on its photodegradation. The small decrease (1-2%) in %photodegradation on increasing the loading amount of TiO_2NPs may be due to the slight increase in agglomeration

of TiO_2NPs. At higher TiO_2 concentration, the collisional deactivation may also decrease degradation rate (TiO_2^* + TiO_2 → $TiO_2^\#$ +TiO_2, where TiO_2^* and $TiO_2^\#$ are activated and deactivated species, respectively) [5]. Further, q_t remains unchanged up to TiO_2 loading amount of 300 µL but it significantly decreased in the composite prepared by dosing of 500 µL suspension which may also be due to the aggregation of TiO_2NPs leading to bigger sized TiO_2 particles and thereby reducing the specific surface area [5]. Further detailed studies of varying the amount of photocatalysts, pH and concentration of both the dyes were done by using the composite prepared by using 150 µL suspensions of TiO_2NPs and are discussed in the next subsections.

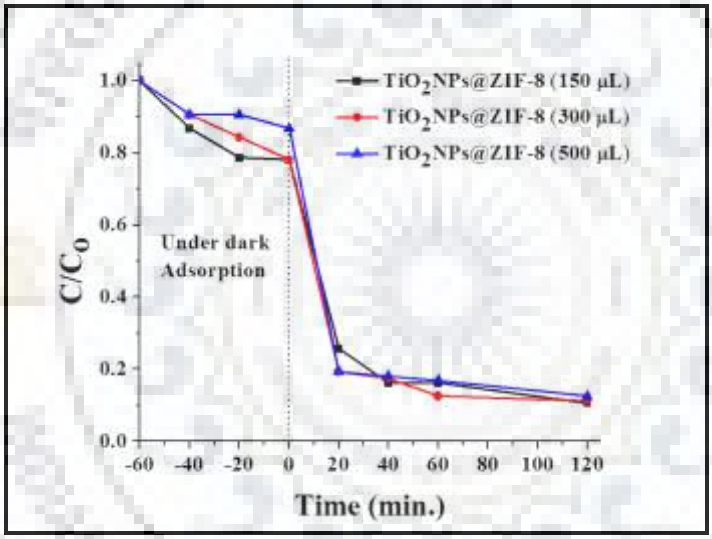

Fig. 3.11. The effect of amount of TiO_2NPs encapsulated in ZIF-8 for adsorption and photodegradation of [MB] = 1.64 mg L^{-1}; pH 8.5; photocatalyst amount 10 mg.

Table 3.3. Effect of amount of TiO_2NPs encapsulated in ZIF-8 for adsorption (after 60 min) and photodegradation (after 120 min) of [MB] (1.64 mg L^{-1}); pH 8.5; 10 mg of composite.

S.N.	Amount of TiO_2NPs in µL	Adsorption capacity (q_t) in mg/g	%Dye removal	%Photodegradation
1.	150	0.70	21.78	89.37
2.	300	0.70	21.78	88.75
3.	500	0.42	13.12	87.50

3.3.8.2. Effect of Photocatalyst's Amount

The results of effect of photocatalyst's (ZIF-8 and TiO_2NPs@ZIF-8 composite) amount for adsorption and photodegradation of MB and RB are given in Table 3.4 and plot between concentration (C/C_o) vs time is shown in Fig. 3.12(a-b). %Photodegradation of MB (1.64 mg L^{-1}; 0.5×10^{-5} M) increased significantly with increasing the amount of both the photocatalysts up to 10 mg, and then decreased (17.5% decrease in case of ZIF-8 and 11.25% decrease using TiO_2NPs@ZIF-8 composite). With increasing the amount of photocatalyst, the number of active sites and available adsorption sites increases which results in increase of adsorption. But the decrease in %photodegradation with further increase in the amount of photocatalyst could be attributed to the particle interaction, such as aggregation and sedimentation, which would lead to decrease in total surface area, and more pronounced decrease in case of ZIF-8 may be due to its microporous structure. For RB (2.40 mg L^{-1}; 0.5×10^{-5} M), the %photodegradation increases with increasing the amount of both the photocatalysts up to 15 mg because the initial concentration of RB is approximately twice than that of MB, and % increase of its photodegradation is less with 15 mg than that with 10 mg of TiO_2NPs@ZIF-8 composite, and it remains almost same in case of ZIF-8.

Table 3.4. Effect of photocatalyst's amount; Experimental conditions: [MB] = 1.64 mg L^{-1} (0.5×10^{-5} M); pH 8.5; [RB] = 2.40 mg L^{-1} (0.5×10^{-5} M); pH 8.6; time length: 120 min except for adsorption studies of MB time length: 60 min.

Dye	Amount of catalysts in mg	Adsorption capacity, q_t (mg/g); [%dye removal]		% Photodegradation	
		ZIF-8	TiO_2NPs@ZIF-8	ZIF-8	TiO_2NPs@ZIF-8
MB	5	1.20 [18.7]	3.60 [56.2]	76.25	72.50
	10	0.64 [20.0]	0.70 [21.8]	84.37	89.37
	15	0.12 [5.6]	0.45 [21.2]	66.87	78.12
RB	5	2.27 [23.7]	2.07 [21.6]	30.50	26.48
	10	1.32 [27.5]	1.69 [35.3]	38.91	48.49
	15	1.27 [39.9]	1.43 [44.8]	48.87	61.25

The adsorption capacity of TiO_2NPs@ZIF-8 composite for MB decreases almost more than five times with an increase in its amount up to 10 mg, which is mainly because of the partially occupied adsorption sites and its tendency to agglomerate; but it remains almost same for further increase in the amount of catalyst due to decrease in the total surface area, an equilibrium is achieved, whereas q_t of ZIF-8 decreases continuously for MB due to agglomeration. The adsorption capacity (q_t) of TiO_2NPs@ZIF-8 composite and ZIF-8 for RB also decreases with an increase in their amount. Therefore, 10 mg of TiO_2NPs@ZIF-8 composite was used for further studies for both the dyes.

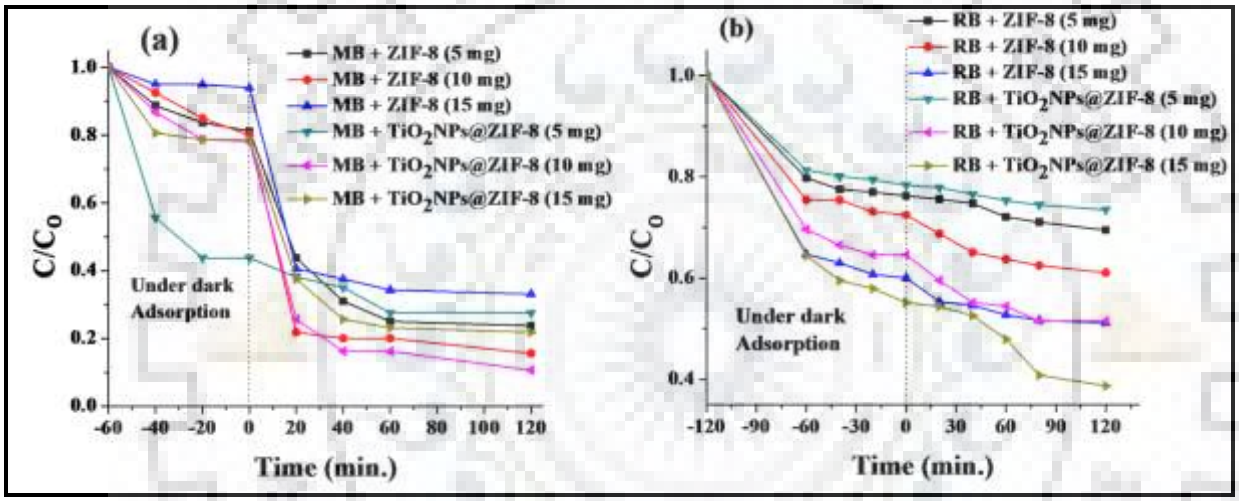

Fig. 3.12. The effect of photocatalyst's amount for adsorption and photodegradation of [MB] = 1.64 mg L^{-1} at pH 8.5 (a); and [RB] = 1.64 mg L^{-1} at pH 8.6 (b).

3.3.8.3. Effect of Initial pH

The effect of pH was studied over the entire pH range of 3 to 12 for the adsorption and photodegradation of both the dyes using ZIF-8, TiO_2NPs and TiO_2NPs@ZIF-8. The photodegradation of same concentration of the dye solution was also studied as control. The results are given in Table 3.5 and concentration (C/C_o) vs time plots are represented in Fig. 3.13(a-c) for MB and Fig. 3.13(d-f) for RB. The pH of the dye (pollutant) solution is another important parameter which influences the amount of adsorbed pollutant and its photocatalytic degradation reactions due to change in surface charge properties of the photocatalyst and size of aggregates formed, and also the number of hydroxyl radicals formed. The results indicate that increasing the pH of MB and RB solutions leads to increasing adsorption capacity and

photodegradation efficiency of all the photocatalysts except TiO_2NPs. This may be due to the formation of more $^{\bullet}OH$ in alkaline medium. The removal of MB is mainly due to solubulization of unprotonated form of the dye because it has very low pK_a value (less than 1). The high adsorption capacity of ZIF-8 for MB may be due to the electrostatic attraction between the positively charged cationic dye and negative charged ZIF-8 adsorbent surface [11], while the pH of the solution was greater than pH_{pzc} (9.52) [21], much higher than pK_a.

Table 3.5. Effect of pH; Experimental conditions: 10 mg of ZIF-8 or TiO_2NPs@ZIF-8; Amount of TiO_2NPs equivalent to that present in its 150 µL suspension; [MB] = 1.64 mg L^{-1} ; [RB] = 2.40 mg L^{-1}; time length: 120 min except for adsorption studies of MB time length: 60 min.

pH of dye	Adsorption capacity, q_t (mg/g); [%dye removal]				%Photodegradation		
	ZIF-8	TiO_2NPs	TiO_2NPs @ZIF-8	Pure dye	ZIF-8	TiO_2NPs	TiO_2NPs @ZIF-8
3.1 (MB)	0.32 [10.0]	1.20 [37.5]	0.16 [5.0]	18.1	56.2	41.8	70.6
8.5 (MB)	0.64 [20.0]	0.66 [20.6]	0.70 [21.8]	21.2	84.3	26.8	89.3
11.5 (MB)	0.94 [29.3]	1.32 [41.2]	0.48 [15.0]	32.5	90.0	44.3	89.3
3.3 (RB)	1.12 [23.5]	0.24 [5.0]	0.80 [16.7]	2.2	23.8	5.8	40.6
8.6 (RB)	1.32 [27.5]	0.54 [11.2]	1.69 [35.3]	4.1	38.9	12.5	48.4
12.6 (RB)	1.60 [33.4]	0.59 [12.4]	1.13 [23.7]	11.1	46.0	31.8	56.8

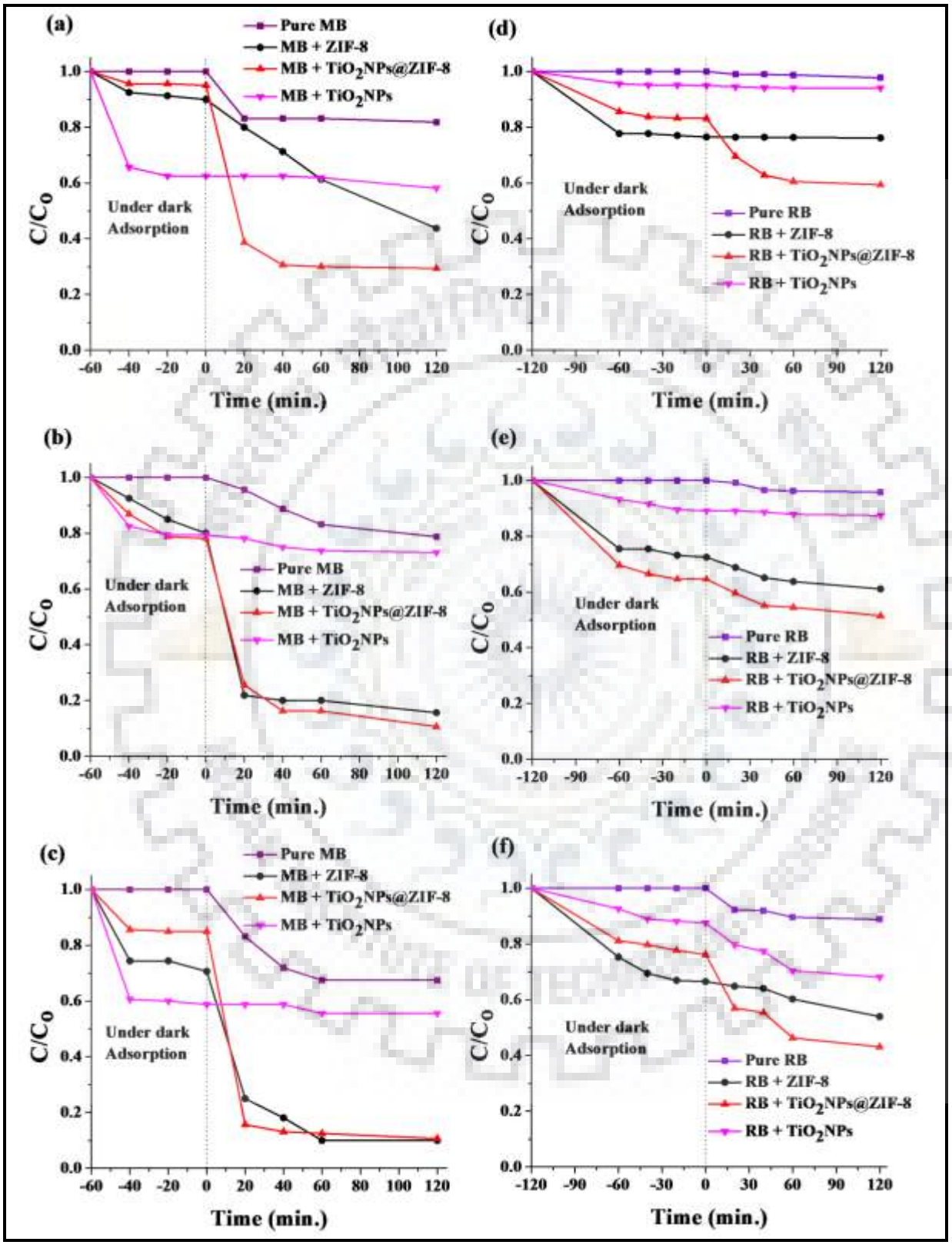

Fig. 3.13. The effect of pH for adsorption and photodegradation of [MB] = 1.64 mg L^{-1} at pH = 3.1, 8.5 and 11.5, represented as (a), (b) and (c), respectively, and [RB] = 2.4 mg L^{-1}at pH = 3.3, 8.6 and 12.6 represented as (d), (e) and (f), respectively.

Further, it is as already reported [11] that the increased OH^- concentration may be the possible reason for the high photodegradation efficiency for MB as OH^- could neutralize the H^+ generated by photocatalysts. In addition to this, the adsorption of dye on adsorbent surface may influence its photodegradation process as higher adsorption should enhance the photodegradation. Further, for UV/TiO_2 film system and aqueous TiO_2NPs suspension [22, 23], higher dye (MB) colour removal efficiency has been reported at pH 4 which is consistent with our observed higher adsorption capacity (%dye removal) and %photodegradation (MB) using TiO_2NPs at pH 3.1 than that at pH 8.5. The results indicate that TiO_2NPs@ZIF-8 composite is better photocatalyst than ZIF-8 for RB whereas both the catalysts have comparable degradation efficiency for MB in alkaline environment.

3.3.8.4. Effect of Initial Dye Concentration

The results of the influence of the initial concentration of dye for adsorption and photodegradation of MB at pH 11.5 and RB at pH 12.6 are given in Table 3.6 and concentration (C/C_o) vs time plots are represented in Fig. 3.14(a, b) and Fig. 3.14(c, d), respectively. The photodegradation of same concentrations of the dye solution was also studied as control. The results indicate that both the adsorption and %photodegradation of MB and RB are strongly dependent on their initial concentration. In control (MB/RB), %photodegradation decreases with increasing the concentration of dye solution but in presence of photocatalyst, %photodegradation increases slightly then decreases for MB, whereas it decreases continuously for RB. The reaction in photodegradation of both the dyes involves interaction between $^{\bullet}OH$ generated at the active OH^- sites and the molecules of the dye solution. At lower concentration, the number of available active site is more than the dye molecules, whereas the increase of the dye molecules at its higher concentration around the active sites resulted in inhibiting the penetration of light to the surface of the photocatalyst. Therefore, the generation of relative amount of $^{\bullet}OH$ and $^{\bullet}O_2^-$ on the surface of the photocatalyst decreased with the intensity of light and irradiation times are constant. The slight increase in %photodegradation of MB with increase in its concentration may be due to the fact that 10 mg of photocatalyst may have some unoccupied or partially occupied active sites, whereas %photodegradation of RB continuously decreases for all the photocatalysts because the initial concentration of RB was 2.40 mg L^{-1} for the same amount (10 mg) of the photocatalysts. Similar trends in the adsorption of both the dyes have been observed for TiO_2NPs@ZIF-8 composite and TiO_2NPs, but adsorption capacity

of ZIF-8 decreases continuously for MB and increases continuously for RB with increase in the initial concentration of the dye. The photocatalytic activity of ZIF-8 and TiO_2NPs@ZIF-8 composite for degradation of MB and RB is much better than TiO_2NPs.

Table 3.6. Effect of initial concentration of MB; Experimental conditions: 10 mg of ZIF-8 or TiO_2NPs@ZIF-8; Amount of TiO_2NPs equivalent to that present in 150 µL encapsulated TiO_2NPs@ZIF-8 composite; pH 11.5 for MB; pH 12.6 for RB; time length: 120 min except for adsorption studies of MB time length: 60 min.

Conc. of dye	Adsorption capacity, q_t (mg/g); [%dye removal]				%Photodegradation		
	ZIF-8	TiO_2NPs	TiO_2NPs @ZIF-8	Pure dye	ZIF-8	TiO_2NPs	TiO_2NPs @ZIF-8
1.6 [MB]	0.94 [29.3]	1.32 [41.2]	0.48 [15.0]	32.5	90.0	44.3	89.3
3.19 [MB]	0.83 [12.9]	2.14 [33.5]	0.68 [10.6]	23.5	91.2	61.1	93.4
6.38 [MB]	0.48 [3.7]	1.46 [11.4]	0.70 [5.4]	11.5	84.4	30.2	90.9
2.4 [RB]	1.60 [33.4]	0.59 [12.4]	1.14 [23.7]	11.1	46.1	31.8	56.8
4.79 [RB]	2.23 [23.2]	0.73 [7.6]	1.70 [17.7]	1.67	18.9	11.3	33.1
9.58 [RB]	0.7 [3.4]	0.71 [3.7]	2.53 [13.1]	1.8	7.7	6.8	16.9

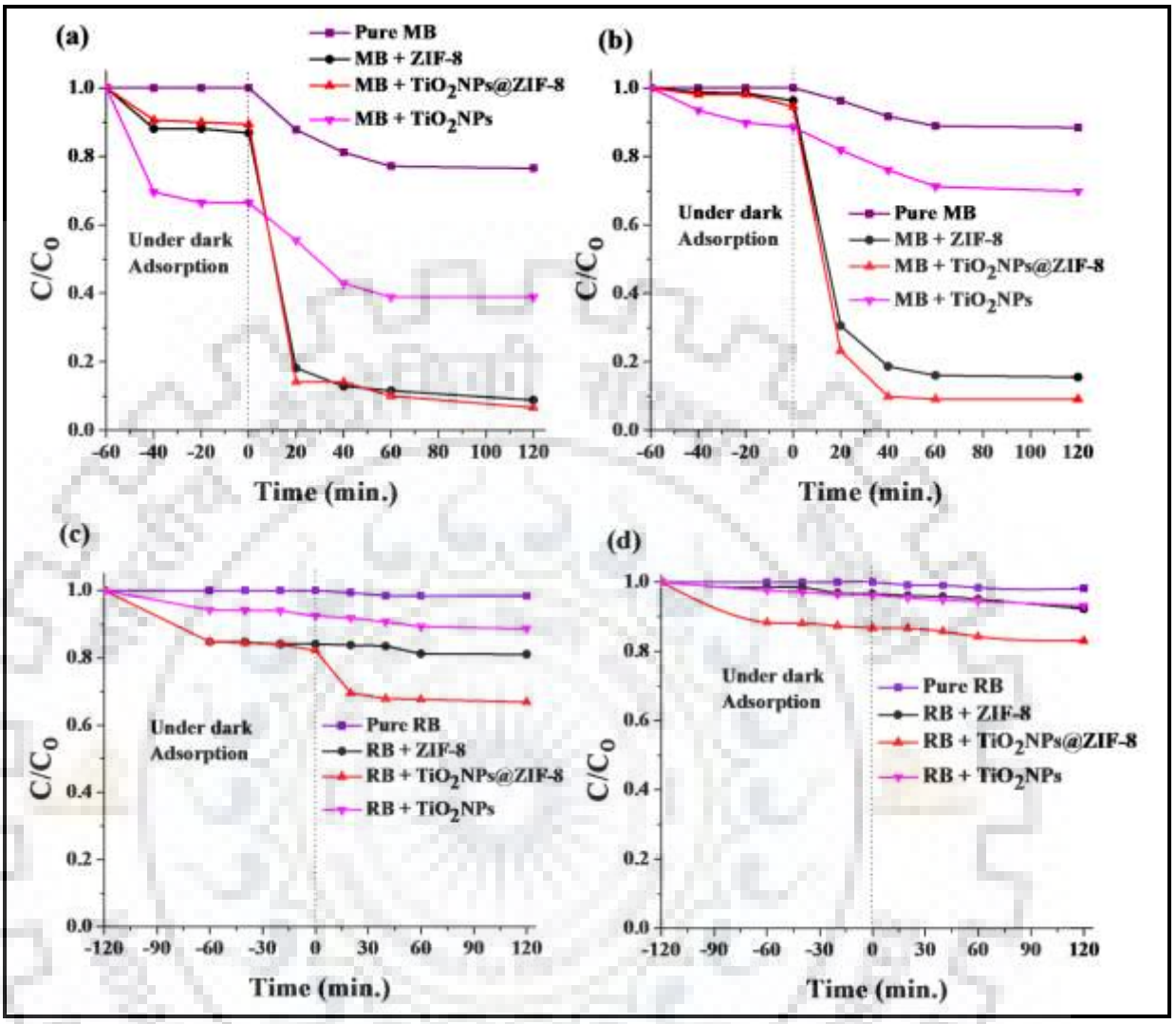

Fig. 3.14. The effect of initial concentration of MB and RB for adsorption and photodegradation of [MB] = 3.19 mg L^{-1} (a) and [MB] = 6.38 (b), at pH = 11.5; [RB] = 4.79 (c) and [RB] = 9.58 (d) at pH = 12.6; photocatalyst's amount 10 mg.

3.3.9. Spectrofluorometric Studies

The active species responsible for photocatalytic degradation of methylene blue is the hydroxyl radicals ($^{\bullet}$OH) [11] and efficiency of photocatalysts for degradation of dyes is mainly influenced by the concentration of the generated $^{\bullet}$OH which can be determined by fluorescence intensity measurements. Hence, the fluorescence spectral changes of terephthalic acid (0.5 mM) have been recorded at the excitation wavelength of 315 nm in the absence of photocatalysts under UV-visible irradiation and dark (Fig. 3.15(a) and Fig. 3.16(a), and in the presence of photocatalysts under UV-visible irradiation as well as under dark (Fig. 3.15(b–d) and Fig.

3.16(b–d), respectively). It has been clearly observed that TiO_2NPs@ZIF-8 composite and ZIF-8 favor the formation of $^{\bullet}OH$ under UV-visible light irradiation because the fluorescence intensity at 425 nm increases sharply with irradiation time, whereas there is almost no increment in the fluorescence intensity observed in the systems under dark condition (Fig. 3.16(b) and Fig. 3.16(c)), except a slight increment in case of TiO_2NPs, indicating that no $^{\bullet}OH$ has been produced in dark. Further, there is a gradual very small increase in the fluorescence intensity is observed with irradiation time in the absence of photocatalysts under UV-visible light irradiation (Fig. 3.15(a)), which indicates clearly that $^{\bullet}OH$ can be generated moderately by UV-visible light irradiation.

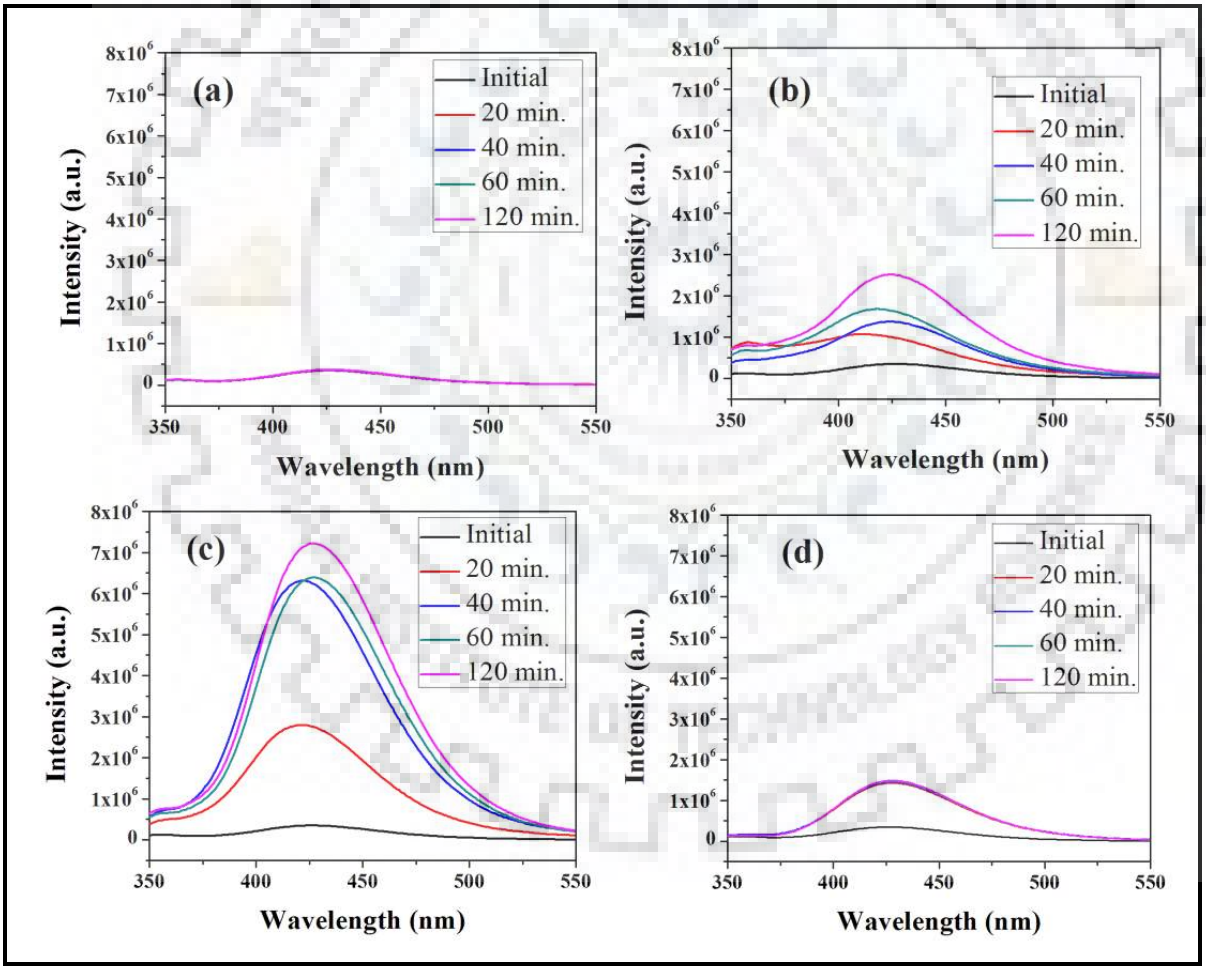

Fig. 3.15. Fluorescence spectral changes (excitation at 315 nm; under UV-visible light) of terephthalic acid (0.5 mM; NaOH 2 mM) (a); in presence of ZIF-8 (10 mg) (b); in presence of TiO_2NPs@ZIF-8 composite (10 mg) (c); in presence of TiO_2NPs (equivalent amount present in 150 µL encapsulated TiO_2NPs@ZIF-8 composite) (d).

The maximum increase in the fluorescence intensity has been seen in TiO_2NPs@ZIF-8/UV-visible system followed by ZIF-8/UV-visible system suggested their greater photocatalytic efficiency resulted by synergistic effect of the combination of photocatalysts and UV-visible light irradiation.

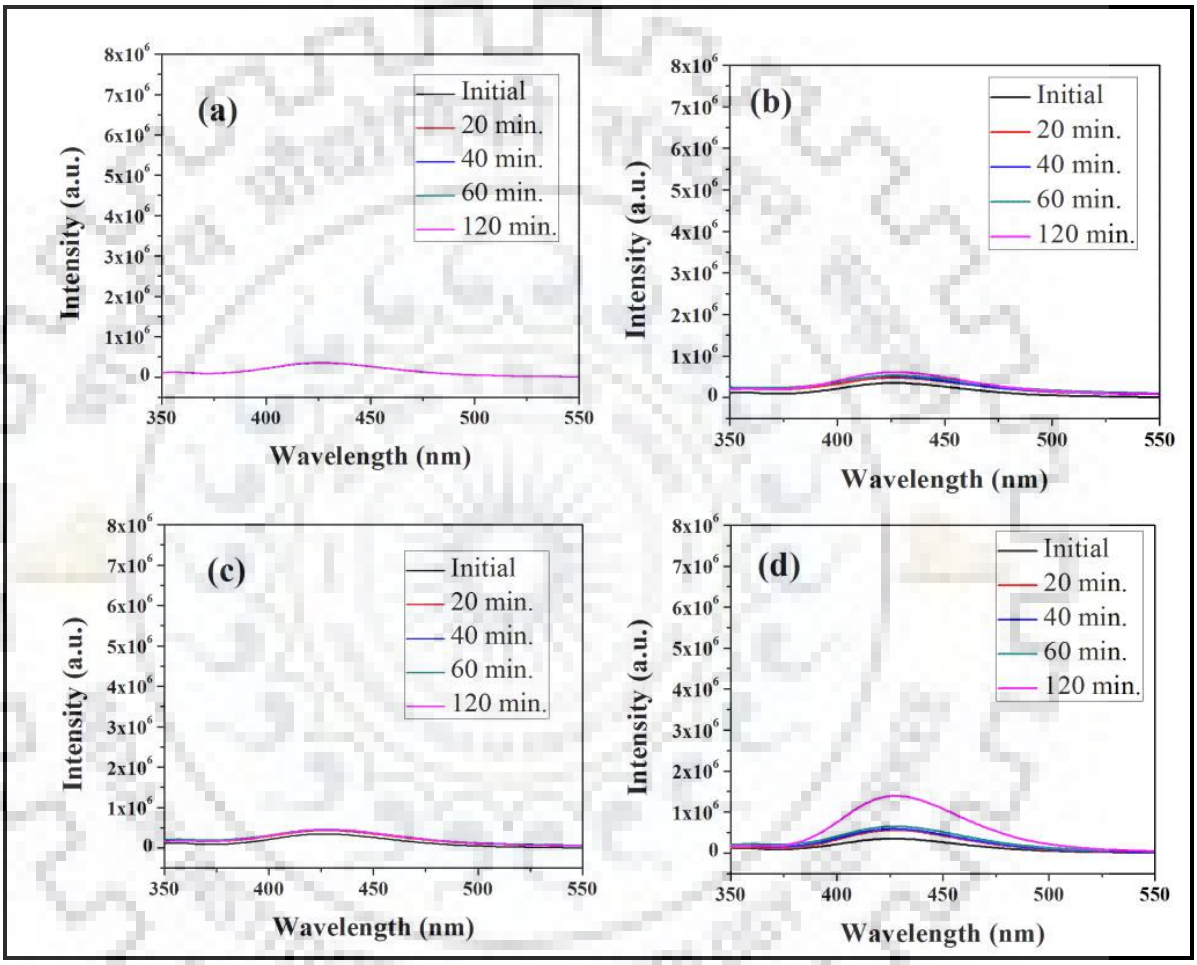

Fig. 3.16. Fluorescence spectral changes (excitation at 315 nm; under dark) of terephthalic acid (0.5 mM; NaOH 2 mM) (a); in presence of ZIF-8 (10 mg) (b); in presence of TiO_2NPs@ZIF-8 composite (10 mg) (c); in presence of TiO_2NPs (equivalent amount present in 150 µL suspension) (d).

3.3.10. Plausible Degradation Mechanism

The basic mechanism of photocatalysis of multi-core–shell TiO_2NPs@ZIF-8 composite involves the synergetic effect of TiO_2 NPs and ZIF-8. The photogenerated e^- and h^+ pair in the conduction band (CB) and valance band (VB) of TiO_2NPs can either recombine or undergo an interfacial electron transfer processes. However, in visible light, the generation of exciton of

TiO_2NPs seems to be difficult as the band gap of TiO_2NPs is slightly higher than the energy provided by visible light. In case of TiO_2NPs@ZIF-8 composite material, the band gap is slightly reduced. Here, the core (TiO_2NPs) acts as a main photocatalyst and shell material (ZIF-8) could act as a co-catalyst. Further, ZIF-8 helps to reduce the recombination of e^- and h^+ pair and is beneficial to the charge separation as well as narrowing the band gap. The photocatalysis of ZIF-8 is due to ligand-to-metal charge transfer mechanism [11]. The photon induced e^- and h^+ pair can easily move to the surface of composite material where they undergo reactions to produce hydroxyl radicals [24]. It has been confirmed experimentally that the $^{\bullet}OH$ radicals are most effectively generated in the presence of TiO_2NPs@ZIF-8 composite under UV-visible light, which enhances photo-induced catalytic degradation of organic dyes taken in the present study. Therefore, the ease of excited e^- and h^+ to react with dissolved oxygen and water to generate hydroxyl radicals enhances photo-induced catalytic degradation of organic dyes owing to synergic effect of TiO_2NPs and ZIF-8. The photodegradation mechanism of dye is shown in Fig.3.17.

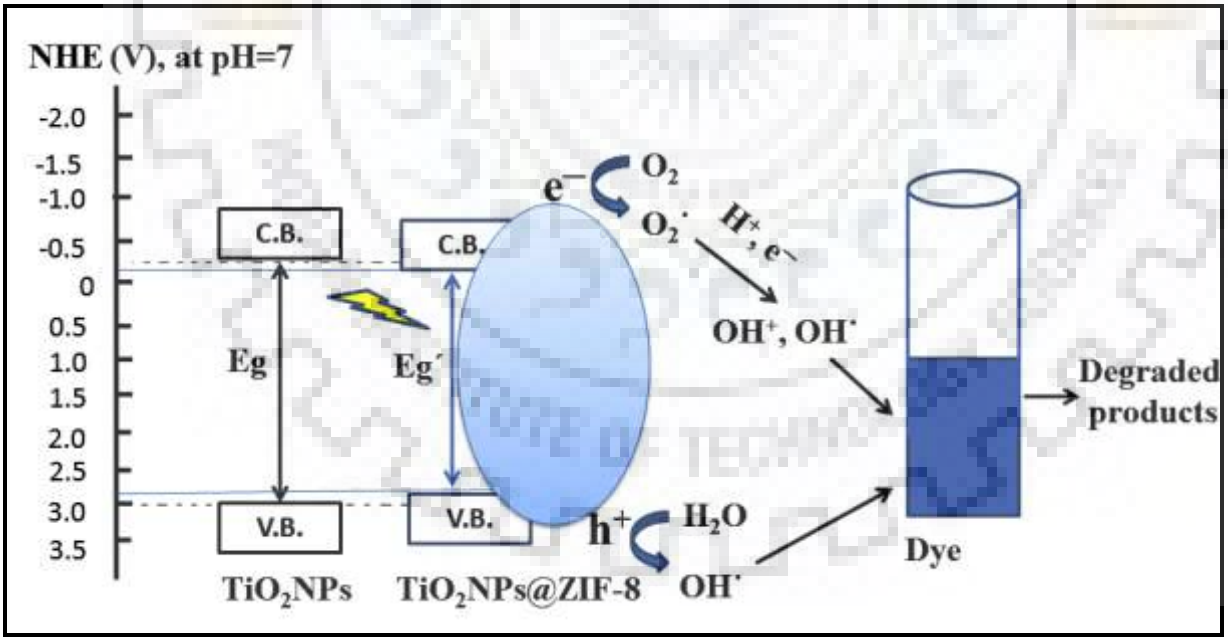

Fig. 3.17. Mechanism of photocatalytic activity of TiO_2NPs@ZIF-8 composite. The dashed lines indicate VB and CB of TiO_2NPs, whereas E'_g represents decreased band gap of TiO_2NPs after encapsulation. The solid lines indicate VB and CB of TiO_2NPs@ZIF-8 composite and E_g represents band gap of TiO_2NPs.

3.3.11. GC-MS Analysis

After the photodegradation process, the degradation by-products were analyzed by GC-MS and identified their plausible fragment ions in the mass spectra. The possible degradation pathway is proposed as shown in scheme 3.2 for MB and in scheme 3.3 for RB based on the information provided by GC-MS, which are according to the reactions reported previously for the degradation pathways of MB [11, 24] and RB [25]. Mass spectra of fragments of MB and RB are given in the Fig. 3.18 and Fig. 3.19, respectively. The molecular ion peaks of various intermediates are very small indicating their very small fraction left after photodegradation (irradiation period of 120 min.), whereas their fragmented ions/molecules are observed in comparatively larger amounts in GC-MS spectra. In case of MB, some hydroxylated intermediates have certainly been formed but could not be extracted due to their hydrophilic character. Further, the complete mineralization of organic dyes to inorganic ions (CO_2, NO_3^-, SO_4^- and NH_4^+ as ultimate end products) could be taken place after a long period of irradiation as reported (say 1000 min) [24].

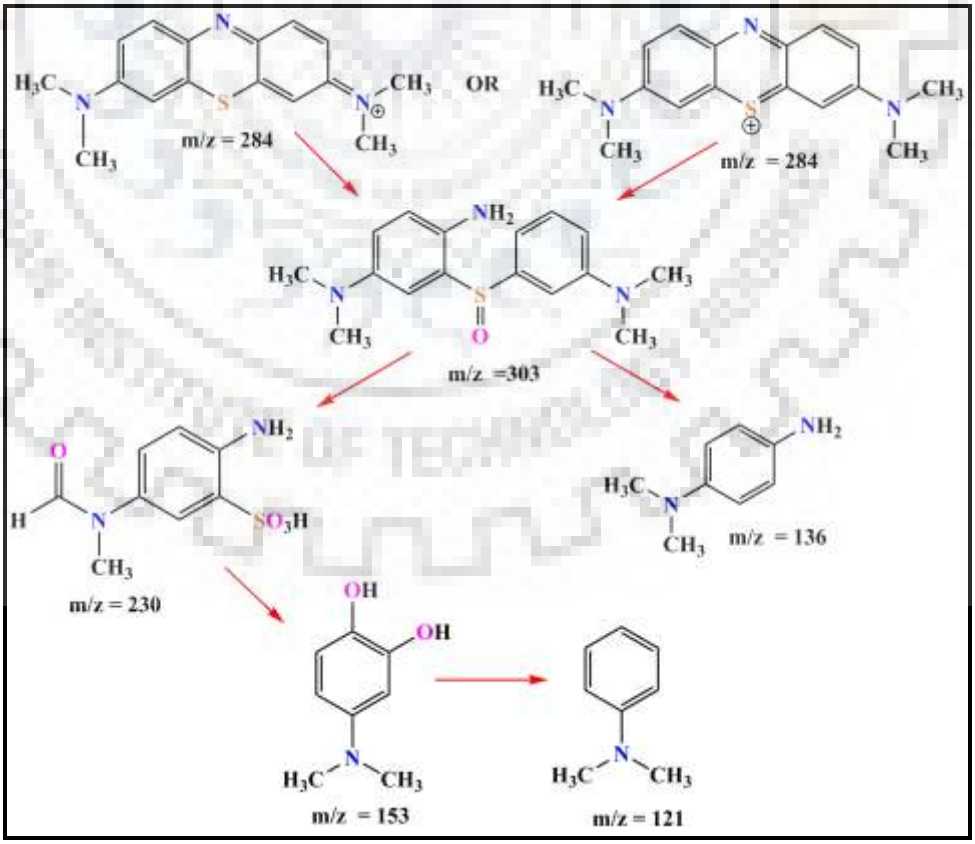

Scheme 3.2. Proposed photocatalytic degradation pathway of MB by using TiO_2NPs@ZIF-8 composite.

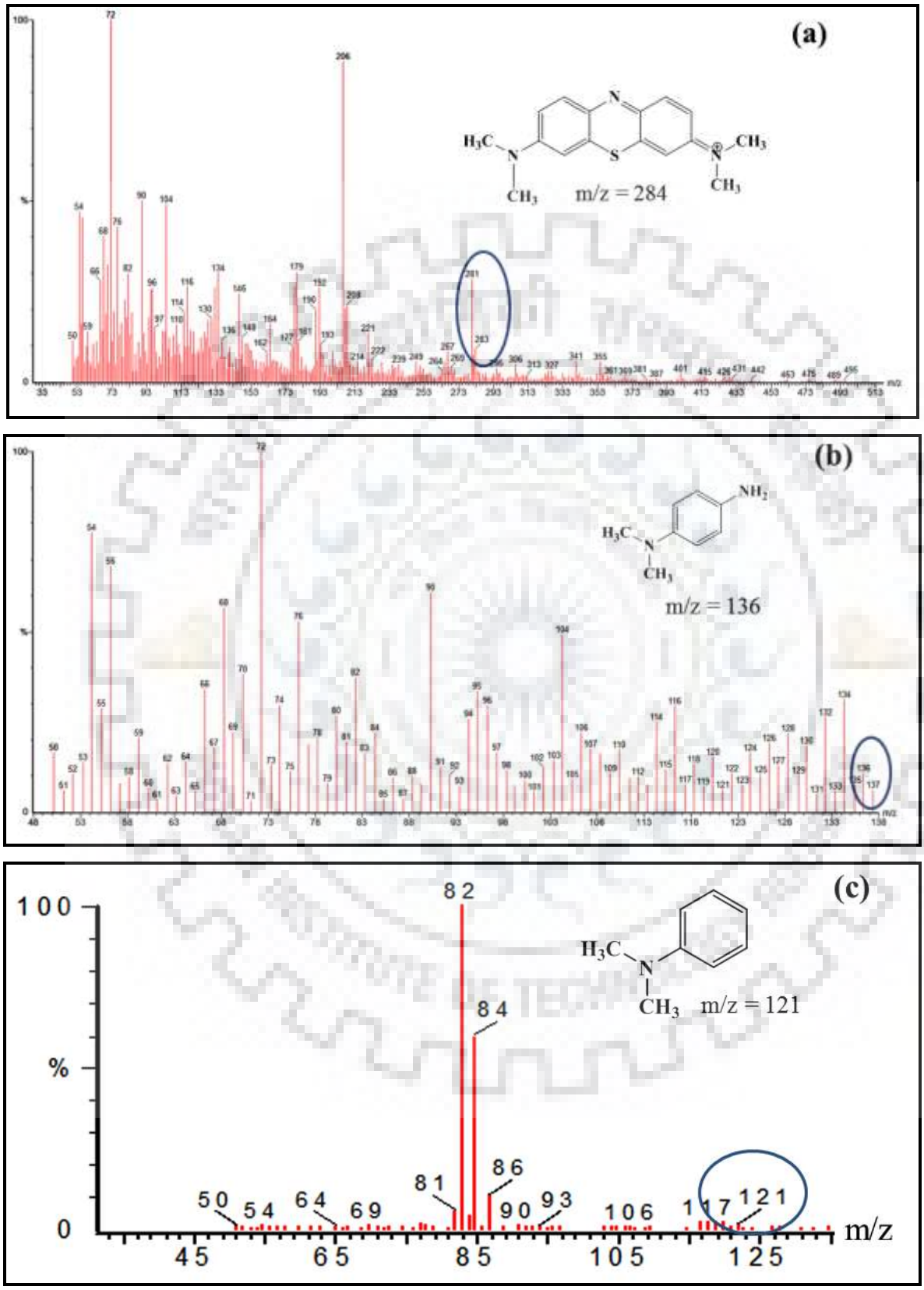

Fig. 3.18. The GC-MS spectra of identified intermediates structure (Proposed in Scheme 3.2) after the degradation of MB are shown (a-c), respectively.

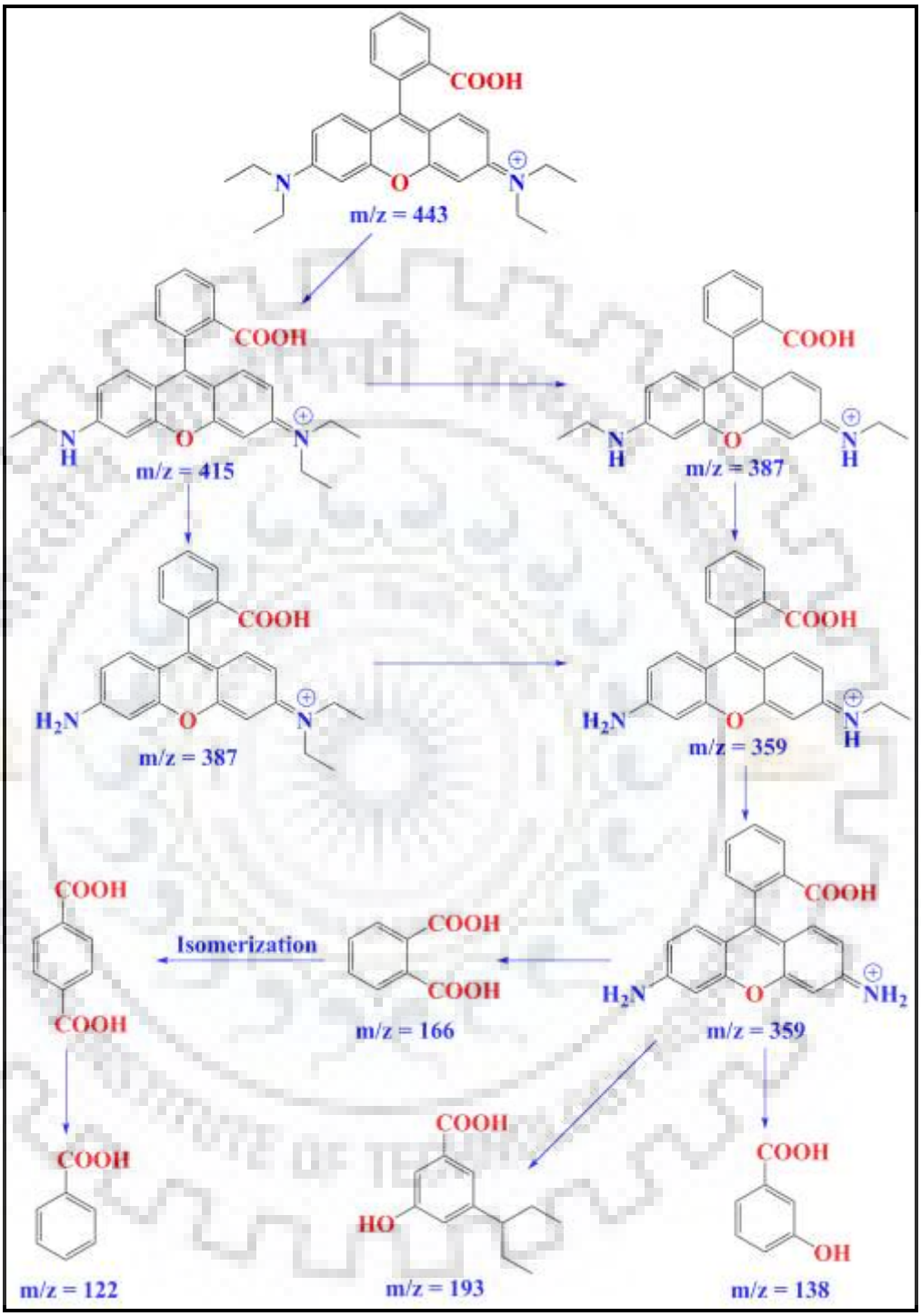

Scheme 3.3. Proposed photocatalytic degradation pathway of RB by using TiO_2NPs@ZIF-8 composite.

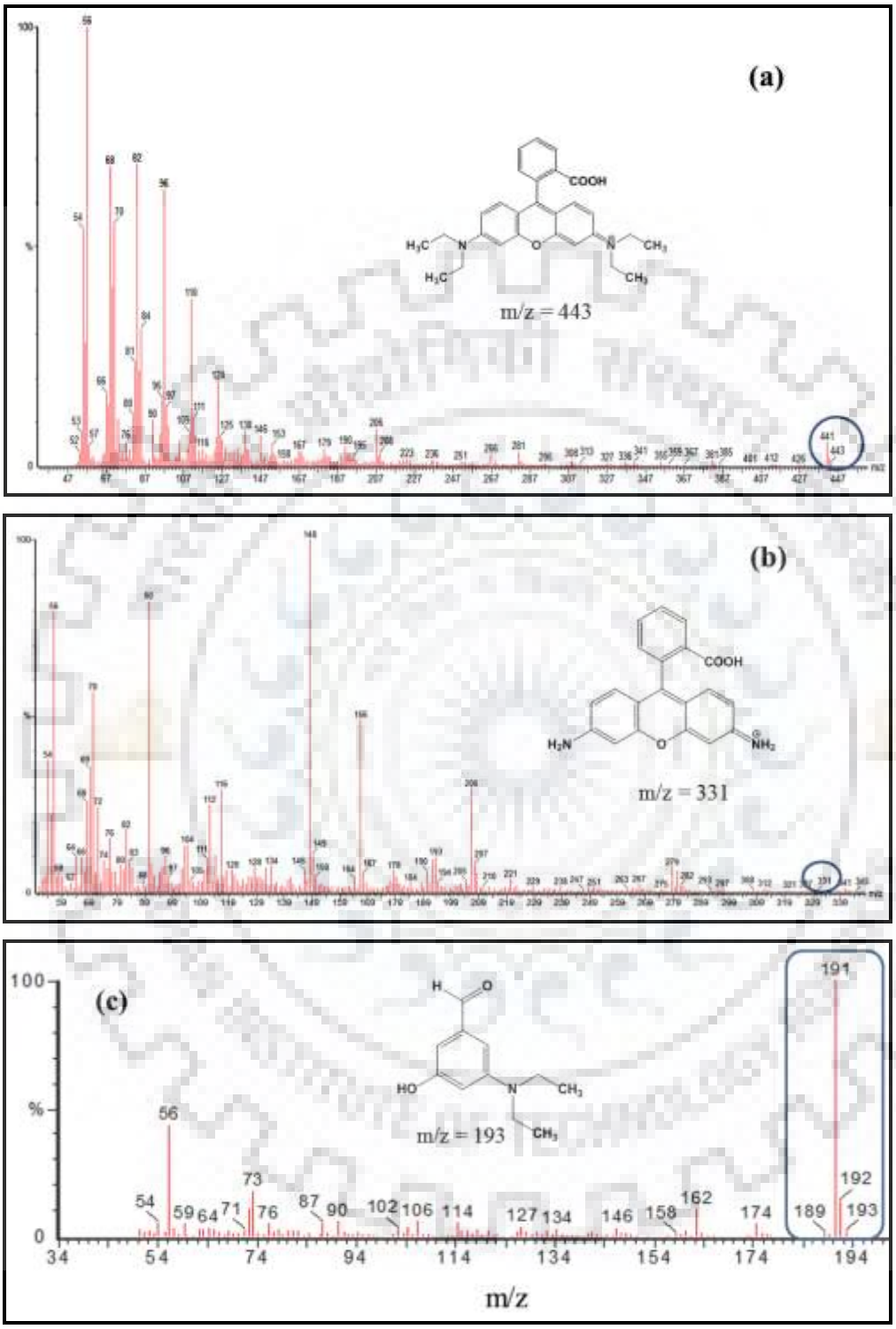

Continued

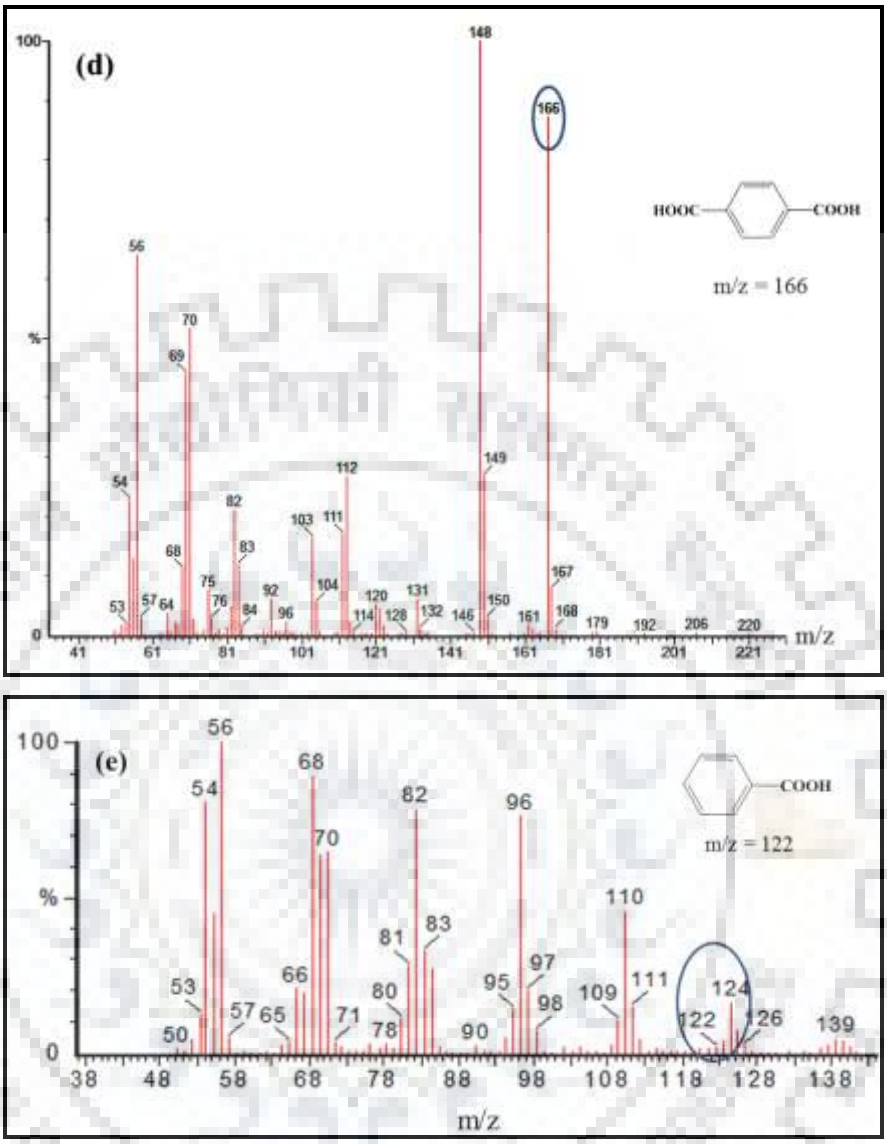

Fig. 3.19. The GC-MS spectra of identified intermediates structure (Proposed in Scheme 3.3) after degradation of RB are shown (a-e), respectively.

3.3.12. Chemical Kinetics

Kinetic studies for photocatalytic degradation of MB and RB have been observed at pH = 8.5 for MB and 8.6 for RB and it was found the degradation of dyes follow the first order of kinetics. Plot between $\ln(C_o/C_t)$ vs time (t) has been found linear which is shown in Fig. 3.20. The rate constant was calculated by using equation (3.3).

$$\ln (C_o/C_t) = k \times t \qquad \text{(Eq. 3.3)}$$

Where C_o is initial concentration and C_t is concentration at "t" time, "t" represents time and k is rate constant. The rate constant value for the degradation of MB and RB dyes were obtained from the slope of the straight lines when ln (C_o/C_t) is plotted against time "t". The rate constant value and r^2 for both dyes are tabulated in Table 3.7.

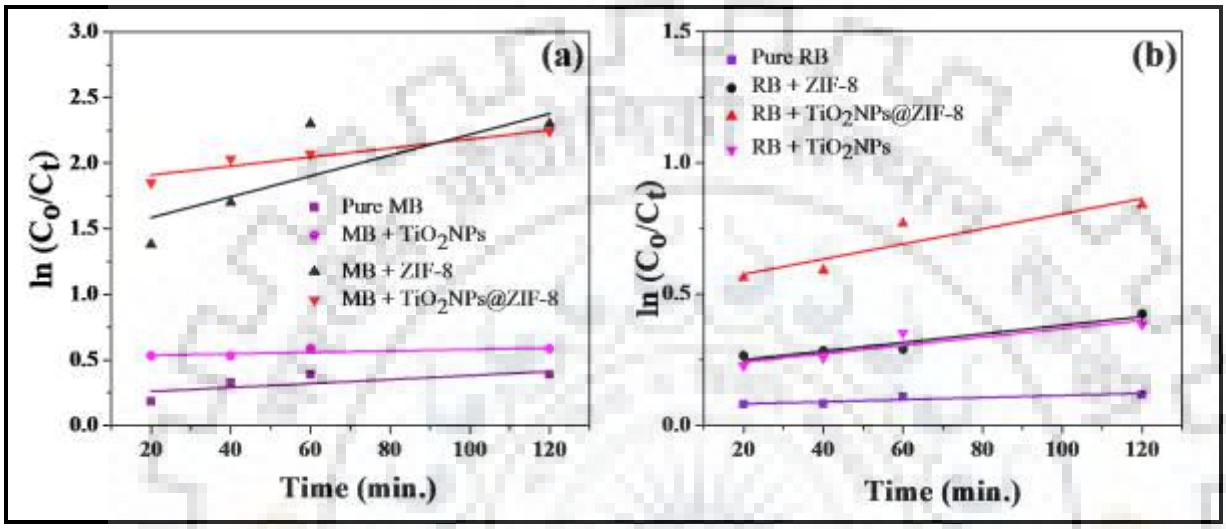

Fig. 3.20. (a, b) Kinetic plots of MB and RB dye are shown, respectively.

Table 3.7. Kinetic parameters of studied pollutants (MB and RB).

S.N.	Substrate/Materials	r^2	k (min^{-1})
1.	Pure MB	0.46	0.0015
2.	MB + ZIF-8	0.61	0.0020
3.	MB + TiO_2NPs	0.59	0.0020
4.	MB + TiO_2NPs@ZIF-8	0.91	0.0023
5.	Pure RB	0.73	0.0020
6.	RB + ZIF-8	0.90	0.0016
7.	RB + TiO_2NPs	0.74	0.0015
8.	RB + TiO_2NPs@ZIF-8	0.76	0.0028

3.4. CONCLUSION

In nutshell, ZIF-8 and multi-core-shell TiO_2NPs@ZIF-8 composite can be considered as effective photocatalysts for degradation of methylene blue and rhodamine-B under UV-visible light irradiation. The proper encapsulation of TiO_2NPs within ZIF-8 framework provided the best yet mode of employing TiO_2NPs for photocatalytic degradation of industrial dyes as here the efficiency for photocatalysis was enhanced as well as the chance to reuse the same core-shell nanoparticles-metal-organic framework composite for several catalytic cycles was much higher. Further, multi-core-shell TiO_2NPs@ZIF-8 composite as well as ZIF-8 worked over a wide range of pH, and showed high adsorption and degradation efficiency for the industrial dyes under strong alkaline medium. The possible mechanism for photocatalytic degradation of both the dyes by hydroxyl radicals as confirmed by fluorescence spectral studies has been proposed. The plausible pathways involving possible intermediates formed during the photodegradation of both the dyes have also been proposed. In comparison to ZIF-8, the multi-core-shell composite TiO_2NPs@ZIF-8 is much superior and effective photocatalyst and has reusability after several cycles.

NOTE: The work of this Chapter was published into two parts as *communication* and *Full length* paper in peer reviewed journal as given below.

1. R. Chandra, S. Mukhopadhyay and M. Nath, "TiO_2@ZIF-8: A novel approach of modifying micro-environment for enhanced photo-catalytic dye degradation and high usability of TiO_2 nanoparticles" Mater. Lett. 164 (2016) 571-574.
2. R. Chandra and M. Nath, "Multi-Core–shell TiO_2NPs@ZIF-8 Composite for Enhanced Photocatalytic Degradation and Adsorption of Methylene Blue and Rhodamine-B" ChemistrySelect 2 (2017) 7711-7722.

- The supporting data also available on given links
  https://www.sciencedirect.com/science/article/pii/S0167577X15308399#s0035
  https://doi.org/10.1002/slct.201701195

3.5. REFERENCES

(1) Dong, S.; Feng, J.; Fan, M.; Pi, Y.; Hu, L.; Han, X.; Liu, M.; Sun, J.; Sun, J. Recent Developments in Heterogeneous Photocatalytic Water Treatment Using Visible Light Responsive Photocatalysts: A Review. *RSC Adv.* **2015**, *5*, 14610-14630.

(2) Hernández-Alonso, M. D.; Fresno, F.; Suárez, S.; Coronado, J. M. Development of Alternative Photocatalysts to TiO_2: Challenges and Opportunities. *Energy Environ. Sci.* **2009**, *2* (12), 1231-1257.

(3) Kim, S. P.; Choi, M. Y.; Choi, H. C. Photocatalytic Activity of SnO_2 Nanoparticles in Methylene Blue Degradation. *Mat. Res. Bull.* **2016**, *74*, 85-89.

(4) Wang, M.; Ioccozia, J.; Sun, L.; Lin, C.; Lin, Z. Inorganic-Modified Semiconductor TiO_2 nanotube arrays for photocatalysis. *Energy Environ. Sci.* **2014**, *7* (7), 2182-2202.

(5) Faghihian, H.; Bahranifard, A. Application of TiO_2-Zeolite as Photocatalyst for Photodegradation of Some Organic Pollutants. *Iran. J. Catal.* **2011**, *1* (1), 45-50.

(6) Sima, J.; Hasal, P. Photocatalytic Degradation of Textile Dyes in aTiO_2/UV System. *Chem. Engg. Trans.* **2013**, *32*, 1974-1984.

(7) Daghrir, R.; Drogui, P.; Robert, D. Modified TiO_2 for Environmental Photocatalytic Applications: A Review. *Ind. Eng. Chem. Res.* **2013**, *52* (10), 3581-3599.

(8) Asahi, R.; Morikawa, T.; Ohwaki, T.; Aoki, K.; Taga, Y. Visible-Light Photocatalysis in Nitrogen-doped Titanium Oxides. *Science* **2001**, *293* (5528), 269-271.

(9) Yu, J. C.; Yu, J.; Ho, W.; Jiang, Z.; Zhang, L. Effects of F-doping on the Photocatalytic Activity and Microstructures of Nanocrystalline TiO_2 Powders. *Chem. Mater.* **2002**, *14*(9), 3808-3816.

(10) Chen, X.; Mao, S. S. Titanium dioxide Nanomaterials: Synthesis, Properties, Modifications, and Applications. *Chem. Rev.* **2007**, *107* (7), 2891-2959.

(11) Jing, H. P.; Wang, C. C.; Zhang, Y. W.; Wang, P.; Li, R. Photocatalytic Degradation of Methylene Blue in ZIF-8. *RSC Adv.* **2014**, *4* (97), 54454-54462.

(12) Jiang, W.; Joens, J. A.; Dionysiou, D. D.; O'Shea, K. E. Optimization of Photocatalytic Performance of TiO_2 Coated Glass Microspheres Using Response Surface Methodology and the Application for Degradation of Dimethyl Phthalate. *J. Photochem. Photobiol. A* **2013**, *262*, 7-13.

(13) Ai, L.; Zhang, C.; Li, L.; Jiang, J. Iron Terephthalate Metal-Organic Framework: Revealing the Effective Activation of Hydrogen Peroxide for the Degradation of

Organic Dye Under Visible Light Irradiation. *Appl. Catal. B: Environ.* **2014**, *148*, 191-200.

(14) Biswal, B. P.; Shinde, D. B.; Pillai, V. K.; Banerjee, R. Stabilization of Graphene Quantum Dots (GQDs) by Encapsulation Inside Zeolitic Imidazolate Framework Nanocrystals for Photoluminescence Tuning. *Nanoscale* **2013**, *5* (21), 10556-10561.

(15) Ray, K. G.; Olmsted, D. L.; Houndonougbo, Y.; Laird, B. B.; Asta, M. Origins of CH_4/CO_2 Adsorption Selectivity in Zeolitic Imidazolate Frameworks: A Vander Waals Density Functional Study. *J. Phy. Chem. C* **2013**, *117* (28), 14642-14651.

(16) Bobrova, A.; Zhigun, I.; Bragina, M.; Fotiev, A. Infrared Absorption Spectra of Various Titanium Compounds. *J. Appl. Spectrosc.* **1968**, *8* (1), 59-63.

(17) Tauc, J.; Grigorovici, R.; Vancu, A. Optical Properties and Electronic Structure of Amorphous Germanium. *Phy. status solidi. B* **1966**, *15* (2), 627-637.

(18) Nazarkovsky, M.; Gun'ko, V.; Wójcik, G.; Czech, B.; Sobieszek, A.; Skubiszewska-Zięba, J.; Janusz, W.; Skwarek, E. Band-gap Change and Photocatalytic Activity of Silica/Titania Composites Associated with Incorporation of CuO and NiO. *Chem. Phys. Technol. Surf.* **2014**, *5*, 421-437.

(19) Ettireddy, P. R.; Ettireddy, N.; Mamedov, S.; Boolchand, P.; Smirniotis, P. G. Surface Characterization Studies of TiO_2 Supported Manganese Oxide Catalysts for Low Temperature SCR of NO with NH_3. *Appl. Catal. B: Environ.* **2007**, *76* (1-2), 123-134.

(20) Abidov, A.; Allabergenov, B.; Lee, J.; Jeon, H. W.; Jeong, S. W.; Kim, S. X-ray Photoelectron Spectroscopy Characterization of Fe Doped TiO_2 Photocatalyst. *Int. J. Mater. Mech. Manuf.* **2013**, *1* (3), 294-296.

(21) Ngah, W. W.; Teong, L.; Toh, R.; Hanafiah, M. Comparative Study on Adsorption and Desorption of Cu (II) Ions by Three Types of Chitosan-Zeolite Composites. *Chem. Eng. J.* **2013**, *223*, 231-238.

(22) Kuo, W.; Ho, P. Solar Photocatalytic Decolorization of Methylene Blue in Water. *Chemosphere* **2001**, *45* (1), 77-83.

(23) Lee, B. N.; Liaw, W. D.; Lou, J. C. Photocatalytic Decolorization of Methylene Blue in Aqueous TiO_2 Suspension. *Environ. Eng. Sci.* **1999**, *6*, 165-175.

(24) Houas, A.; Lachheb, H.; Ksibi, M.; Elaloui, E.; Guillard, C.; Herrmann, J. M. Photocatalytic Degradation Pathway of Methylene Blue in Water. *Appl. Catal. B: Environ.* **2001**, *31* (2), 145-157.

(25) He, Z.; Sun, C.; Yang, S.; Ding, Y.; He, H.; Wang, Z. Photocatalytic Degradation of Rhodamine-B by Bi_2WO_6 with Electron Accepting Agent under Microwave Irradiation: Mechanism and Pathway. *J. Hazard. Mater.* **2009**, *162* (2-3), 1477-1486.

Chapter Four

Synthesis of SnO_2NPs@ZIF-8 Composite: Potential Antiviral Agent and Effective Photocatalyst for Waste-water Treatment

"The roots of education are bitter, but the fruit is sweet"

Aristotle

4.1. INTRODUCTION

Metal organic frameworks (MOFs) are very useful in drug release application on account of their fascinating hydrophilic-hydrophobic internal microenvironments [1, 2]. In the past several years, MOFs have been reported as excellent nanocarriers, *for instance*, iron metal based MOFs used as nanocarrier for the controlled delivery of antitumoral and retroviral drugs [3, 4]. Further, zeolitic imidazole framework (ZIF-8) has been exclusively exploited for the delivering of drugs, including 5-fluorouracil [5], curcumin [6] and doxorubicin [7]. Moreover, due to high surface area, uniform porosity and high thermal stability of ZIF-8, it also has many potential applications such as gas storage, gas separation, photocatalysis, selective sensing and so on [8-10]. Additionally, multifunctional core-shell composites of ZIF-8 with various metals (M@ZIF-8) [11-17], metal oxides (MO_x@ZIF-8) [18-25] and molecules (Molecules@ZIF-8) [26, 27] have been investigated and successfully employed in various applications *viz.*, catalysis, oxidation, reduction, photocatalysis, and electrochemical supercapacitors. However, these hybrid materials have not been explored for the biological application such as anti-bacterial, anti-fungal and anti-viral agents so far, except very recently ZnO@ZIF-8 and CdS@ZIF-8 composites have been reported as antimicrobial catheters [28] and anti-bacterial agent against GFP-expressing *E. coli* and *S. aureus* [29], respectively. In view of this, it is envisioned and encouraged to focus on the biological application of ZIF-8 and its hybrid nanostructures, especially their anti-viral application.

The viral infection is a world-wide problem and causing the life-threatening diseases by different viruses' *viz., Influenza, Hepatitis, Chickenpox, Herpes keratitis, Human Immunodeficiency virus, Viral Encephalitis, Ebola, Norovirus, Dengue,* and *Chikungunya virus* (CHIKV). CHIKV is a mosquito-transmitted re-emerging alphavirus which causes intense joint pain, swelling and high fever in humans. The main transmittance factors of CHIKV are *Aedes aegypti* and *Aedes albopictus*. The CHIKV belongs to alphavirus genus which is constructed by single standard positive-sense RNA virus [30, 31]. The nitrogen containing heterocyclic organic molecules have been exploited for design and synthesis of anti-viral drug molecules [32]. Recently, interferons, ribavirin and mercaptopurine [32] have been proposed as potent anti-viral agents against CHIKV. In the last decade CHIKV has caused outbreaks in the America, Asia and Indian oceans. However, there are no effective vaccines for the treatment of the Chikungunya according to World Health Organization [30]. A large number of semiconducting nanomaterials have been reported as photocatalysts, antiviral and antibacterial agents *e.g.* Fe_3O_4, TiO_2, ZnO and SnO_2 nanoparticles [33-41]. SnO_2 nanoparticles (NPs) have received

much attention due to their excellent chemical stability, optical and electrical properties [21]. SnO_2NPs are also very useful in gas sensing, solar cells, optoelectronic devices, lithium ion batteries and catalytic processes like degradation of methyl violet 6B and methylene blue (MB) [41, 42]. Interestingly, SnO_2 nanowires have been reported as potential antiviral agent [43]. Owing to non-toxic, bio-applicability and photocatalytic properties of SnO_2NPs and ZIF-8, it is worthwhile to synthesize core@shell material wherein SnO_2NPs act as core and ZIF-8 as shell material.

This chapter describes the one pot facile synthesis of multi-core-shell SnO_2NPs@ZIF-8 composite which can be utilized as a potential antiviral agent against chikungunya virus and as a photocatalyst for the degradation of MB dye for a sustainable environment.

4.2. EXPERIMENTAL SECTION

4.2.1. Cells and Viruses

Using standard virus adsorption techniques, an Indian Chikungunya Virus (CHIKV) isolate (strain DRDE-07; GenBank: EU372006) was propagated on *Vero* cell line (The NCCS, Pune) monolayer which were grown in Dulbecco's Modified Eagle's Medium (DMEM) supplemented with 10% fetal bovine serum (FBS) (Gibco, catalogue # 10270-106) incubated at 37 ^{o}C with 5% CO_2, and were further titrated for plaque assay. The aliquots of viral stock were stored at -80°C until needed.

4.2.2. Synthesis of SnO_2NPs

0.01 M $SnCl_4.5H_2O$ (3.5 g) and 0.01 M KCl (0.745 g) were ground for 30 min, and after that 0.04 M KOH (2.24 g) was added to the reaction mixture and ground for another 30 min at room temperature as depicted in Scheme 4.1. The resultant reaction mixture was transferred into a round bottom flask (250 mL) with 100 mL de-ionized water and kept on stirring for 3 h. The product was washed with de-ionized water and white precipitate was collected by centrifugation. The white precipitate was calcined at 200, 400 and 800 °C [44].

4.2.3. Synthesis of ZIF-8 and SnO_2NPs@ZIF-8 Composites

ZIF-8 was synthesized by the bench method whose details are given in Chapter three while SnO_2NPs@ZIF-8 composites were synthesized *via* encapsulation of pre-synthesized SnO_2NPs using bench method which is described in Scheme 4.2. During the addition of anhydrous zinc chloride methanol solution (0.341 g, 2.5 mM in 20 mL methanol) into 2-

methylimidazole methanol solution (1.642 g, 20 mM in 25 mL methanol) at room temperature, 150 µL suspension of SnO_2NPs (Average particle size *ca.* 16.23 ± 3.76 nm; 20 mg SnO_2NPs sonicated in 10 mL of methanol for 1 h) was added to the above reaction mixture at certain intervals of time in smaller volume. The reaction mixture was allowed to stand for 24 h without disturbing the interface. The solution was centrifuged, washed with methanol several times and dried in *vacuo* at 70 °C for 6 h. White crystalline powder of the composite was collected and stored in an airtight container. Similar method has been adopted for the encapsulation of 300 and 500 µL suspensions of SnO_2NPs. Hence, three multi-core-shell SnO_2NPs@ZIF-8 composites have been synthesized by encapsulation of 150, 300 and 500 µL SnO_2NPs suspension within ZIF-8 and named as NC1, NC2 and NC3, respectively.

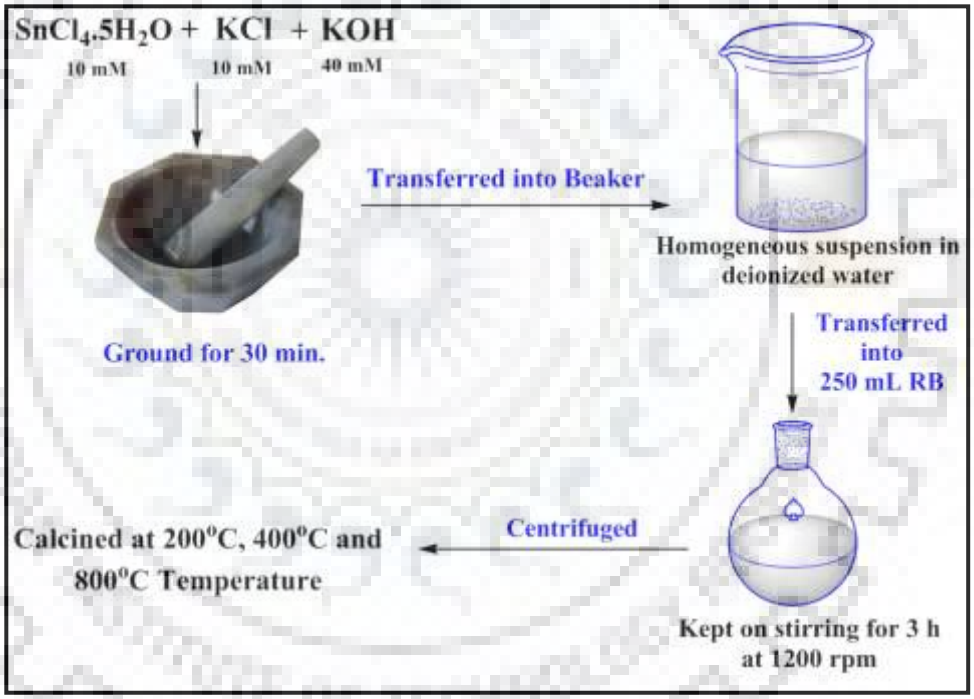

Scheme 4.1. Schematic presentation of synthesis of SnO_2NPs.

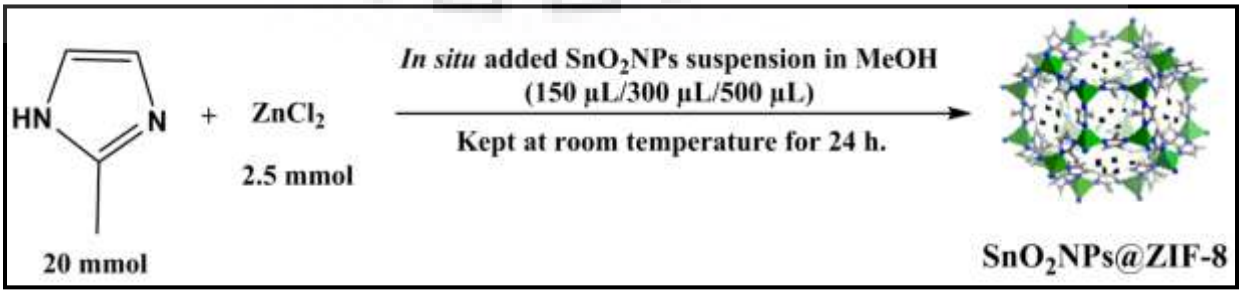

Scheme 4.2. Schematic presentation of synthesis of multi-core-shell SnO_2NPs@ZIF-8 composites.

4.2.4. Cytotoxicity Testing

Toxicity of SnO_2NPs, ZIF-8 and SnO_2NPs@ZIF-8 composites (NC1, NC2 and NC3) were determined *via* MTT (3-(4,5-dimethylthiazol-2-yl)-2,5-diphenyltetrazolium bromide) assay against *Vero* cell line. The assay is based on reduction of yellowish MTT reagent (0.5 mg mL^{-1}) to insoluble and dark blue formazan by metabolically active viable cells after 72 h after treatment. For this assay, cells were grown in 96 well plates with different concentration of SnO_2NPs, ZIF-8 and SnO_2NPs@ZIF-8 composites in triplicates for 48 h at 37 °C. Following the addition of 20 µL of MTT, the cells were incubated for 4 h at 37 °C. Further, 100 µL dimethyl sulphoxide (DMSO) was added and the absorbance was measured at 570 nm using multi-mode plate reader cytation 3 (BioTek Instruments, Inc.). All the readings were normalized with the control experiment in which *Vero* cells were grown in DMEM with 10 % FBS only without any treatment.

4.2.5. Time of Inhibitor Addition Assay

Multiplicity of infection (MOI) of 0.1 was selected to infect the *Vero* cells with CHIKV and incubated for 1.5 h at 37 °C and 5% CO_2. In addition, 0.04 mg mL^{-1} PBS suspension of SnO_2NPs, ZIF-8 and SnO_2NPs@ZIF-8 composites were added to the cells prior to infection (pre), during the infection (co) and after infection (post). Each of these treatment steps determines the stage at which virus is inhibited. The supernatant was collected after 24 h of post-infection (hpi) to determine the viral titers by employing plaque assay. The viral induced cytopathic effect (CPE) was recorded after 48 hpi by using light microscope (Leica, Germany). Control cells were only infected with CHIKV but were not given any treatment with SnO_2NPs, ZIF-8 and SnO_2NPs@ZIF-8 composite. In order to observe the effect of light on virus inhibition, the samples (SnO_2NPs, ZIF-8 and SnO_2NPs@ZIF-8 composites) aliquot were exposed under UV-visible irradiation (50 W Halogen lamp) for 20 min with gentle mixing of every 5 min interval. After incubation under UV-visible irradiation, SnO_2NPs, ZIF-8 and SnO_2NPs@ZIF-8 composites were added in similar way as non-photo-irradiated samples.

4.2.6. Plaque Reduction Assay

The reductions in virus titers due to addition of inhibitors were determined by using plaque assay. The 10-fold serial dilutions of CHIKV supernatant collected at 24 h were added to *Vero* cells for 1.5 h incubation and later carboxy methylcellulose (CMC)(2.5%) mixed with MEM (minimum essential media) and 2% FBS were added to the wells after removing viral

inoculum. After 3 days of incubation at the 37 °C in 5% CO_2, cells were stained with crystal violet to count the number of plaques. The assays were performed in triplicates. Virus titer was quantified as plaque forming unit per milliliter (PFU mL^{-1}). Using the viral titer values, percentage inhibition was determined as compared to the control wherein no any treatment was added at any time-of-inhibitor addition stage.

4.2.7. Statistical Methods

Quoted errors bars correspond to samples were calculated by standard deviation for plaque assay.

4.2.8. Adsorption and Photodegradation Studies

Adsorption and photodegradation studies were performed according to previously written in Chapter two and Chapter three.

4.3. RESULTS AND DISCUSSION

4.3.1. PXRD Analysis

The crystalline nature/structure of synthesized SnO_2NPs, ZIF-8 and their composites NC1, NC2 and NC3 have been analyzed by employing powder X-ray diffraction (PXRD) analysis. Fig. 4.1(a) shows the PXRD pattern of synthesized SnO_2NPs annealed at various temperatures *viz.*, 200, 400 and 800 °C. The PXRD pattern of SnO_2NPs matches with tetragonal rutile (caseterite form of SnO_2NPs) structure indexed with JCPDS No. 01-072-1147. The average crystallite size (D) of synthesized SnO_2NPs has been calculated from more intense peak (110) by using the Debye-Scherrer equation (Eq).

$$\boldsymbol{D = \frac{0.89\lambda}{\beta cos\theta}} \qquad \text{(Eq 4.1)}$$

Where λ is the X-ray wavelength, β is the full width at half maxima corresponding to the most intense peak and θ is the Bragg angle. It has been found that on increasing the calcination temperature *viz.*, 200, 400 and 800 °C, particle size increases *i.e.* 3.18, 4.64 and 15.48 nm, respectively. SnO_2NPs@ZIF-8 composites were synthesized by using SnO_2NPs calcined at 800 °C. PXRD patterns of ZIF-8 and its respective composites NC1, NC2 and NC3 clearly indicate that encapsulation of SnO_2NPs within ZIF-8 matrix has no effect on the crystallinity of ZIF-8

as illustrated in Fig. 4.1(b). Further, the PXRD analysis has been performed with composite NC1 after performing the adsorption and photocatalytic studies. It has been observed that the PXRD pattern remained unchanged with a slight reduction in peak intensity, indicating their remarkable chemical stability which is depicted in Fig. 4.1(c).

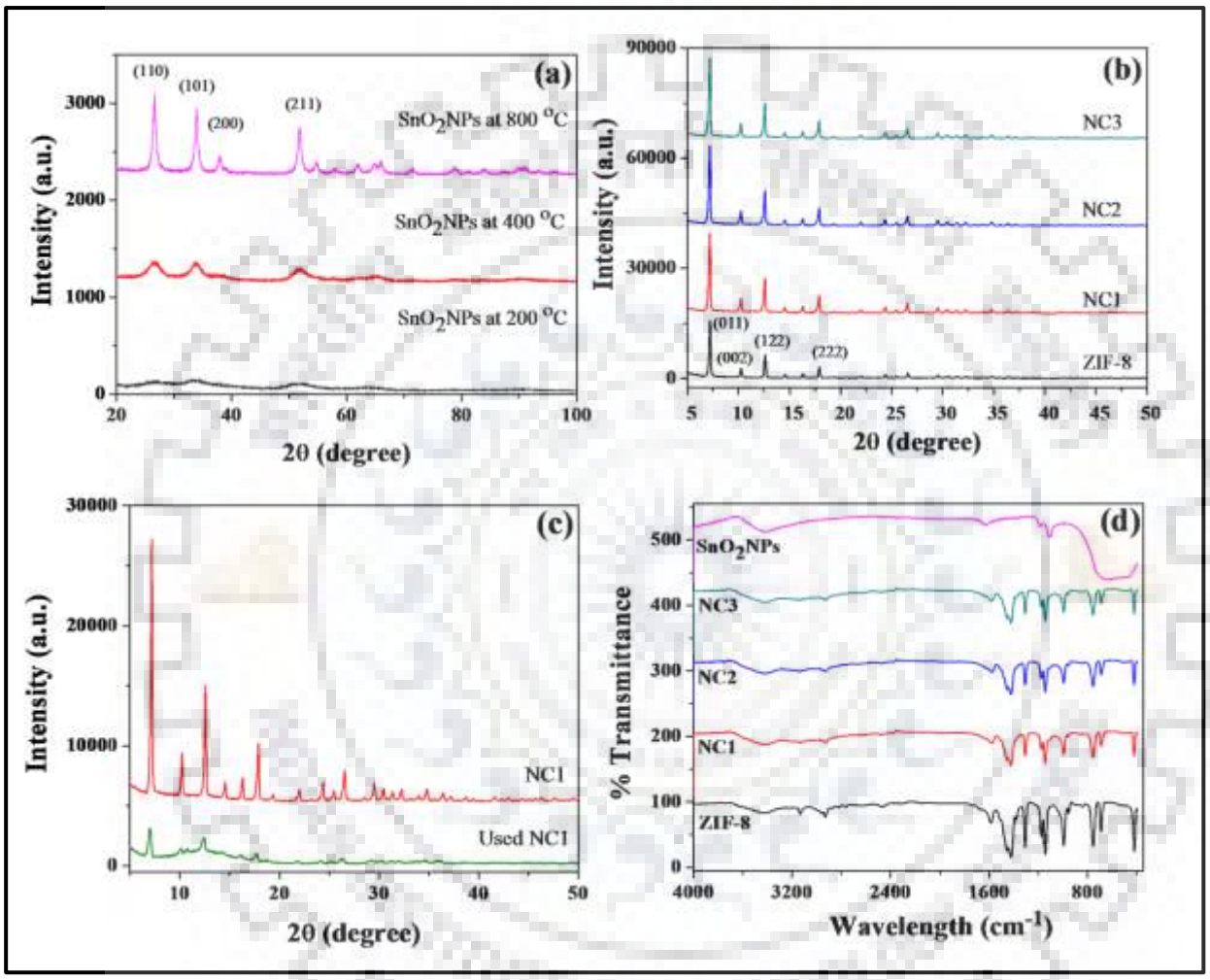

Fig. 4.1. (a) PXRD patterns of SnO_2NPs calcined at various temperatures; (b) PXRD patterns of ZIF-8 and its composites NC1, NC2 and NC3; (c) PXRD patterns of used and unused composite NC1; (d) IR spectra of SnO_2NPs, ZIF-8 and composites NC1, NC2 and NC3.

4.3.2. FT-IR Spectroscopic Studies

The FT-IR spectra of the synthesized SnO_2NPs, ZIF-8 and composites NC1, NC2 and NC3 have been shown in Fig. 4.1(d). The FT-IR spectra of ZIF-8, NC1, NC2 and NC3 appear identical displaying characteristics imidazole ring frequencies at 421, 1584, 996 and 1425 cm^{-1}

due to ν(Zn-N), ν(C=N), δ(C-N) and ν(C-N), respectively [45]. In case of pure SnO_2NPs, Sn-O stretching frequency [46] appears at 618 cm^{-1} while it does not clearly appear in composites which may presumably be attributed to a very less amount of SnO_2NPs encapsulated within ZIF-8/or overlapping with ZIF-8 frequency.

4.3.3. FE-SEM and HR-TEM Analysis

The morphology of SnO_2NPs, ZIF-8 and composites NC1, NC2 and NC3 have been examined by field emission scanning electron microscopy (FE-SEM) and high-resolution transmission electron microscopy (HR-TEM). The SnO_2NPs were found to acquire a spherical (Fig. 4.2(a) and (b)) whereas ZIF-8 and NC1 (Fig. 4.2(d)) exhibit a hexagonal morphology which firmly indicates the fact that proper encapsulation of SnO_2NPs within ZIF-8 matrix does not affect its surface morphology. HR-TEM images of SnO_2NPs, ZIF-8 and NC1 are shown in Fig. 4.3(a), (b) and (c), respectively. The TEM image of NC1 (Fig. 4.3(c)) reveals that SnO_2NPs are properly encapsulated within ZIF-8 matrix. The selected area electron diffraction (SAED) patterns of SnO_2NPs, ZIF-8 and NC1 clearly indicate their polycrystalline nature (Fig. 4.3(d), (e) and (f), respectively). The SAED pattern of SnO_2NPs appears in the composite also provide an evidence for its proper encapsulation in ZIF-8 matrix. The average particle size of encapsulated SnO_2NPs is found to be 16.23 ± 3.76 nm as determined by the particle size distribution plot of NC1 (Fig. 4.4) using *ImageJ* software on HR-TEM images. On increasing the dosing amount of SnO_2NPs suspension such as 300 and 500 µL, a considerable agglomeration of SnO_2NPs has been observed in SEM and HR-TEM images as depicted in Fig. 4.5. Further, energy dispersive X-ray (EDX) analysis has been performed for elemental composition of SnO_2NPs, ZIF-8 and their composites (Table 4.1; Fig. 4.6) which indicate that Sn-atomic percentage increases within ZIF-8 on increasing the dosing amount of SnO_2NPs.

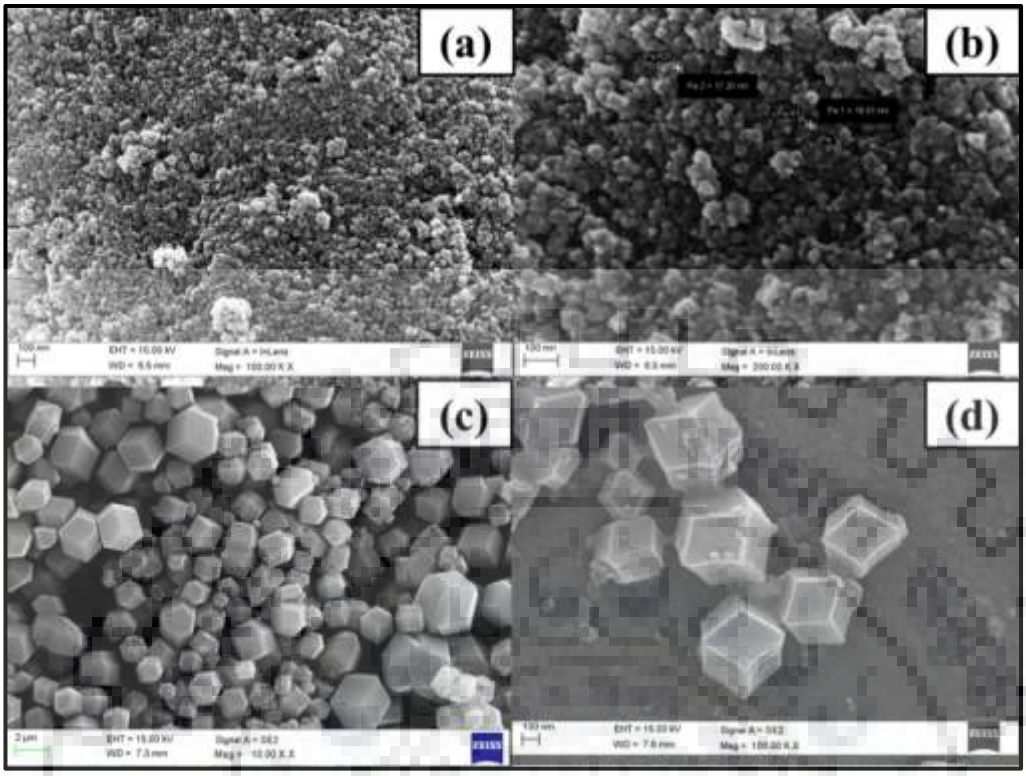

Fig. 4.2. SEM images of SnO_2NPs at (a) 100 Kx; (b) 200 Kx; (c) SEM image of ZIF-8 at 50 Kx and (d) SEM image of composite NC1 at 100 Kx.

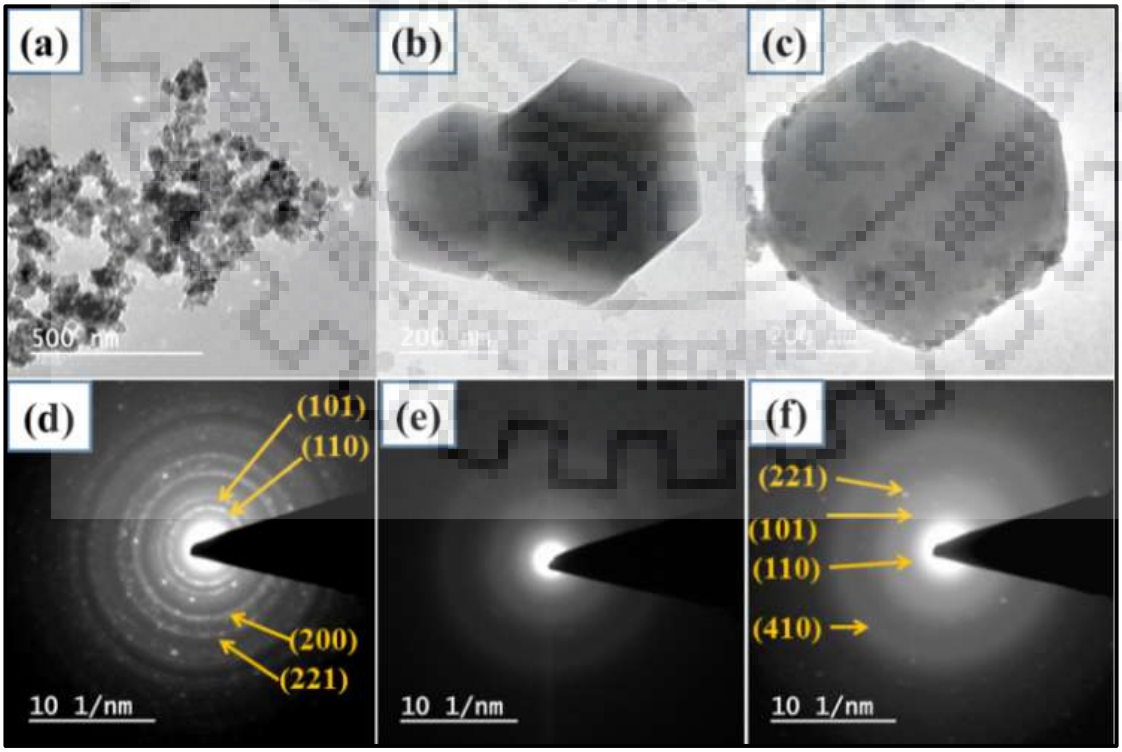

Fig. 4.3. (a-c) TEM images and (d-f) the SAED patterns of SnO_2NPs, ZIF-8 and composite NC1, respectively.

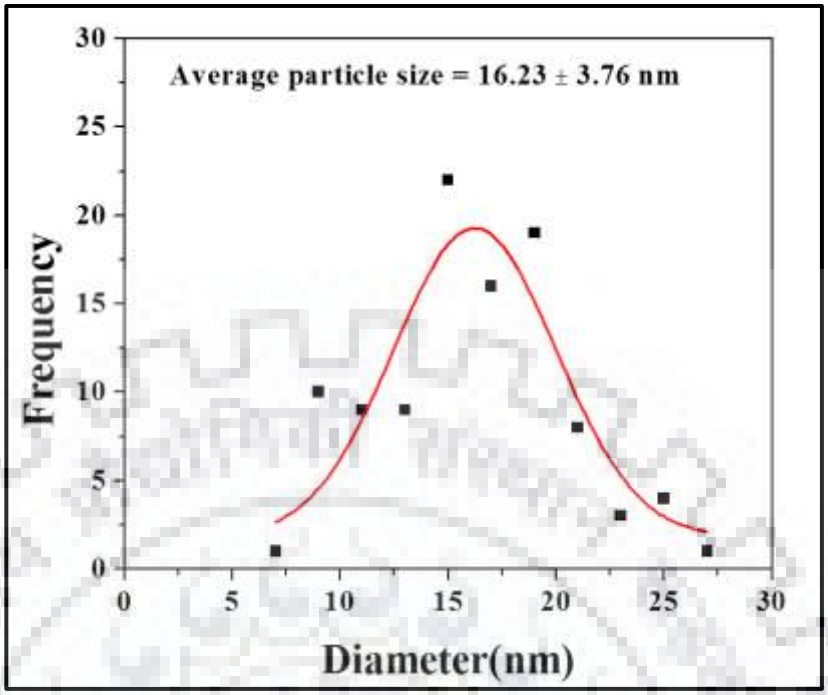

Fig. 4.4. Particle size distribution plot of encapsulated SnO_2NPs within NC1 composite.

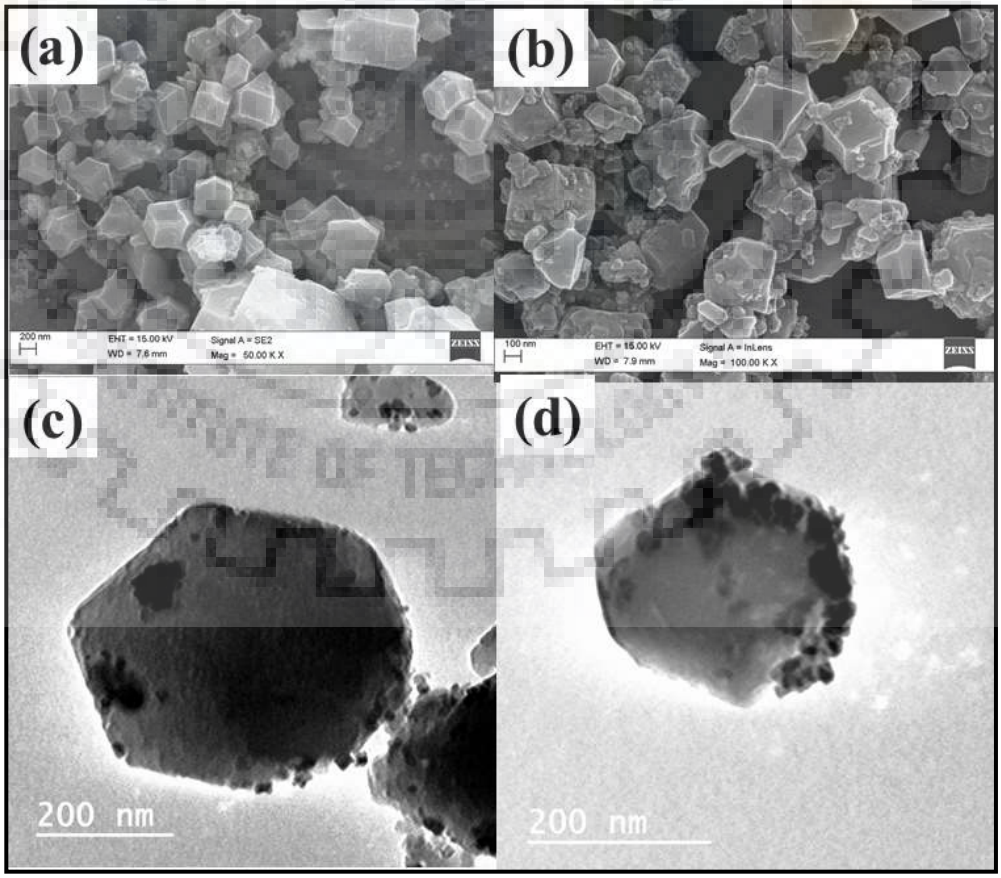

Fig. 4.5. (a, b) SEM and (c, d) TEM images of NC2 and NC3 composites, respectively.

Table 4.1. EDX analysis of SnO_2NPs, ZIF-8 and composites NC1, NC2 and NC3.

S.N.	Samples	Atomic %				
		C	N	O	Zn	Sn
1.	SnO_2NPs	-	-	53.04	-	46.96
2.	*ZIF-8	55.51	37.5	-	6.99	-
3.	NC1	46.30	42.89	7.72	3.06	0.02
4.	NC2	54.46	29.99	10.57	4.94	0.03
5.	NC3	54.43	32.0	9.39	4.13	0.05

* EDX analysis of ZIF-8 is already reported in chapter three.

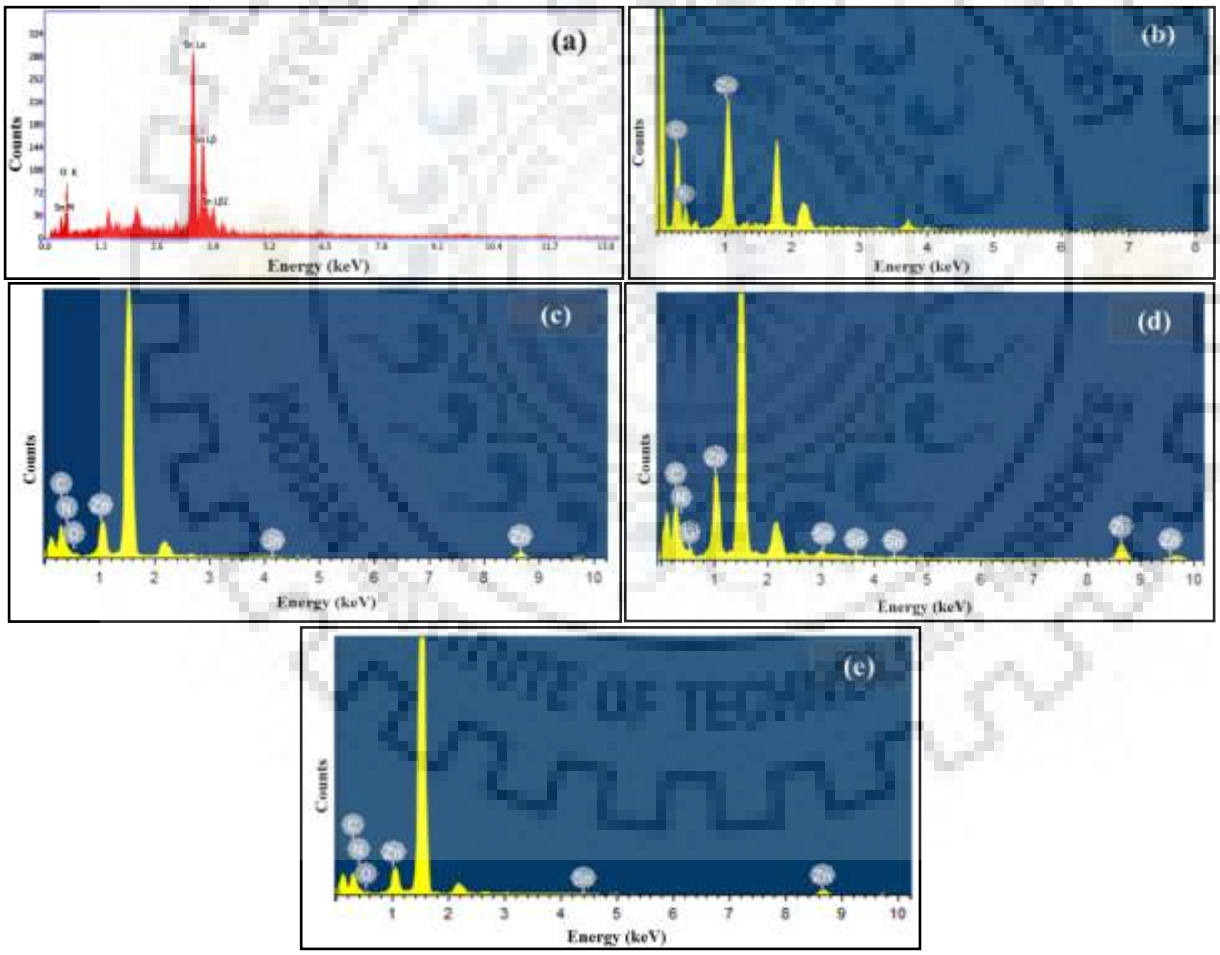

Fig. 4.6. (a-e) EDX spectra of SnO_2NPs, ZIF-8 and NC1, NC2 and NC3 composites respectively.

4.3.4. UV-DRS Studies

The optical properties of SnO_2NPs, ZIF-8, NC1, NC2 and NC3 have been studied by UV-Visible diffuse reflectance spectroscopy (UV-DRS). The UV-DRS spectra have been plotted $(\alpha h\nu)^2$ *vs* $h\nu$ and $(\alpha h\nu)^{1/2}$ *vs* $h\nu$ for the direct and indirect transitions, respectively, by using Tauc method [47] (Fig. 4.7). In general, the band gap of semiconducting materials depends on crystallite size, structural parameter, lattice strain and impurities [48]. ZIF-8 and its composites NC1, NC2 and NC3 have similar band gap 5.23 – 5.22 eV while SnO_2NPs has 3.58 eV for direct transition. For indirect transition, flat band gap of composites are observed at 2.49 – 2.50 eV owing to microenvironment of SnO_2NPs within ZIF-8 while the sharp band is observed at 5.07 – 5.10 eV due to ZIF-8.

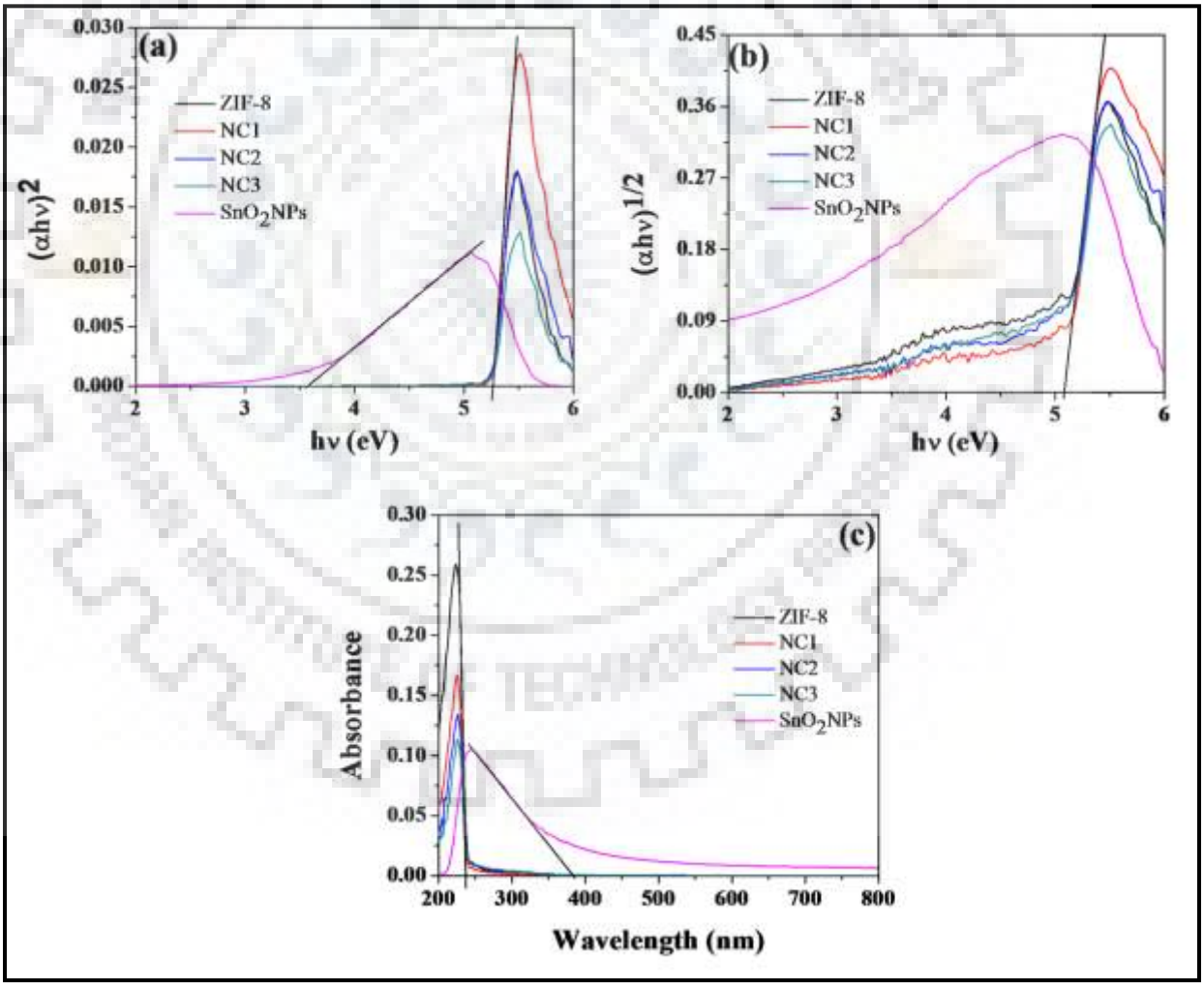

Fig. 4.7. (a, b) Combined UV-DRS spectra of SnO_2NPs, ZIF-8 and composites NC1, NC2 and NC3 by direct and indirect method, respectively, and (c) UV-visible absorbance spectra of SnO_2NPs, ZIF-8 and their composites NC1, NC2 and NC3.

4.3.5. BET Surface Area Analysis

The N_2 adsorption-desorption isotherms and the surface area of SnO_2NPs, ZIF-8 and composites NC1, NC2 and NC3 have been examined by Brunauer-Emmett-Teller (BET) analysis. The N_2 adsorption-desorption isotherms, pore size distribution and BET surface area of ZIF-8 are already reported in the previous Chapter three. A decrease in the surface area from ≈ 1357 to 987 m^2g^{-1} has been observed with increasing the dosing amount of SnO_2NPs suspensions within ZIF-8. This is due to the fact that the voids of ZIF-8 are occupied by SnO_2NPs. The results are compiled in Table 4.2 and adsorption-desorption isotherm plots of composites NC1, NC2, NC3, and SnO_2NPs are shown in Fig. 4.8 while the pore size distribution plots are illustrated in Fig. 4.9.

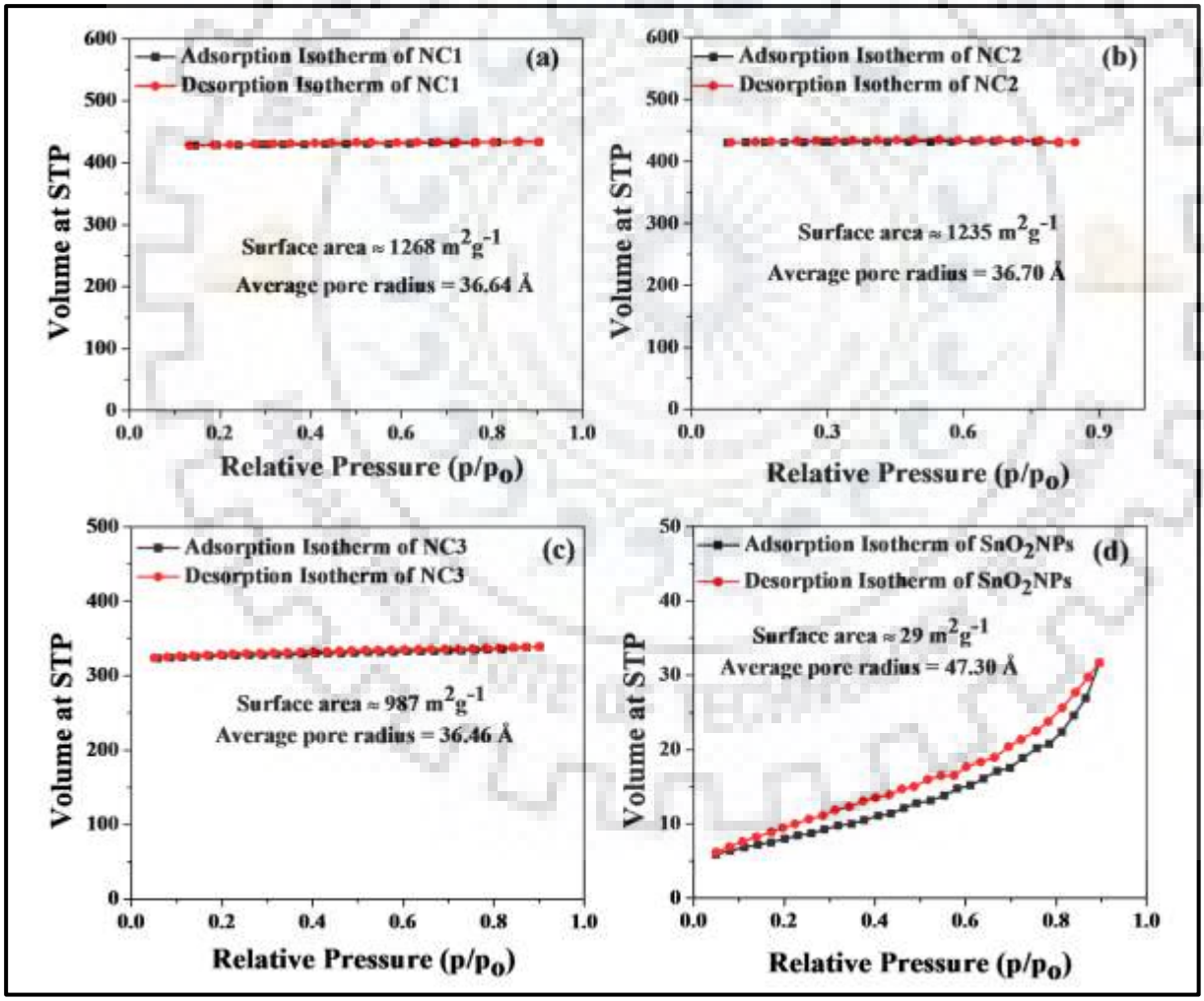

Fig. 4.8. (a-d) BET analysis of composites NC1, NC2, NC3, and SnO_2NPs, respectively.

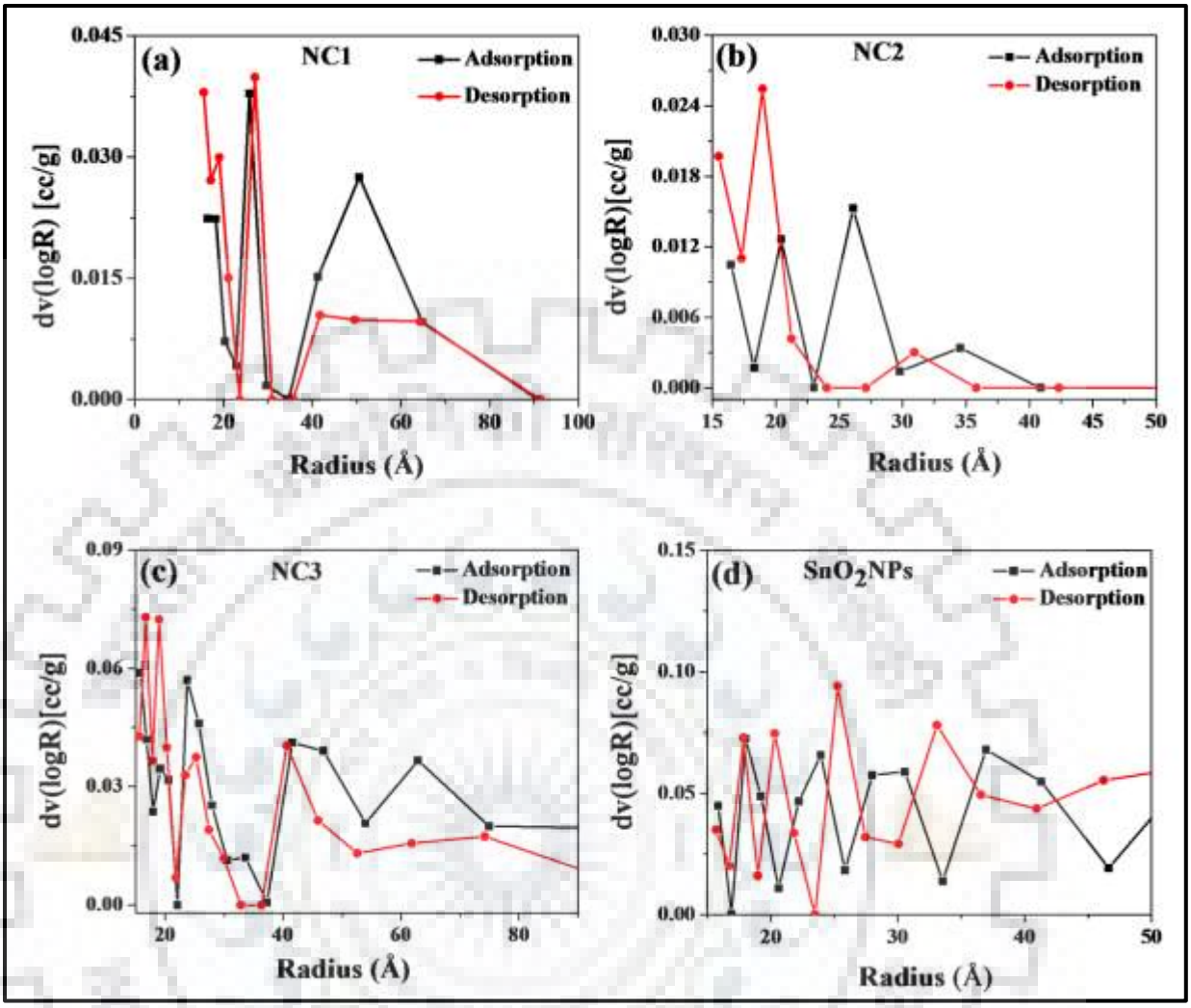

Fig. 4.9. (a-d) Pore size distribution plots of composites NC1, NC2, NC3, and SnO_2NPs, respectively.

Table 4.2. BET surface area analysis of SnO_2NPs, ZIF-8 and composites NC1, NC2 and NC3.

S.N.	Materials	S_{BET} (m^2g^{-1})	Pore Vol. (ccg^{-1})	Average Pore radius (Å)
1.	SnO_2NPs	29	4.898×10^{-2}	47.30
2.	*ZIF-8	1357	7.643×10^{-1}	11.26
3.	NC1	1268	6.707×10^{-1}	36.64
4.	NC2	1235	6.647×10^{-1}	36.70
5.	NC3	987	5.242×10^{-1}	36.46

S_{BET} refers the Brunauer-Emmett-Teller surface area. *BET surface area of ZIF-8 is already reported in Chapter three.

4.3.6. XPS Analysis

The full scan X-ray photoelectron spectra (XPS) of SnO_2NPs, ZIF-8 and composite NC1 are shown in Fig. 4.10(a), (b) and (c), respectively and the expanded XPS spectra of the close fitting of the metals with their orbital position are given in Fig. 4.10(d), (e) and (f). Fig. 4.10(a) illustrates the presence of Sn and O element and expanded spectrum of close fitting of Sn 3d orbital (Fig. 4.10(d)) shows two major peaks with binding energy 485.37 eV and 493.74 eV which are attributed to $3d_{5/2}$ and $3d_{3/2}$ implying the Sn(IV) oxidation state [49]. Fig. 4.10(e) shows the close fitting of Zn $2p_{3/2}$ and $2p_{1/2}$ in ZIF-8 which are sharp and more intense peaks having binding energy 1021.66 and 1044.79 eV, respectively. However, Sn 3d peak in composites are less intense and broad due to encapsulation [50] and the intensity increases on increasing the dosing amount of SnO_2NPs which are shown in Fig. 4.10(f).

In the composites, Sn $3d_{5/2}$ and $3d_{3/2}$ peaks are shifted toward higher binding energy 495.84 eV and 498.91 eV, respectively, as a result of the weak interaction of Sn(IV)-N between incorporated SnO_2NPs and N-atom of imidazole ring [51]. The expanded XPS spectra of the close fitting with their orbital positions of non-metals such as O 1s of SnO_2NPs, C 1s and N 1s of ZIF-8 are given in Fig. 4.11(a-c), respectively. Moreover, XPS survey scan and close fitting with their orbital positions of metal/non-metals of NC1, NC2 and NC3 composites have been illustrated in Fig. 4.12, 4.13 and 4.14, respectively, and the results are given in Table 4.3.

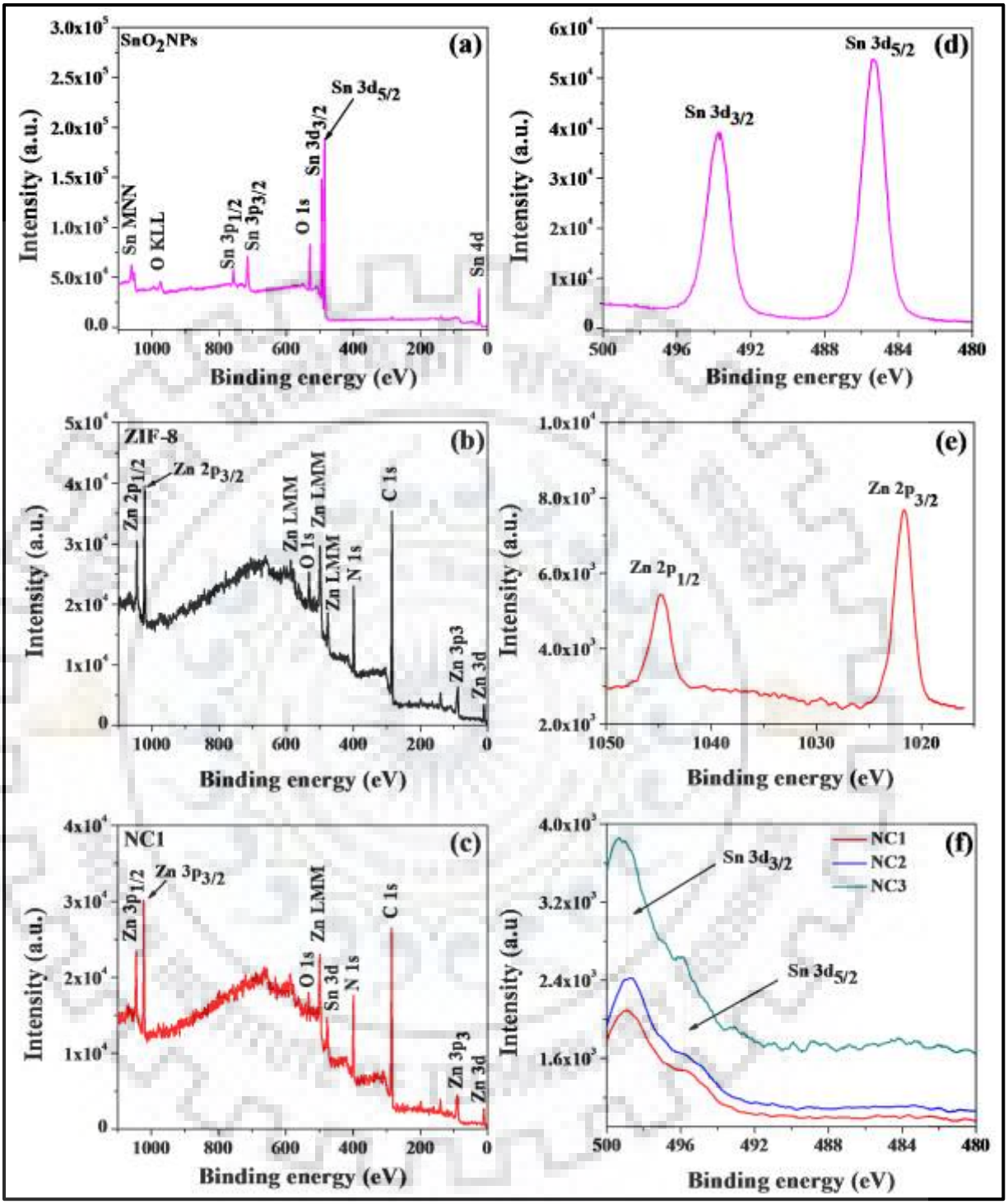

Fig. 4.10. Survey XPS spectra of (a) SnO_2NPs, (b) ZIF-8 and (c) composite NC1. Expanded XPS spectra of (d) Sn 3d of SnO_2NPs, (e) Zn 2p of ZIF-8 and (f) combined Sn 3d of composites NC1, NC2 and NC3.

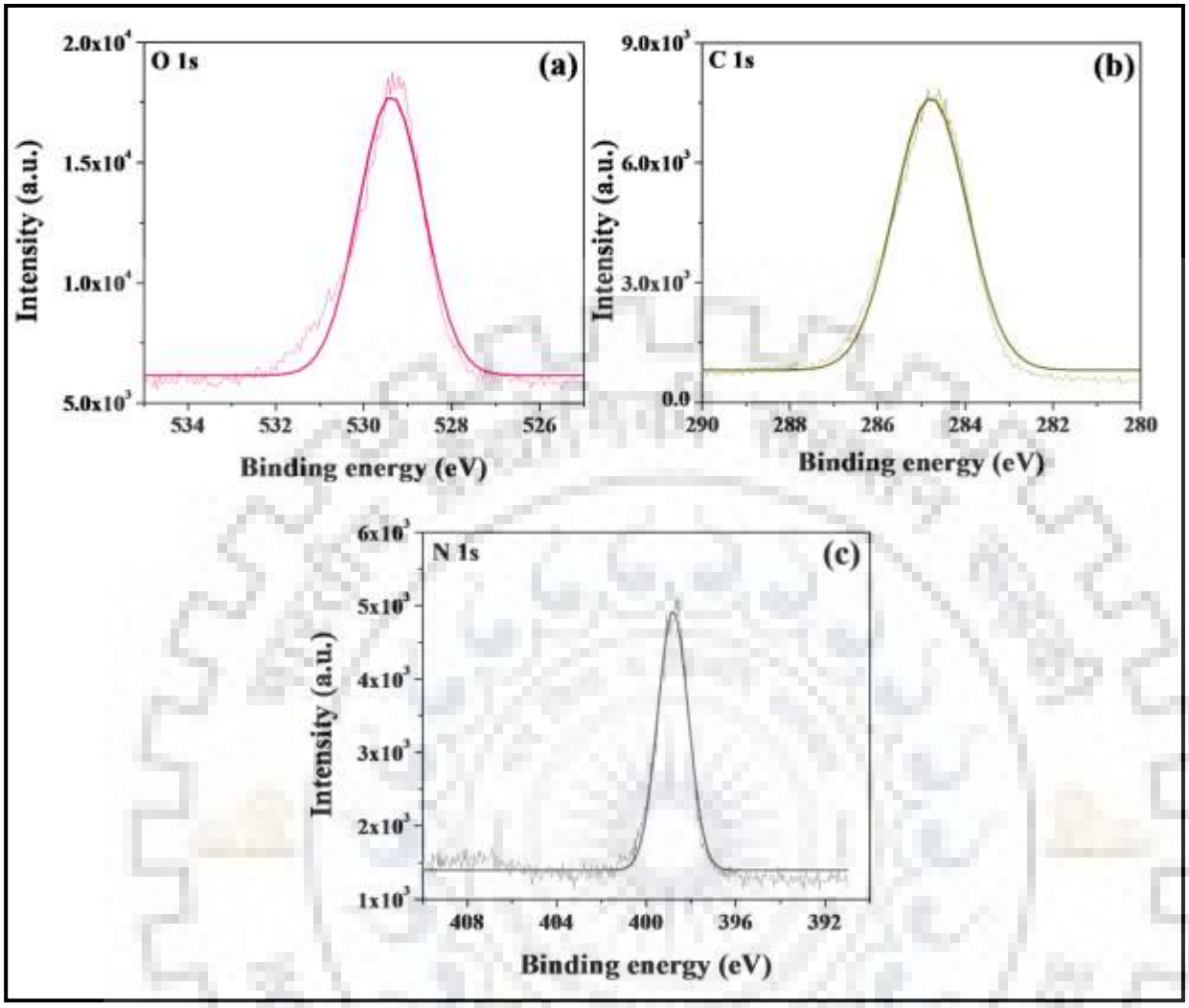

Fig. 4.11. Expanded XPS spectra of close fitting of (a) O 1s of SnO_2NPs; (b) C 1s and (c) N 1s of ZIF-8.

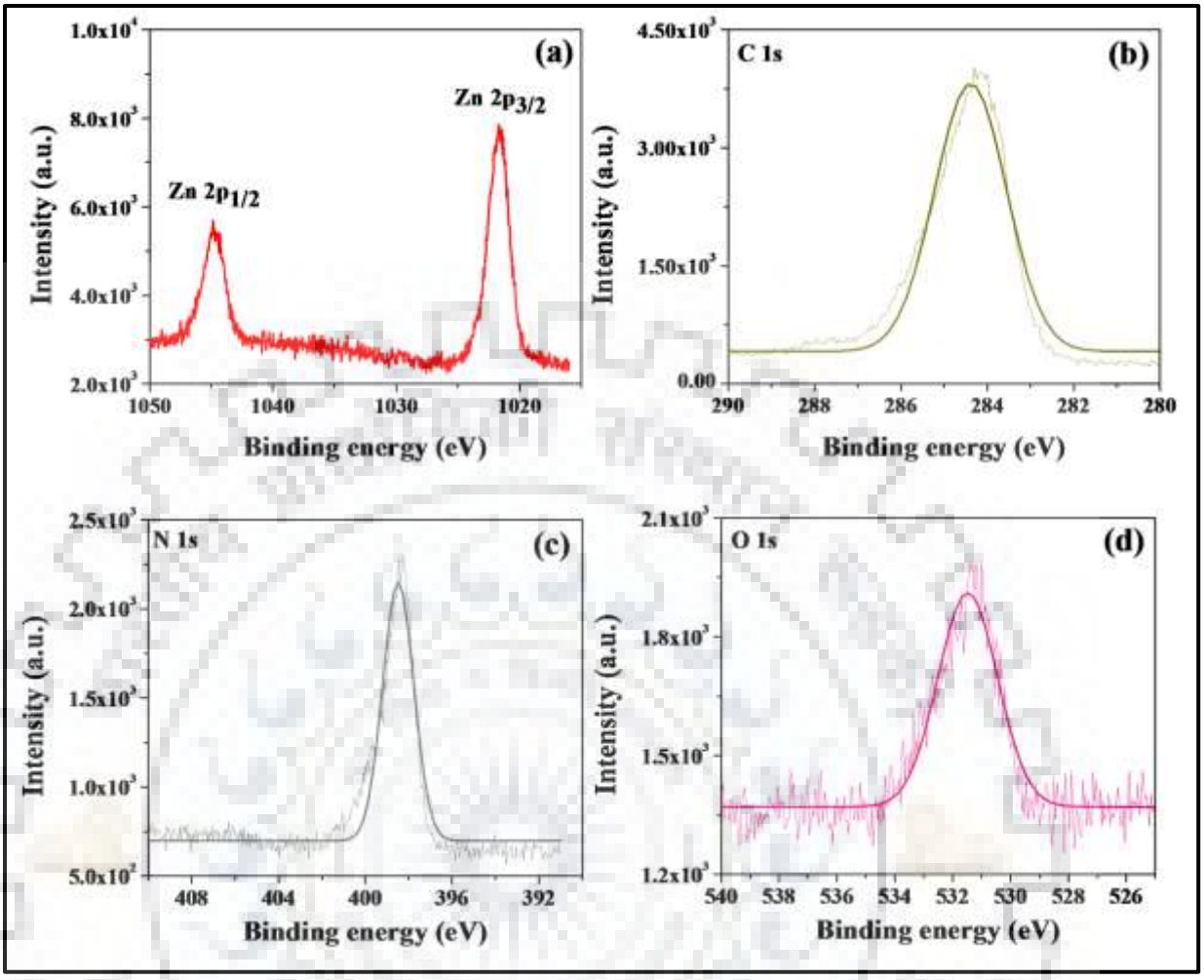

Fig. 4.12. Expanded XPS spectra of close fitting of (a) Zn 2p, (b) C 1s, (c) N 1s and (d) O 1s of composite NC1.

4.3.7. Thermal Analysis

Thermal stability of SnO_2NPs, ZIF-8 and its composite NC1 has been examined by TGA (Thermal Gravimetric Analysis) analysis. The TGA plots between weight% *vs* temperature are given in Fig 4.15. The SnO_2NPs are highly stable up to 900 °C, approximately 94.5% (wt.%) remains in aerial atmosphere and 97.6% in N_2 atmosphere, while ZIF-8 and NC1 are stable up to 350 °C. Above this temperature ZIF-8 and NC1 started decompose and remain 34 and 47% in aerial atmosphere and 32 and 46% in N_2 atmosphere, respectively. The remaining wt.% of NC1 is slightly higher (*ca.* 13%) as compared to that in ZIF-8 due to presence of micro-environment of SnO_2NPs within ZIF-8 matrix.

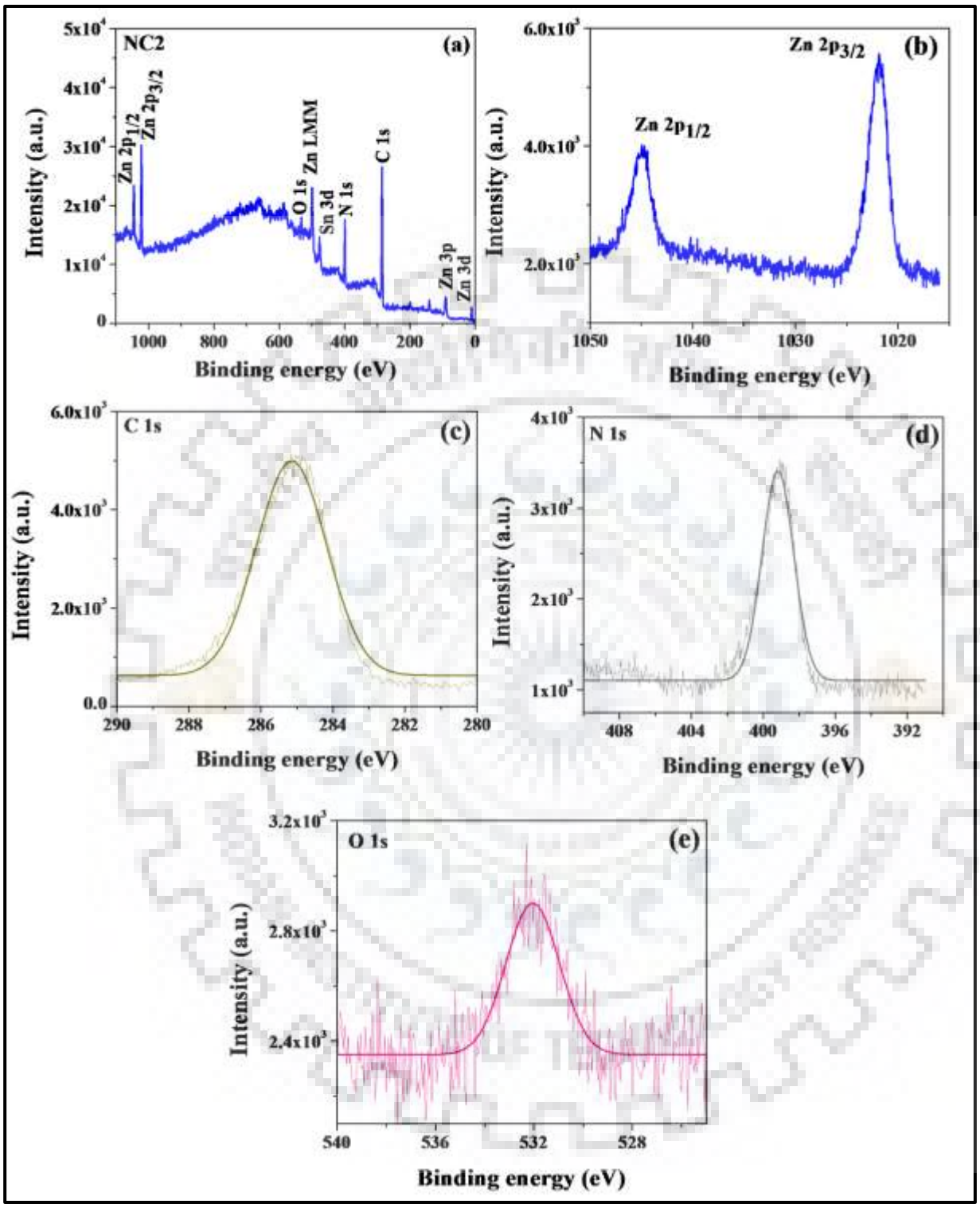

Fig. 4.13. Survey XPS spectra of (a) NC2 and expanded XPS spectra of close fitting of (b) Zn 2p (c) C 1s, (d) N 1s and (e) O 1s of composite NC2.

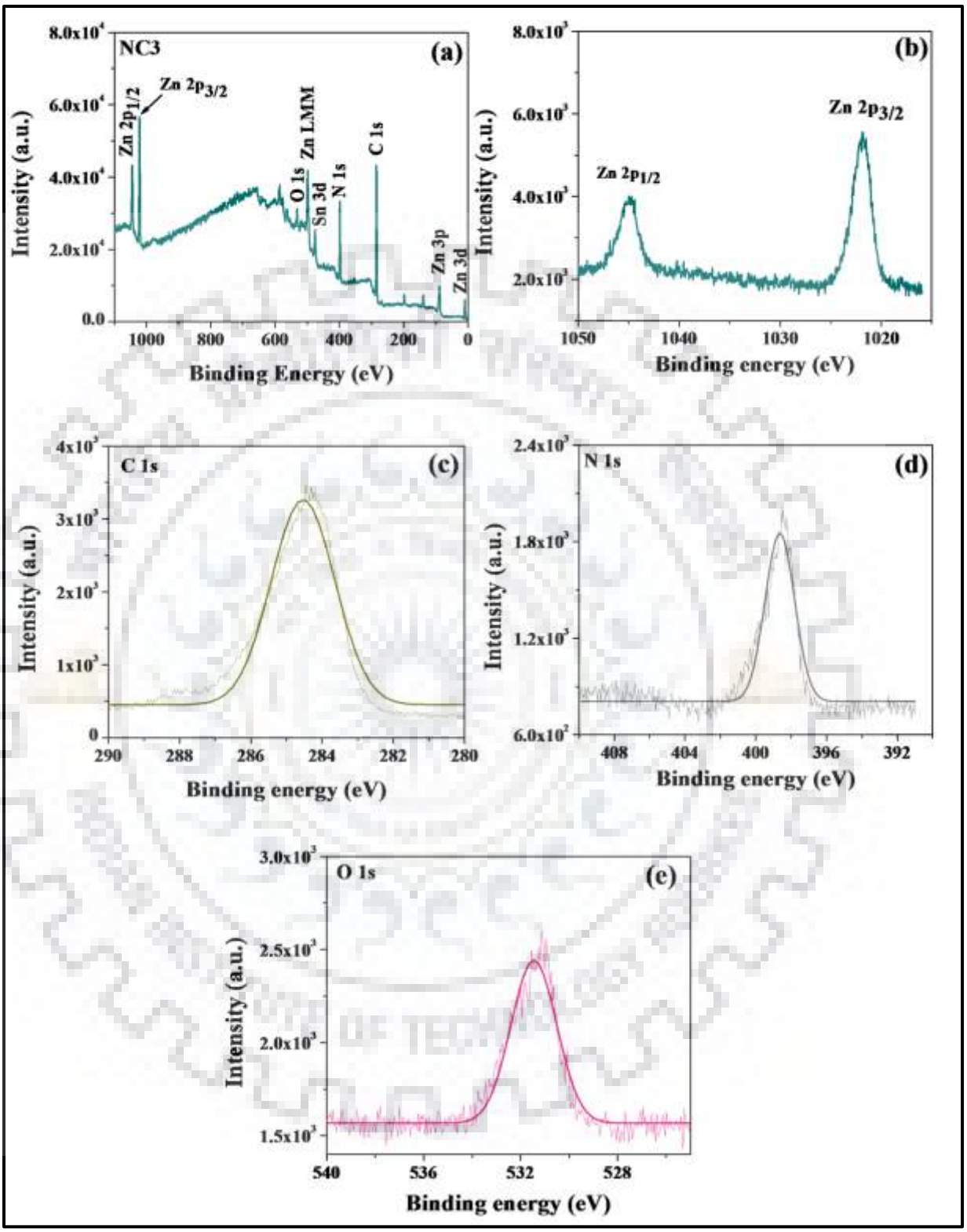

Fig. 4.14. Survey XPS spectra of (a) NC3 and expanded XPS spectra of close fitting of (b) Zn 2p (c) C 1s, (d) N 1s and (e) O 1s of composite NC3.

Table 4.3. XPS analysis of SnO_2NPs, ZIF-8 and their composites NC1, NC2 and NC3.

S.N.	Materials	Atom/Element	State/Term	Binding energy (eV)
1.	SnO_2NPs	Sn	$3d_{3/2}$	493.74
			$3d_{5/2}$	485.37
		O	1s	529.37
2.	ZIF-8	Zn	$2p_{1/2}$	1044.79
			$2p_{3/2}$	1021.66
		C	1s	284.79
		N	1s	398.81
3.	NC1	Zn	$2p_{1/2}$	1044.91
			$2p_{3/2}$	1022.02
		Sn	$3d_{3/2}$	498.91
			$3d_{5/2}$	495.84
		C	1s	284.38
		N	1s	398.48
		O	1s	531.48
4.	NC2	Zn	$2p_{1/2}$	1044.92
			$2p_{3/2}$	1021.86
		Sn	$3d_{3/2}$	498.91
			$3d_{5/2}$	495.84
		C	1s	285.14
		N	1s	399.19
		O	1s	532.05
5.	NC3	Zn	$2p_{1/2}$	1044.90
			$2p_{3/2}$	1021.84
		Sn	$3d_{3/2}$	498.91
			$3d_{5/2}$	495.84
		C	1s	284.53
		N	1s	398.64
		O	1s	531.45

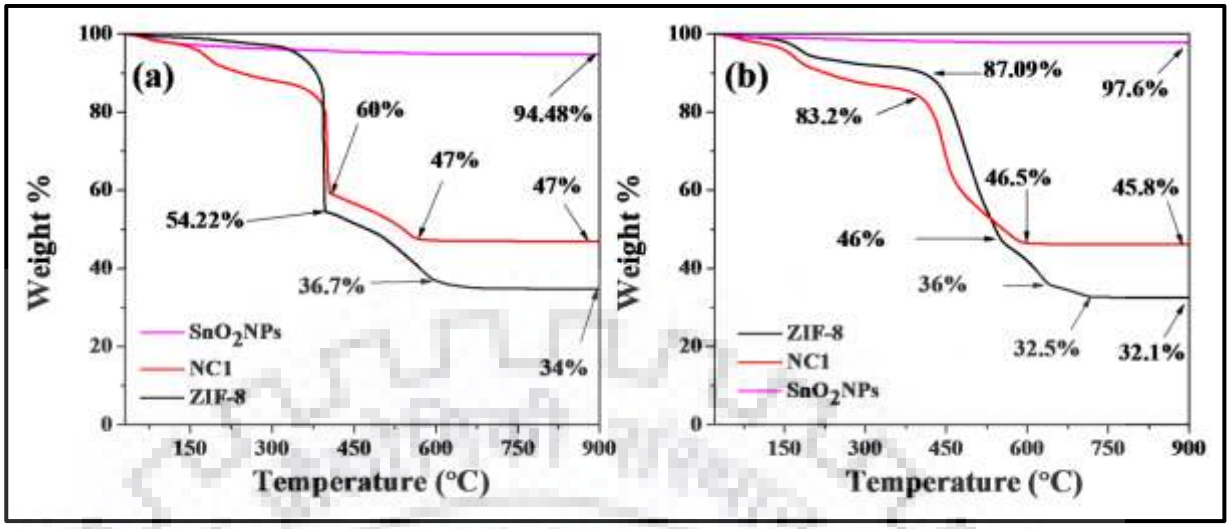

Fig. 4.15. (a-b) TGA analysis of SnO_2NPs, ZIF-8 and composite NC1 in air and N_2 atmosphere, respectively.

4.3.8. Anti-viral Activity on CHIKV using SnO_2NPs, ZIF-8 and SnO_2NPs@ZIF-8 Composites

From MTT assay against *Vero* cell line, the maximum non-toxic dose (MNTD) has been found 0.04 mg mL^{-1} for ZIF-8 and SnO_2NPs@ZIF-8 composites (NC1, NC2 and NC3) and 0.1 mg mL^{-1} for SnO_2NPs. No effect on cell viability is observed up to 0.04 mg mL^{-1} concentration of SnO_2NPs, ZIF-8, and SnO_2NPs@ZIF-8 composites as well. The cell viability (%) *vs* concentration plot is illustrated in Fig. 4.16. During the time-of-inhibitor-addition, 0.04 mg mL^{-1} concentration of SnO_2NPs, ZIF-8, and their SnO_2NPs@ZIF-8 composites have been taken for comparison of their respective antiviral activity on CHIKV. The viral plaques have been observed after 48 h of incubation at 37 °C in 5% CO_2 and then further stained the plaque assay plate with crystal violet to count the number of viral plaques. Reduction in the number of plaques has been observed after the serial dilution of the virus concentration for plaque assay. The orange coloured square frame denotes the antiviral effect of composite NC1 against CHIKV as compared to the control (where no other treatment was added) which is illustrated in Fig. 4.17.

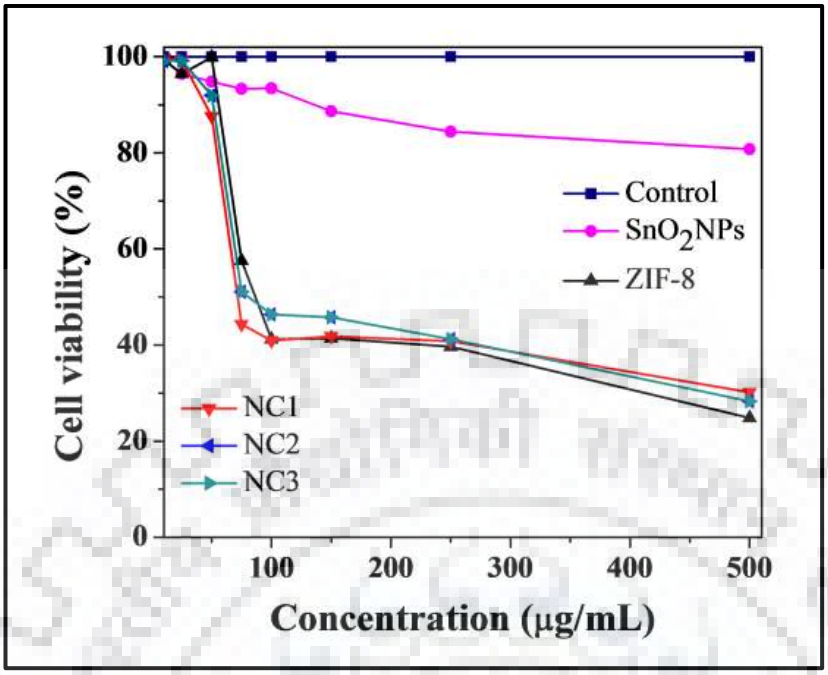

Fig. 4.16. Cell viability *versus* Concentration plots of SnO_2NPs, ZIF-8 and composites NC1, NC2 and NC3.

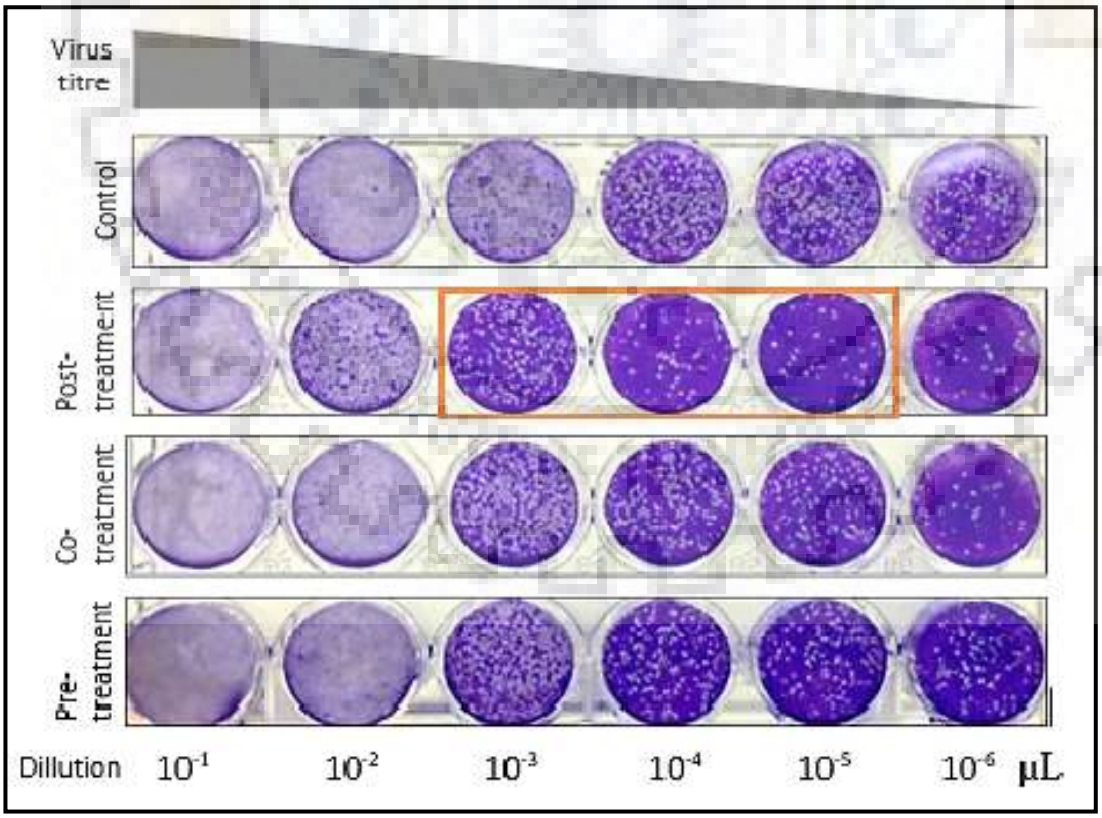

Fig. 4.17. The wells plate image of plaque assay result for composite NC1.

Plaque reduction assay confirms the antiviral activity of SnO_2NPs, ZIF-8 and composites NC1, NC2 and NC3 on CHIKV. The reduction in viral load/titers has been observed up to >80% during post-treatment and >50% during pre-treatment for composite NC1 while NC2 and NC3 composites showed lower level of inhibition on CHIKV during pre-treatment and post-treatment. SnO_2NPs showed very less antiviral activity which is <15% in pre-treatment stage and post treatment stage but around 15% during co-treatment stage as compared to the control (Table 4.4(a, b)). Thus composite NC1 has been optimised for the antiviral activity on CHIKV *in vitro* and the results are shown in Fig. 4.18(a), as it showes reduction in viral load/titers up to >80% during post-treatment and >50% during pre-treatment which is greater than that of ZIF-8 and SnO_2NPs. The effect of light on antiviral activity of ZIF-8, SnO_2NPs and SnO_2NPs@ZIF-8 composites has also been investigated through plaque assay. The results are shown in Fig. 4.18(b). No any significant changes have been observed in the antiviral activity of SnO_2NPs, ZIF-8, and SnO_2NPs@ZIF-8 composites after the photo-irradiation treatment.

Table 4.4(a) Plaque reduction assays with SnO_2NPs, ZIF-8 and composites NC1, NC2 and NC3 without photo-irradiation condition.

S.N.	Treatment condition	% Inhibition				
		SnO_2NPs	ZIF-8	NC1	NC2	NC3
1.	Pre-treatment	11.54	46.08	55.0	22.0	28.26
2.	Co-treatment	15.38	19.61	46.08	18.0	19.57
3.	Post-treatment	9.62	79.41	87.25	60.0	58.7

Table 4.4(b) Plaque reduction assays with SnO_2NPs, ZIF-8 and composites NC1, NC2 and NC3 under photo-irradiation condition.

S.N.	Treatment condition	% Inhibition				
		SnO_2NPs	ZIF-8	NC1	NC2	NC3
1.	Pre-treatment	0.54	44.08	57.88	23.88	27.67
2.	Co-treatment	6.38	19.11	44.08	18.67	18.57
3.	Post-treatment	0.72	80.41	88.23	60.98	54.7

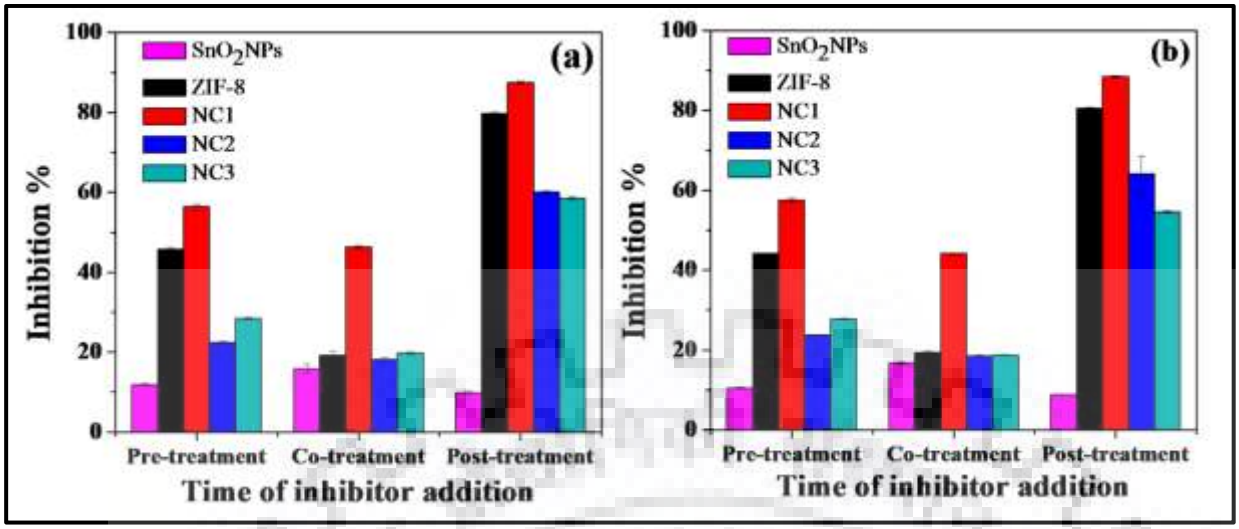

Fig. 4.18. (a, b) Plaque reduction assays with SnO_2NPs, ZIF-8 and composites NC1, NC2 and NC3 during pre-treatment, co-treatment and post-treatment without light and under photo-irradiation, respectively.

Composite NC1 has also been analyzed by TEM analysis after post-treatment. HR-TEM images indicate that surface of the composite plays an important role for inhibition of CHIKV which is illustrated in Fig. 4.19. It has been reported that inhibition of α-viruses occurs due to N-terminal domain participate in protein-protein interactions with N-containing organic molecule [31]. In case of ZIF-8 and SnO_2NPs@ZIF-8 composite, imidazole ring may be responsible for better inhibition% of CHIKV.

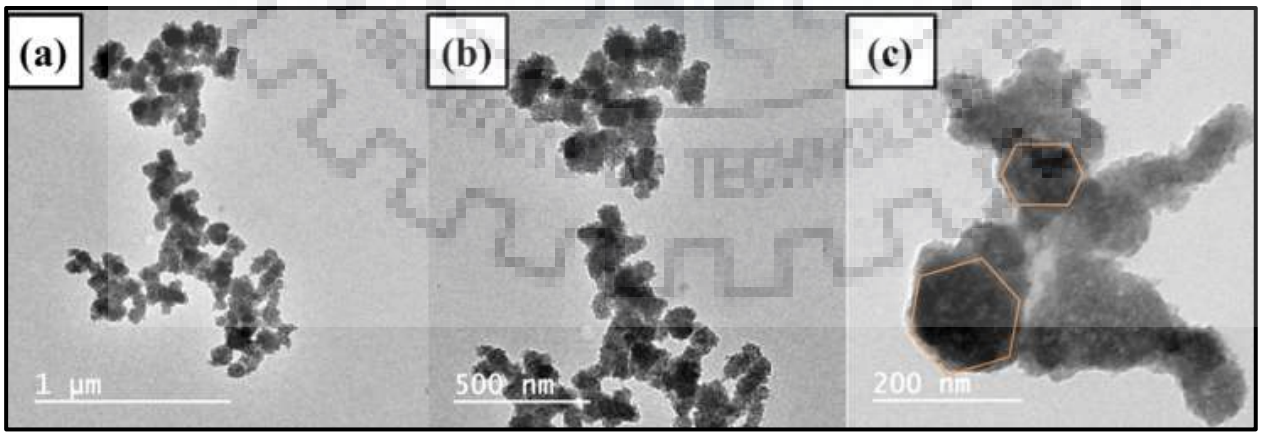

Fig. 4.19. TEM images of NC1 composite after post-treatment.

4.3.9. Adsorption and Photodegradation Studies of Methylene Blue (MB) by using SnO_2NPs@ZIF-8 Composites

4.3.9.1. Effect of Encapsulation Amount of SnO_2NPs

Adsorption and photodegradation of MB has been investigated by employing UV-visible spectrophotometer using 10 mg of NC1, NC2 and NC3 composites prepared by *in situ* encapsulation of 150, 300 and 500 µL suspension of SnO_2NPs. At pH 8.55, 1.64 mg L^{-1} initial concentration of MB has been used for the determination of effect of dosing amount and the results of adsorption and photodegradation are compiled in Table 4.5 and C/C_0 *vs* time plot is shown in Fig. 4.20.

Table 4.5. Effect of encapsulated amount of SnO_2NPs of NC1, NC2 and NC3 for adsorption and photodegradation (after 120 min) of [MB] = 1.64 mg L^{-1} at pH 8.55; photocatalyst amount = 10 mg (0.5 g L^{-1}).

S.N.	Dosing amount of SnO_2NPs suspension in µL	Adsorption % (q_t)	Photodegradation %
1.	150 (NC1)	30.87 (0.988)	94.12
2.	300 (NC2)	13.68 (0.438)	92.68
3.	500 (NC3)	12.68 (0.406)	93.68

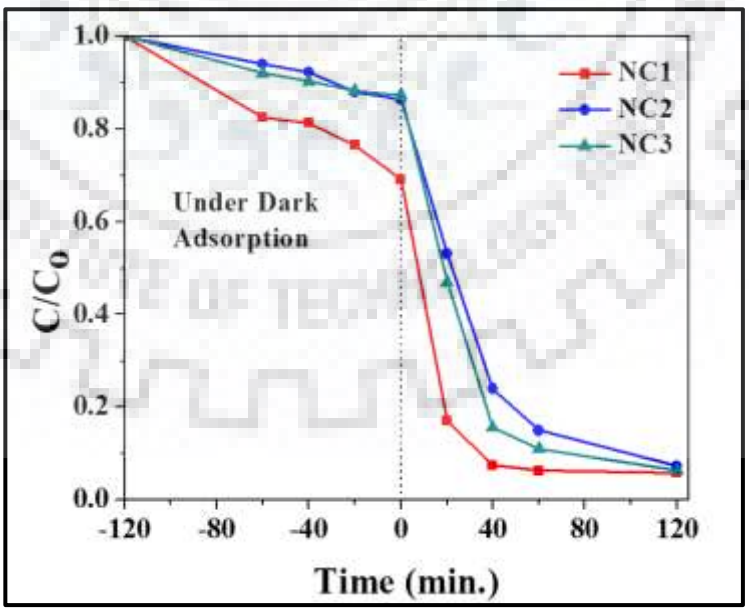

Fig. 4.20. Effect of encapsulated amount of SnO_2NPs in ZIF-8 for adsorption and photodegradation of [MB] = 1.64 mg L^{-1}; pH = 8.55; photocatalyst's amount = 10 mg (0.5 g L^{-1}).

4.3.9.2. Effect of Photocatalyst's Amount

The results of the effect of amount of composite NC1 has been compiled in Table 4.6 and C/C_0 *vs* time plots are shown in Fig. 4.21. The adsorption capacity and %photodegradation of MB is found to increase up to 10 mg, and then decrease for 15 mg. On increasing the amount of photocatalyst, the number of active sites/available adsorption sites increases which ultimately results in an increase of the amount of the adsorbed dye molecules up to 10 mg. But a decrease on further increase in the amount of photocatalyst could be attributed to particle interaction such as aggregation or sedimentation. This would lead to a decrease in total surface area. Therefore, 10 mg of SnO_2NPs@ZIF-8 composite (NC1) has been used for further studies of MB degradation.

Table 4.6. Adsorption and %photodegradation of MB (0.5×10^{-5} M) at pH = 8.55, by varying the amount of composite NC1.

S.N.	Amount of Photocatalyst (mg)	Adsorption % (q_t)	Photodegradation %
1.	5	20.31 (1.30)	84.0
2.	10	30.87 (0.988)	94.12
3.	15	23.56 (0.502)	93.25

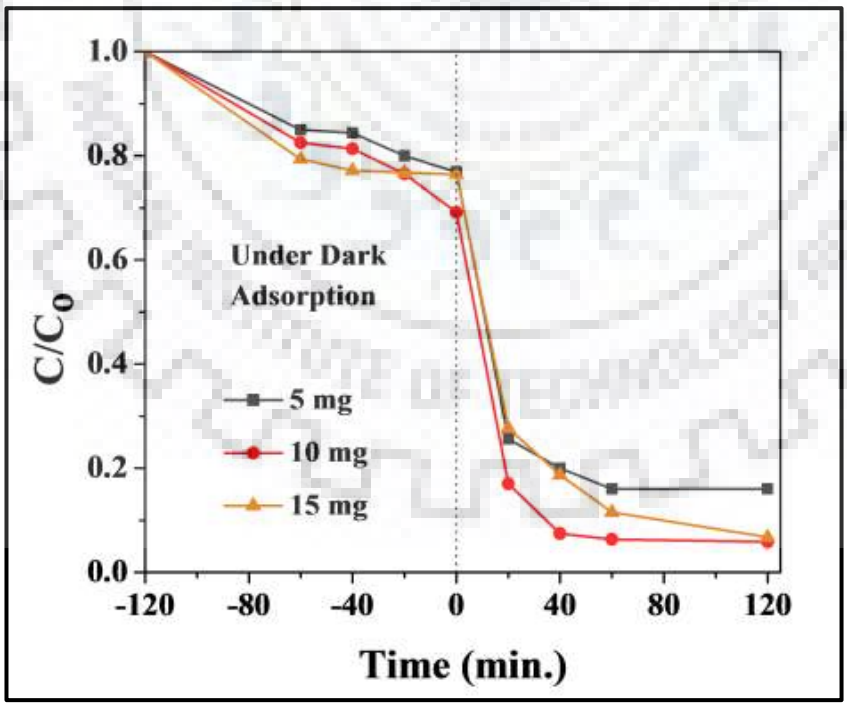

Fig. 4.21. The effect of photocatalyst's amount for adsorption and photodegradation of [MB] = 1.6 mg L^{-1} at pH 8.55.

4.3.9.3. Effect of pH

The surface charge of the materials and the pH of dye solution are very important parameters for the adsorption and photodegradation study. The results of effect of pH for adsorption and photodegradation of MB are compiled in Table 4.7 and C/C_0 *vs* time plots are shown in Fig. 4.22.

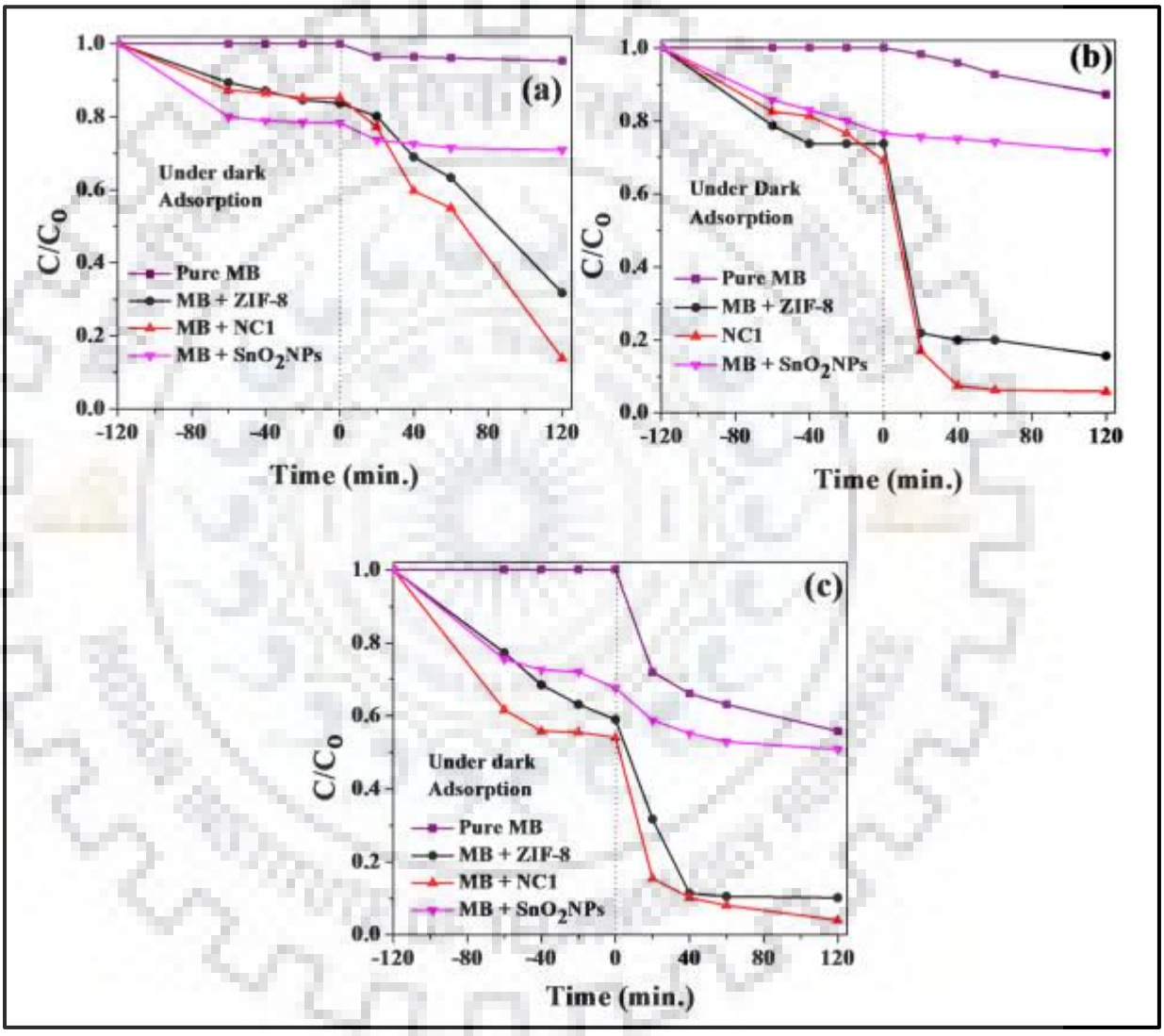

Fig. 4.22. The effect of pH for adsorption and photodegradation of [MB] = 1.6 mg L^{-1} at pH (a) 3.1, (b) 8.5 and (c) 11.5; photocatalyst's amount 10 mg (0.5 g L^{-1}).

It is obvious that the adsorption and photodegradation efficiency of SnO_2NPs, ZIF-8 and composite NC1 increases on increasing the pH of dye solution. SnO_2NPs, ZIF-8 and composite NC1 are found to carry negative charge on their surface at higher pH as examined by zeta potential analyzer (Zeta potential value *vs* pH plots are shown in Fig. 4.23 and the results are

tabulated in Table 4.8) whereas MB is observed to be a cationic dye [52]. So, there is more probability for interaction of MB dye with active sites of all materials at higher pH due to electrostatic attractions. Further, it has been already reported that the higher concentration of $^{\bullet}OH$ radicals in an alkaline medium are responsible for effective photodegradation of MB solution [8].

Table 4.7. Effect of pH varying on adsorption and % photodegradation of 0.5×10^{-5} M MB solution.

pH	Adsorption % (q_t)				Photodegradation %		
	ZIF-8	SnO_2NPs@ ZIF-8	SnO_2NPs	Pure MB	ZIF-8	SnO_2NPs@ ZIF-8	SnO_2NPs
3.1	16.25 (0.52)	14.75 (0.47)	21.68 (0.69)	4.62	68.2	86.12	29.06
8.5	26.25 (0.84)	30.87 (0.988)	23.43 (0.38)	12.68	84.37	94.12	28.75
11.48	40.93 (1.31)	45.93 (1.47)	32.37 (1.03)	44.12	89.75	95.93	49.12

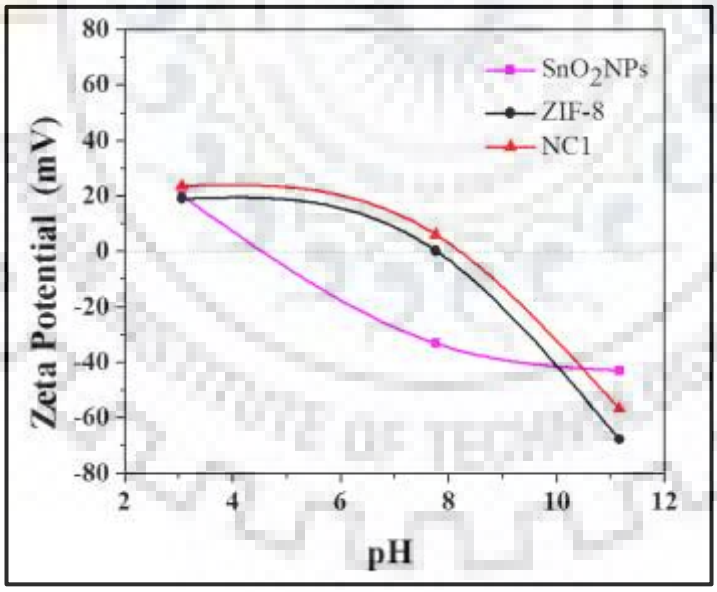

Fig. 4.23. Zeta potential of SnO_2NPs, ZIF-8 and composite NC1 at pH = 3.06; 7.76; 11.16.

Table 4.8. Zeta Potentials of SnO_2NPs, ZIF-8 and composite NC1 at various pH.

S.N.	pH	SnO_2NPs	ZIF-8	NC1 Composite
1.	3.06	20.1	19.1	23.7
2.	7.76	-33.1	0.32	6.12
3.	11.16	-42.9	-67.7	-56.5

4.3.9.4. Effect of Initial Dye Concentration

The effect of initial concentration of MB for the adsorption and photodegradation at pH 11.48 has been studied by using photocatalysts *viz.*, ZIF-8, SnO_2NPs and composite NC1. The adsorption and photodegradation of MB are strongly dependent on its initial concentration. The results are compiled in Table 4.9 and C/C_o *vs* time plots are shown in Fig. 4.24. The results indicate that both adsorption and photo-degradation decrease on increasing the initial concentration of MB. This is because of the number of surface active site is more available at lower concentration of MB while at its higher concentration, dye molecules inhibit the penetration of light through the surface of photocatalysts [53]. Consequently, the generation of active species *viz.* $^{\bullet}OH$ and $^{\bullet}O^{2-}$ decreases on increasing [MB] in the reaction vessels [8].

Table 4.9. Adsorption and % photodegradation of MB solution by varying the concentration at pH = 11.48.

Conc. (mg L^{-1})	Adsorption% (q_t)				Photodegradation %		
	ZIF-8	SnO_2NPs @ZIF-8	SnO_2NPs	Pure MB	ZIF-8	SnO_2NPs @ZIF-8	SnO_2NPs
1.6	40.93 (1.31)	45.93 (1.47)	32.37 (1.03)	44.12	89.75	95.93	49.12
3.1	15.95 (1.018)	11.94 (0.762)	7.49 (0.478)	20.31	81.88	92.13	15.73
6.3	5.48 (0.7)	7.99 (1.02)	5.01 (0.64)	14.26	71.94	84.48	11.92

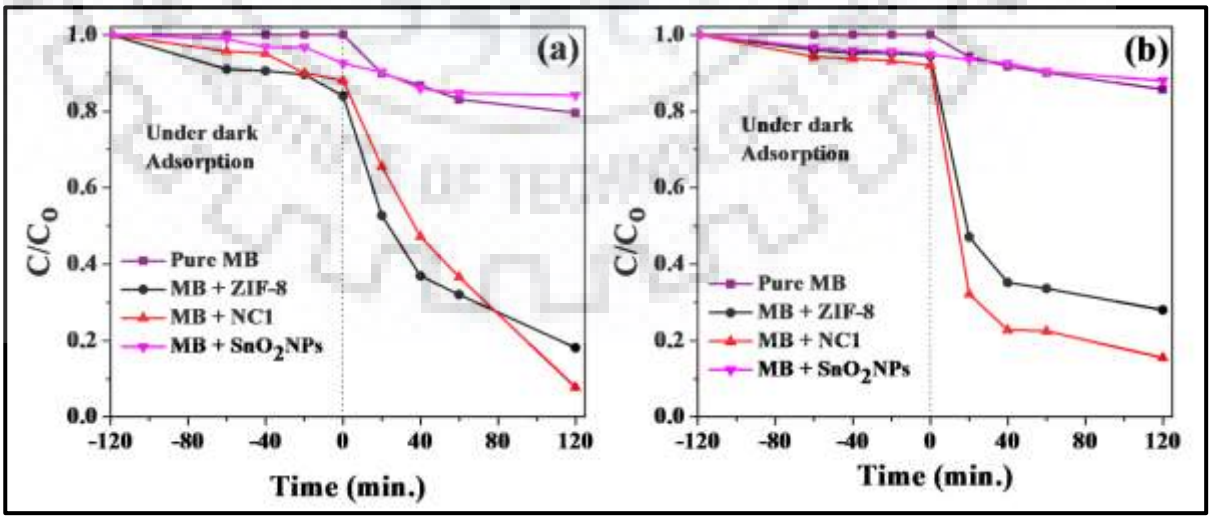

Fig. 4.24. The effect of initial dye concentration for adsorption and photodegradation of [MB] (a) 3.1 mg L^{-1} ; (b) 6.3 mg L^{-1} at pH 11.5; photocatalyst's amount 10 mg (0.5 g L^{-1}).

4.3.9.5. Spectrofluorometric Studies

It has been widely accepted that ˙OH radicals are the active species for the photocatalytic degradation of MB dye [8, 41]. The efficiency of photocatalysts has been ensured by the generation of ˙OH radicals which can be investigated by fluorescence intensity measurement with the help of spectrofluorometer. The fluorescence spectra of terephthalic acid (0.5 mM) have been recorded at 315 nm excitation wavelength with photocatalysts under dark and UV-visible irradiation. It has been found that there is no any increment in fluorescence intensity of terephthalic acid at 425 nm under dark (Fig. 4.25) while under UV-visible irradiation it increases on account of the synergic effect of light and photocatalysts (Fig. 4.26).

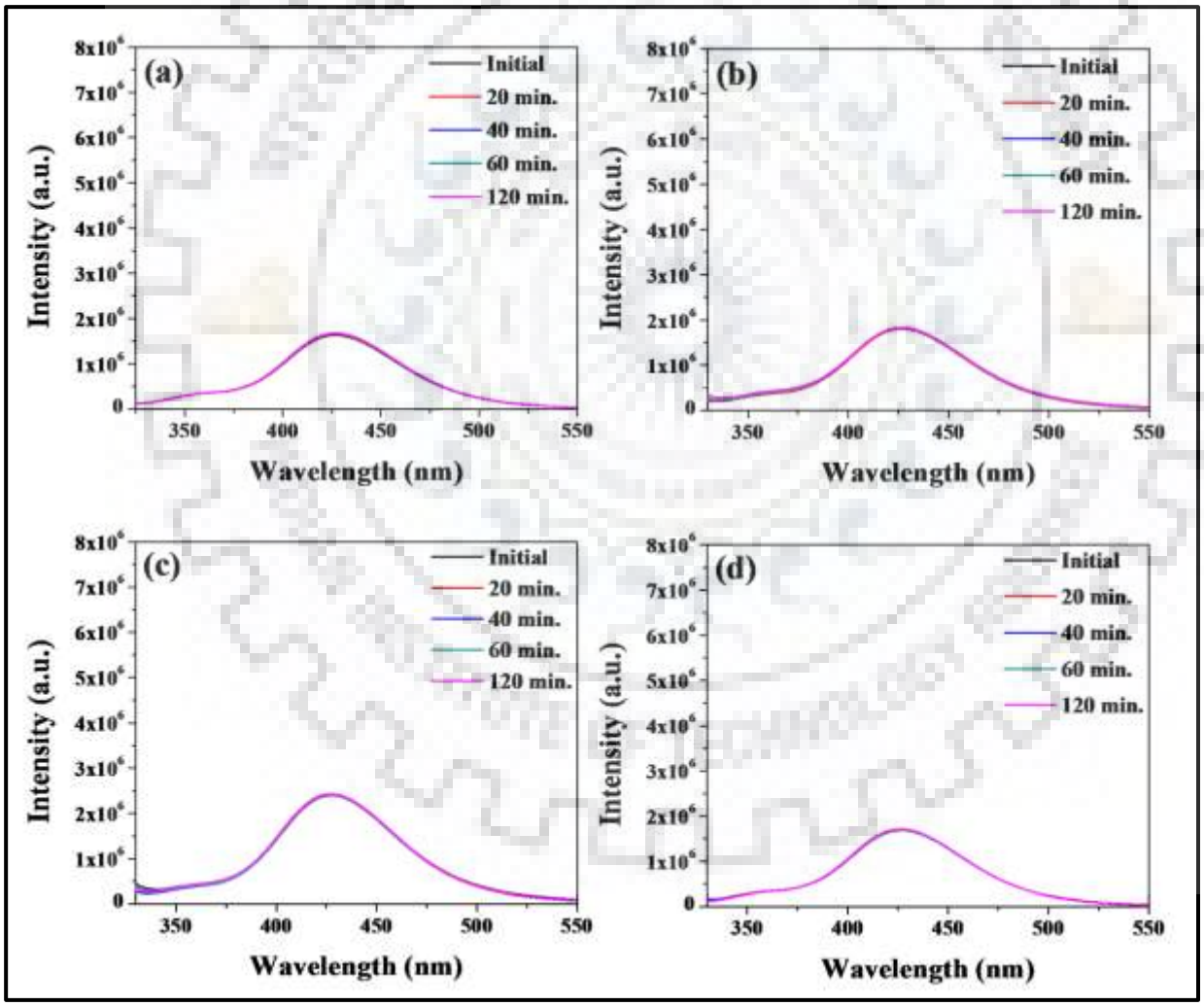

Fig. 4.25. Fluorescence spectral changes (excitation at 315 nm; under dark) of terephthalic acid (0.5 mM; NaOH 2 mM), (a) without any photocatalyst; (b) in presence of ZIF-8 (10 mg); (c) in presence of composite NC1 (10 mg); (d) in presence of SnO_2NPs (equivalent amount present in 150 µL suspension).

Further, the efficiency of composite NC1 towards the generation of $^{\bullet}OH$ radicals is found to be more as compared to that of ZIF-8 and SnO_2NPs under UV-visible light irradiation. These results indicate the greater efficiency of composite NC1 towards the photocatalytic degradation of MB under UV-visible light irradiation.

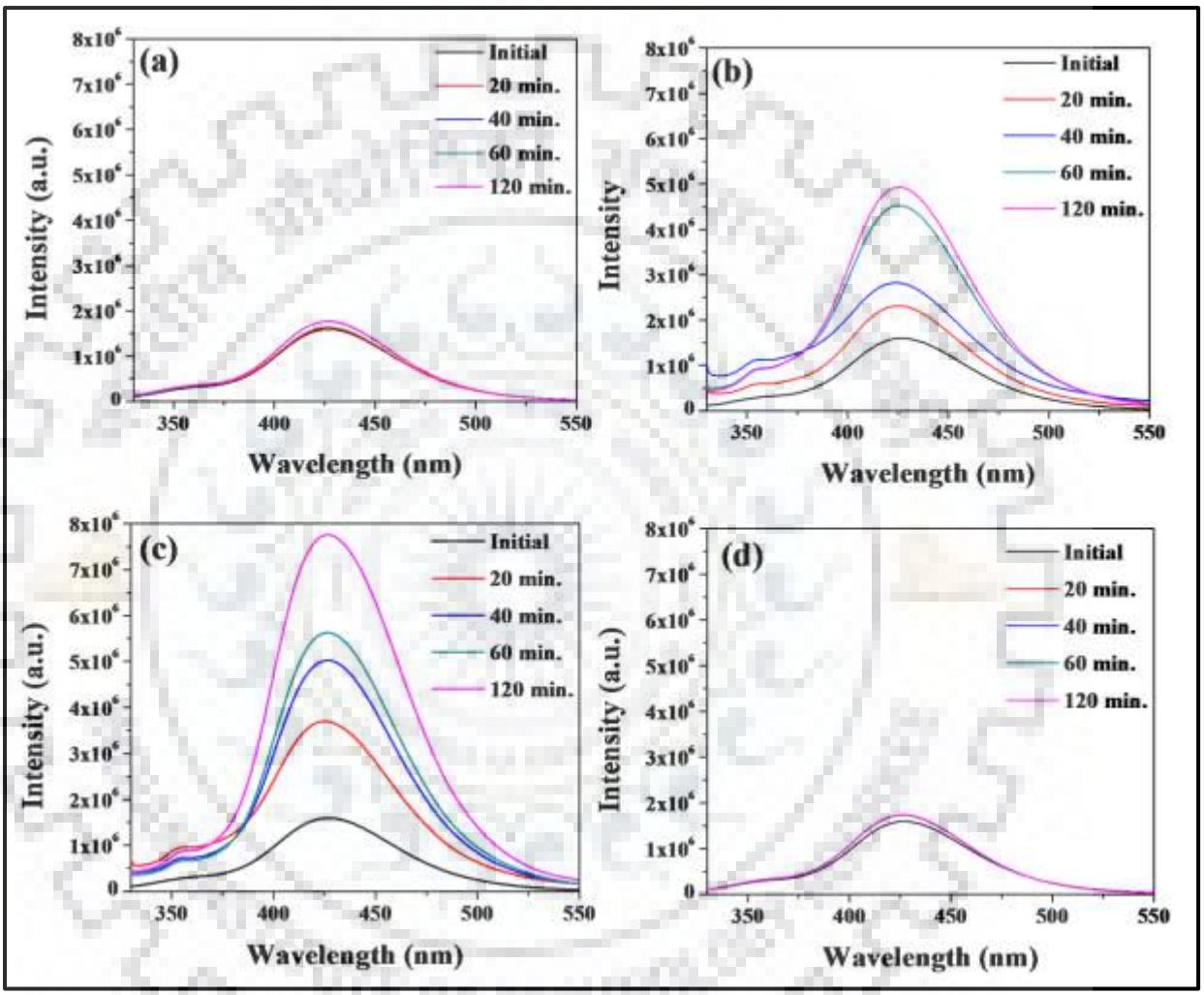

Fig. 4.26. Fluorescence spectral changes (excitation at 315 nm; under UV-visible light) of terephthalic acid (0.5 mM; NaOH 2 mM), (a) without any photocatalyst; (b) in presence of ZIF-8 (10 mg); (c) in presence of composite NC1 (10 mg); (d) in presence of SnO_2NPs (equivalent amount present in 150 µL Suspension).

4.3.9.6. Scavenger Analysis

The scavenger experiments have been employed for the detection of main reactive species ($^{\bullet}OH$, $O_2^{\bullet-}$, and h^+) responsible for the photocatalytic degradation of dye. Ethylenediaminetetra acetic acid (EDTA), *p*-benzoquinone (BQ) and tertiary butyl alcohol (*t*-

BuOH) are used as h^+, $O_2^{\bullet-}$, and $^{\bullet}OH$ scavenger, respectively [54, 29, 55]. 2 mL of 2 mM BQ, 500 μL *t*-BuOH and 33 mg EDTA has been added separately into MB solution prior to addition of composite NC1 in the experiment. It has been found that the photocatalytic efficiency of composite NC1 decreases significantly in the presence of *t*-BuOH while a small decrease is observed in presence of BQ and EDTA (Fig. 4.27). The observed results indicate that $^{\bullet}OH$ radicals play an important role in photocatalytic degradation of MB while h^+ and $O_2^{\bullet-}$ radicals play a minor role.

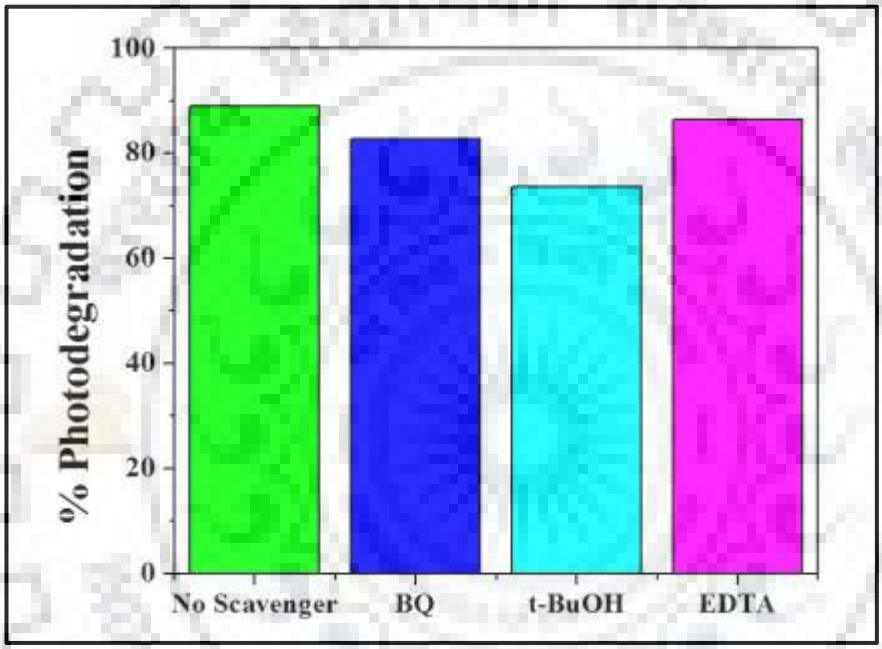

Fig. 4.27. Effect of scavengers (BQ, *p*-benzoquinone; *t*-BuOH, *t*-butanol; EDTA, ethylenediaminetetraacetic acid) on photocatalytic degradation of MB in the presence of composite NC1 under UV-visible irradiation.

4.3.9.7. Plausible Degradation Mechanism

The general photocatalytic mechanism of multi-core-shell SnO_2NPs@ZIF-8 (NC1) involves the synergic effect of SnO_2NPs and ZIF-8 where SnO_2NPs act as a core (main photocatalysts) and ZIF-8 acts as a shell (co-catalysts) material. In case of bare SnO_2NPs, there is more probability for recombination of the generated e^- and h^+ pair under UV-visible light irradiation (Fig. 4.28). However, in case of SnO_2NPs@ZIF-8 the generated e^- and h^+ pair in the conduction band (CB) and valance band (VB) of SnO_2NPs can move on the surface of ZIF-8 that helps to reduce the recombination of e^- and h^+ pair. These e^- and h^+ pair can easily react oxygenated water and so produce $^{\bullet}OH$ radicals, responsible for photo-induced catalytic

degradation of dye which is already confirmed by spectrofluorometric analysis. In case of pure ZIF-8, photocatalytic degradation of dye occurs as a results of HOMO-LUMO charge transfer from N 2p bonding orbital of imidazole ring to the vacant orbital of Zn^{+2}. In the excited state, electron returns from LUMO to HOMO to stabilize the system. Therefore, remaining electron combines with oxygenated water to form $^{\bullet}OH$ radicals [8].

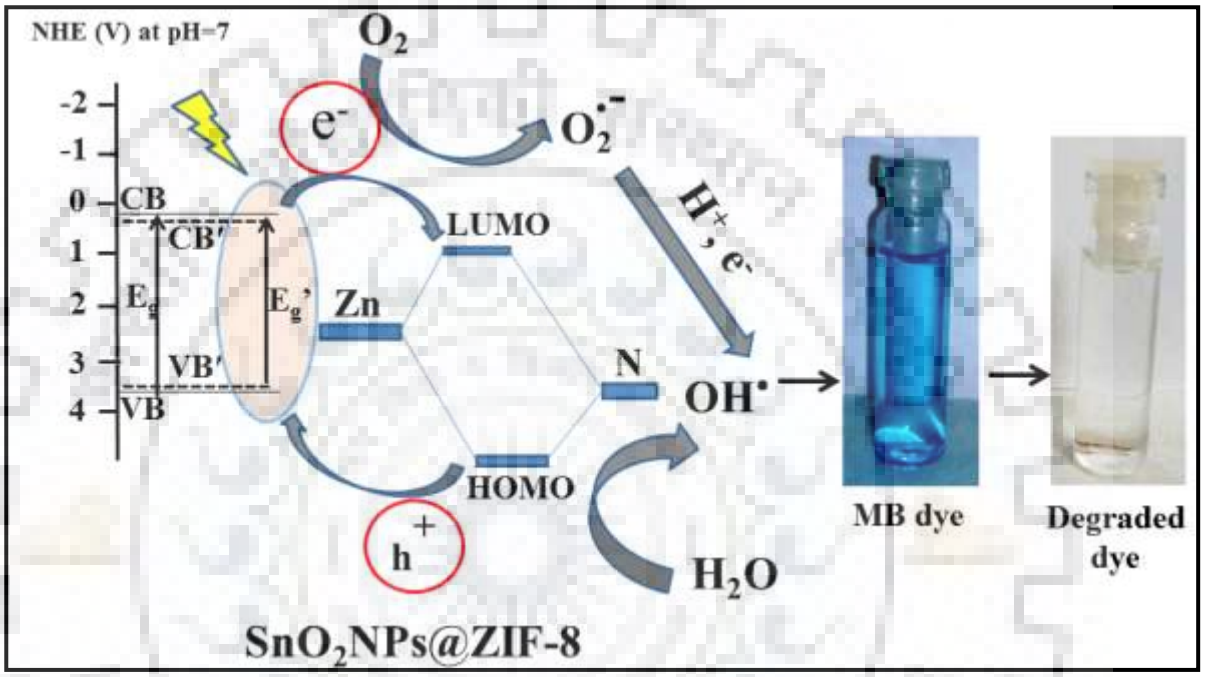

Fig. 4.28. Mechanism for photocatalytic degradation of MB by SnO_2NPs@ZIF-8 composite (NC1). The solid lines indicate VB and CB of SnO_2NPs and Eg represents band gap of SnO_2NPs while the dashed lines indicate VB' and CB' of encapsulated SnO_2NPs whereas E'g represents decreased band gap of SnO_2NPs after encapsulation.

4.3.9.8. GC-MS Analysis

The possible degraded pathway of MB is proposed in Scheme 3.2 (Chapter three). The degraded by-products and their plausible fragments have been identified by GC-MS analysis [8, 56]. Mass spectra of the plausible fragments are provided in Fig. 4.29. A very weak molecular ion peak of MB appears in the GC-MS spectra after its photodegradation which indicates a very small fraction of MB is remained. Further, MB is reported to undergo a complete mineralization into inorganic ions, CO_2, NO_3^-, SO_4^- and NH_4^+ after a prolonged photo-irradiation [56].

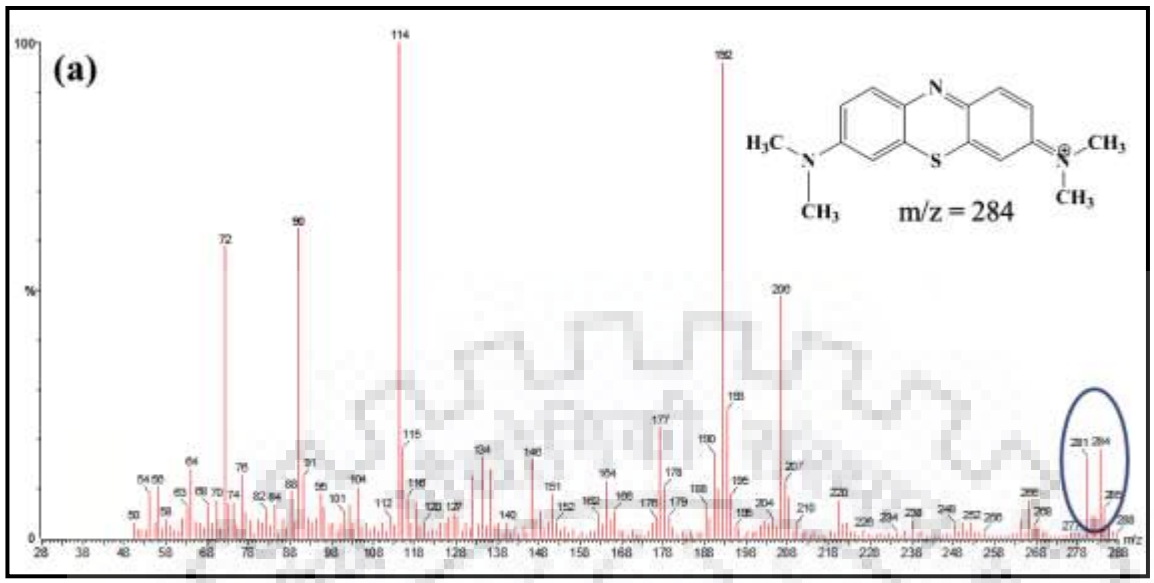

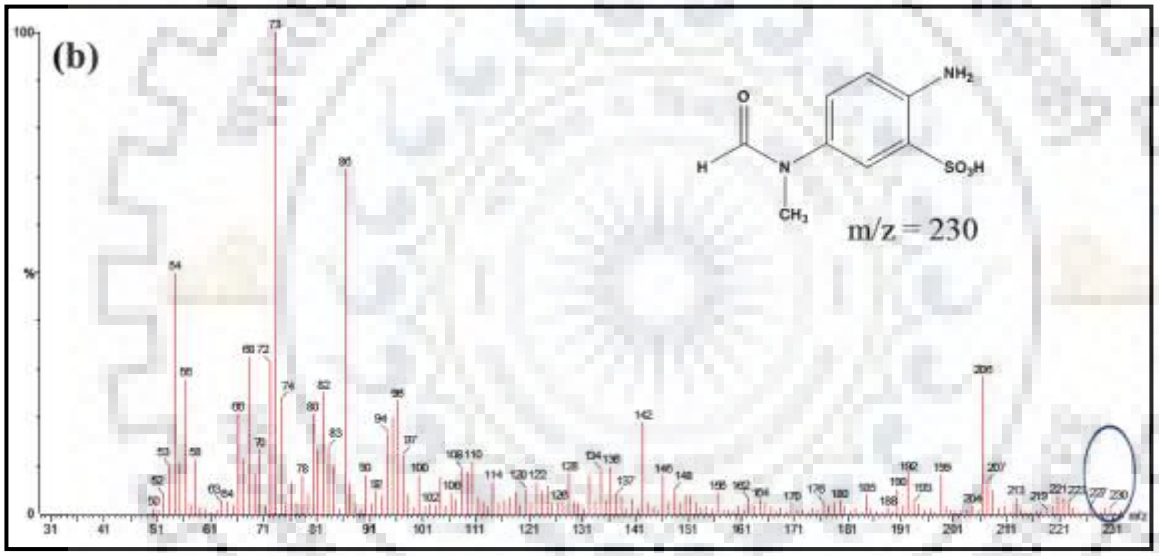

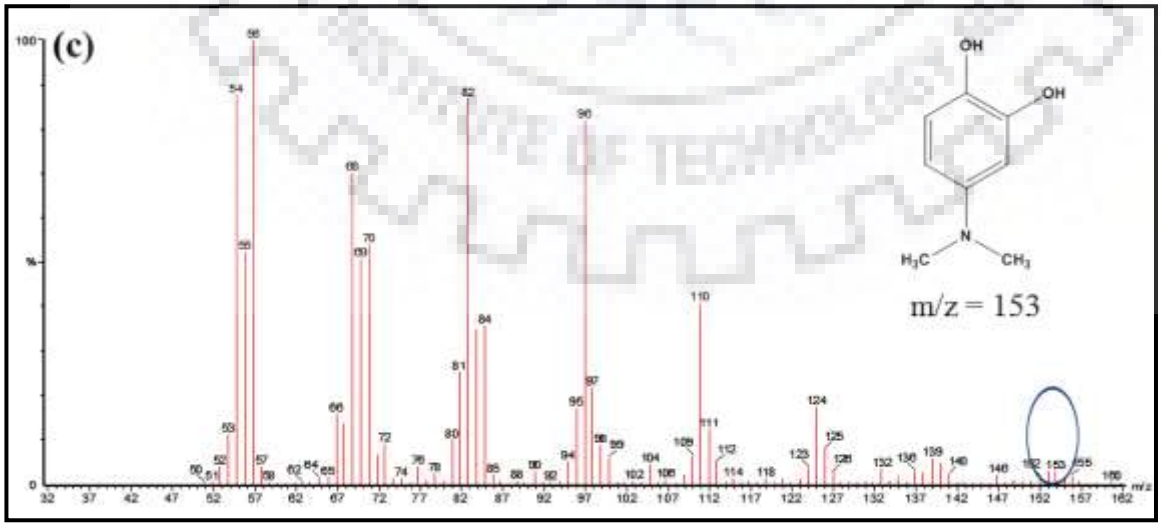

Continued

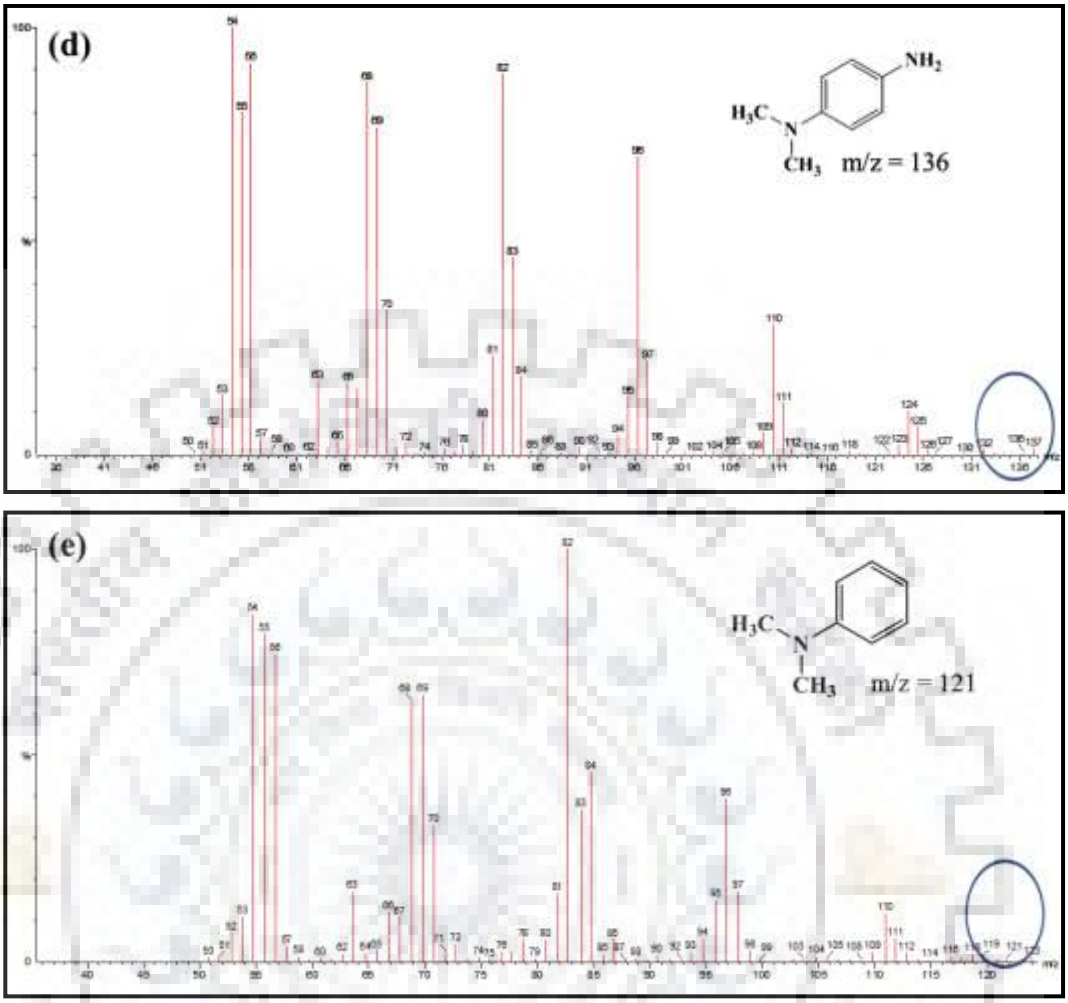

Fig. 4.29. The GC-MS spectra of identified intermediates structures (a-e) after the degradation of MB is shown above, respectively.

4.4. CONCLUSIONS

In summary, an easily executable and sustainable route to synthesize multi-core-shell SnO_2NPs@ZIF-8 composites has been developed by encapsulation of varied amounts of SnO_2NPs within ZIF-8 at ambient temperature. For the first time, it has been reported that SnO_2NPs@ZIF-8 (NC1) shows maximum reduction in viral load/titers up to >80% during post-treatment and >50% during pre-treatment for the *Chikungunya virus* which is greater than that of the ZIF-8 and bare SnO_2NPs. Further, NC1 was found to display an enhanced photocatytic activity for the degradation (96%) of MB (0.5×10^{-5} M) at higher pH >7.0 by involving $^{\bullet}OH$ radicals as major active species.

NOTE: The work of this chapter was published in repute journal as given below.

R. Chandra, V. Singh, S. Tomar and M. Nath*, "Multi-core-shell Composite SnO_2NPs@ZIF-8: Potential Antiviral Agent and Effective Photocatalyst for Waste-water Treatment" Environ. Sci. Pollu. R. (2019) 23346–23358.

- The supporting data are also avialable on given link. https://doi.org/10.1007/s11356-019-05646-5.

4.5. REFERENCES

(1) McKinlay, A. C.; Morris, R. E.; Horcajada, P.; Férey, G.; Gref, R.; Couvreur, P.; Serre, C. BioMOFs: Metal-Organic Frameworks for Biological and Medical Applications. *Angew. Chem., Int. Ed.* **2010**, *49*, 6260-6266.

(2) Wang, H.; Hu, T. L.; Wen, R. M.; Wang, Q.; Bu, X. H. *In-vitro* Controlled Release of Theophylline from Metal-Drug Complexes. *J. Mater. Chem. B* **2013**, *1*, 3879-3882.

(3) Horcajada, P.; Chalati, T.; Serre, C.; Gillet, B.; Sebrie, C.; Baati, T.; Eubank, J. F.; Heurtaux, D.; Clayette, P.; Kreuz, C.; Chang, J. S.; Hwang, Y. K.; Marsaud, V.; Bories, P. N.; Cynober, L.; Gil, S.; Ferey, G.; Couvreur, P.; Gref, R. Porous Metal–Organic-Framework Nanoscale Carriers as a Potential Platform for Drug Delivery and Imaging. *Nat. Mater.* **2010**, *9*, 172.

(4) Horcajada, P.; Serre, C.; Maurin, G.; Ramsahye, N. A.; Balas, F.; Vallet-Regi, M.; Sebban, M.; Taulelle, F.; Férey, G. Flexible Porous Metal-Organic Frameworks for a Controlled Drug Delivery. *J. Am. Chem. Soc.* **2008**, *130*, 6774-6780.

(5) Sun, C. Y .; Qin, C.; Wang, X. L.; Yang, G. S.; Shao, K. Z.; Lan, Y. Q.; Su, Z. M.; Huang, P.; Wang, C. G.; Wang, E. B. Zeolitic Imidazolate Framework-8 as Efficient pH-sensitive Drug Delivery Vehicle. *Dalton Trans.* **2012**, *41*, 6906-6909.

(6) Zheng, M.; Liu, S.; Guan, X.; Xie, Z. One-Step Synthesis of Nanoscale Zeolitic Imidazolate Frameworks with High Curcumin Loading for Treatment of Cervical Cancer. *ACS Appl. Mater. Interfaces* **2015**, *7*, 22181-22187.

(7) Vasconcelos, I. B.; Silva, T. G. D.; Militao, G. C. G.; Soares, T. A.; Rodrigues, N. M.; Rodrigues, M. O.; Costa, N. B. D.; Freire R. O.; Junior, S. A. Cytotoxicity and Slow Release of the Anti-Cancer Drug Doxorubicin from ZIF8. *RSC Adv.* **2012**, *2*, 9437-9442.

(8) Jing, H. P.; Wang, C. C.; Zhang, Y. W.; Wang, P.; Li, R. Photocatalytic Degradation of Methylene Blue in ZIF-8. *RSC Adv.* **2014**, *4*, 54454-54462.

(9) Mu, L.; Liu, B.; Liu, H.; Yang, Y.; Sun, C.; Chen, G. A Novel Method to Improve the Gas Storage Capacity of ZIF-8. *J. Mater. Chem.* **2012**, *22*, 12246-12252.

(10) Lu, G.; Hupp, J. T. Metal-Organic Frameworks as Sensors: a ZIF-8 Based Fabry-Pérot Device as a Selective Sensor for Chemical Vapour and Gases. *J. Am. Chem. Soc.* **2010**, *132*, 7832-7833.

(11) Jiang, H. L.; Liu, B.; Akita, T.; Haruta, M.; Sakurai, H.; Xu, Q. Au@ZIF-8:CO Oxidation over Gold Nanoparticles Deposited to Metal-Organic Framework. *J. Am. Chem. Soc.* **2009**, *131*, 11302-11303.

(12) Esken, D.; Turner, S.; Lebedev, O. I.; Van Tendeloo, G.; Fischer, R. A. Au@ZIFs: Stabilization and Encapsulation of Cavity-Size Matching Gold Clusters Inside Functionalized Zeolite Imidazolate Frameworks, ZIFs. *Chem. Mater.* **2010**, *22*, 6393-6401.

(13) Jiang, H. L.; Akita, T.; Ishida, T.; Haruta, M.; Xu, Q. Synergistic Catalysis of Au@Ag Core-shell Nanoparticles Stabilized on Metal-Organic Framework. *J. Am. Chem. Soc.* **2011**, *133*, 1304-1306.

(14) Zahmakiran, M. Iridium Nanoparticles Stabilized by Metal Organic Frameworks (IrNPs@ ZIF-8): Synthesis, Structural Properties and Catalytic Performance. *Dalton Trans.* 2012, **41**, 12690-12696.

(15) Wang, P.; Zhao, J.; Li, X.; Yang, Y.; Yang, Q.; Li, C. Assembly of ZIF Nanostructures Around Free Pt Nanoparticles: Efficient Size-Selective Catalysts for Hydrogenation of Alkenes under Mild Conditions. *Chem. Commun.* **2013**, *49*, 3330-3332.

(16) Dang, T. T.; Zhu, Y.; Ngiam, J. S.; Ghosh, S. C.; Chen, A.; Seayad, A. M. Palladium Nanoparticles Supported on ZIF-8 as an Efficient Heterogeneous Catalyst for Aminocarbonylation. *ACS Catal.* **2013**, *3*, 1406-1410.

(17) Zhang, M.; Yang, Y.; Li, C.; Liu, Q.; Williams, C. T.; Liang, C. PVP-Pd@ZIF-8 as Highly Efficient and Stable Catalysts for Selective Hydrogenation of 1, 4-butynediol. *Catal. Sci. Technol.* **2014**, *4*, 329-332.

(18) Kuo, C. H.; Tang, Y.; Chou, L. Y.; Sneed, B. T.; Brodsky, C. N.; Zhao, Z.; Tsung, C. K. Yolk-shell Nanocrystal@ZIF-8 Nanostructures for Gas-phase Heterogeneous Catalysis with Selectivity Control. *J. Am. Chem. Soc.* **2012**, *134*, 14345-14348.

(19) Zhang, T.; Zhang, X.; Yan, X.; Kong, L.; Zhang, G.; Liu, H.; Qiu, J.; Yeung, K. L. Synthesis of Fe_3O_4@ZIF-8 Magnetic Core-Shell Microspheres and Their Potential Application in a Capillary Microreactor. *Chem. Eng. J.* **2013**, *229*, 398-404.

(20) Zhan, W. W.; Kuang, Q.; Zhou, J. Z.; Kong, X. J.; Xie, Z. X.; Zheng, L. S. Semiconductor@metal-organic Framework Core-Shell Heterostructures: A Case of ZnO@ZIF-8 Nanorods with Selective Photoelectrochemical Response. *J. Am. Chem. Soc.* **2013**, *135*, 1926-1933.

(21) Gao, Y.; Wu, J.; Zhang, W.; Tan, Y.; Zhao, J.; Tang, B. The Electrochemical Performance of SnO_2 Quantum Dots@Zeolitic Imidazolate Frameworks-8 (ZIF-8) Composite Material for Supercapacitors. *Mater. Lett.* **2014**, *128*, 208-211.

(22) Liu, J.; He, J.; Wang, L.; Li, R.; Chen, P.; Rao, X.; Deng, L.; Rong, L.; Lei, J. NiO-PTA Supported on ZIF-8 as a Highly Effective Catalyst for Hydrocracking of Jatropha Oil. *Sci. Rep.* **2016**, *6*, 23667.

(23) Isimjan, T. T.; Kazemian, H.; Rohani, S.; Ray, A. K. Photocatalytic Activities of Pt/ZIF-8 Loaded Highly Ordered TiO_2 Nanotubes. *J. Mater. Chem.* **2010**, *20*, 10241-10245.

(24) Wu, M.; Ye, H.; Zhao, F.; Zeng, B. High-Quality Metal-Organic Framework ZIF-8 Membrane Supported on Electrodeposited ZnO/2-Methylimidazole Nanocomposite: Efficient Adsorbent for the Enrichment of Acidic Drugs. *Sci. rep.* **2017**, *7*, 39778.

(25) Yu, B.; Wang, F.; Dong, W.; Hou, J.; Lu, P.; Gong, J. Self-Template Synthesis of Core-Shell ZnO@ZIF-8 Nanospheres and the Photocatalysis under UV Irradiation. *Mater. Lett.* **2015**, *156*, 50-53.

(26) Liédana, N.; Galve, A.; Rubio, C. S.; Téllez, C.; Coronas, J. CAF@ZIF-8: One-Step Encapsulation of Caffeine in MOF. *Appl. Mater. Interfaces* **2012**, *4*, 5016-5021.

(27) Mahdi, E.; Tan, J. C., Dynamic Molecular Interactions between Polyurethane and ZIF-8 in a Polymer-MOF Nanocomposite: Microstructural, Thermo-Mechanical and Viscoelastic Effects. *Polym. J.* **2016**, *97*, 31-43.

(28) Redfern, J.; Geerts, L.; Seo, J. W.; Verran, J.; Tosheva, L.; Wee, L. H. Toxicity and Antimicrobial Properties of ZnO@ZIF-8 Embedded Silicone Against Planktonic and Biofilm Catheter-Associated Pathogens. *ACS Appl. Nano Mater.* **2018**, *1*, 1657-1665.

(29) Malik, A.; Nath, M.; Mohiyuddin, S.; Packirisamy, G. Multifunctional CdSNPs@ZIF-8: Potential Antibacterial Agent against GFP-expressing Escherichia coli and Staphylococcus aureus and Efficient Photocatalyst for Degradation of Methylene Blue. *ACS Omega* **2018**, *3*, 8288−8308.

(30) Aggarwal, M.; Sharma, R.; Kumar, P.; Parida, M.; Tomar, S. Kinetic Characterization of Trans-Proteolytic Activity of Chikungunya Virus Capsid Protease and Development of a FRET-based HTS Assay. *Sci. Rep.* **2015**, *5*, 14753.

(31) Sharma, R.; Fatma, B.; Saha, A.; Bajpai, S.; Sistla, S.; Dash, P. K.; Parida, M.; Kumar, P.; Tomar, S. Inhibition of Chikungunya Virus by Picolinate that Targets Viral Capsid Protein. *Virology* **2016**, *498*, 265-276.

(32) Jadav, S. S.; Sinha, B. N.; Hilgenfeld, R.; Pastorino, B.; de Lamballerie, X.; Jayaprakash, V. Thiazolidone Derivatives as Inhibitors of Chikungunya Virus. *Eur. J. Med. Chem.* **2015**, *89*, 172-178.

(33) Kumar, B.; Smita, K.; Cumbal, L.; Debut, A.; Galeas, S.; Guerrero, V. H. Phytosynthesis and Photocatalytic Activity of Magnetite (Fe_3O_4) Nanoparticles using the Andean Blackberry Leaf. *Mater. Chem. Phys.* **2016**, *179*, 310-315.

(34) Kumar, S. R.; Paulpandi, M.; ManivelRaja, M.; Mangalaraj, D.; Viswanathan, C.; Kannan, S.; Ponpandian, N. An *in vitro* Analysis of H1N1 Viral Inhibition using Polymer Coated Superparamagnetic Fe_3O_4 Nanoparticles. *RSC Adv.* **2014**, *4*, 13409-13418.

(35) Prabhu, Y.; Rao, K. V.; Kumari, B. S.; Kumar, V. S. S.; Pavani, T. Synthesis of Fe_3O_4 Nanoparticles and its Antibacterial Application. *Int. Nano. Lett.* **2015**, *5*, 85-92.

(36) Zimbone, M.; Buccheri, M.; Cacciato, G.; Sanz, R.; Rappazzo, G.; Boninelli, S.; Reitano, R.; Romano, L.; Privitera, V.; Grimaldi, M. Photocatalytical and Antibacterial Activity of TiO_2 Nanoparticles Obtained by Laser Ablation in Water. *Appl. Catal. B* **2015**, *165*, 487-494.

(37) Levina, A. S.; Repkova, M. N.; Bessudnova, E. V.; Filippova, E. I.; Mazurkova, N. A.; Zarytova, V. F. High Antiviral Effect of TiO_2 PL–DNA Nanocomposites Targeted to Conservative Regions of (−) RNA and (+) RNA of Influenza A Virus in Cell Culture. *Beilstein J. Nanotechnol.* **2016**, *7*, 1166-1173.

(38) Nair, M. G.; Nirmala, M.; Rekha, K.; Anukaliani, A. Structural, Optical, Photo Catalytic and Antibacterial Activity of ZnO and Co Doped ZnO Nanoparticles. *Mater. Lett.* **2011**, *65*, 1797-1800.

(39) Antoine, T. E.; Mishra, Y. K.; Trigilio, J.; Tiwari, V.; Adelung, R.; Shukla, D. Prophylactic, Therapeutic and Neutralizing Effects of Zinc Oxide Tetrapod Structures Against Herpes Simplex Virus Type-2 Infection. *Antiviral Res.* **2012**, *96*, 363-375.

(40) Amininezhad, S. M.; Rezvani, A.; Amouheidari, M.; Amininejad, S. M.; Rakhshani, S. The Antibacterial Activity of SnO_2 Nanoparticles Against Escherichia coli and Staphylococcus aureus. *Zahedan J. Res. Med. Sci.* **2015**, *17*, 1053-1058.

(41) Kim, S. P.; Choi, M. Y.; Choi, H. C. Photocatalytic Activity of SnO_2 Nanoparticles in Methylene Blue Degradation. *Mater. Res. Bull.* **2016**, *74*, 85-89.

(42) Bhattacharjee, A.; Ahmaruzzaman, M.; Sinha, T. A Novel Approach for the Synthesis of SnO_2 Nanoparticles and its Application as a Catalyst in the Reduction and Photodegradation of Organic Compounds. *Acta Mol. Biomol. Spectrosc.* **2015**, *136*, 751-760.

(43) Trigilio, J.; Antoine, T. E.; Paulowicz, I.; Mishra, Y. K.; Adelung, R.; Shukla, D. Tin Oxide Nanowires Suppress Herpes Simplex Virus-1 Entry and cell-to-cell Membrane Fusion. *Plos One* **2012**, *7*, 48147-48156.

(44) Li, F.; Xu, J.; Yu, X.; Chen, L.; Zhu, J.; Yang, Z.; Xin, X. One-Step Solid-State Reaction Synthesis and Gas Sensing Property of Tin Oxide Nanoparticles. *Sens. Actuator B-Chem.* **2002**, *81*, 165-169.

(45) Hu, Y.; Kazemian, H.; Rohani, S.; Huang, Y.; Song, Y. *In situ* High Pressure Study of ZIF-8 by FTIR Spectroscopy. *Chem. Commun.* **2011**, *47*, 12694-12696.

(46) Dutta, K.; De, S. Optical and Nonlinear Electrical Properties of SnO_2-Polyaniline Nanocomposites. *Mater. Lett.* **2007**, *61*, 4967-4971.

(47) Tauc, J.; Grigorovici, R.; Vancu, A. Optical Properties and Electronic Structure of Amorphous Germanium. *Phys. Status Solidi B* **1996**, *15*, 627-637.

(48) Nazarkovsky, M. A.; Gun'ko, V.; Wójcik, G.; Czech, B.; Sobieszek, A.; Skubiszewska-Zięba, J.; Janusz, W.; Skwarek, E. Band-gap Change and Photocatalytic Activity of Silica/Titania Composites Associated with Incorporation of CuO and NiO. *Chem. Phys. Technol. Surf.* **2014**, *5*, 421-437.

(49) Rajesh, K.; Santhanalakshmi, J. Fabrication of a SnO_2-graphene Nanocomposite Based Electrode for Sensitive Monitoring of an Anti-Tuberculosis Agent in Human Fluids. *New J. Chem.* **2018**, *42*, 2903-2915.

(50) Abidov, A.; Allabergenov, B.; Lee, J.; Jeon, H. W.; Jeong, S. W.; Kim, S. X-ray Photoelectron Spectroscopy Characterization of Fe Doped TiO_2 Photocatalyst. *Int. J. Mater. Mech. Manuf.* **2013**, *3*, 294-296.

(51) Pan, S. S.; Li, G.; Wang, L.; Shen, Y.; Wang, Y.; Mei, T.; Hu, X. Atomic Nitrogen Doping and p-type Conduction in SnO_2. *Appl. Phys. Lett.* **2009**, *95*, 222112-222115.

(52) Li, J.; Liu, S.; He, Y.; Wang, J. Adsorption and Degradation of the Cationic Dyes Over Co Doped Amorphous Mesoporous Titania-Silica Catalyst under UV and Visible Light Irradiation. *Mesopor. Mater.*, **2008**, *115*, 416-425.

(53) Faghihian, H.; Bahranifard, A. Application of TiO_2-Zeolite as Photocatalyst for Photodegradation of Some Organic Pollutants. *Iran. J. Catal.* **2011**, *1*, 45-50.

(54) Wang, Y.; Deng, K.; Zhang, L. Visible Light Photocatalysis of BiOI and its Photocatalytic Activity Enhancement by *in situ* Ionic Liquid Modification. *J. Phys. Chem. C* **2011**, *115*, 14300-14308.

(55) Kumar, S.; Khanchandani, S.; Thirumal, M.; Ganguli, A. K. Achieving Enhanced Visible-light-driven Photocatalysis using type-II $NaNbO_3$/CdS Core/Shell Heterostructures. *ACS Appl. Mater. Interfaces* 2014, *6*, 13221-13233.

(56) Houas, A.; Lachheb, H.; Ksibi, M.; Elaloui, E.; Guillard, C.; Herrmann, J. M. Photocatalytic Degradation Pathway of Methylene Blue in Water. *Appl. Catal. B* **2001**, *31*, 145-157.

Chapter Five

Synthesis and Characterization of AgNPs@ZIFs: Effective Photocatalyst for Industrial Pollutants

"Education, that is the preservation, the handling, and the enhancement of these racial gains generation by generation"

James Francis Ross

This chapter comprises two sections. **Section-A** deals with synthesis and characterization of AgNPs, ZIF-11 and AgNPs@ZIF-11 composites, while **Section-B** describes synthesis of AgNPs doped ZIF-8 *in situ*; synthesis of ZIF-8 as well as AgNPs and photocatalytic application of core-shell composite.

SECTION A

5A.1. INTRODUCTION

Zeolitic imidazole frameworks (ZIFs) are well known metal organic frameworks. ZIFs have been synthesized having various topologies like rhombic dodecahedron (RHO) and sodalite (SOD) topology [1]. ZIF-11 is one of the most auspicious zeolitic imidazole frameworks for gas separation and H_2 adsorption [2] due to its huge porosity. It has large cavities (14.6 Å) connected with small pore apertures (3.0 Å) [3].

From the last few decades, much effort has been devoted for the synthesis of core-shell hetro-structures because such hybrid materials are being utilized as promising and effective heterogeneous photocatalyst due to synergic effect of core-shell materials. Recently, very few researchers have reported modified ZIF-11 for the various applications such as PBI mixed matrix membranes with ZIF-11 for H_2/CO_2 separation [4], ZIF-11/Pebax®2533 mixed matrix membranes for $CO/N_2/CH_4$ gas adsorption [5] and 6FDA-DAM-ZIF-11 mixed-matrix membranes for H_2/CH_4 and CO_2/CH_4 separation [6]. From an overview of the literature, ZIF-11 is not modified with any semiconductors (ZnO, TiO_2, SnO_2 and Fe_3O_4 etc.) or any novel metal nanoparticles such as Au, Ag, Pd, and Pt etc., so far. Further, these novel metal nanoparticles allow the extension of the light absorption of wide band gap of materials due to its *Surface Plasmon Resonance* (SPR) and enhance the photo conversion yield [7]. Recently, it has been reported that wide band gap of semiconductors TiO_2 and CeO_2 activated toward visible light due to modification with novel metal nanoparticles [8-11].

. Therefore, it is envisioned for the synthesis of AgNPs@ZIF-11 composite, whereas AgNPs acts as a core material and ZIF-11 acts as a shell material. This section concerns about the synthetic optimization of ZIF-11, synthesis of AgNPs@ZIF-11 composite and its utilization as a potential photocatalysts for degradation of industrial pollutants such as methylene blue and 4-nitrophenol.

5A.2. EXPERIMENTAL SECTION

5A.2.1. Synthesis of AgNPs

A typical synthetic method [12] has been adopted for the synthesis of Ag nanoparticle (NPs) as schematically illustrated in Scheme 5A.1. Stock solution was prepared of 50 mM $NaBH_4$, 30 mM of trisodium citrate, and 50 mM $AgNO_3$ separately and labelled as A, B and C respectively. 2 mL of solution C was taken in a tri-necked round flask bottle and added 50 mL DI H_2O and kept on stirring (in ice-bath at 4 °C) for 30 min under N_2 purging. After that 1 mL of each solution A and B were added dropwise with constant stirring. Resultant, a pale yellow colour solution was obtained after 30 min which indicates the formation of AgNPs. For trigger the reduction of $AgNO_3$, the RBF was removed from the ice-bath and kept on stirring for another 30 min. The resultant solution was aged for few days and after that gray silver powder was collected by centrifugation and stored in air tight container and wrapped with aluminum foil to protect from sunlight.

5A.2.2. Synthesis of ZIF-11

ZIF-11 was synthesized by toluene assisted synthesis method [13] with some modification. The various reaction conditions were employed in order to attain the optimized synthesis of ZIF-11 as compiled in Table 5A.1. Herein, three metal salts *viz.*, zinc acetate dihydrate, zinc nitrate pentahydrate and anhydrous zinc chloride for three reaction conditions *i.e.* stirring of reaction mixture at room temperature, bench method (keeping reaction mixture solution at room temperature without disturbing liquid-liquid interface) and hydrothermal method involving heating of reaction mixture at 120 °C for 12 h were employed. Consequently, nine products of ZIF-11 were obtained and represented as Z-1 to Z-9, respectively. It is observed that ZIF-11 was successfully synthesized by stirring method using anhydrous zinc chloride metal salts at room temperature.

In the optimized process, 1 mmol (0.12 g) of benzimidazole was dissolved in a binary mixture of solvents (10 mL methanol and 10 mL of toluene) and kept on stirring (in ice-bath at 4 °C) for 30 min. During the stirring of ligand solution, 2.5 mL Liq. NH_3 was added for the deprotonation of imidazole ring. After that 1 mmol anhydrous zinc chloride solution (0.136 g in 4 mL methanol) was added dropwise into ligand solution and stirred for another 30 min. Resultant white precipitate was aged for 12 h at room temperature (*ca.* 25 °C). Further, precipitate was washed with ethanol twice and collected *via* centrifugation and dried at 60 °C. Synthesis of ZIF-11 is schematically illustrated in Scheme 5A.2.

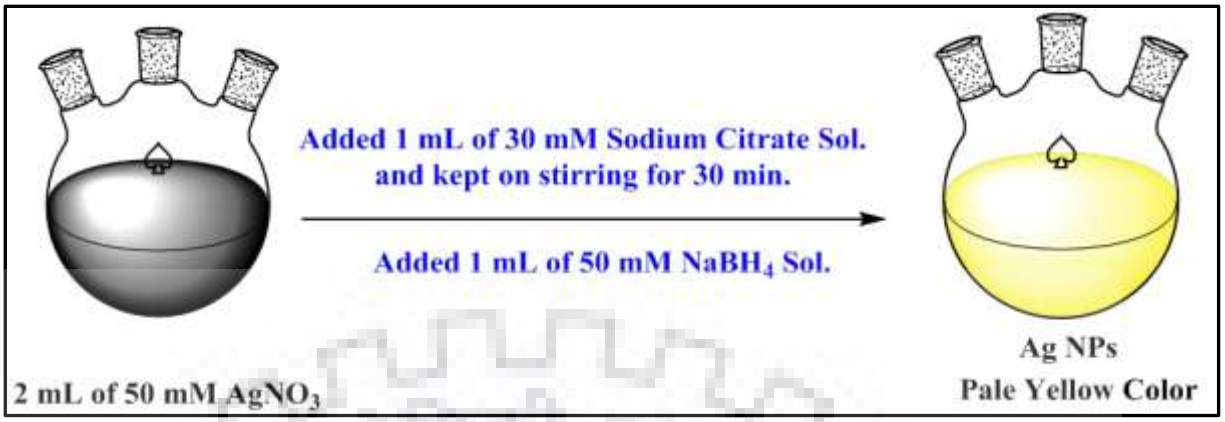

Scheme 5A.1. Schematic presentation of synthesis of AgNPs.

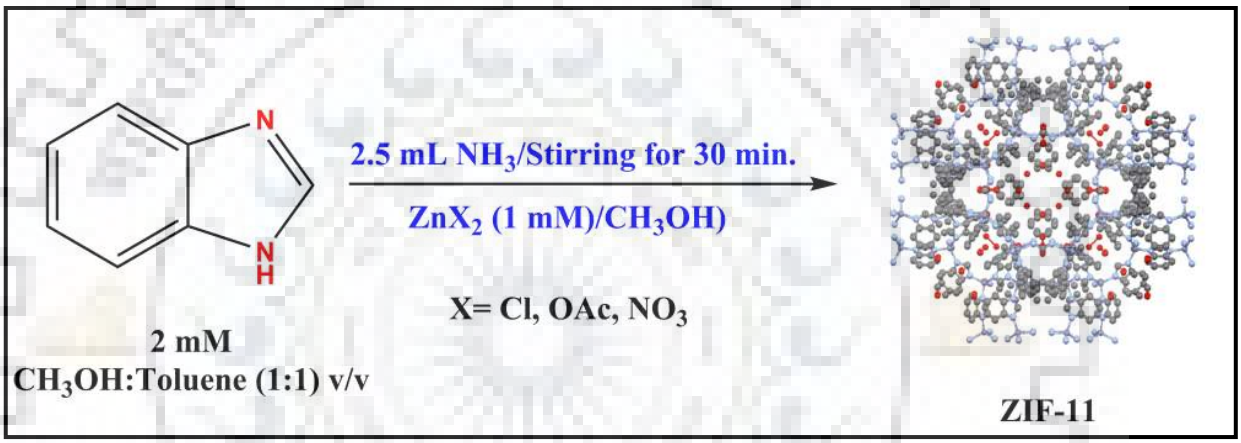

Scheme 5A.2. Schematic presentation of synthesis of ZIF-11.

Table 5A.1. The various synthetic conditions using different zinc metal salts.

S.N.	Metal salts (MX_2)	Conditions		
		Stirring	Bench	Hydrothermal
1.	X= OAc	Z-1	Z-4	Z-7
2.	X= NO_3^{-1}	Z-2	Z-5	Z-8
3.	X= Cl^{-1}	Z-3	Z-6	Z-9

5A.2.3. Synthesis of AgNPs@ZIF-11

A novel multi-core-shell AgNPs@ZIF-11 composite was synthesized by *in situ* encapsulation of AgNPs in ZIF-11 (employed Z-3, prepared by stirring method). The similar procedure has been adopted for the synthesis of AgNPs@ZIF-11 as used for synthesis of ZIF-11. During the addition of metal solution (0.136 g in 4 mL methanol) solution into the benzimidazole solution (0.12 g in 10-10 mL of binary solvent methanol-toluene), AgNPs

suspensions (1 mg of AgNPs powder dispersed in 2 mL methanol) in different amounts *i.e.* 150 µL, 300 µL and 500 µL methanol suspensions were simultaneously added to yield AgNPs@ZIF-11 composites which are represented as AZ1, AZ2 and AZ3, respectively.

5A.2.4. Adsorption and Photodegradation Studies

Details of adsorption and photodegradation studies of MB are similar as reported in Chapter two. For the reduction of 4-nitrophenol (4-NP), following four sets of 4-NP (1×10^{-4} M) solution in 50 mL ungraduated test tubes were prepared as per the details given below-

(i) 20 mL of 1×10^{-4} M 4-NP solution.

(ii) 10 mL of 0.1M $NaBH_4$ solution was added in 20 mL of 1×10^{-4} M 4-NP solution.

(iii) 20 mg ZIF-11 was suspended in 20 mL solution of 4-NP + 10 mL of 0.1M $NaBH_4$ solution.

(iv) 20 mg AZ1 composite was suspended in 20 mL solution of 4-NP + 10 mL of 0.1M $NaBH_4$ solution.

The reaction was started with addition of $NaBH_4$ and catalysts (ZIF-11 and AZ1 composite) under UV-visible irradiation. All the four sets were kept under UV-visible irradiation with continue stirring for 120 min and at certain interval of time the UV-visible spectra were recorded. The reduction percentage of 4-NP into 4-AP (4-aminophenol) was calculated by using following equation (5A.1).

$$\text{Reduction \%} = [(A_0 - A_t) \div A_0] \times 100 \qquad (5A.1)$$

Where A_0 is initial absorbance and A_t is the absorbance at certain time "t".

5A.3. RESULTS AND DISCUSSION

5A.3.1. PXRD Analysis

Three reaction conditions *i.e.* stirring, bench and hydrothermal method have been applied using three zinc metal salts for the synthesis of ZIF-11. Hence, nine products of ZIF-11 have been synthesized and characterized by powder X-ray diffraction (PXRD) analysis. The PXRD spectra of nine products of ZIF-11 are given in Fig. 5A.1. The PXRD pattern of Z-3 matches with PXRD pattern of ZIF-11 (RHO) exported from single crystal data (CCDC no. 602545) with the help of mercury and X'Pert HighScore software. Hence, it has been observed that ZIF-11 can be synthesized by optimized stirring method using anhydrous zinc chloride

metal salt and benzimidazole ligand in a binary solvent (methanol and toluene) at room temperature.

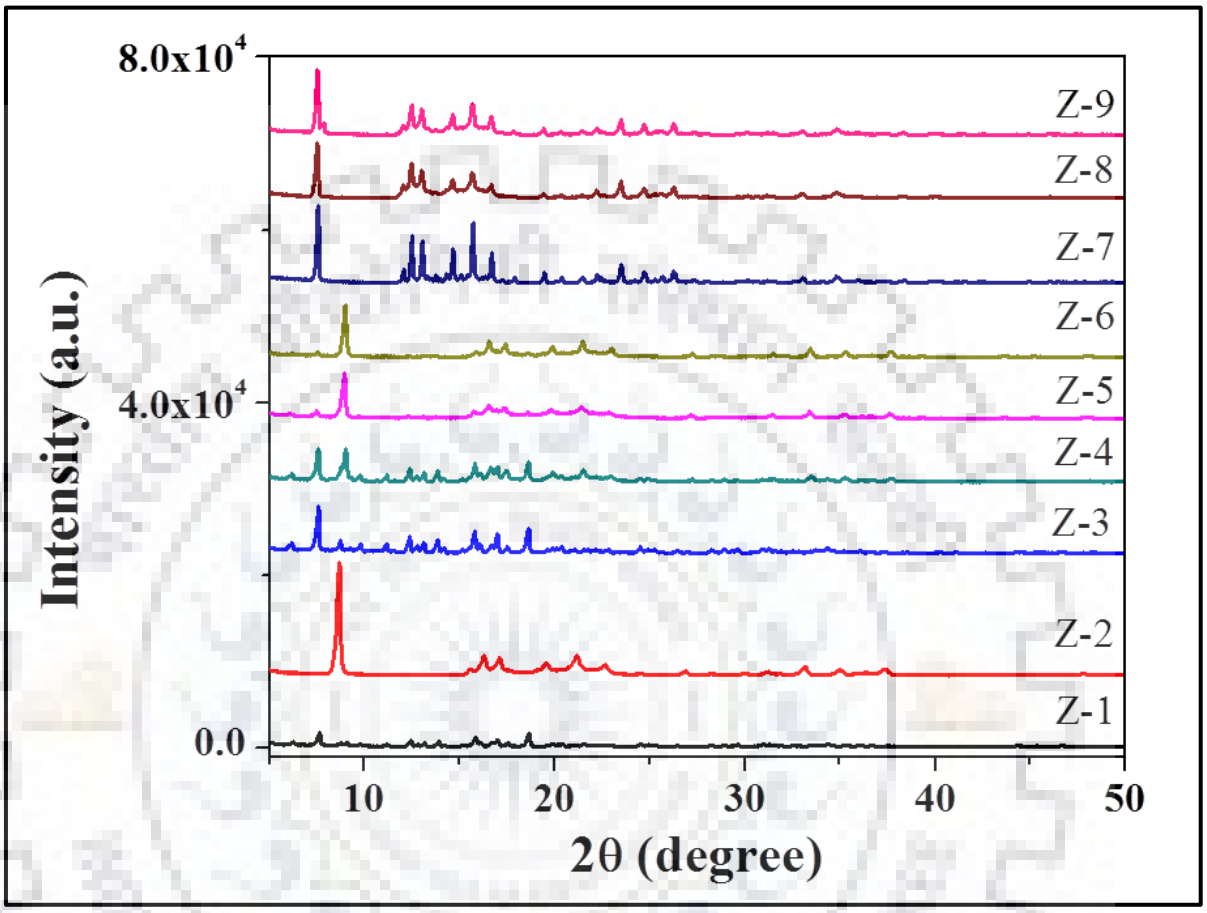

Fig. 5A.1. PXRD pattern of ZIF-11 as synthesized various conditions.

The PXRD peaks of ZIF-11 are at 6.211°, 7.623°, 8.733°, 12.365°, 13.778°, 15.695°, 16.603° and 18.52° corresponding to the planes (200), (211), (220), (400), (420), (510), (520), and (600), respectively, which have been shown in Fig. 5A.2(a) and indexed with reported ZIF-11 PXRD pattern. Further, ZIF-11 and AgNPs@ZIF-11 composites (AZ1, AZ2 and AZ3) reveal the same PXRD pattern which indicates that AgNPs does not affect the morphology and crystallinity of ZIF-11 as illustrated in Fig. 5A.2(a). AgNPs also has been characterized by PXRD analysis (Fig. 5A.2(b)). The major PXRD peaks of AgNPs are at 38.117°, 44.279°, 64.428°, 77.475°, 81.539° and 97.891° corresponding to the planes (110), (200), (220), (311), (222), and (400), respectively, which have been indexed with the JCPDS No. 00-004-0783. Arial and chemical stability of ZIF-11 and its composites have also been examined by PXRD analysis. Fig. 5A.2(c) shows that

there are no any significant change in the PXRD pattern of ZIF-11, AZ1, AZ2 and AZ3 composites which firmly proves their high stability (after six months) while after the fifth cycle of photodegradation study, ZIF-11 and AZ1 have started slightly degraded which is ensured by slight reduction of PXRD peak intensity (Fig. 5A.2(d)).

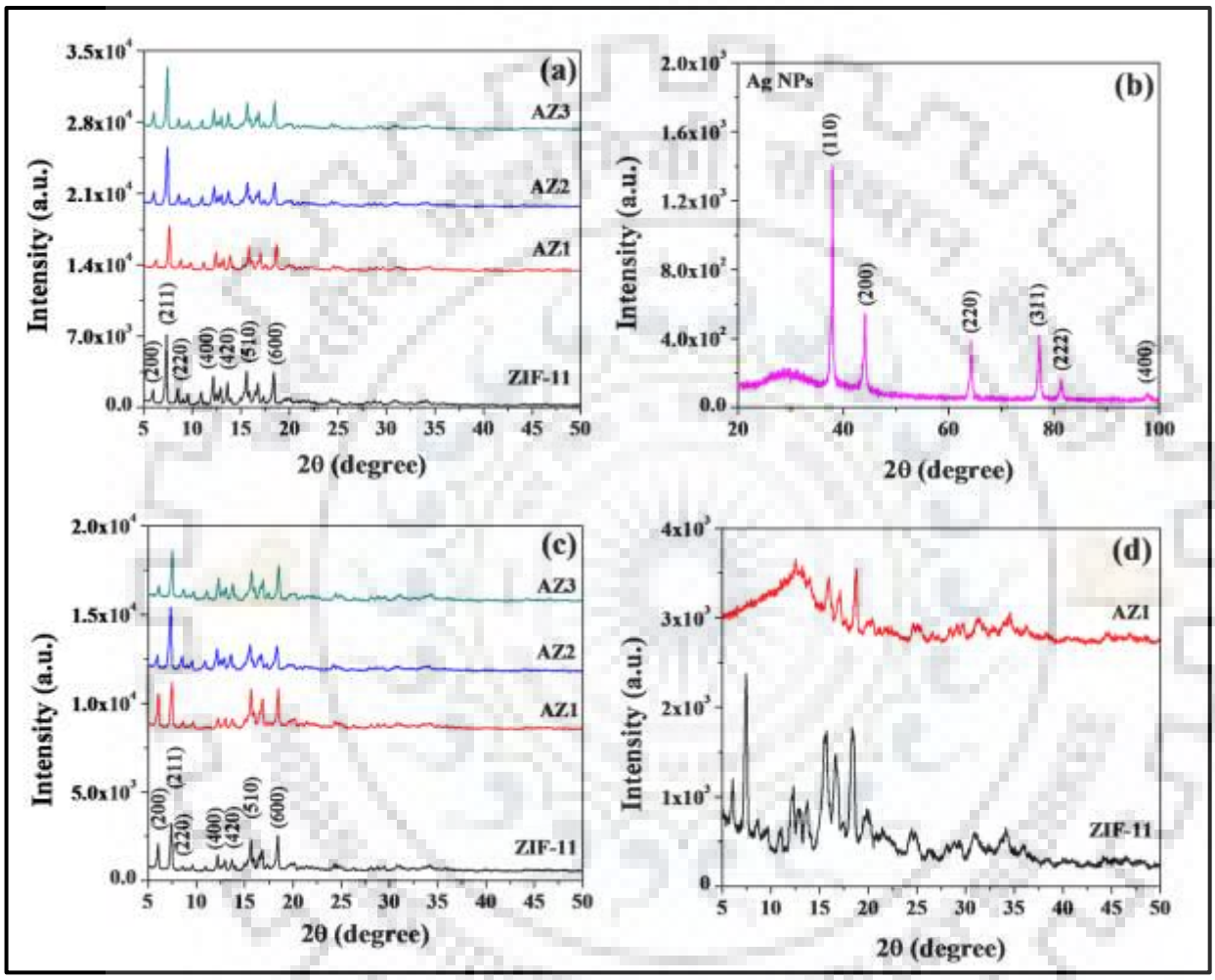

Fig. 5A.2. (a) PXRD patterns of ZIF-11 and its composites AZ1, AZ2 AZ3; (b) PXRD pattern of AgNPs; (c) PXRD patterns of ZIF-11 and its composites AZ1, AZ2 AZ3 after six months; (d) PXRD patterns of used ZIF-11 and AZ1 composite.

5A.3.2. FT-IR Spectroscopic Studies

FT-IR spectra of ZIF-11 and its composites *viz.*, AZ1, AZ2 and AZ3 are given in Fig. 5A.3. The characteristic peaks of imidazole ring are similar in ZIF-11 and their composites. The bands at 3088 cm^{-1}, 3057 cm^{-1}, 3032 cm^{-1} are assigned to $\nu(=C\text{-}H)_{aromatic\ ring}$, 1611 cm^{-1}, 1465 cm^{-1} to $\nu(\text{-}C\text{-}C\text{-})_{aromatic\ ring}$ and 435 cm^{-1} to $\nu(Zn\text{-}N)$ [6, 14]. A

stretching frequency due to C_{sp3}-H at 2920 cm^{-1} disappears which indicates the complete removal of toluene [6].

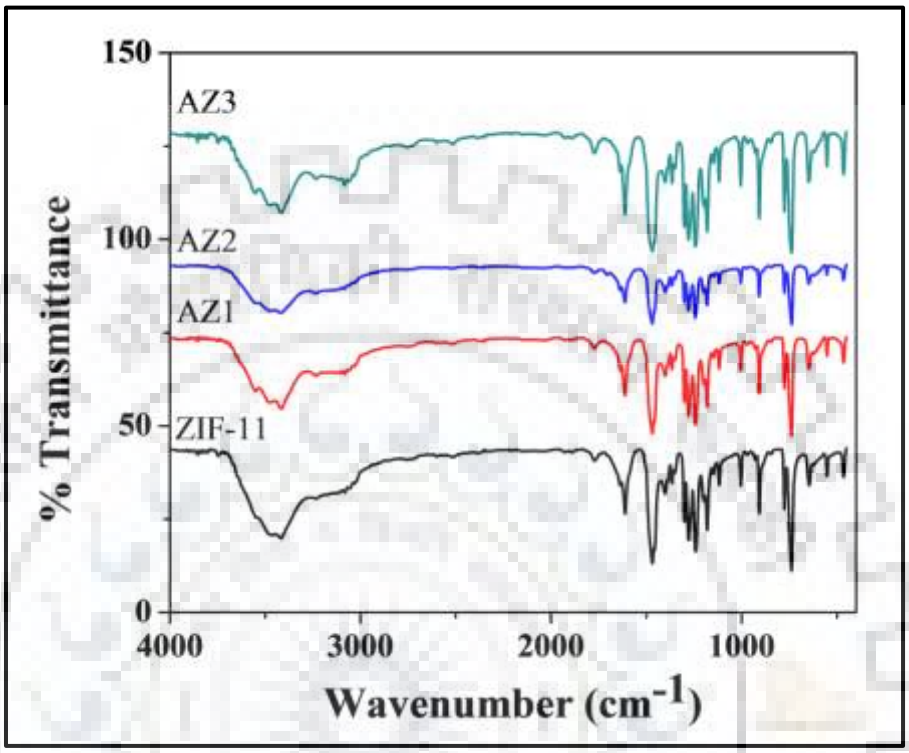

Fig. 5A.3. FT-IR spectra of ZIF-11 and its composites AZ1, AZ2 and AZ3.

5A.3.3. FE-SEM and HR-TEM Analysis

Fig. 5A.4 shows SEM images of nine products of ZIF-11. SEM image of Z-3 indicates the formation of ZIF-11 having rhombic dodecahedron (RHO) geometry. RHO topology of ZIF-11 and AZ1 composite has been examined by FE-SEM analysis (Fig. 5A.5(a-b)). It is apparently seen that encapsulation of AgNPs does not affect the topology of ZIF-11. FE-SEM mapping of C, N and Zn elements are illustrated in Fig. 5A.5(c-e) which ensured the elemental composition of ZIF-11. Further, the EDX analysis of AgNPs, ZIF-11 and their AgNPs@ZIF-11 composites have been performed which also ensured their elemental composition. The EDX results are tabulated in Table 5A.2 and spectra are given in Fig. 5A.6.

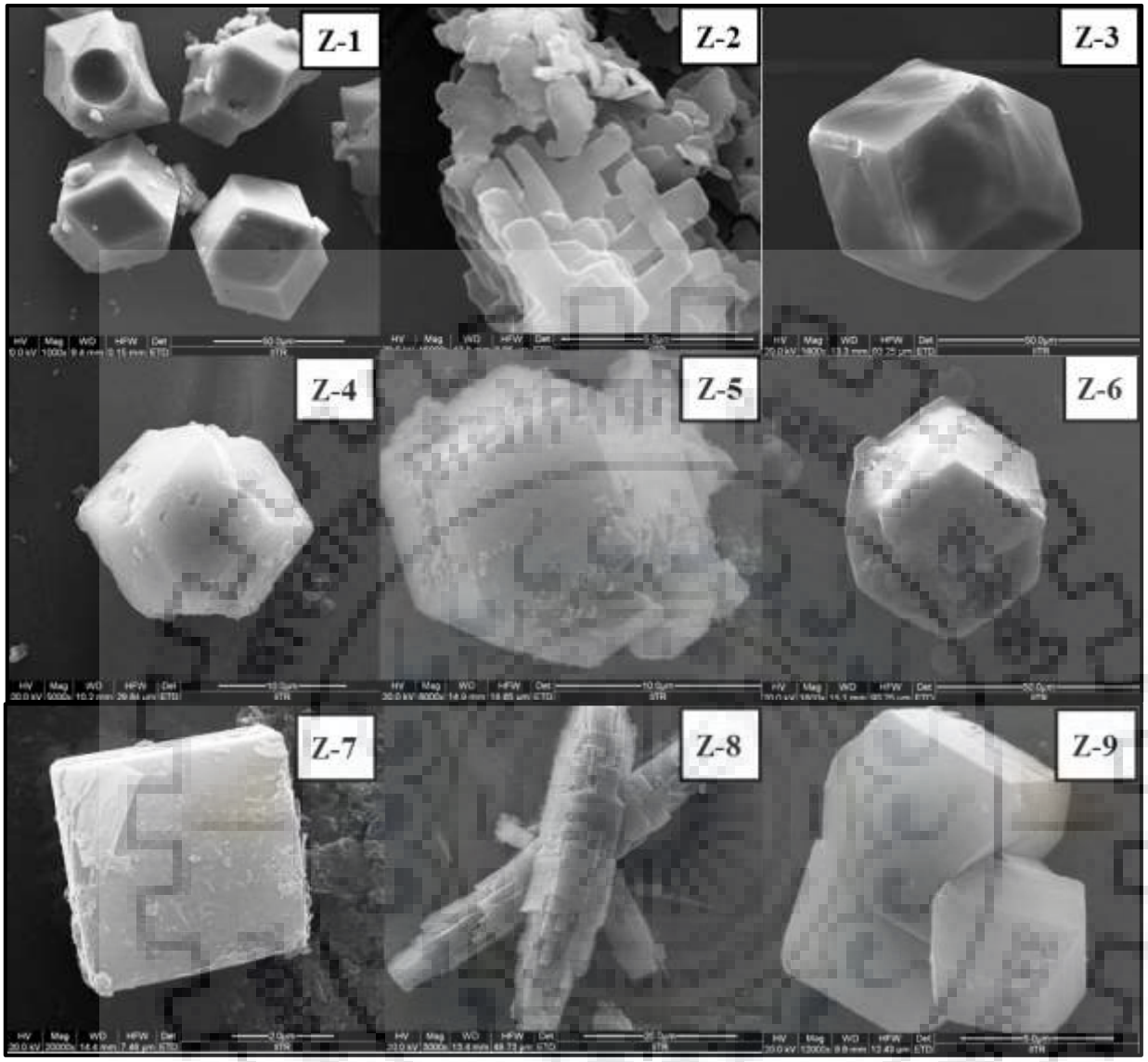

Fig. 5A.4. SEM analysis of ZIF-11 as synthesized by various conditions.

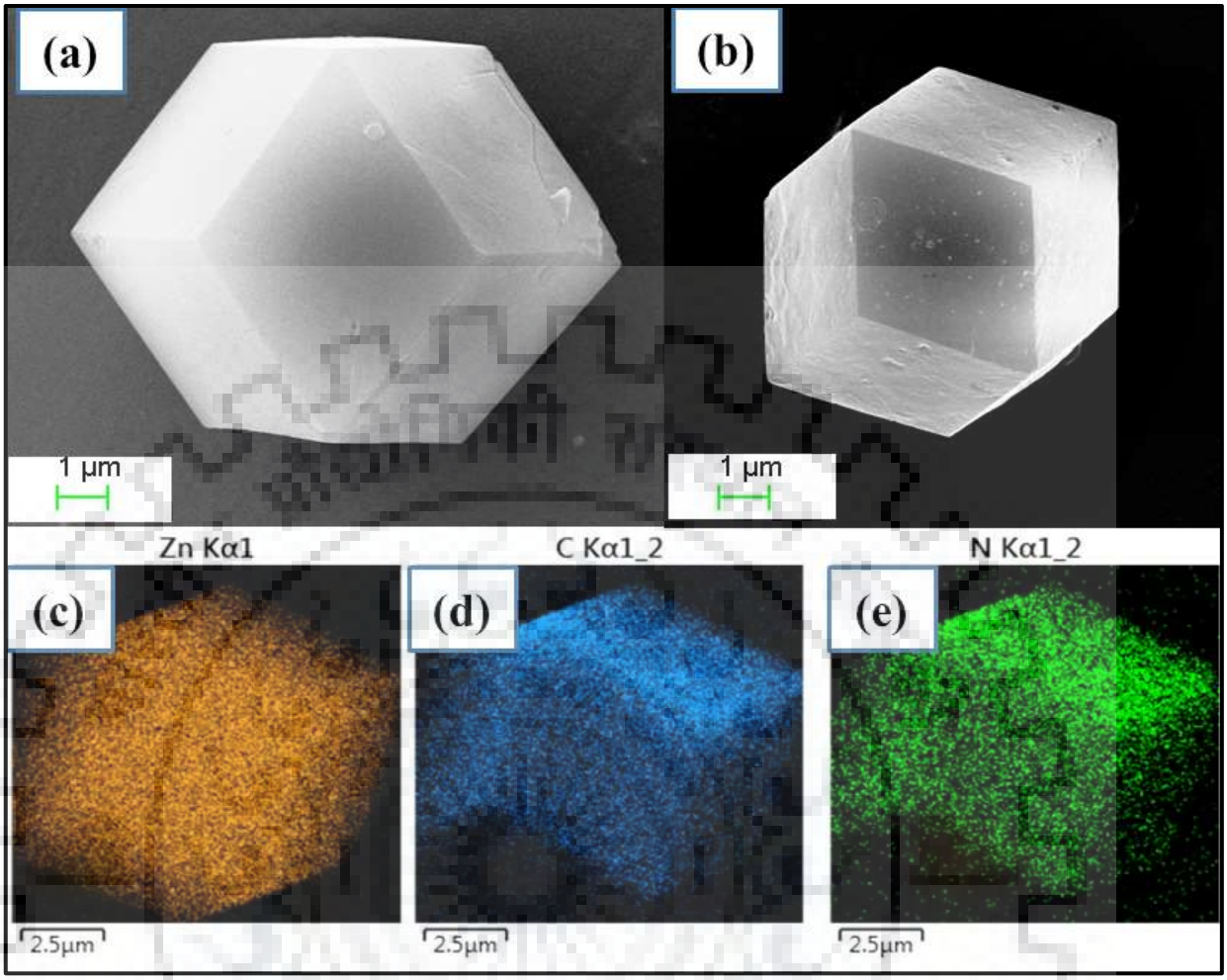

Fig. 5A.5 (a, b) FE-SEM images of ZIF-11 and AZ1 composite, respectively. Fig. 5A.5(c-e) represents the mapping of C, N and Zn elemental composition, respectively, of ZIF-11.

Table 5A.2: EDX analysis of Ag NPs, ZIF-11 and AgNPs@ZIF-11 composites.

S.N.	Materials	Atomic %			
		C	N	Zn	Ag
1.	ZIF-11	72.54	23.56	3.91	-
2.	AZ1	70.91	25.42	3.65	0.02
3.	AZ2	70.89	25.41	3.67	0.03
4.	AZ2	76.64	21.35	1.97	0.04
5.	AgNPs	-	-	-	100

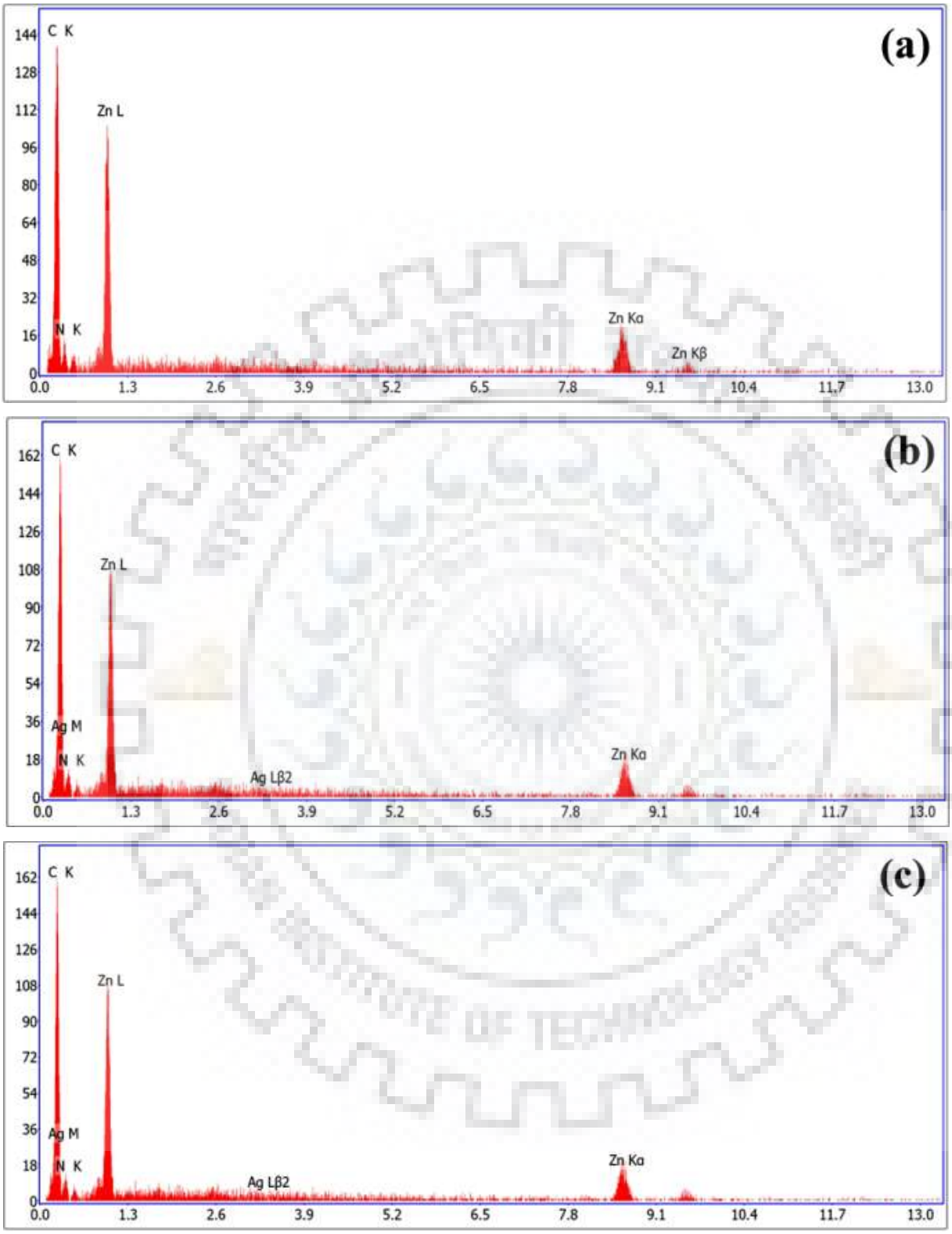
(a)
C K
Zn L
N K
Zn Kα
Zn Kβ
(b)
C K
Zn L
Ag M
N K
Ag Lβ2
Zn Kα
(c)
C K
Zn L
Ag M
N K
Ag Lβ2
Zn Kα

Continued

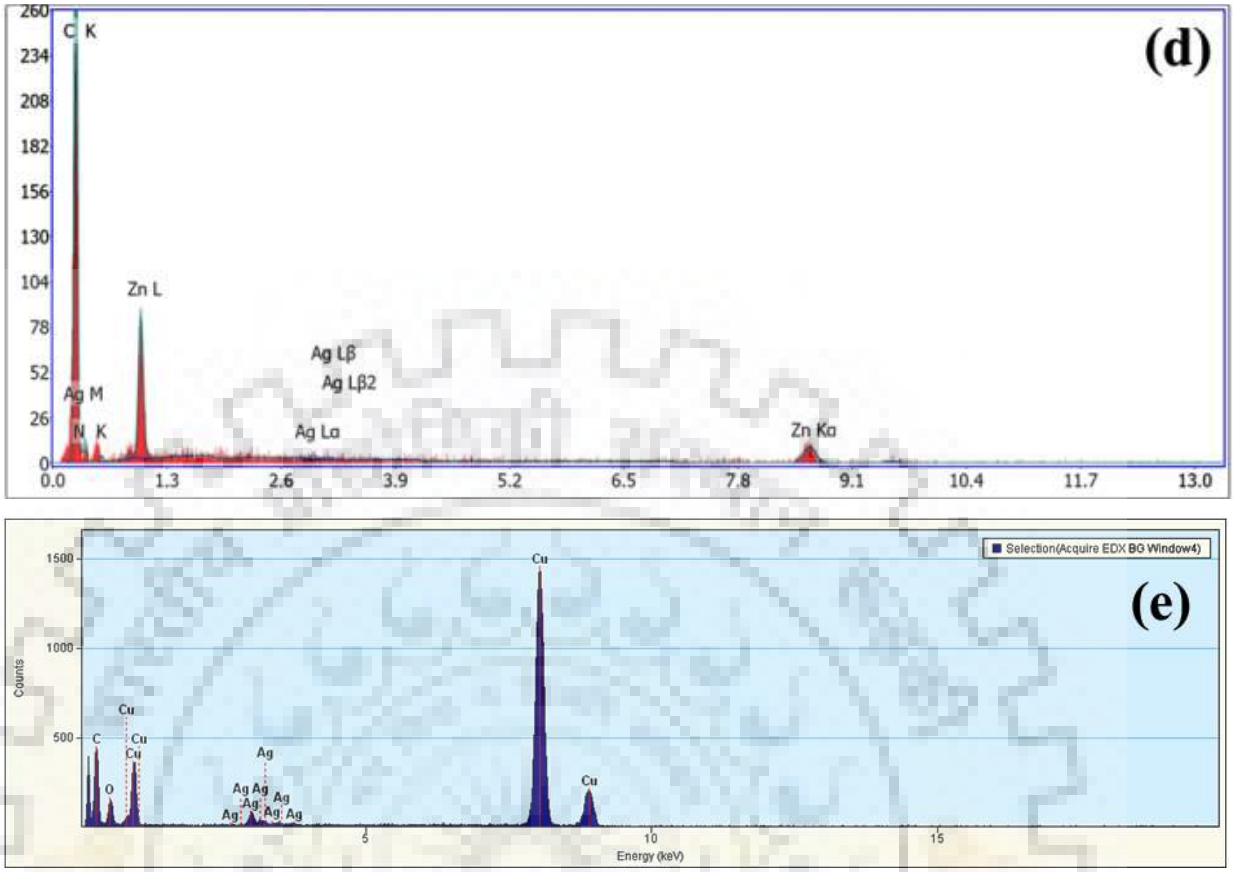

Fig. 5A.6. (a-e) The EDX spectra of ZIF-11, AZ1, AZ2, AZ3 and AgNPs, respectively.

Morphology and particle size of synthesized AgNPs were also studied by HR-TEM analysis (Fig. 5A.7(a)). The SEAD pattern of AgNPs indicates the polycrystalline nature (Fig. 5A.7(e)). Fig. 5A.7(b) shows the TEM images of ZIF-11 and Fig. 5A.7(c-d) reveals TEM images of AZ1 composite in increasing magnification order. TEM image of AZ1 composite depicts the definite encapsulation of AgNPs. The SEAD pattern (Fig. 5A.7(f)) of AZ1 composite also insured crystalline nature and the presence of AgNPs within AZ1 composite. The particle size of synthesized AgNPs varies between 5 to 25 nm while the particle size of the encapsulated AgNPs within ZIF-11 is found to be 11.76 ± 2.3 nm, determined by particle size distribution plot (Fig. 5A.8) with the help of *ImageJ* software.

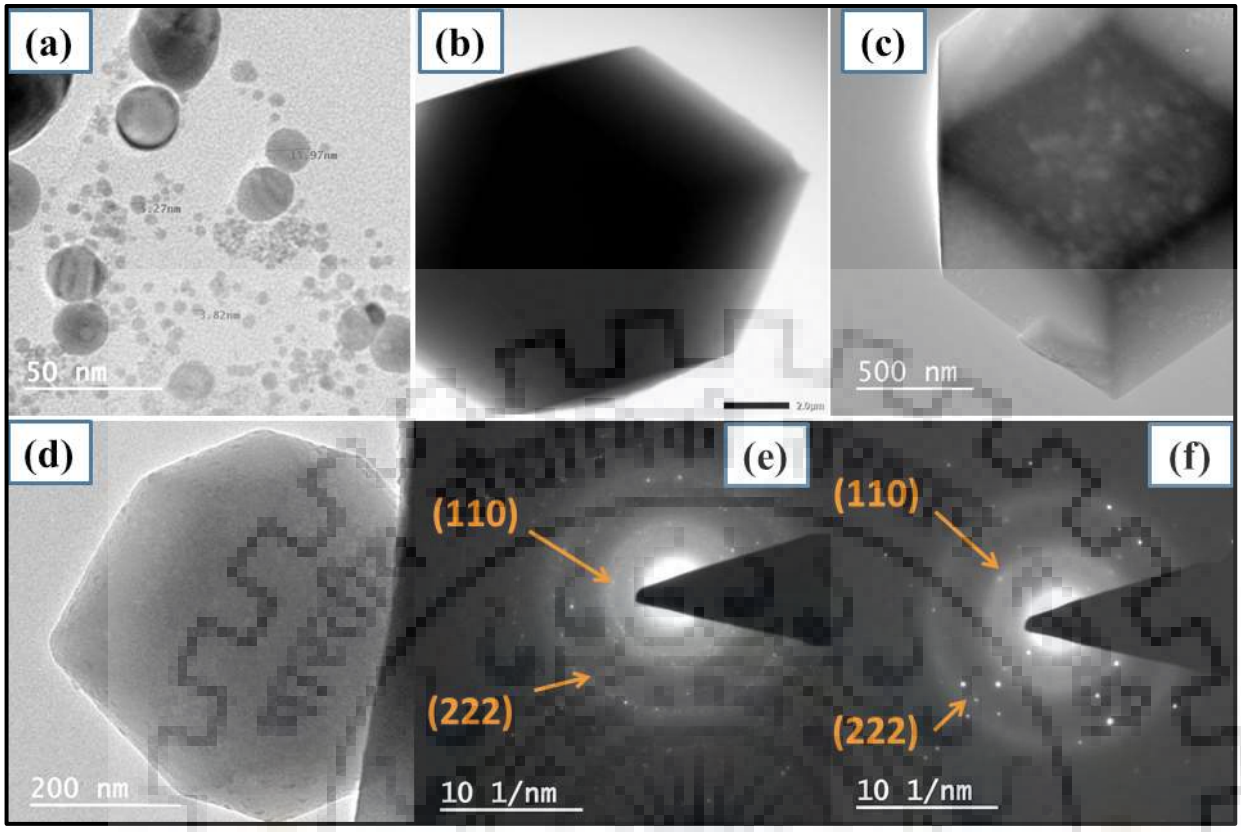

Fig. 5A.7. TEM image of (a) AgNPs, (b) ZIF-11, (c, d) AZ1 composite in order of increasing magnification, SEAD pattern of (e) AgNPs and (f) AZ1 composite, respectively.

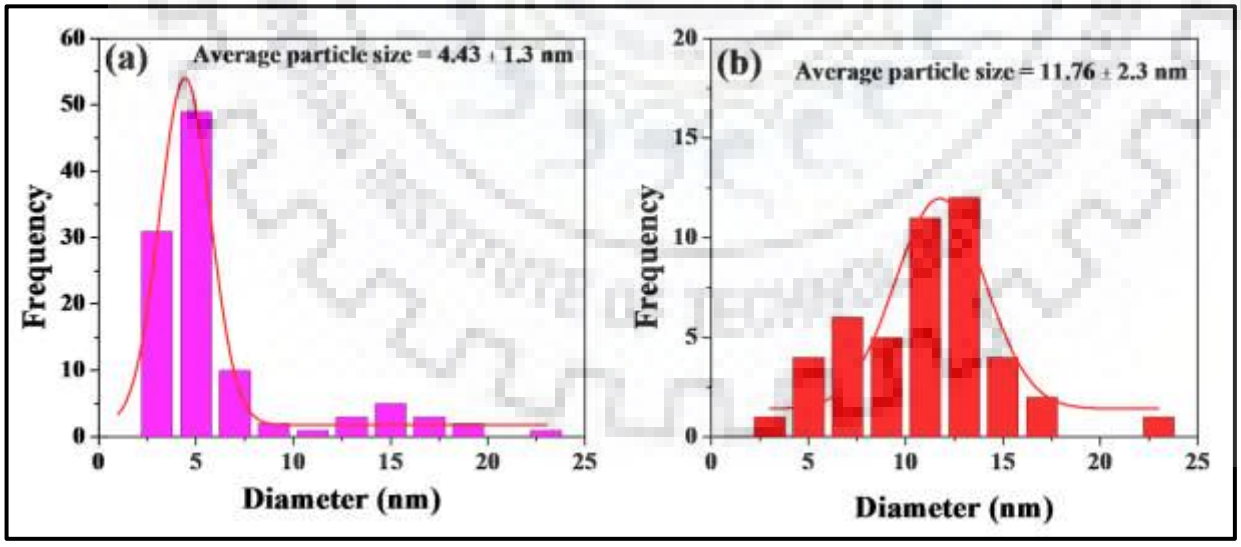

Fig. 5A.8. (a, b) Particle size distribution plots of AgNPs as synthesized and after encapsulation within ZIF-11, respectively.

5A.3.4. UV-DRS Studies

The optical behaviour of ZIF-11, AZ1, AZ2 and AZ3 has been studied by UV-DRS analysis. Typical UV-DRS spectra have been plotted using direct and indirect transitions by employing Tauc method [15]. The UV-DRS analysis shows the lowering of band gap of ZIF-11 due to incorporation of AgNPs from 4.36 eV to 4.21 eV (Fig. 5A.9(a)) for direct transitions and 4.18 eV to 4.05 eV (Fig. 5A.9(b)) for indirect transitions which indicates the presence of micro-environment of AgNPs within ZIF-11 frameworks.

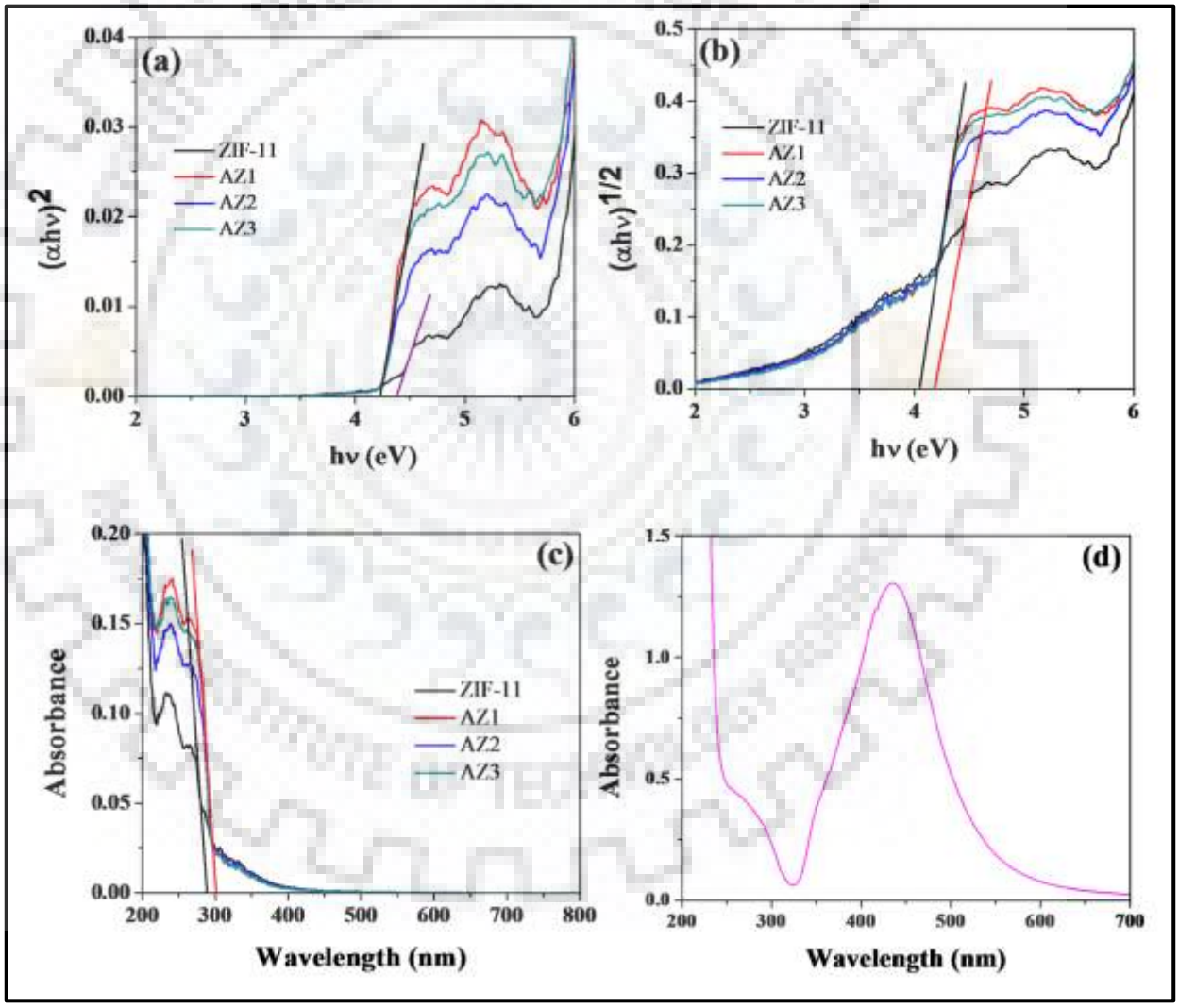

Fig. 5A.9. (a, b) Combined DRS spectra of ZIF-11, AZ1, AZ2 and AZ3 composites by direct and indirect transition method, respectively, and (c) UV-Visible absorbance spectra of ZIF-11 and composites AZ1, AZ2 AZ3. Fig. 5A.9(d) UV-Visible absorbance spectra of synthesized AgNPs suspension.

Absorbance spectra also show the red shift (Fig. 5A.9(c)) which indicates the micro-environment of AgNPs within ZIF-11 frameworks. The UV-visible absorption spectrum of AgNPs exhibits a sharp band at 435 nm and a broad band at 280 nm due to SPR (Fig. 5A.9(d)).

5A.3.5. BET Surface Area Analysis

Porosity of ZIF-11 and its composites has been examined by N_2 sorption isotherms at 77K and Brunauer-Emmett-Teller (BET) sorption isotherms were indexed with pore size distribution plot as shown in Fig. 5A.10. However, the results are tabulated in Table 5A.3. This measurement exhibits the surface area of ZIF-11 *i.e.* ≈ 392 $m^2 g^{-1}$ according to BET model and 869 $m^2 g^{-1}$ according to Langmuir model which is much better as compared to recently reported [6]. It has also been observed that surface area of composites is decreased on increasing the dosing amount, because the voids of ZIF-11 are occupied by doped AgNPs.

5A.3.6. XPS Analysis

The surface profile of AgNPs, ZIF-11 and AZ1 composite was analysed by X-ray photoelectron spectroscopy (XPS). Fig. 5A.11 illustrates the survey scan of AgNPs (Fig. 5A.11(a)) and expended XPS spectrum of Ag 3d orbital (Fig. 5A.11(b)) with two major peaks having binding energy 373.08 eV and 367.08 eV which are ascribed to $3d_{3/2}$ and $3d_{5/2}$, respectively. The spin orbit coupling was calculated *ca.* 6.0 eV which is the evidence of Ag^+ reduction into Ag^0 [16]. The loss features were also observed at higher binding energy of splitting between $3d_{3/2}$ and $3d_{5/2}$ which indicates the metallic nature of AgNPs. In case of composites, binding energy of Ag 3d orbital slightly deviates due to short interaction of metal-ligand moiety of ZIF-11. The XPS survey scan of ZIF-11, AZ1, AZ2 and AZ3 composites are shown in Fig. 5A.12(a), Fig. 5A.13(a), 5A.14(a) and 5A.15(a), respectively. Zn 2p expanded XPS spectra of ZIF-11 have two major and sharp peaks at 1045.02 eV and 1021.81 eV due to $2p_{1/2}$ and $2p_{3/2}$ (Fig. 5A.12(b)). Similarly, Zn 2p expanded XPS spectra of composites AZ1, AZ2 and AZ3 are given Fig. 5A.13(b), 5A.14(b) and 5A.15(b), respectively, and the corresponding binding energy is tabulated in Table 5A.4.

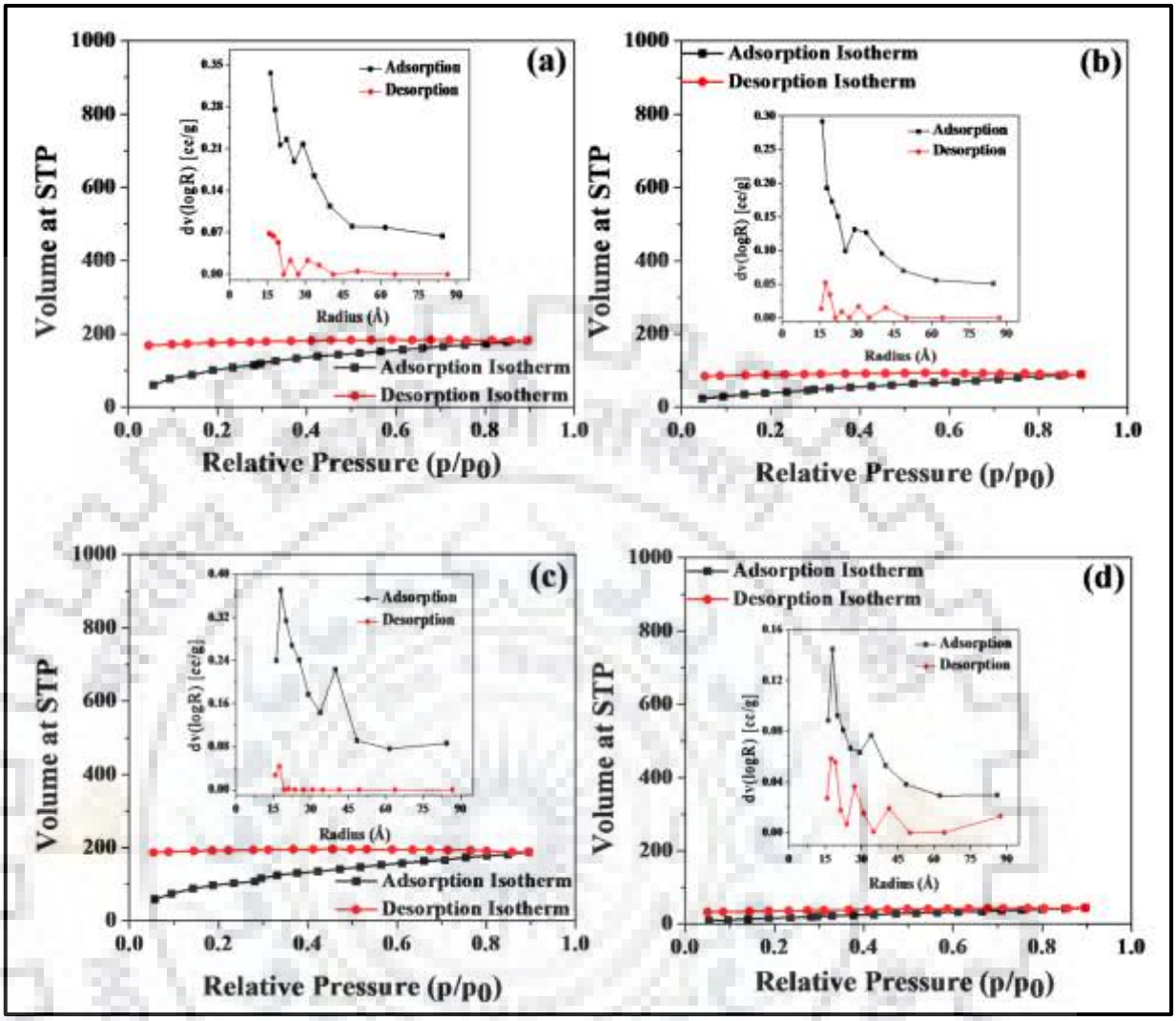

Fig. 5A.10. (a-d) BET adsorption-desorption isotherm indexed with pore size distribution plot of ZIF-11 and its composite AZ1, AZ2 and AZ3, respectively.

Table 5A.3: Textural properties of ZIF-11 and its composites (AZ1, AZ2 and AZ3).

S.N.	Materials	S_{BET} (m^2g^{-1})	$S_{Langmuir}$ (m^2g^{-1})	Pore Vol. (ccg^{-1})	Average Pore radius (Å)
1.	ZIF-11	393	869	2.815×10^{-1}	36.13
2.	AZ1	210	451	1.391×10^{-1}	36.29
3.	AZ2	374	908	2.907×10^{-1}	36.02
4.	AZ3	69	236	6.794×10^{-2}	37.41

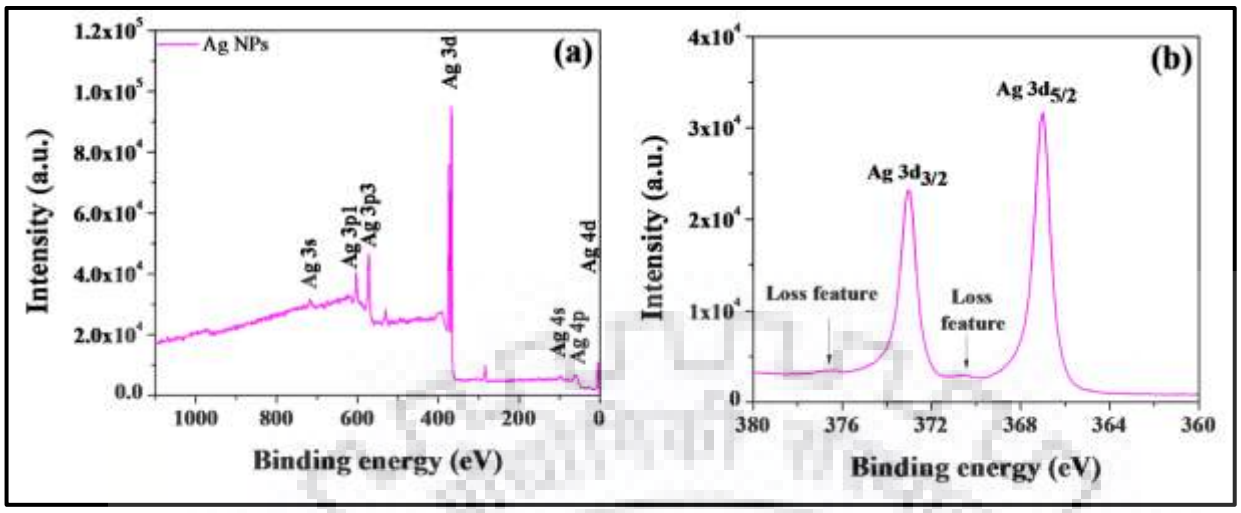

Fig. 5A.11. (a, b) Survey scan and expanded XPS spectra of Ag 3d of AgNPs.

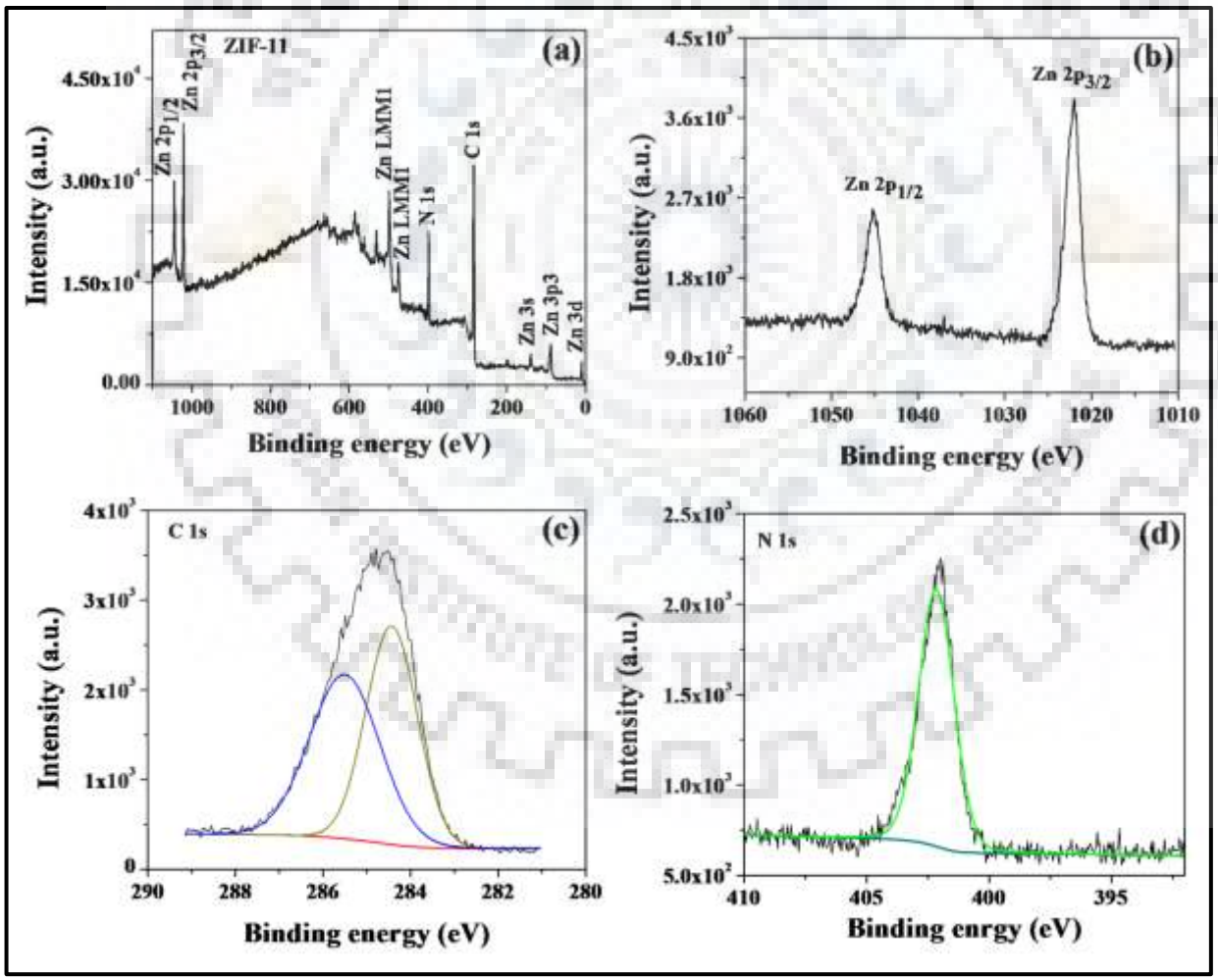

Fig. 5A.12. (a-d) Survey scan and expanded XPS spectra of Zn 2p, C 1s and N 1s of ZIF-11 are shown as (a), (b), (c) and (d), respectively.

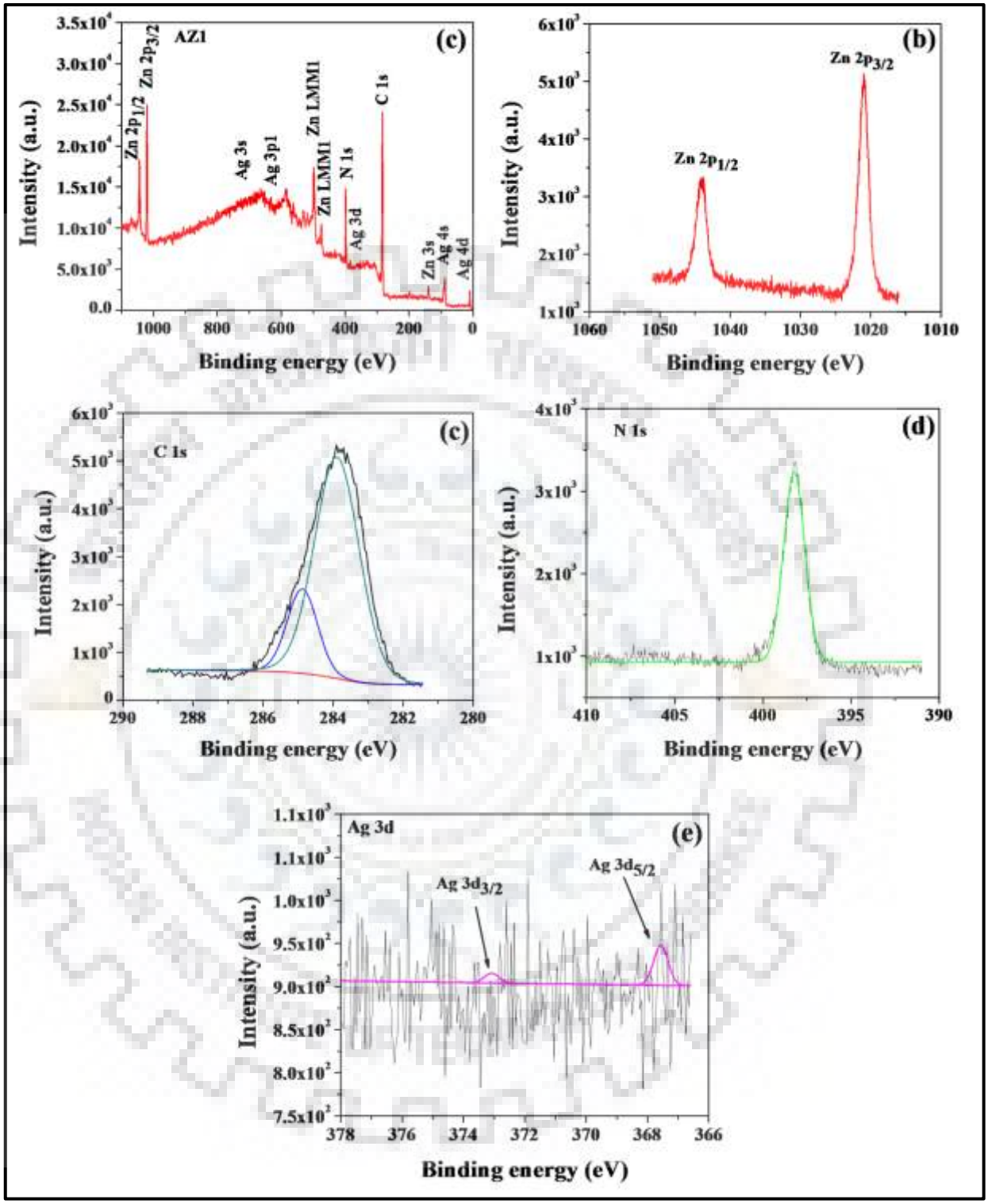

Fig. 5A.13. (a-e) Survey scan and expanded XPS spectra of Zn 2p, C 1s, N 1s and Ag 3d of AZ1 are shown as (a), (b), (c), (d) and (e), respectively.

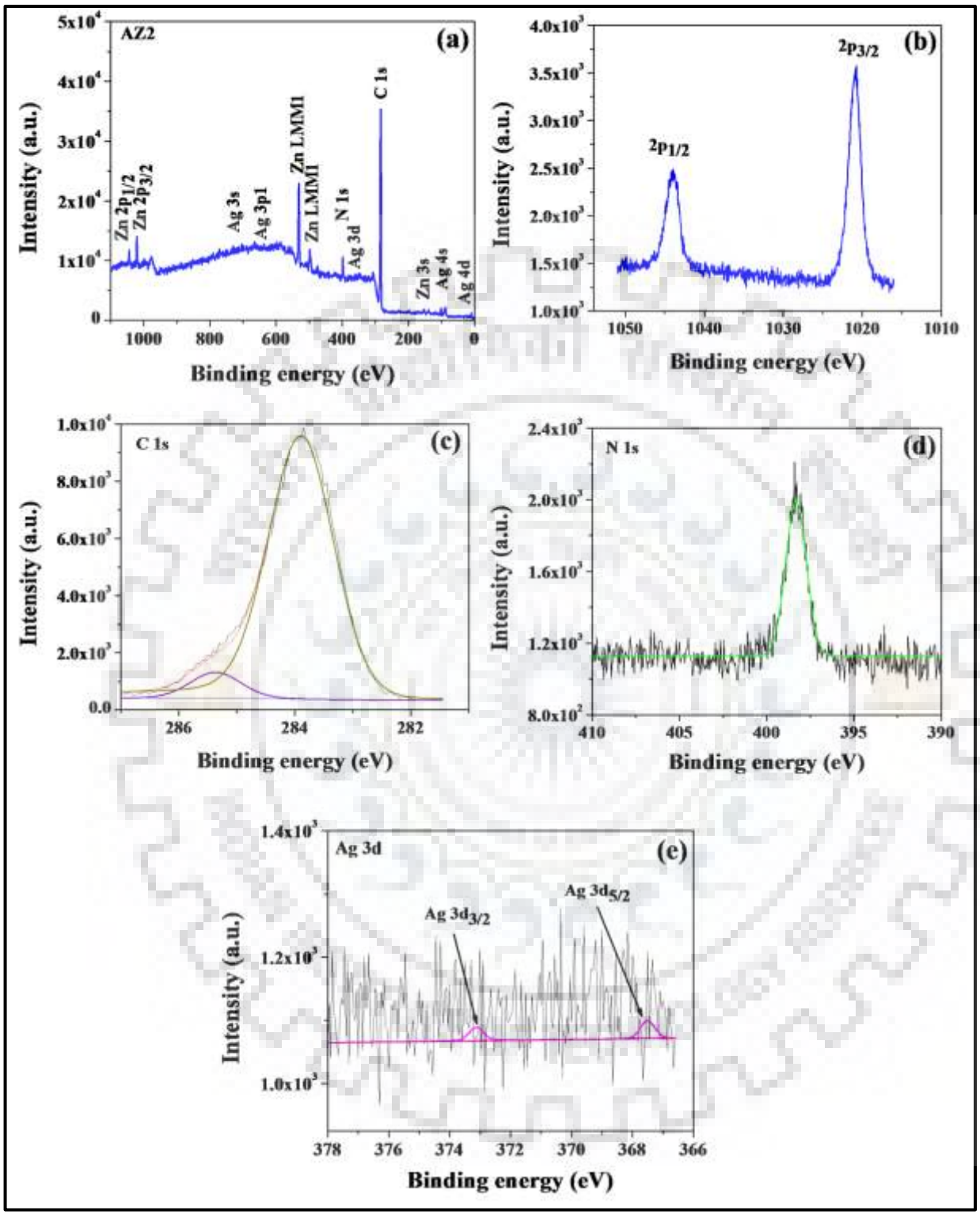

Fig. 5A.14. (a-e) Survey scan and expanded XPS spectra of Zn 2p, C 1s, N 1s and Ag 3d of AZ2 are shown as (a), (b), (c), (d) and (e), respectively.

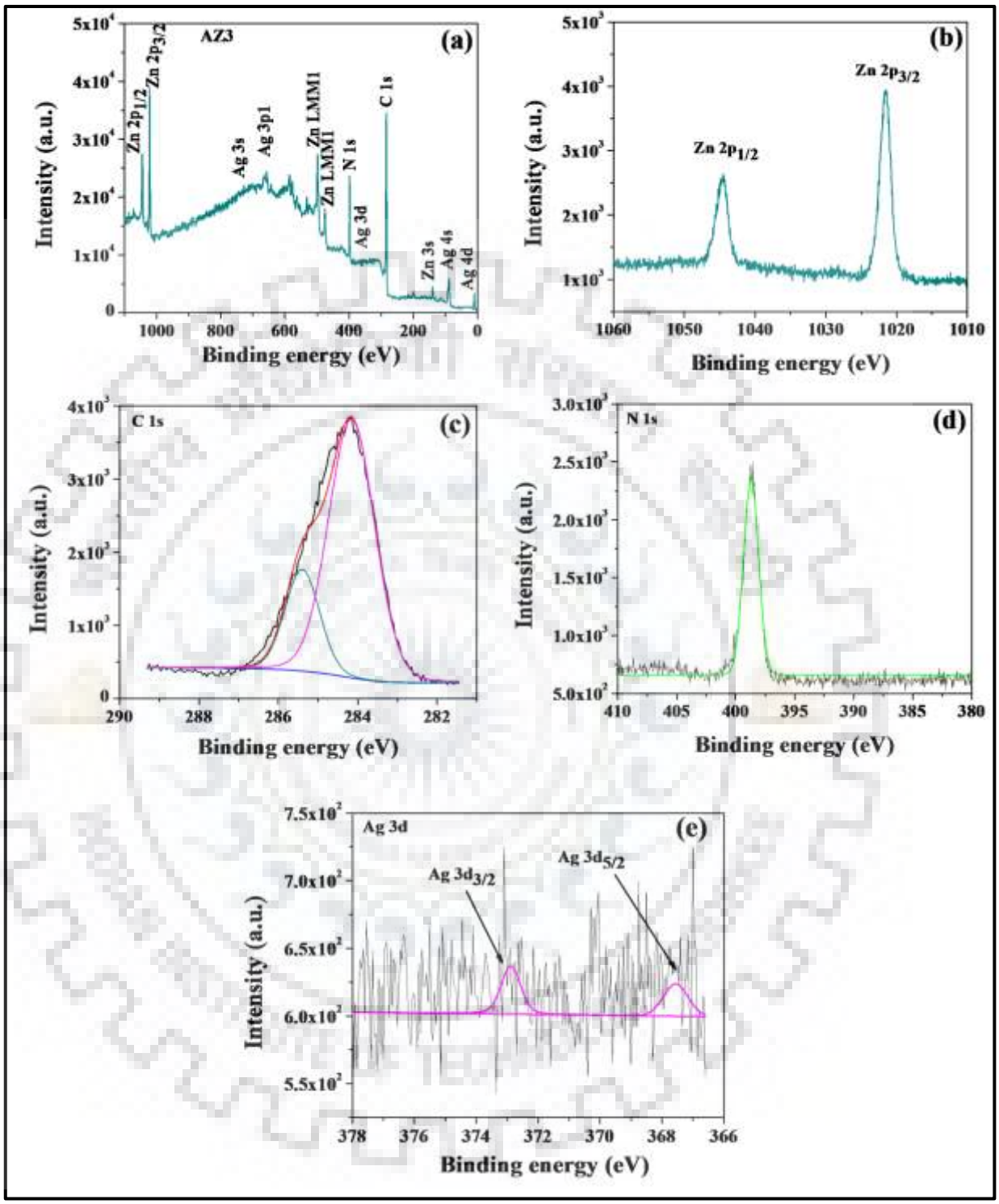

Fig. 5A.15. (a-e) Survey scan and expanded XPS spectra of Zn 2p, C 1s, N 1s and Ag 3d of AZ3 are shown as (a), (b), (c), (d) and (e), respectively.

Table 5A.4. XPS analysis of AgNPs, ZIF-11 and their composites.

S.N.	Materials	Atom/Element	State/Term	Binding energy (eV)
1.	AgNPs	Ag	$3d_{3/2}$	373.08
			$3d_{5/2}$	367.05
2.	ZIF-11	Zn	$2p_{1/2}$	1045.02
			$2p_{3/2}$	1021.81
		C	1s	285.52
				284.45
		N	1s	398.77
3.	AZ1	Zn	$2p_{1/2}$	1044.17
			$2p_{3/2}$	1021.04
		Ag	$3d_{3/2}$	373.07
			$3d_{5/2}$	367.56
		C	1s	285.41
				284.17
		N	1s	398.22
4.	AZ2	Zn	$2p_{1/2}$	1044.10
			$2p_{3/2}$	1021.13
		Ag	$3d_{3/2}$	373.13
			$3d_{5/2}$	367.51
		C	1s	285.38
				283.90
		N	1s	398.30
5.	AZ3	Zn	$2p_{1/2}$	1044.67
			$2p_{3/2}$	1021.55
		Ag	$3d_{3/2}$	372.88
			$3d_{5/2}$	367.56
		C	1s	285.39
				284.18
		N	1s	398.68

The deconvolution of C 1s of ZIF-11 involves two peaks at higher binding energy (285.52 eV) due to sp^2C-N and at lower binding energy (284.45 eV) due sp^2C-C interaction [17]. Similar pattern is also observed in composites AZ1, AZ2 and AZ3, the XPS spectra of C 1s of ZIF-11 and all three composites (AZ1, AZ2 and AZ3) are given in Fig. 5A.12(c), 5A.13(c), 5A.14(c) and 5A.15(c), respectively. The XPS spectra of N 1s of ZIF-11 (-N= B.E. 398.77 eV) and its composites (-N= B.E. 398.22 eV for AZ1, 398.30 eV for AZ2 and 398.68 eV for AZ3) are given in Fig. 5A.12(d), 5A.13(d), 5A.14(d) and 5A.15(d), respectively, which suggests the similar environment of nitrogen in ZIF-11 and all three composites [4]. Expanded XPS spectra of Ag 3d of all three composites are also depicted in Fig. 5A.13(e), 5A.14(e) and 5A.15(3), respectively, and the results are given in the Table 5A.4.

5A.3.7. Thermal Analysis

Thermal stability of ZIF-11, AZ1, AZ2 and AZ3 composites has been examined by thermal gravimetric analysis (TGA) under air/N_2 atmosphere. TGA plot of ZIF-11 and AgNPs@ZIF-11 composites are shown in Fig. 5A.16(a, b) under air and N_2 atmosphere, respectively. It is found that ZIF-11 and composite are highly stable up to 500 °C and above 500 °C they have started to decompose under both the environments.

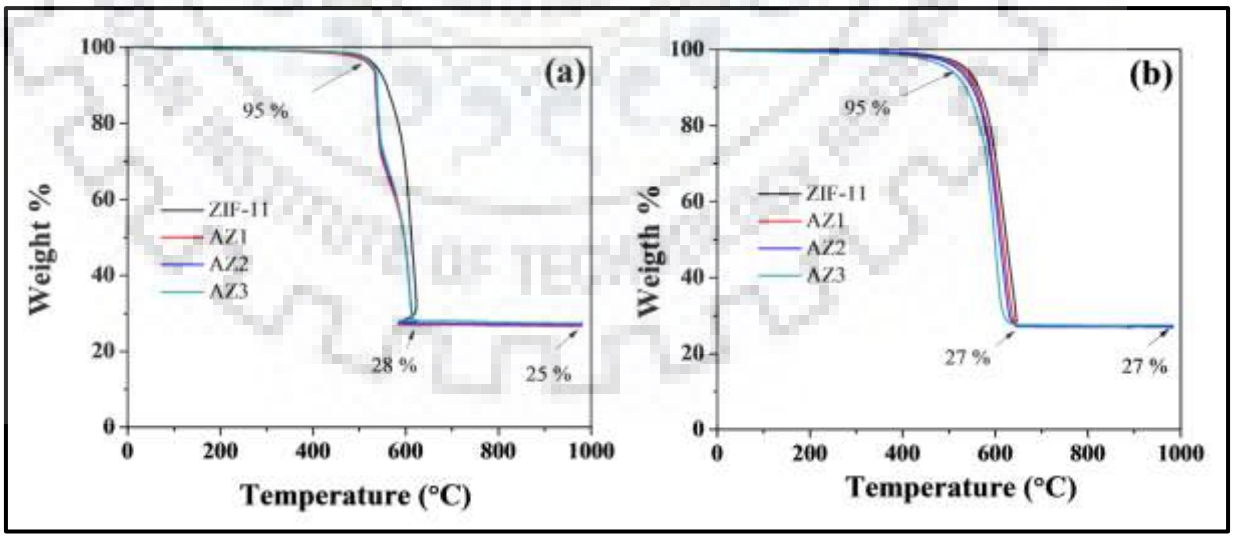

Fig. 5A.16. (a, b) TGA analysis of ZIF-11 and AgNPs@ZIF-11 composites (AZ1, AZ2 and AZ3) under air and N_2 atmosphere, respectively.

5A.3.8. Adsorption and Photocatalytic Degradation Studies of Methylene Blue (MB) Dye Using AgNPs@ZIF-11 Composites

Adsorption and photocatalytic degradation activity of ZIF-11 and AgNPs@ZIF-11 composites were investigated by observing the photocatalytic degradation of MB as model dye with the help of UV-visible spectrophotometer under UV-visible light irradiation as energy source (50 Watt halogen lamp). The details of adsorption and photodegradation factors such as dosing amount of AgNPs, amount of catalysts and concentration of dye solution have been discussed. The similar method has been employed as mentioned in Chapter two.

5A.3.8.1. Effect of Encapsulation Amount of AgNPs

In order to examine the optimum amount of encapsulation, it is found that all three composites (AZ1, AZ2 and AZ3 composite) exhibit enhanced photocatalytic activity as compared to ZIF-11. Before examine the photocatalytic activity of composites, the adsorption capacity of all three composites have been examined. The results of adsorption capacity and photodegradation efficiency are tabulated in Table 5A.5 and C/C_0 *vs* time plots are shown in Fig. 5A.17. It is found that AZ1, AZ2 and AZ3 composite can remove/adsorb 80.62%, 58.75% and 37.50% MB dye solution, respectively. On exposure to UV-visible irradiation after attaining adsorption-desorption equilibrium, the colour of MB dye completely disappeared (100% degradation) by all three composites in 120 minutes; 100% degradation was achieved in 40 min with AZ1, and in 60 min with AZ2. This may be due to the increase in agglomeration of AgNPs with increasing the dosing amount of AgNPs; at higher concentration the collisional deactivation may also decrease degradation rate. AZ1 composite was selected for further studies due to its maximum photocatalytic efficiency.

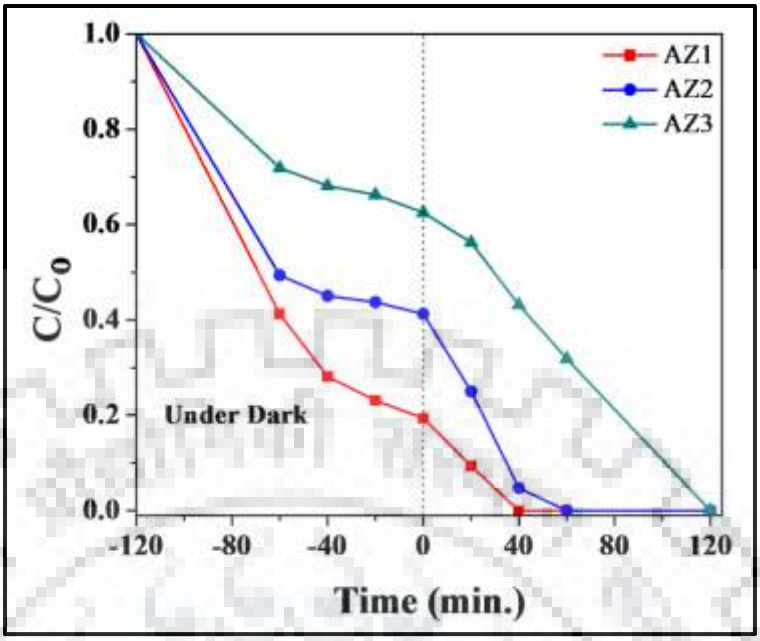

Fig. 5A.17. Effect of encapsulation amount of AgNPs suspensions within ZIF-11 framework for adsorption and photodegradation of [MB] = 1.64 mg L^{-1}; pH = 8.35; photocatalyst's amount = 10 mg (0.5 g L^{-1}).

Table 5A.5: Effect of dosing amount of AgNPs suspension, catalyst amount = 10 mg; at pH = 8.35; [MB] = 1.6 mg L^{-1}.

S.N.	Dosing amount of AgNPs suspensions in µL	Adsorption capacity [% Dye removal]	% Photodegradation
1.	150 (AZ1)	2.58 [80.62]	100
2.	300 (AZ2)	1.88 [58.75]	100
3.	500 (AZ3)	1.20 [37.50]	100

5A.3.8.2. Effect of Photocatalyst's Amount

The effective amount of catalysts was checked by varying the amount of ZIF-11 and AZ1 composite *i.e.* 5 mg, 10 mg and 15 mg. The results are tabulated in Table 5A.5 and C/C_0 *vs* time plots shown in Fig. 5A.18. It is observed that ZIF-11 degrades off 73.75, 86.25 and 95.62% in 120 min while AZ1 degrades off 84.37 (120 min), 100% (40 min) and 100% (40 min) MB with 5 mg, 10 mg and 15 mg amount of catalyst, respectively. So, 10 mg of ZIF-11 and AZ1 composite was taken to study the effect of MB dye concentration, and ZIF-11 is more than 30 % less effective than composite AZ1.

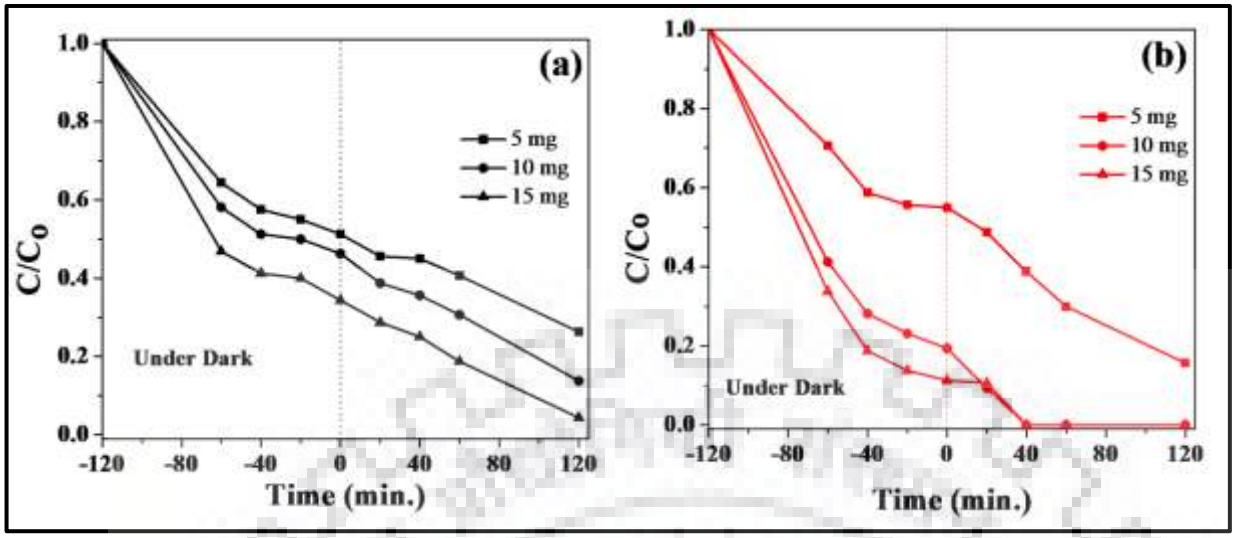

Fig. 5A.18. Effect of photocatalyst's amount for adosrption and photodegradation of [MB] = 1.6 mg L^{-1} at pH = 8.35.

Table 5A.6: Effect of photocatalysts amount (ZIF-11 and AZ1), [MB] = 1.6 mg L^{-1}; at pH = 8.35.

S.N.	Amount (mg)	Adsorption capacity (mg/g) [%dye removal]		% Photodegradation	
		ZIF-11	AZ1	ZIF-11	AZ1
1.	5	3.12 [48.75]	2.88 [45.00]	73.75	84.37
2.	10	1.72 [53.75]	2.58 [80.62]	86.25	100
3.	15	1.40 [65.62]	1.89 [88.75]	95.62	100

5A.3.8.3. Effect of Initial Dye Concentration

The effect of initial dye concentration has been examined for optimizing the maximum efficiency of photocatalysts at the optimum concentration of MB dye solution to be degraded by using 10 mg of ZIF-11 and AZ1. Therefore, the photocatalytic activity experiments at different MB dye concentration (*i.e.* 0.5×10^{-5}, 1×10^{-5} and 2×10^{-5} M solutions) were performed using ZIF-11, AZ1 composite and equivalent amount of AgNPs suspension (150 µL) encapsulated within AZ1 composite. The outcomes of this set of experiments are compiled in Table 5A.7 and C/C_0 *vs* time plots are illustrated in Fig. 5A.19.

Table 5A.7: Effect of concentration of MB dye solution at pH = 8.35; Photocatalysts amount = 10 mg.

Conc. of dye ($mg\ L^{-1}$)	Adsorption capacity (mg/g) [% dye removal]			% Photodegradation			
	ZIF-11	AZ1	AgNPs	Pure MB	ZIF-11	AZ1	AgNPs
1.6	1.72 [53.75]	2.58 [80.62]	0.25 [7.75]	22.75	86.25	100	45.87
3.19	1.48 [23.19]	4.64 [72.78]	0.34 [5.42]	21.63	49.52	100	36.01
6.38	1.72 [13.47]	6.47 [50.73]	0.53 [4.13]	14.10	26.01	80.79	26.89

It is firmly proved that with increasing the concentration of MB dye solutions, the adsorption and photodegradation efficiency of ZIF-11, AgNPs and MB itself decreases while AZ1 composite exhibits same photodegradation (100%) efficiency up to 1×10^{-5} M (3.19 mg L^{-1}) *i.e.* 100% and at 2×10^{-5} M (6.38 mg L^{-1}) concentration, it can degrade off 80.79% MB dye solution. This is because at higher concentration of dye solution around the active sites on photocatalyst resulted in inhibiting the penetration of light to the surface of the photocatalyst. Therefore, the generation of relative amount of $^{\bullet}OH$ and $^{\bullet}O_2^-$ on the surface of photocatalyst decreased with same intensity of light and irradiation times.

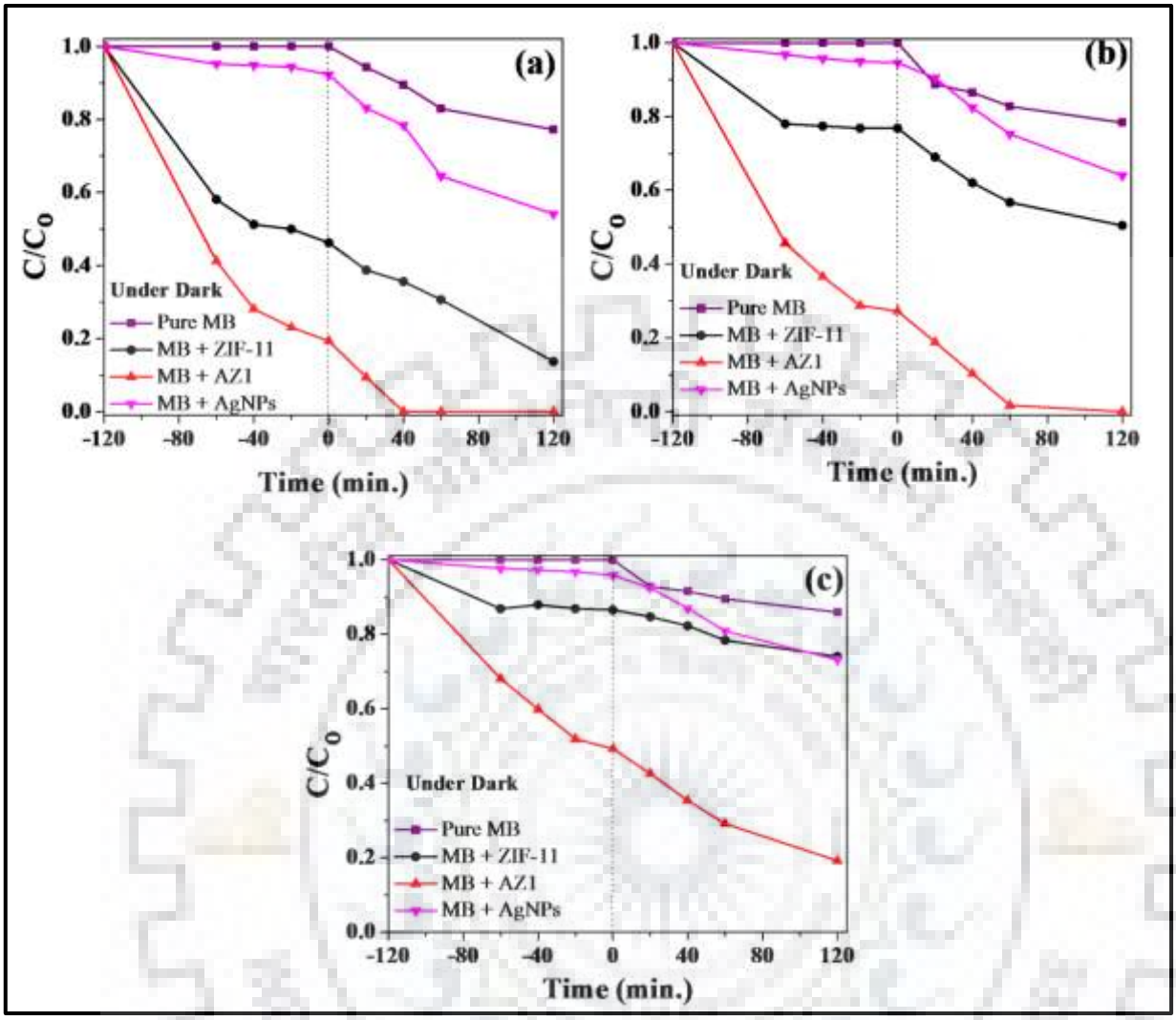

Fig. 5A.19. Effect of initial dye concentration for adsorption and photodegradation of [MB] (a) 1.6 mg L^{-1}; (b) 3.19 mg L^{-1}; (c) 6.38 mg L^{-1} at pH = 8.35; Photocatalyst's amount = 10 mg.

5A.3.8.4. Recyclability Test

The capacious achievement of AZ1 composite is its reusability and recyclability. The recyclability test has been examined at lower concentration of MB dye (photocatalyst's amount = 10 mg; [MB] = 1.6 mg L^{-1} and time length 120 min) solution at pH 8.35. The AZ1 composite exhibits the maximum efficiency (100%) up to three cycle while under fourth and fifth cycle, it can degrade off 92.12% and 72.75% MB, respectively, which is shown in Fig. 5A.20.

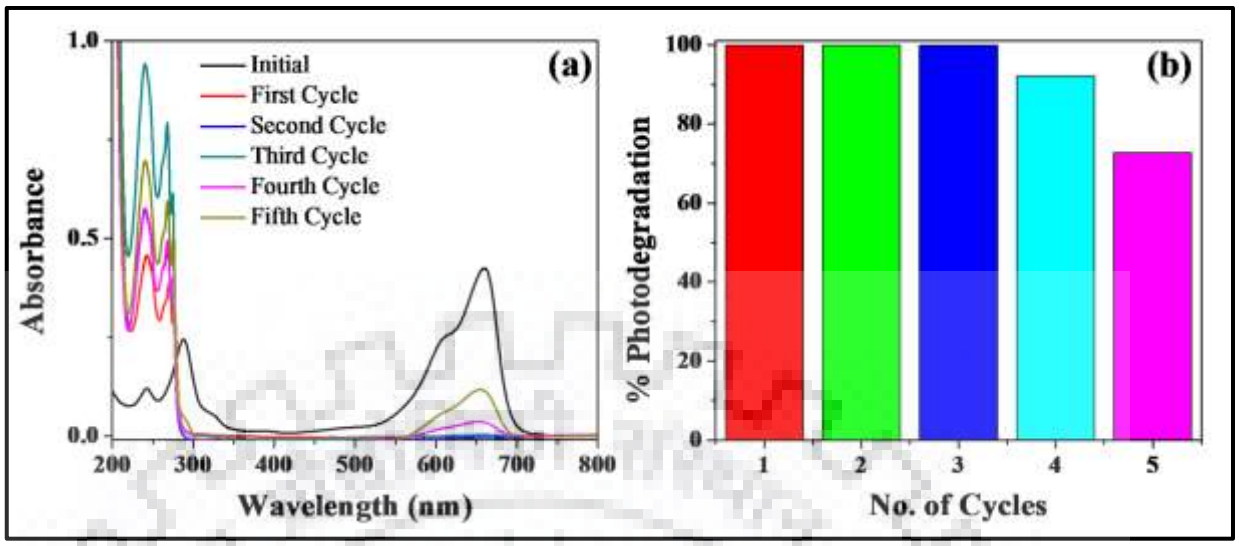

Fig. 5A.20. (a, b) UV-visible absorbance spectra under UV-visible irradiation of MB with AZ1 and pictorial graph for its recyclability test are illustrated respectively.

5A.3.9. Scavenger Analysis

The role of active species for the degradation of MB has been concluded with the help of scavenger analysis. The details of experimental conditions are already explained in the previous Chapter four and the effect of scavengers (ethylenediaminetetra acetic acid (EDTA), *p*-benzoquinone (BQ) and *tertiary* butyl alcohol (*t*-BuOH) are used as h^+, $O_2^{\bullet-}$, and $^{\bullet}OH$ scavenger) on photodegradation is shown in Fig. 5A.21. The scavenger analysis proves that h^+ and $^{\bullet}OH$ radicals play an important role for the degradation of MB dye using AZ1 composite because degradation efficiency decreased significantly with EDTA and *t*-BuOH while no significant change was observed with BQ.

5A.3.10. Plausible Degradation Mechanism

Fig. 5A.22 illustrates the photodegradation mechanism of MB dye using AZ1 composite under UV-visible light source (50 Watt halogen lamp). Black solid line indicates the energy gap (E_g) of ZIF-11 while yellow dashed line indicates the decreased energy gap (E_g') of AZ1 composite due to fabrication of AgNPs within ZIF-11 frameworks. Photocatalytic degradation of MB dye occurs as a result of HOMO-LUMO charge transfer in case of pure ZIF-11 similarly to that in ZIF-8 [18]. In case of AZ1 composite, the separation between valence band (VB) and conduction band (CB) decreased as a result of AgNPs encapsulation within ZIF-11 framework. The photo-

induced e^- and h^+ can easily react with oxygenated water and produce reactive oxidative species (ROS) which is responsible for photocatalytic degradation of MB dye.

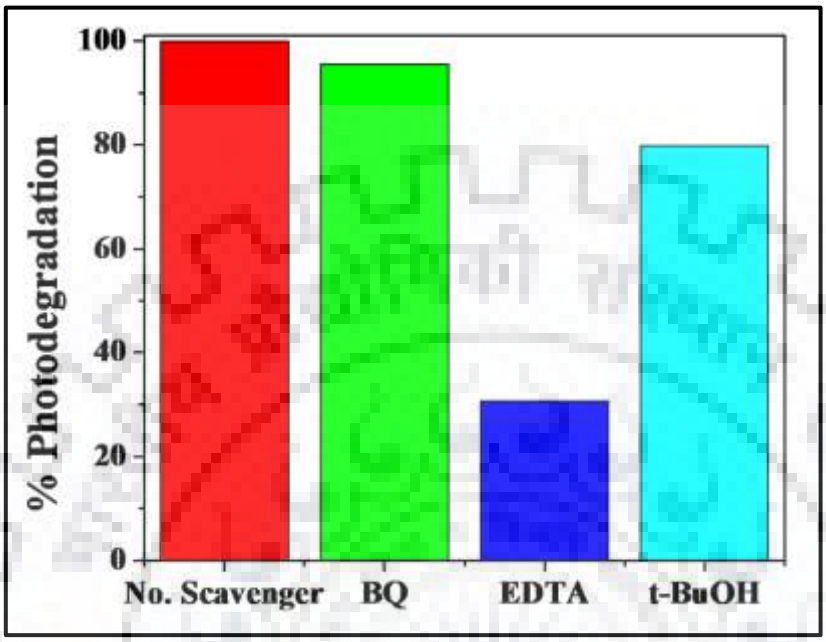

Fig. 5A.21. Effect of scavengers (BQ, EDTA, *t*-BuOH,) on photocatalytic degradation of MB using AZ1 composite under UV-visible irradiation.

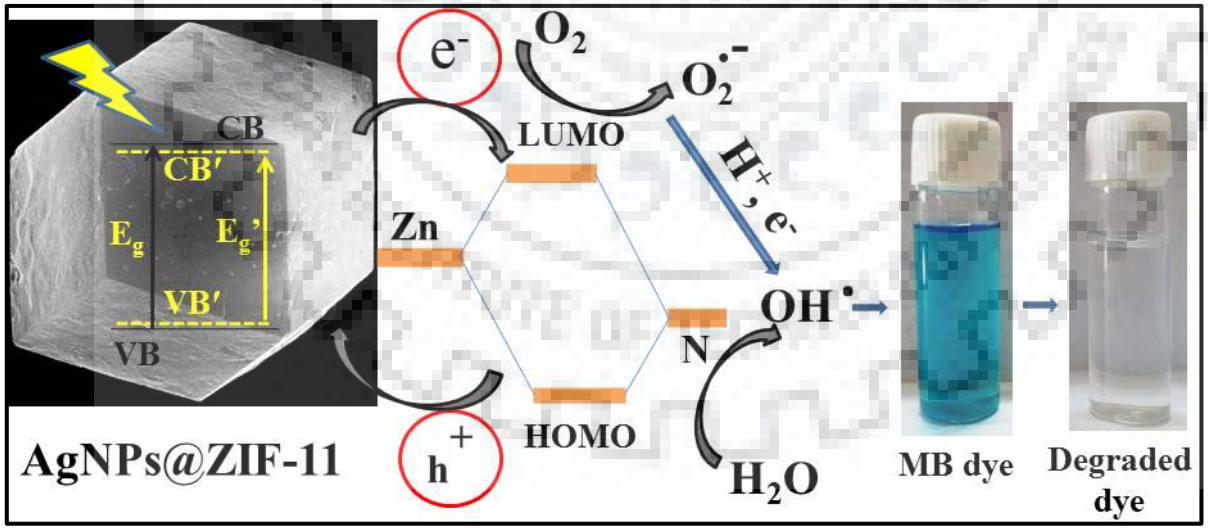

Fig. 5A.22. Illustration of proposed mechanism for MB degradation using AgNPs@ZIF-11 composite under UV-visible light.

5A.3.11. GC-MS Analysis

The degraded by-products of MB were analyzed by GC-MS analysis. The plausible fragments and their mass spectra are provided in Fig. 5A.23. The MB molecules break into smaller molecule after the photodegradation which are already illustrated in Scheme 3.2 of previous Chapter three.

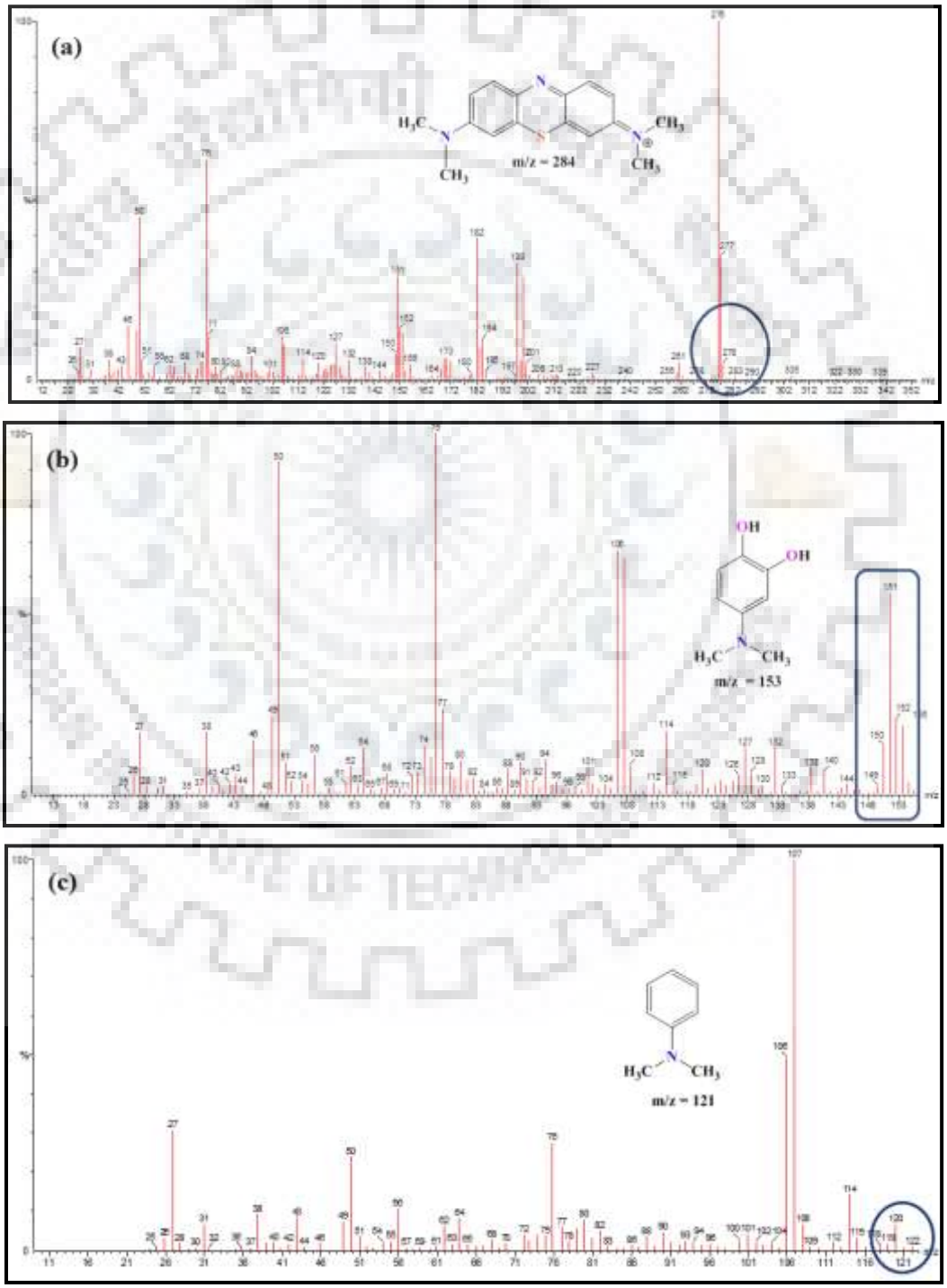

Fig. 5A.23. (a-c) GC-MS spectra of plausible fragments of MB degraded by-products.

5A.3.12. Photocatalytic Reduction of 4-Nitrophenol (4-NP)

During photocatalytic reduction of 4-NP into 4-AP, the red shift (λ_{max} 317 nm → 400 nm) was observed after the addition of $NaBH_4$ in 4-NP solution this is because of formation of 4-nitrophenolate ions. The presence of ZIF-11 and AZ1 in the reaction mixture (20 mL solution of 4-NP + 10 mL of 0.1M $NaBH_4$ solution.), the strong absorption peak at λ_{max} = 400 nm starts decreasing under UV-visible irradiation and a new peak appears at λ_{max} = 268 which indicates the formation of 4-AP. Reduction percentage of 4-NP into 4-AP was calculated by applying equation 5A.1 and it is observed that 20 mg of composite AZ1 and ZIF-11 can reduce 27.13% and 21.13%, respectively, while 100 mg of composite AZ1 and ZIF-11 reduce 86% and 83%, respectively. The absorbance spectra of 4-NP reduction into 4-AP are shown Fig. 5A.24.

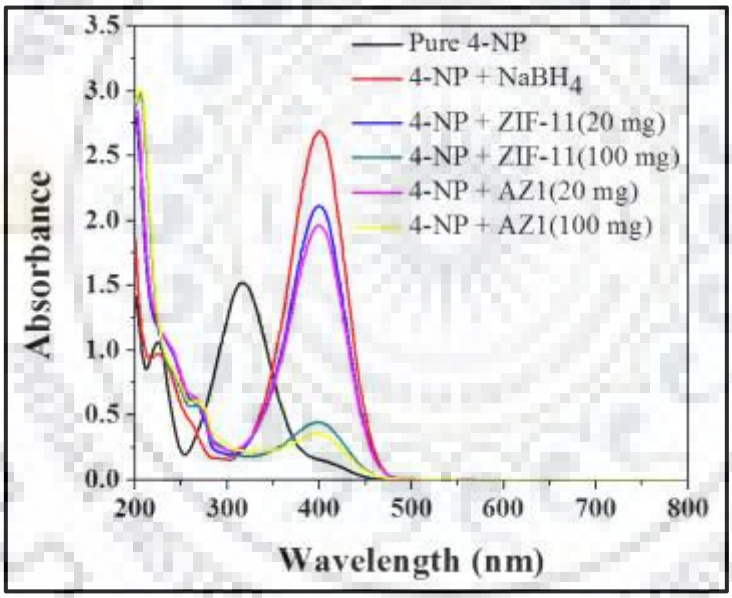

Fig. 5A.24. UV-visible absorbance spectra of 4-NP reduction using ZIF-11 and AZ1.

5A.4. CONCLUSION

In nutshell, toluene assisted synthesis of ZIF-11 and AgNPs@ZIF-11 composites have been demonstrated. The detailed investigation confirmed that the composites exhibit enhanced photocatalytic activity under UV-visible light irradiation for MB degradation and 4-NP reduction into 4-AP which can be utilized for remediation of environmental pollution. The auspicious achievement is that AZ1 composite can be reused for the photocatalytic degradation of MB up to third cycle with same efficiency (100%).

This section describes the controlled synthesis of AgNPs@ZIF-8 via *in situ* synthesis of AgNPs as well as ZIF-8 and they have been utilized as efficient photocatalysts for organic dye degradation such as methylene blue and congo red.

SECTION B

5B.1. Introduction

During last few decades, several efforts have been dedicated for photocatalytic heterogeneous degradation of organic pollutants using *viz.*, Ag nanoparticles (NPs) doped metal oxides *viz.*, Ag/TiO_2, Ag/SnO_2, Ag/ZnO, Ag/Fe_3O_4 and α-Fe_2O_3/Ag/SnO_2 [19-23]. Due to *Surface Plasmon Resonance* (SRP), AgNPs allow the absorption extension of radiation within the wide band gap of semiconducting materials [24] and so enhance the photocatalytic activity. In addition, AgNPs have been also decorated on porous materials such as metal organic frameworks (MOFs). Further, bimetallic nanoparticles, *for instance*, Au@Ag and Ag/Pd have also been successfully deposited on ZIF-8 and used for the reduction of 4-nitrophenol [25] and dehydrogenation of formic acid [26], respectively. Similarly, Ag nanowires have been also fabricated on ZIF-8 and used for the separation of butanol [27] and for antibacterial application [28]. It is quite evident from the careful inspection of available literature that AgNPs doped ZIF-8 has not been explored for the photocatalytic degradation of dyes so far. So, it is envisioned to synthesize AgNPs@ZIF-8 composite in a controlled way, and subsequently exploited it for photocatalytic degradation and removal of methylene blue (MB) and congo red (CR).

This section describes the controlled synthesis of AgNPs@ZIF-8 via *in situ* synthesis of AgNPs as well as ZIF-8. ZIF-8, being a shell material effectively retards the immobilization and agglomeration of AgNPs, and thereby, enhancing the efficiency of AgNPs@ZIF-8 composite, which can be reused for several cycles.

5B.2. EXPERIMENTAL SECTION

5B.2.1. Synthesis of ZIF-8

Zeolitic imidazole framework-8 was synthesized using bench method as explained in the Chapter three.

5B.2.2. Synthesis of AgNPs

Synthesis of the AgNPs has already been discussed in section- A of this Chapter.

5B.2.3. Synthesis of AgNPs@ZIF-8

AgNPs@ZIF-8 composite was synthesized according to the following methods.

5B.2.3.1. Method-A

AgNPs@ZIF-8 composite was synthesized by addition of ZIF-8 *in situ* synthesis of AgNPs as illustrated in Scheme 5B.1. During the synthesis of AgNPs as mentioned in Section A, pre-synthesized ZIF-8 (100 mg) was added to silver nitrate solution under N_2 gas for 30 min. Subsequently, silver nitrate solution was reduced using trisodium citrate and sodium borohydride solution. The precipitate was centrifuged and dried at 60 °C for 6 h. The composite was stored in closed vessels wrapped with aluminium foil and named as SZ.

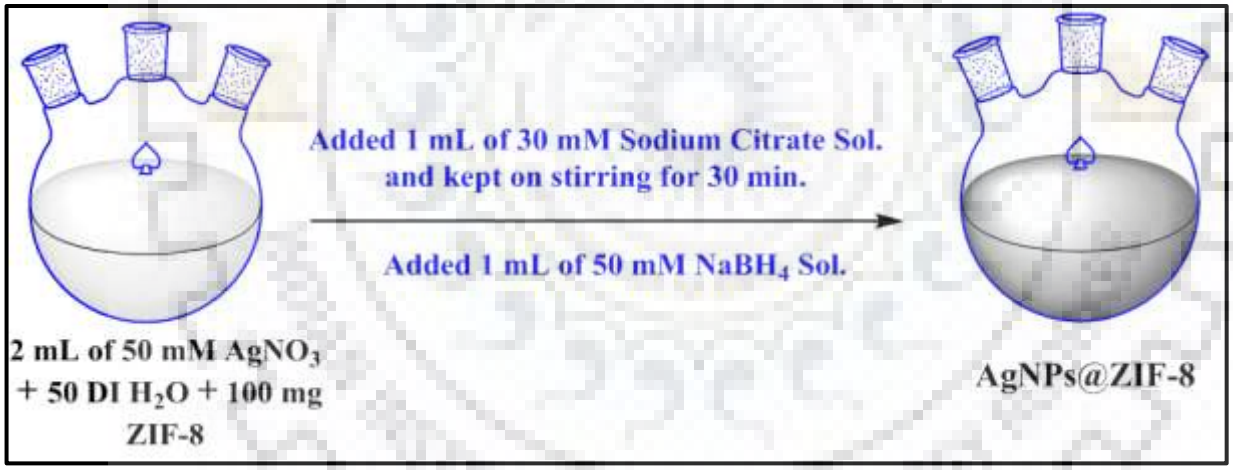

Scheme 5B.1. Synthesis of AgNPs@ZIF-8 by using method-A.

5B.2.3.2. Method-B

According to this method, AgNPs@ZIF-8 composite was synthesized by encapsulation of pre-synthesized AgNPs *in situ* synthesis of ZIF-8 which is depicted in Scheme 5B.2. During the synthesis of ZIF-8, AgNPs suspensions (1 mg of AgNPs powder dispersed in 2 mL methanol) were added in various amounts *i.e.* 150 µL, 300 µL and 500 µL for the synthesis of AgNPs@ZIF-8 composites which are abbreviated as SZ1, SZ2 and SZ3, respectively.

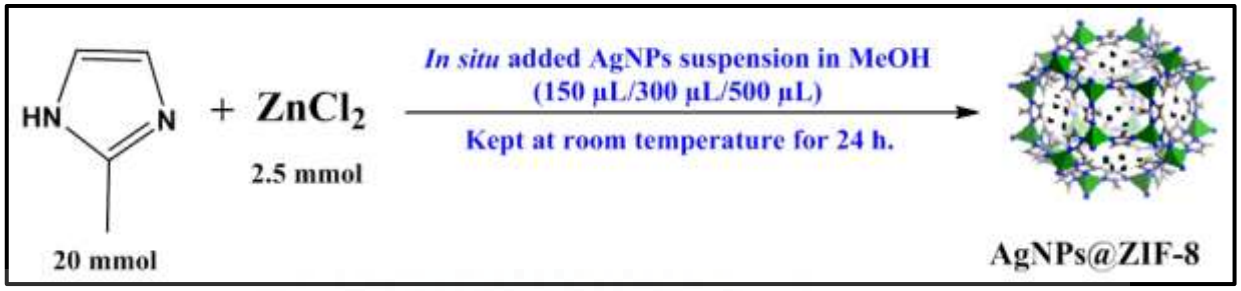

Scheme 5B.2. Synthesis of AgNPs@ZIF-8 by using method-B.

5B.2.4. Adsorption and Photodegradation Studies

For adsorption and photodegradation studies of MB and CR, following sets of each dye ([MB] = 0.5×10^{-5} M and [CR] = 2×10^{-5} M) solutions were prepared in 50 mL ungraduated test tubes as per the details given below-

- 20 mL of MB or CR dye solution was taken as control.
- 10 mg of SZ, SZ1, SZ2, SZ3 and ZIF-8 was suspended in 20 mL dye (MB or CR) solution in a separate test tube.

All samples were sonicated for 30 min and kept under dark for 2 h. Meanwhile, a small aliquot of solution was analyzed spectrophotometrically and the absorbance spectra were recorded at certain time interval. Subsequently, fresh solutions of all samples were sonicated for another 30 min for maintaining the adsorption-desorption equilibrium. Later on, they were exposed for 2 h for MB dye and 40 min for CR dye under UV-visible irradiations emitted from a halogen lamp (50 Watt) and subsequently absorbance spectra were recorded at certain time interval. The remaining concentration of dye was calculated at λ_{max} 663 nm for MB and 497 nm for CR using equation 3.1 (expressed in Chapter three).

5B.3. RESULTS AND DISCUSSION

5B.3.1. PXRD Analysis

Synthesis and detailed characterization of ZIF-8 has been already discussed in the previous Chapter three and four. The crystalline texture of synthesized composites (SZ, SZ1, SZ2 and SZ3) was carefully examined by powder X-ray diffraction analysis (PXRD). There was no significant change observed in the PXRD patterns of composites SZ, SZ1, SZ2 and SZ3 after the encapsulation of AgNPs which supports the proper encapsulation of AgNPs within ZIF-8 cavity. PXRD patterns of composites were indexed with the help of the reported XRD pattern of ZIF-8 (Fig. 5B.1).

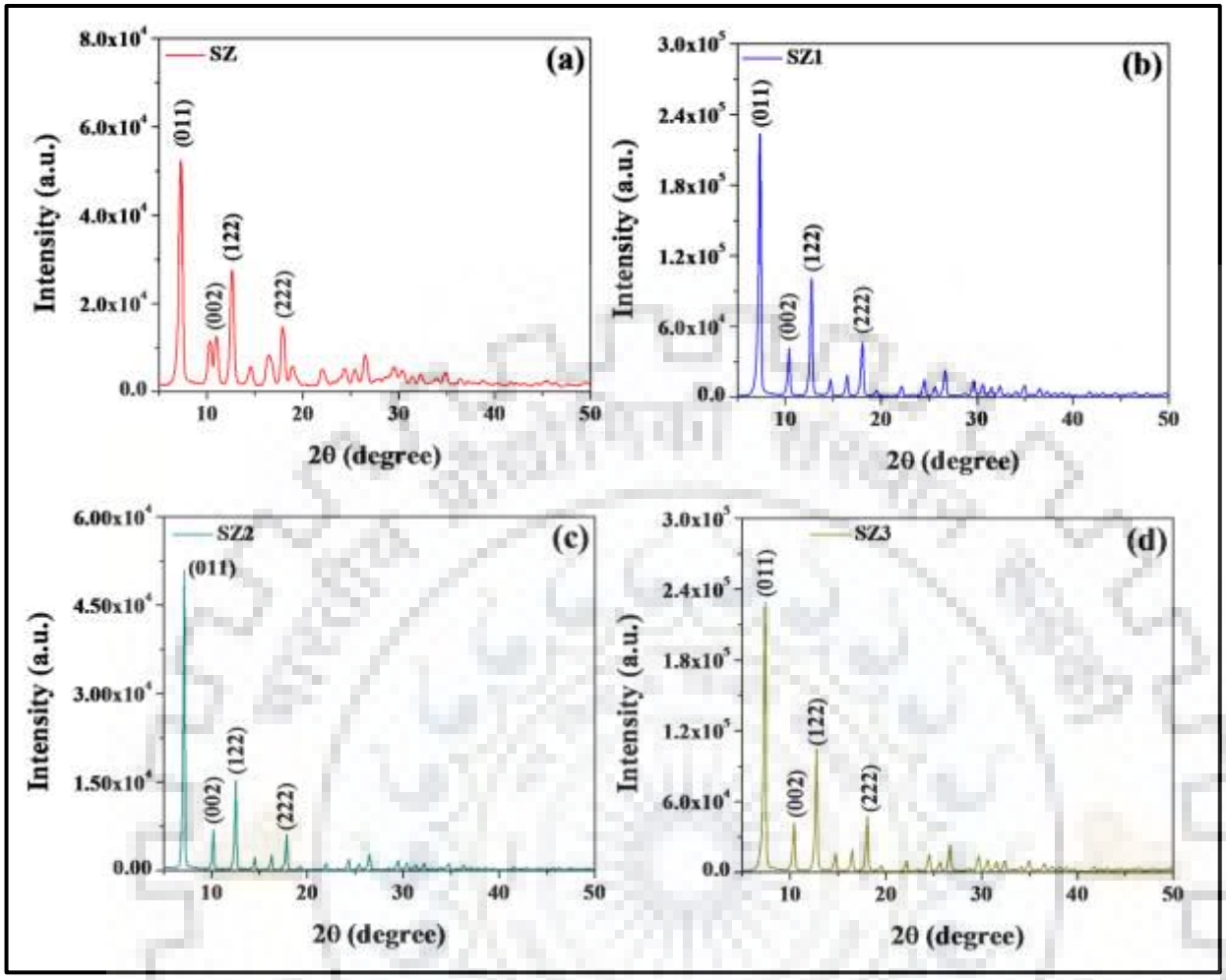

Fig. 5B.1. PXRD patterns of synthesized (a) SZ, (b) SZ1, (c) SZ2 and (d) SZ3 composites.

5B.3.2. FT-IR Spectroscopic Studies

FT-IR spectra of synthesized SZ, SZ1, SZ2 and SZ3 composites have been shown in Fig. 5B.2. The diagnostic peaks of composites seem to locate at 421 cm^{-1}, 955 cm^{-1}, 1412 cm^{-1}, 1587 cm^{-1} for ν(Zn-N), δ(C-N), ν(C-N), ν(C=N), respectively [14].

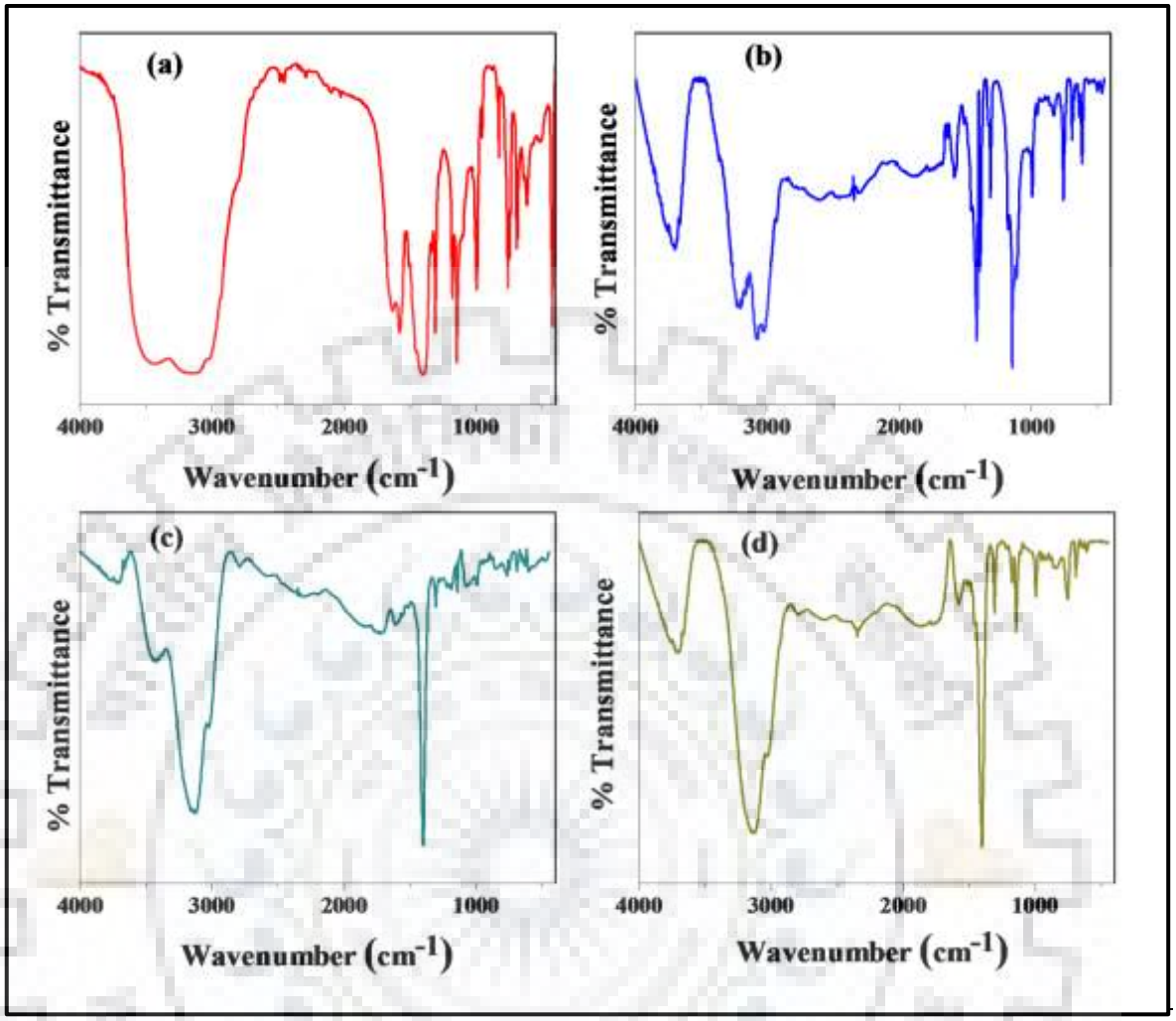

Fig. 5B.2. (a-d) FT-IR spectra of SZ, SZ1, SZ2 and SZ3 composites, respectively.

5B.3.3. FE-SEM and HR-TEM Analysis

A hexagonal morphology of AgNPs@ZIF-8 composites (SZ, SZ1, SZ2 and SZ3) was ascertained by FE-SEM analysis (Fig. 5B.3) which firmly supports that encapsulation of AgNPs does not alter the morphology of ZIF-8. EDX analysis ensured the presence of micro-environment of AgNPs within ZIF-8 frameworks. The EDX spectra are given in Fig. 5B.4 and the results are compiled in Table 5B.1. Encapsulation was also ensured by HR-TEM images of SZ, SZ1, SZ2 and SZ2 (Fig. 5B.5). Fig. 5B.5(a) shows AgNPs appeared as dot in SZ composite. Similar pattern was also observed in SZ1, SZ2 and SZ2. Crystalline nature of SZ1, SZ2 and SZ2 was confirmed by SEAD pattern (Fig. 5B.6(a-d)). Particle size of encapsulated AgNPs was calculated from distribution plot (Fig. 5B.7) which implies that the particle size increases with the dosing amount.

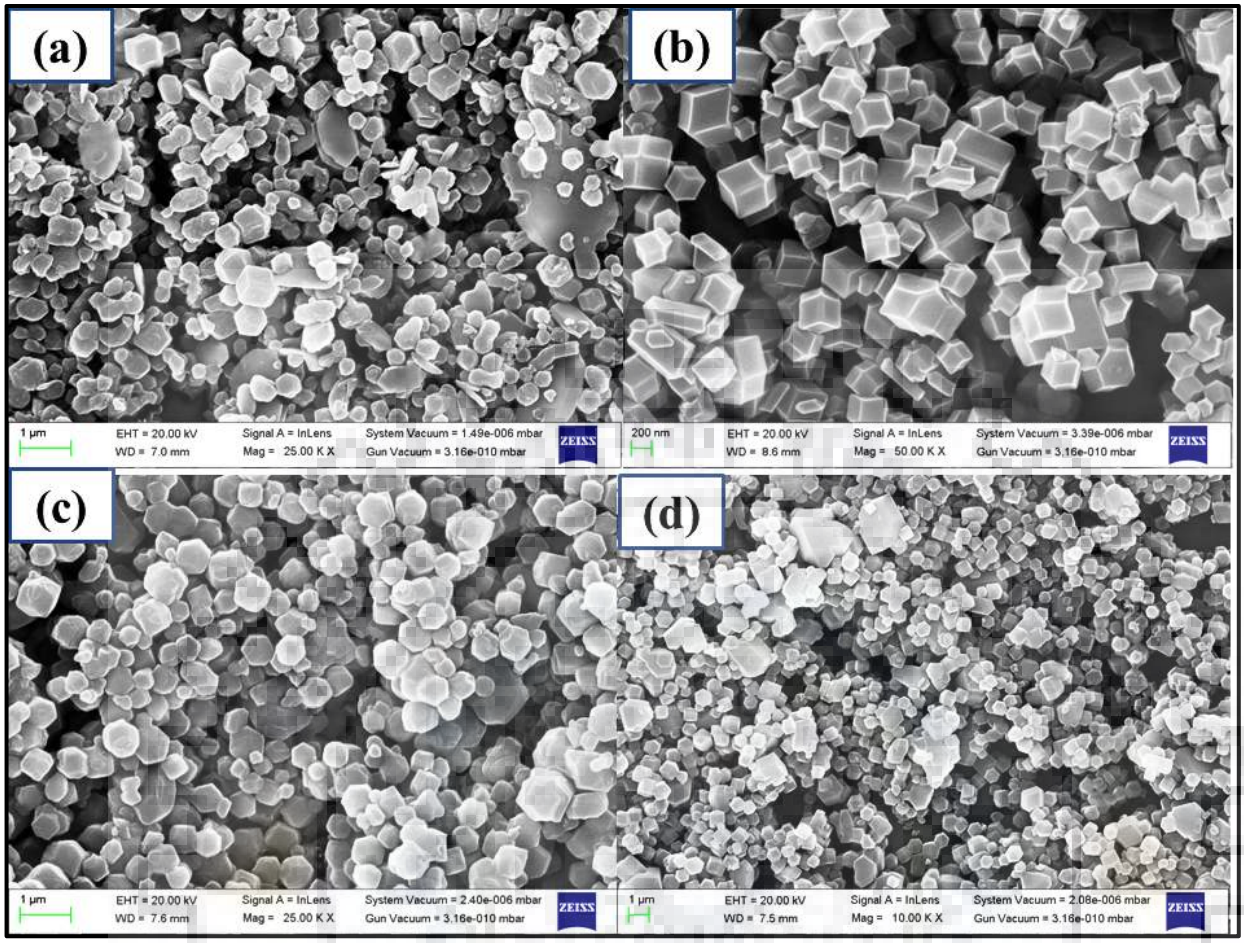

Fig. 5B.3. FE-SEM images of synthesized (a) SZ, (b) SZ1, (c) SZ2 and (d) SZ3 composites.

Table. 5B.1. EDX analysis of SZ, SZ1, SZ2 and SZ3 composites.

S.N.	Materials	Atomic%			
		C	N	Zn	Ag
1.	SZ	51.23	41.01	6.11	1.65
2.	SZ1	78.70	18.90	2.40	0.01
3.	SZ2	76.34	20.99	2.65	0.02
4.	SZ3	69.13	27.99	2.85	0.03

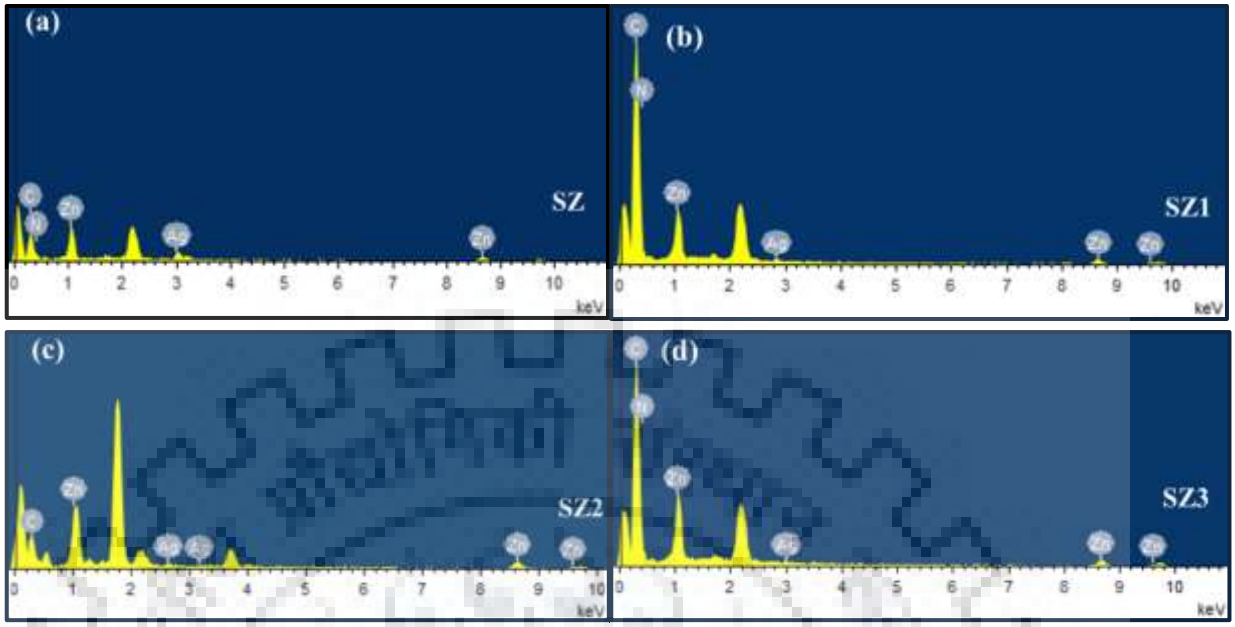

Fig. 5B.4. (a-d) EDX spectra of synthesized composites SZ, SZ1, SZ2 and SZ3, respectively.

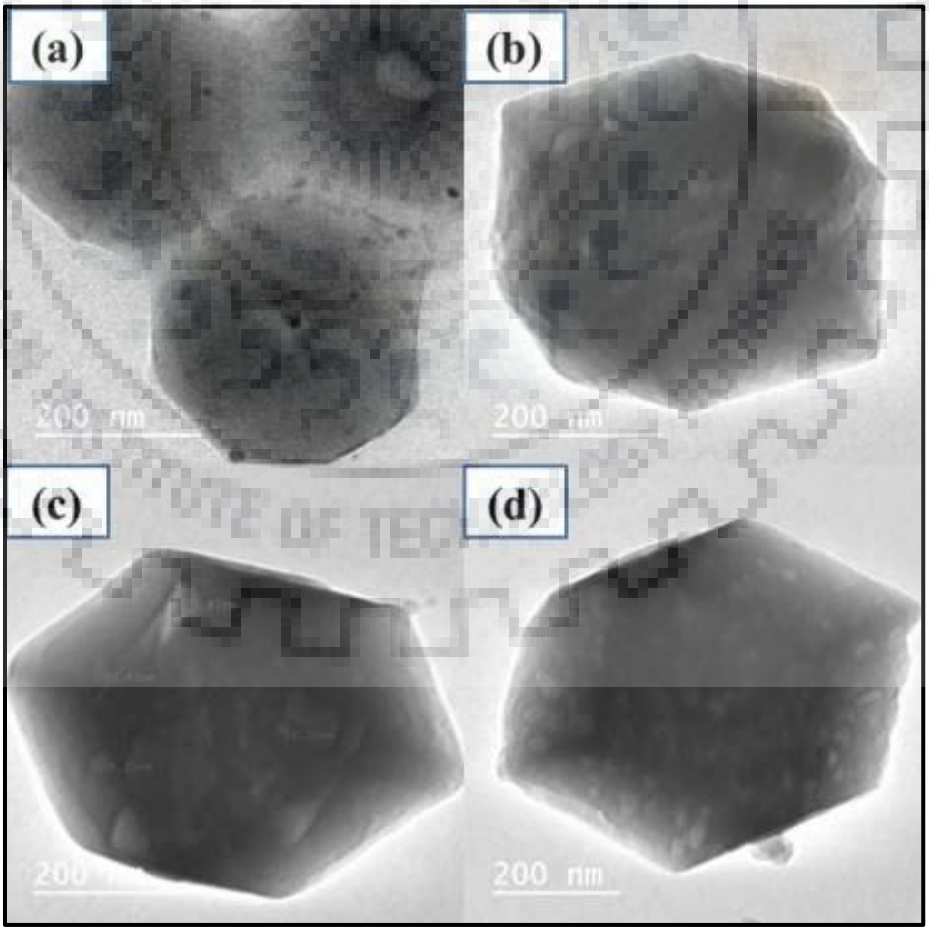

Fig. 5B.5. TEM images of (a) SZ, (b) SZ1, (c) SZ2 and (d) SZ3.

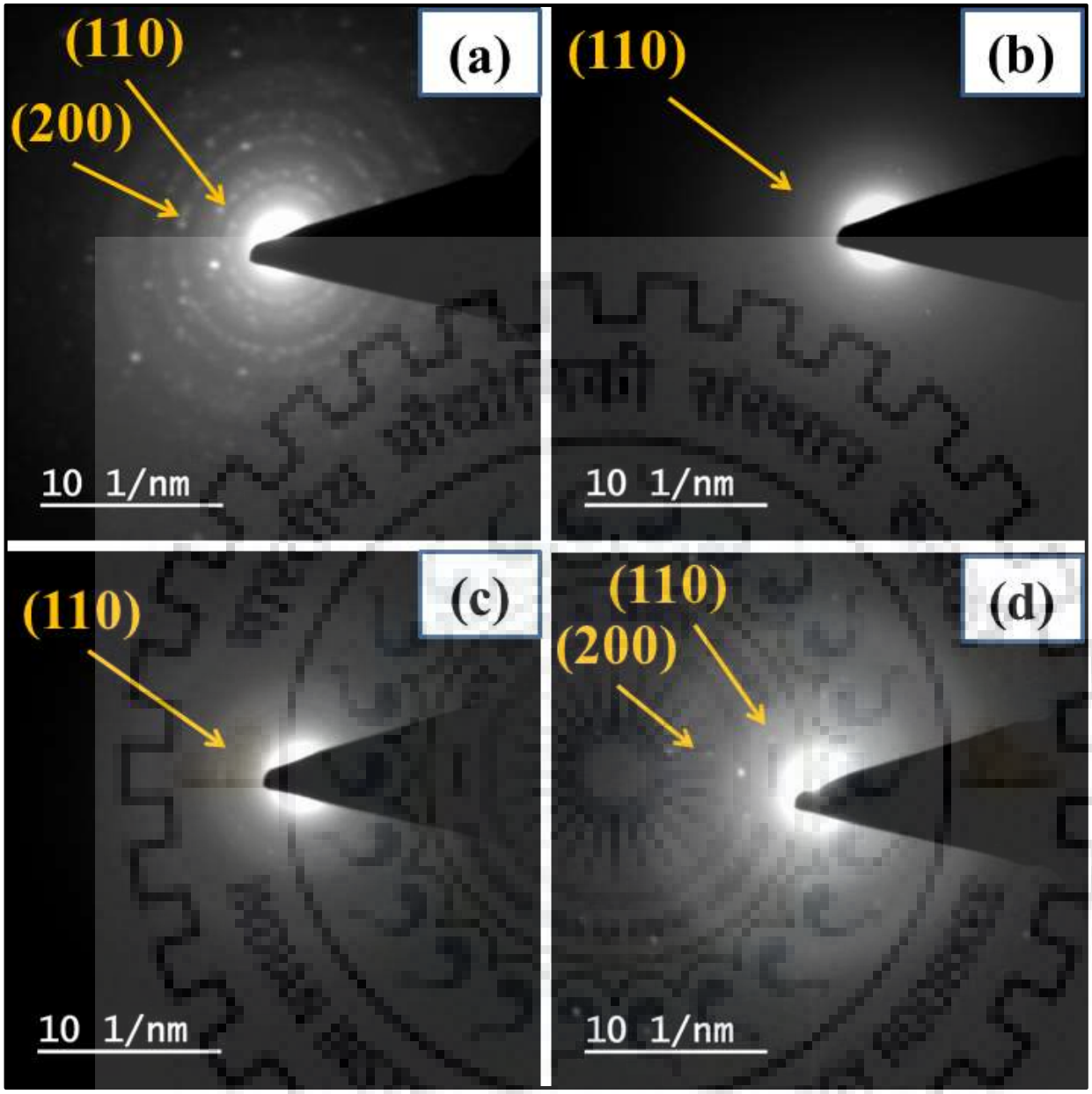

Fig. 5B.6. SEAD patterns of (a) SZ, (b) SZ1, (c) SZ2 and (d) SZ3.

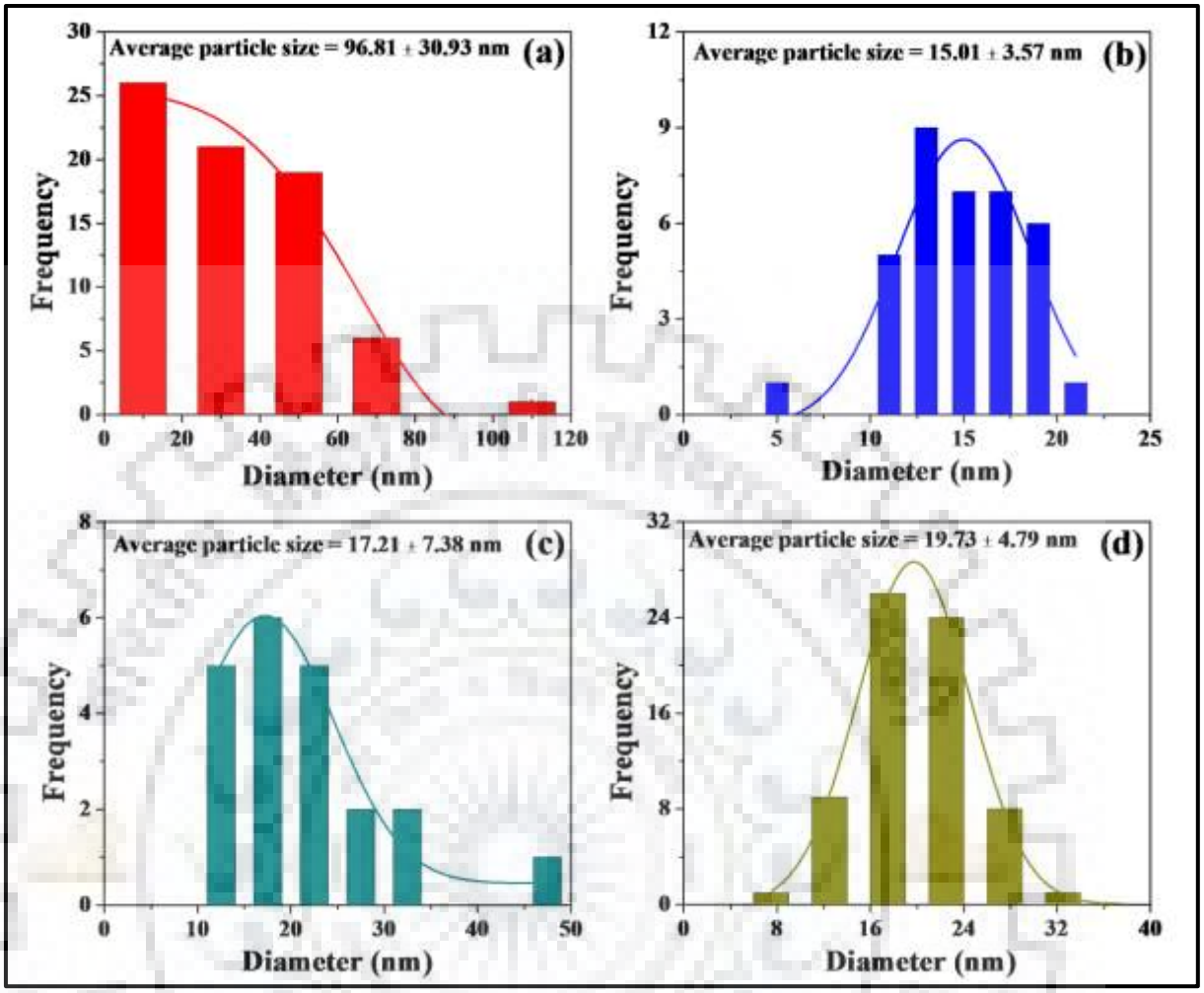

Fig. 5B.7. (a-d) Particle size distribution plots of AgNPs within SZ, SZ1, SZ2, and SZ3 composites, respectively.

5B.3.4. UV-DRS Studies

The band gap of synthesized SZ, SZ1, SZ2, and SZ3 composites has been calculated by employing Tauc method [15] and the typical Tauc plots are illustrated in Fig.5B.8. For direct transitions, it is found that all composites show sharp band at 5.27 eV due to ZIF-8 while SZ composite exhibits narrow band at 2.16 eV due to excess amount of AgNPs encapsulation. This band does not appear in SZ1, SZ2, and SZ3 composites due to small amount of AgNPs. Similarly, for the indirect transitions all composites exhibit sharp band at 5.13 eV due to ZIF-8 while SZ shows a narrow and broad band at 1.62 eV due to excess amounts of AgNPs. In the absorption spectra, two bands appear at 236 nm and 335 nm due to ZIF-8 and micro environment of AgNPs,

respectively, while SZ exhibits a flat absorption at 581 nm due to excess amounts of AgNPs.

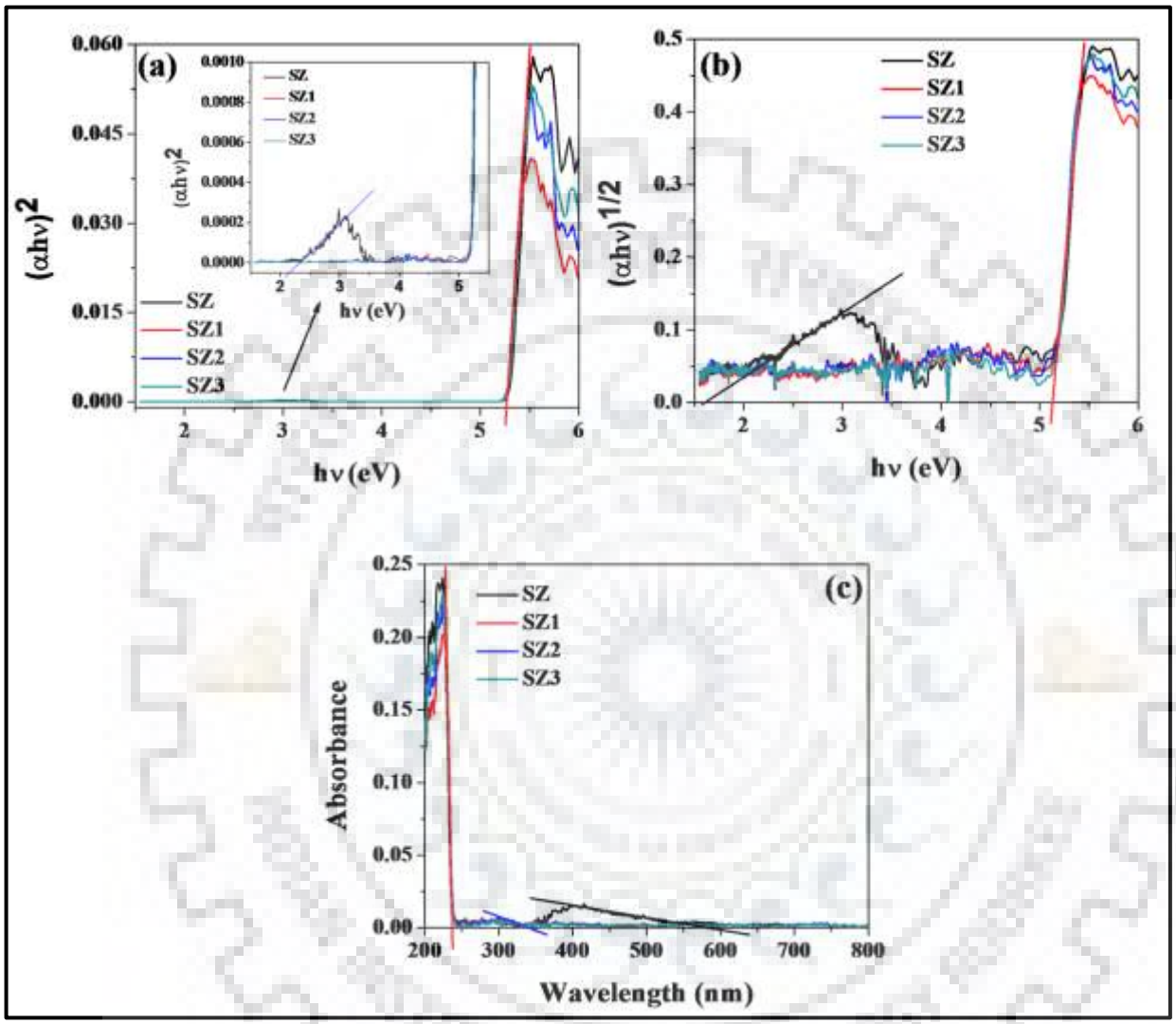

Fig. 5B.8. (a, b) Tauc plots of SZ, SZ1, SZ2 and SZ3 composites by direct and indirect method, respectively. (c) The absorbance spectra of SZ, SZ1, SZ2 and SZ3 composites.

5B.3.5. BET Surface Area Analysis

Porosity and sorption properties of SZ, SZ1, SZ2 and SZ3 composites were examined by Brunauer-Emmett-Teller (BET) adsorption-desorption isotherms using N_2 gas at 77K. The adsorption-desorption isotherm plots are shown in Fig. 5B.9 and the results are compiled in the Table 5B.2. It has been found that the surface area of composites (SZ, SZ1, SZ2 and SZ3) decrease on increasing the dosing amount from

≈1330 $m^2 g^{-1}$ to 902 $m^2 g^{-1}$ except SZ2 composite which exhibits enhanced surface area as compared to SZ1 composite. The porosity of SZ, SZ1, SZ2 and SZ3 composites was analysed by BET pore size distribution plots which are illustrated in Fig.5B.10.

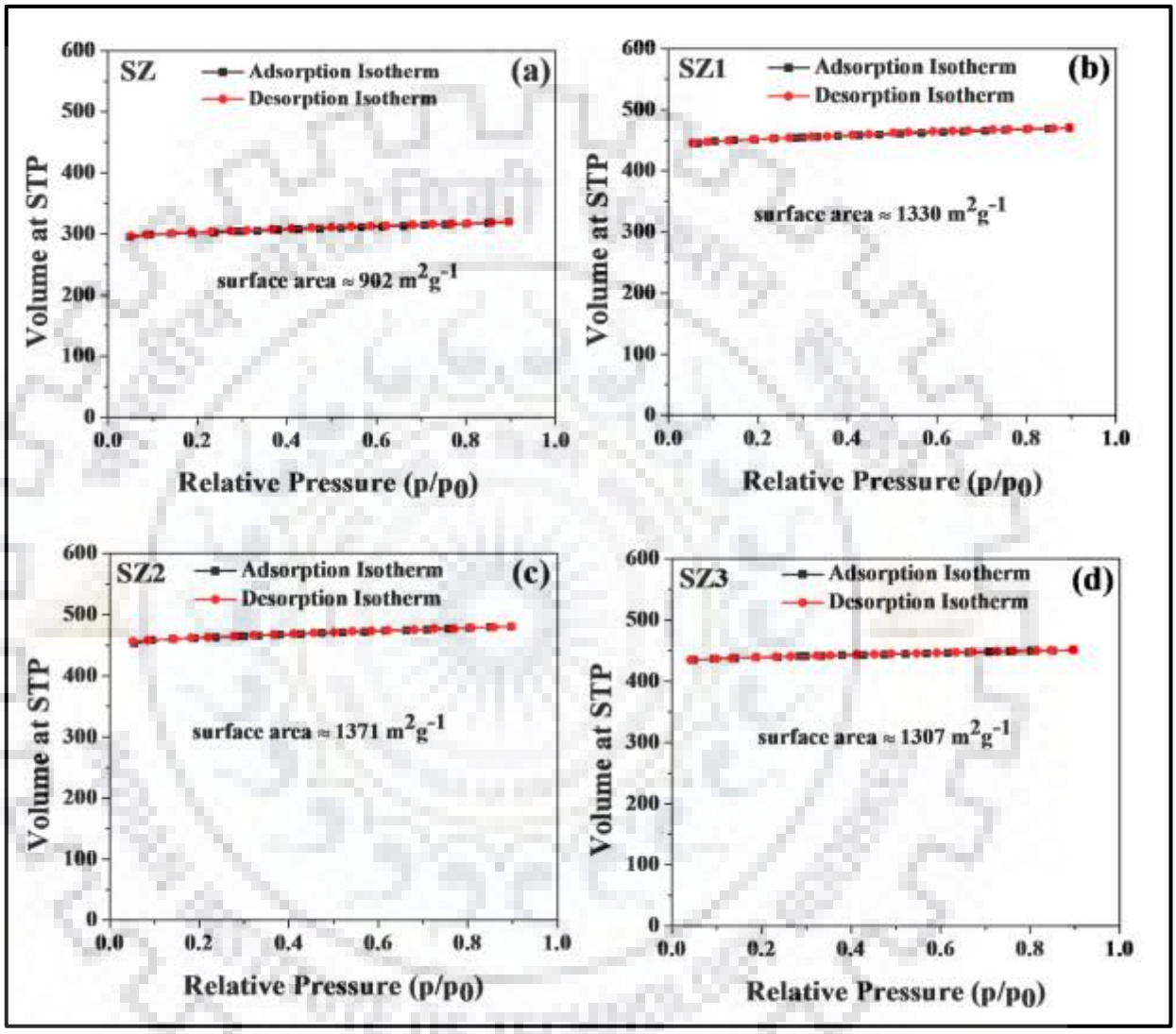

Fig. 5B.9. (a-d) BET adsorption isotherm of SZ, SZ1, SZ2 and SZ3 composites, respectively.

5B.3.6. XPS Analysis

The survey scan and expanded XPS spectra of SZ composite are given in Fig. 5B.11. Zn 2p expanded spectrum of SZ composite (Fig. 5B.11(b)) comprises of two sharp and major peaks with binding energy 1044.20 eV and 1021.17 eV corresponding to $2p_{1/2}$ and $2p_{3/2}$, respectively, while Ag 3d has major peaks at 373.86 eV and 367.80 eV attributable to $3d_{3/2}$ and $3d_{5/2}$, respectively (Fig. 5B.11(c)).

Table. 5B.2. BET analysis of SZ, SZ1, SZ2 and SZ3 composites.

S.N.	Materials	S_{BET} (m^2g^{-1})	Pore Vol. (ccg^{-1})	Average Pore radius (Å)
1.	SZ	902	4.946×10^{-1}	35.71
2.	SZ1	1330	7.278×10^{-1}	35.78
3.	SZ2	1371	7.434×10^{-1}	35.93
4.	SZ3	1307	6.976×10^{-1}	35.38

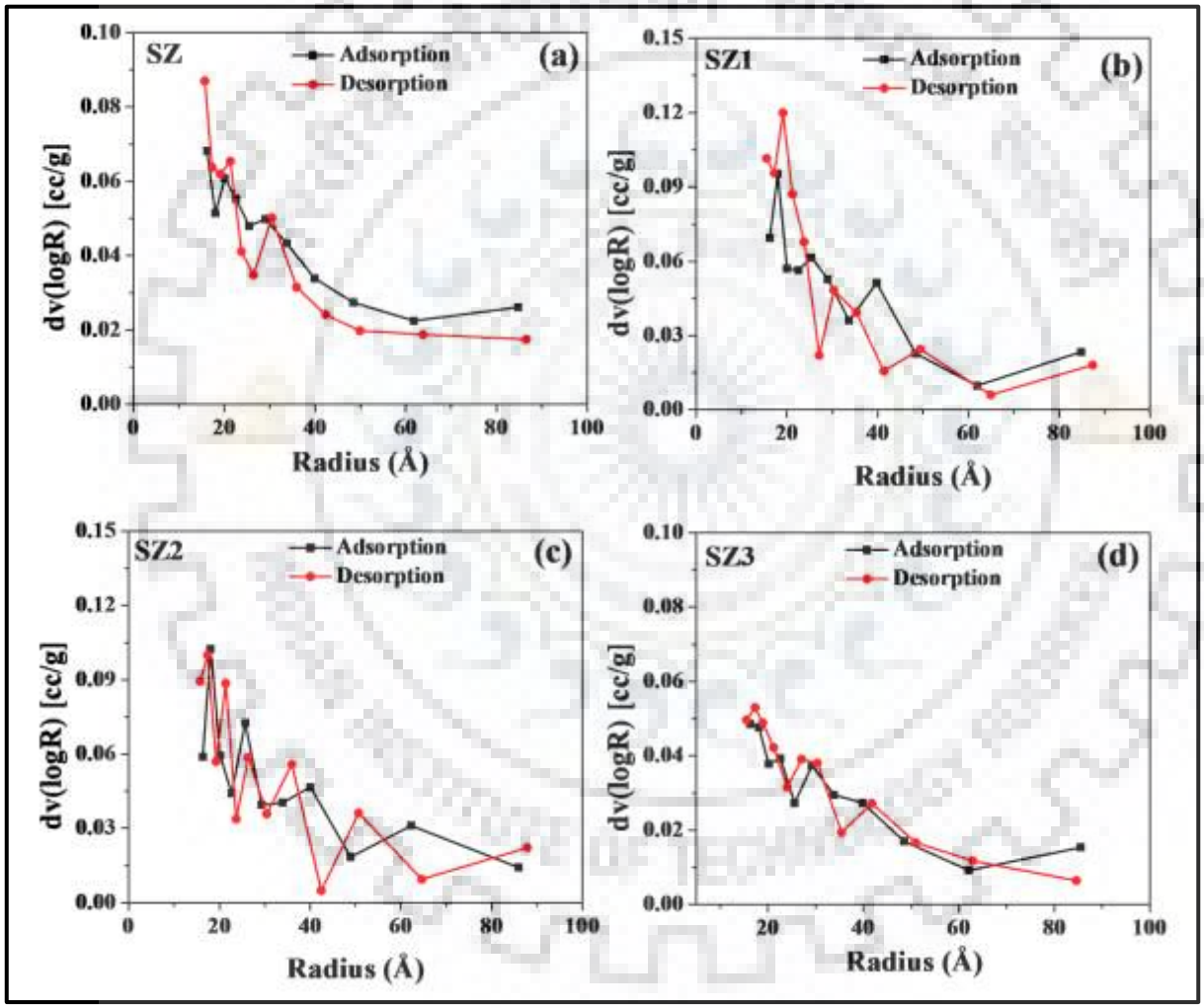

Fig. 5B.10. (a-d) The pore size distribution plots of SZ, SZ1, SZ2 and SZ3 composites, respectively.

Fig. 5B.11(d) exhibits the deconvoluted C 1s peaks having binding energy at 284.81 eV and 283.99 eV correspond to sp^2C-N and sp^2C-C interaction [29] while N 1s peak (Fig. 5B.11(e)) appears at 398.31 eV. Similar XPS patterns were observed in case of SZ1, SZ2 and SZ3

composites, and their XPS spectra are arranged in Fig. 5B.12, Fig. 5B.13 and Fig. 5B.14, respectively, and the corresponding binding energy are tabulated in Table 5B.3.

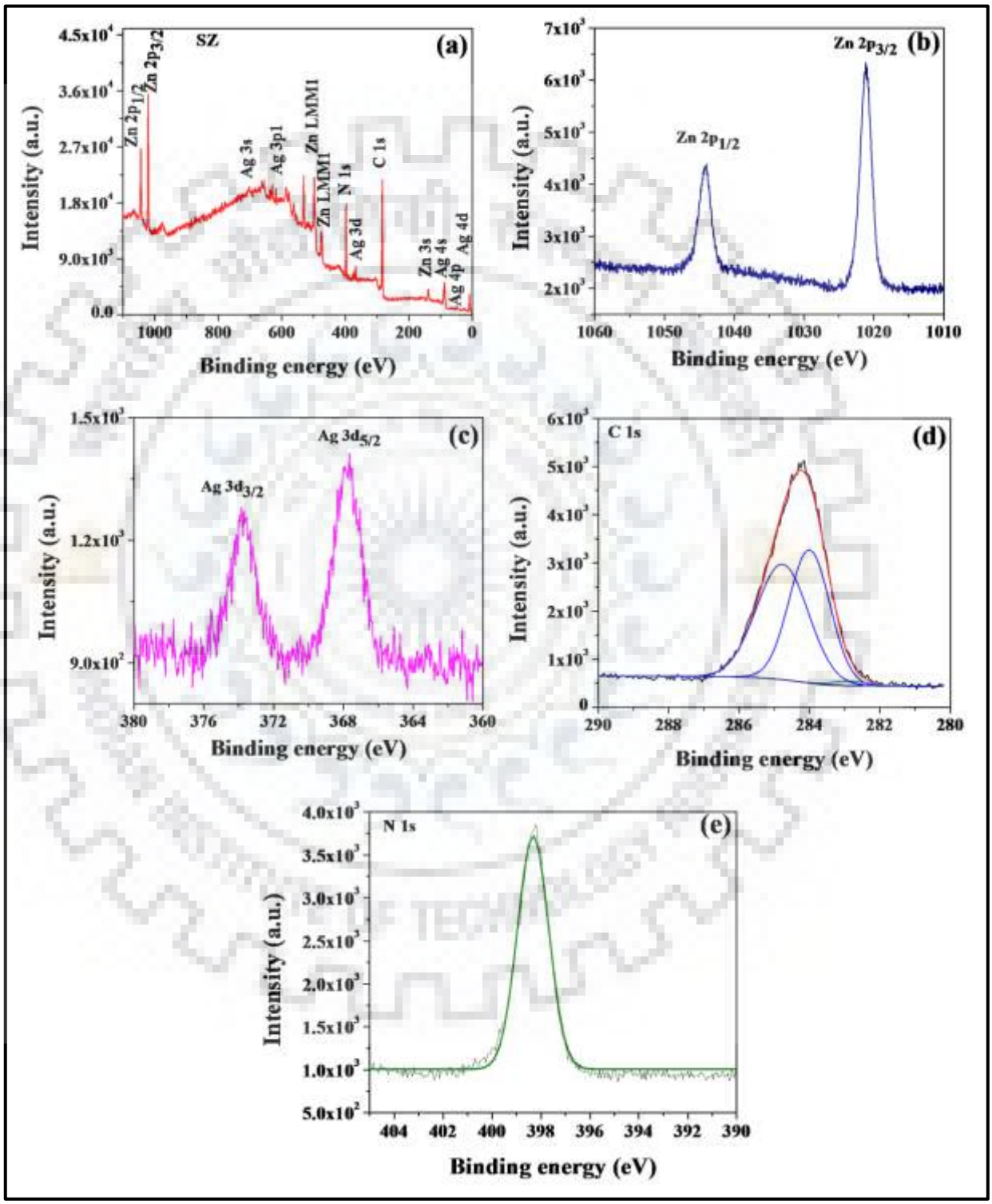

Fig. 5B.11. (a-e) Survey scans of SZ and expanded XPS spectra of Zn 2p, Ag 3d, C 1s and N 1s, respectively.

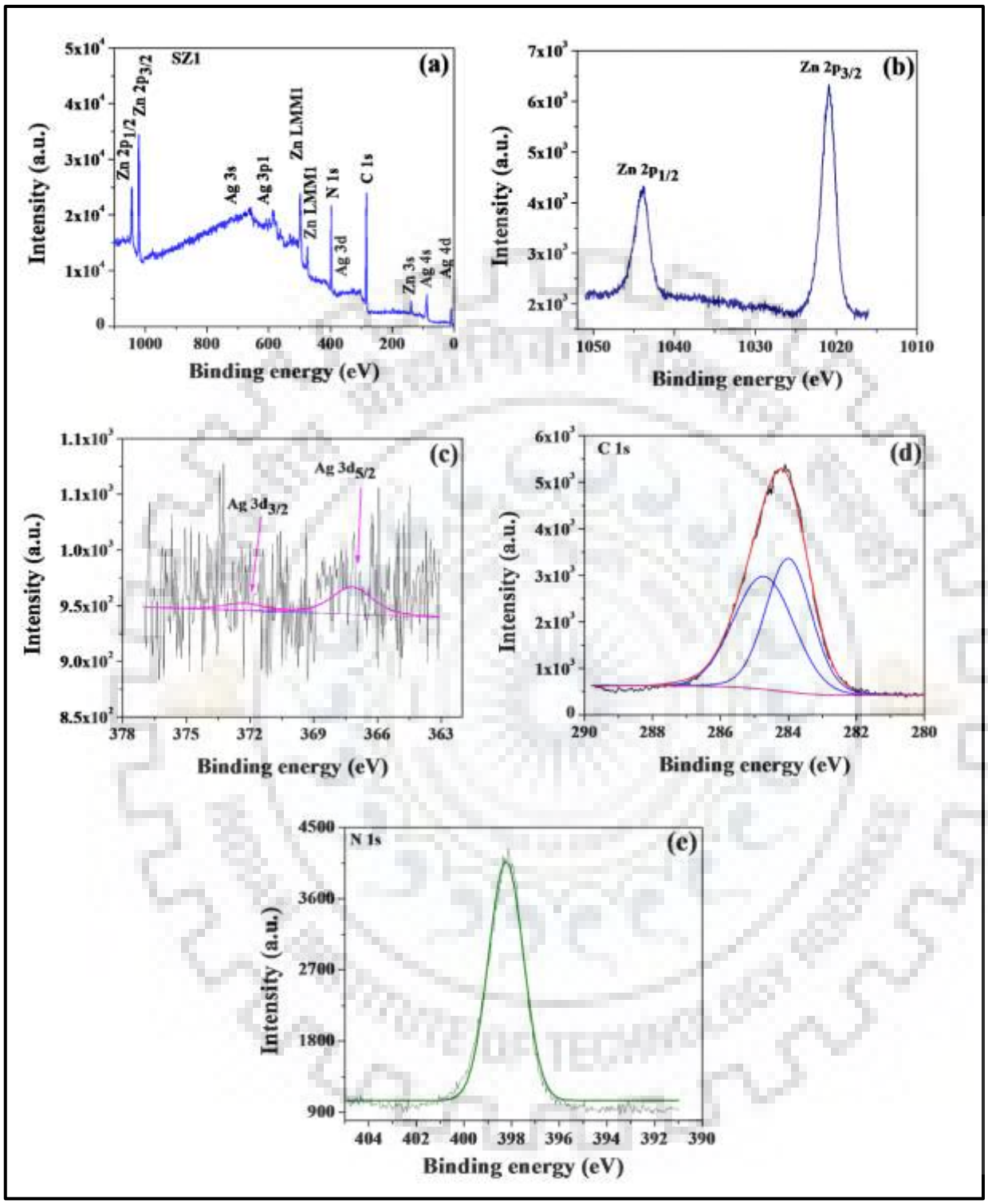

Fig. 5B.12. (a-e) Survey scan of SZ1 and expanded XPS spectra of Zn 2p, Ag 3d, C 1s and N 1s represented, respectively.

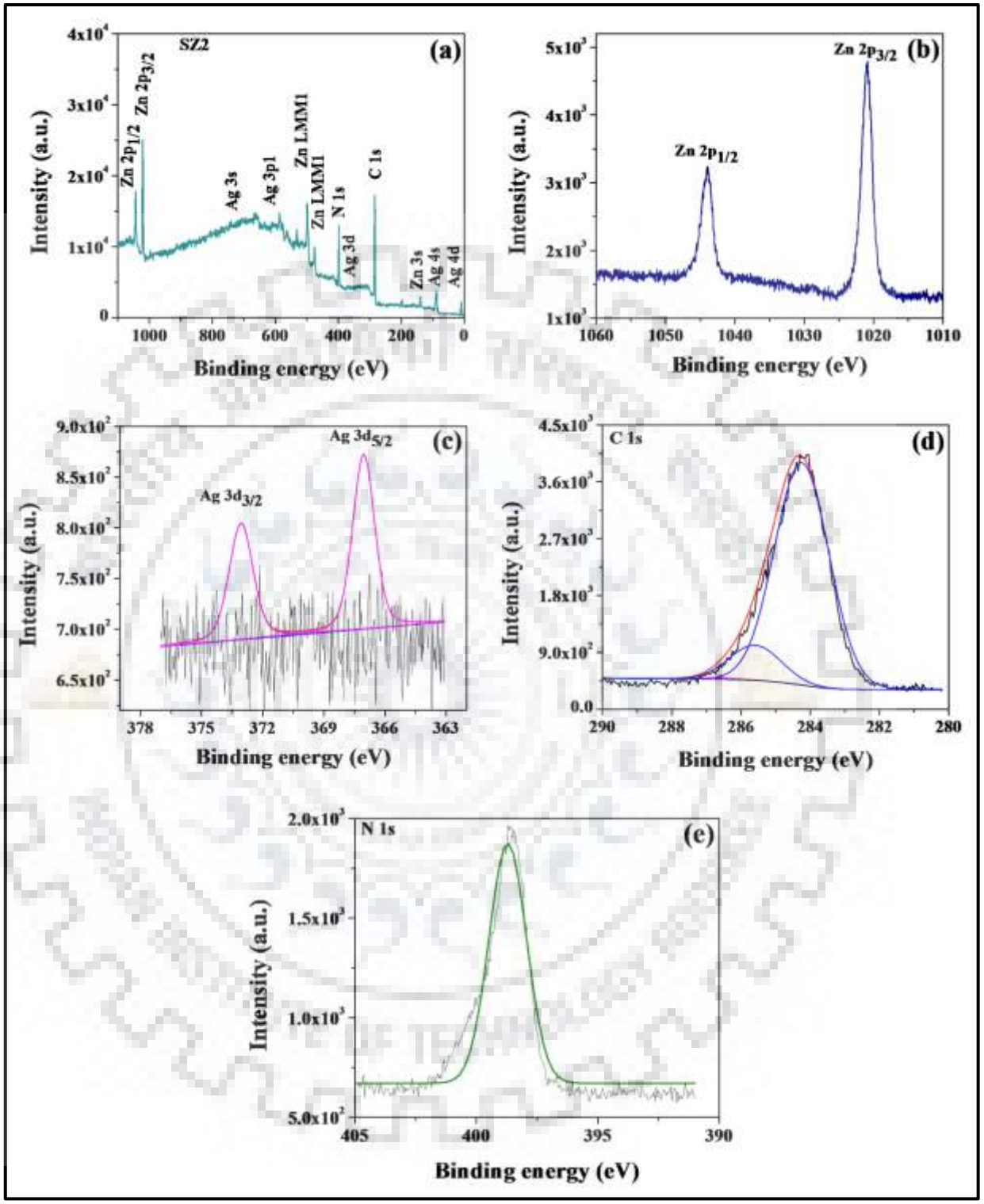

Fig. 5B.13. (a-e) Survey scan of SZ2 and expanded XPS spectra of Zn 2p, Ag 3d, C 1s and N 1s represented, respectively.

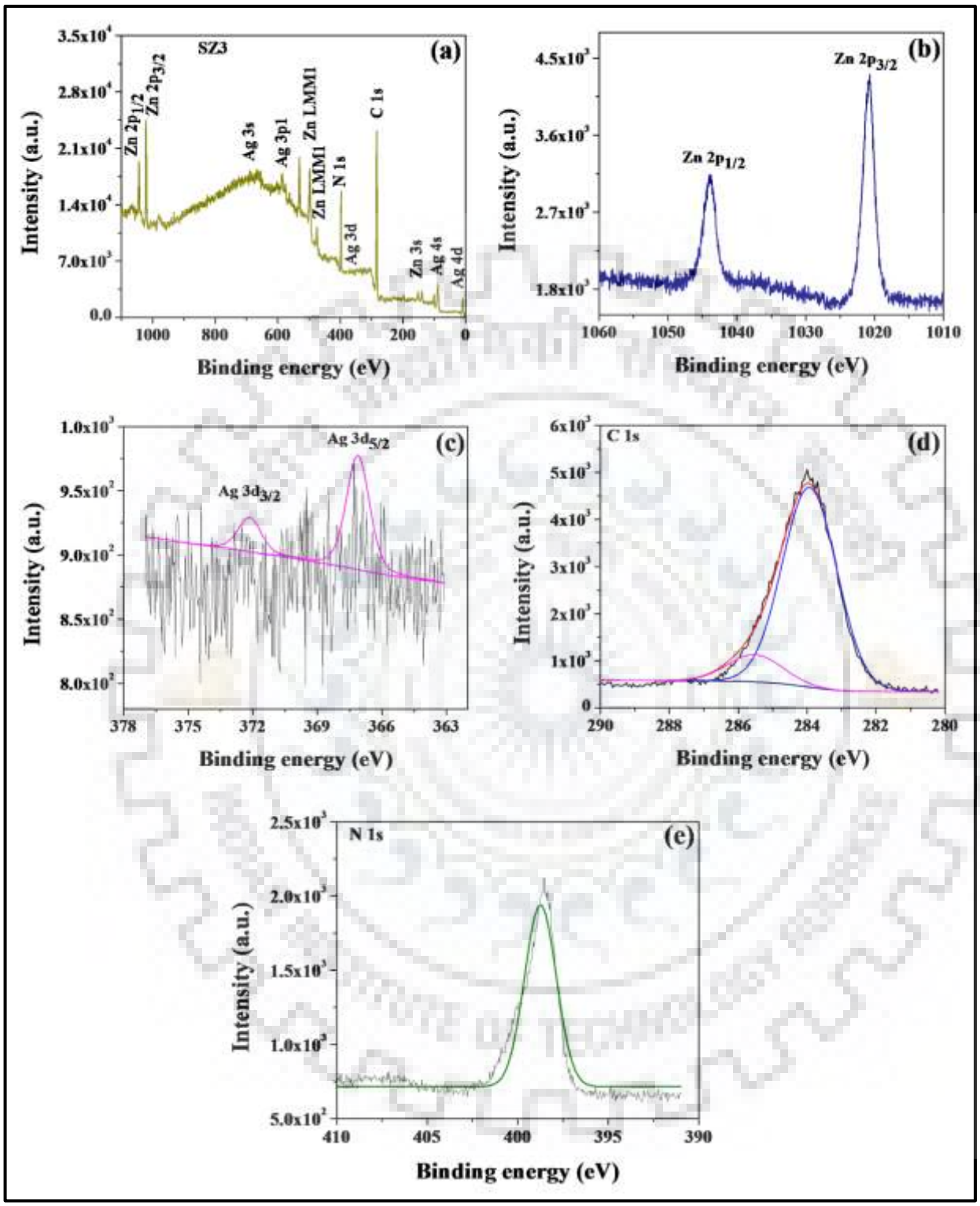

Fig. 5B.14. (a-e) Survey scan of SZ3 and expanded XPS spectra of Zn 2p, Ag 3d, C 1s and N 1s represented, respectively.

Table 5B.3. XPS analysis of AgNPs doped SZ, SZ1, SZ2 and SZ3 composites.

S.N.	Materials	Atom/Element	State/Term	Binding energy (eV)
1.	SZ	Zn	$2p_{1/2}$	1044.20
			$2p_{3/2}$	1021.17
		Ag	$3d_{3/2}$	373.86
			$3d_{5/2}$	367.80
		C	1s	284.81
				283.99
		N	1s	398.31
2.	SZ1	Zn	$2p_{1/2}$	1044.02
			$2p_{3/2}$	1021.05
		Ag	$3d_{3/2}$	372.41
			$3d_{5/2}$	367.21
		C	1s	284.75
				283.97
		N	1s	398.23
3.	SZ2	Zn	$2p_{1/2}$	1044.01
			$2p_{3/2}$	1021.04
		Ag	$3d_{3/2}$	373.09
			$3d_{5/2}$	367.03
		C	1s	285.63
				284.29
		N	1s	398.70
4.	SZ3	Zn	$2p_{1/2}$	1044.13
			$2p_{3/2}$	1021.02
		Ag	$3d_{3/2}$	372.15
			$3d_{5/2}$	367.13
		C	1s	285.54
				283.94
		N	1s	398.74

5B.3.7. Thermal Analysis

Thermal stability of SZ, SZ1, SZ2 and SZ3 composites have been studied by thermal gravimetric analysis (TGA) and TGA plots are illustrated in Fig. 5B.15(a, b) under air and N_2 atmosphere, respectively. It is found that all four composites (SZ, SZ1, SZ2 and SZ3) exhibit remarkable thermal stability *ca.* 95% up to 380 °C and *ca.* 97% up to 400°C under air and N_2 atmosphere, respectively. They started to decompose above 400 °C under both (air and N_2) environments.

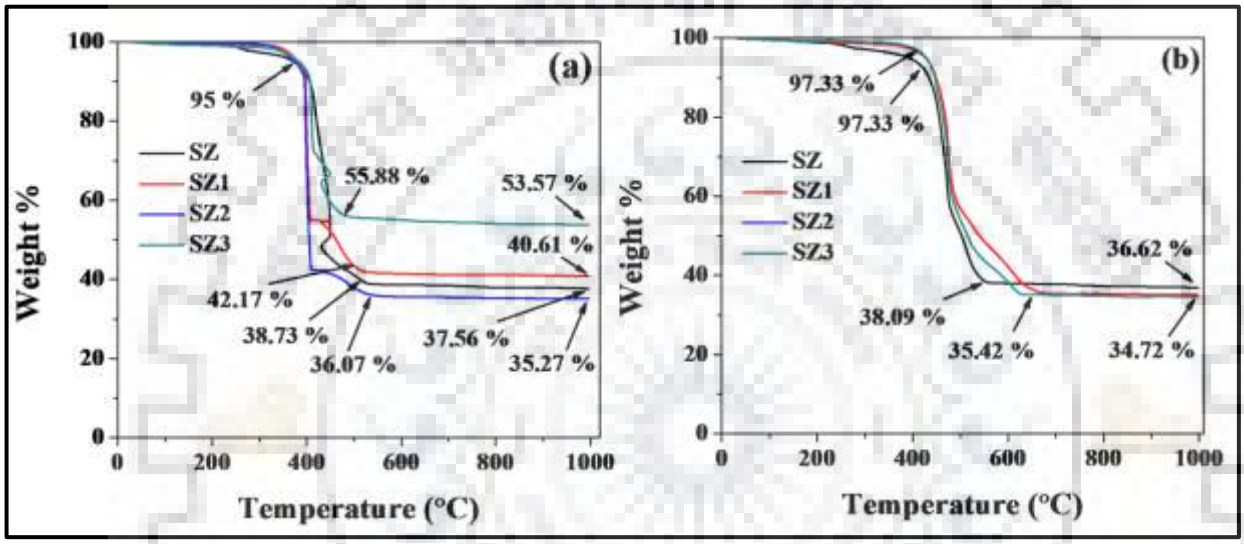

Fig. 5B.15. (a, b) Thermal gravimetric plots of SZ, SZ1, SZ2 and SZ3 under air and N_2 atmosphere, respectively.

5B.3.8. Adsorption and Photocatalytic Studies of Methylene Blue (MB) and Congo Red (CR) dye using AgNPs@ZIF-8 Composites (SZ, SZ1, SZ2 and SZ3)

In order to explore the application, photocatalytic activity of each composite SZ, SZ1, SZ2 and SZ3 was studied and compared with ZIF-8 using MB and CR as model dyes. All details of experimental conditions are mentioned in the above section 5B.2.4 and C/C_0 vs time plot is given in Fig. 5B.16. The results of adsorption and photodegradation of both dye (MB and CR) are compiled in the Table 5B.4 and Table 5B.5, respectively. Prior to the photocatalytic activity of SZ, SZ1, SZ2, SZ3 composites and ZIF-8, adsorption efficiency was observed which shows that SZ1 (16.12%) exhibits maximum adsorption efficiency for the removal of MB dye as compared to SZ (10.31%), SZ2 (4.5%), SZ3 (10%) and ZIF-8 (8.06%). However, for the removal of CR, SZ2 (97.7%) displays maximum adsorption efficiency as compared to SZ (96.18%), SZ1 (93.89%), SZ3 (80.53%) and ZIF-8 (91.6%). The results of

photocatalytic degradation demonstrated that SZ2 composite shows more degradation efficiency for the dyes *i.e.* 97.25% for MB and 100% for CR while SZ, SZ1, SZ3 and ZIF-8 can degrade off 85.56, 90.56, 86.43 and 84.18% MB and 98.09, 96.18, 97.7 and 95.80% CR, respectively.

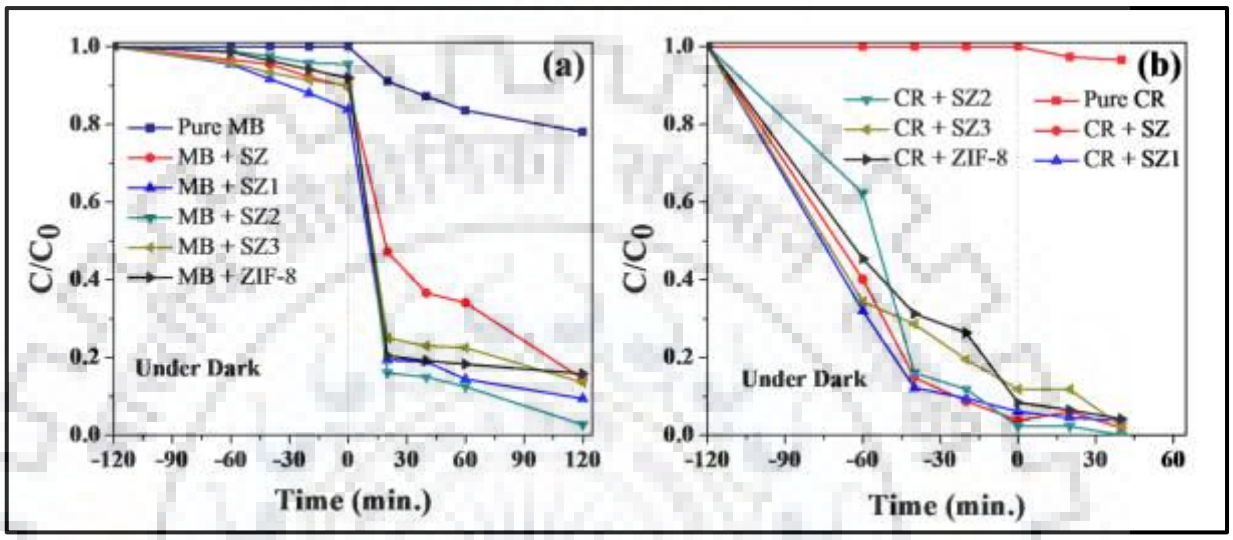

Fig. 5B.16. (a, b) Concentration (C/C_0) *vs* time plots of MB and CR employing AgNPs@ZIF-8 composites SZ, SZ1, SZ2, SZ3 and ZIF-8, respectively.

Table 5B.4. Adsorption and photodegradation of [MB] = 0.5×10^{-5} M or 1.6 mg L^{-1}, catalysts amount = 10 mg, pH = 7.89 and time length for adsorption/photodegradation = 120 min.

S.N.	Materials	Adsorption capacity (mg/g) [% Dye removal]	%Photodehtadation
1.	Control (Pure MB)	-	22.0
2.	SZ	0.33 [10.31]	85.56
3.	SZ1	0.52 [16.12]	90.56
4.	SZ2	0.14 [4.5]	97.25
5.	SZ3	0.32 [10]	86.43
6.	ZIF-8	0.26 [8.06]	84.18

Table 5B.5. Adsorption and photodegradation of [CR] = 2×10^{-5} M, catalysts amount = 10 mg, pH = 7.97, time length for adsorption 120 min while degradation time length was taken only 40 min because SZ2 composite can degrade CR dye within 40 min.

S.N.	Materials	Adsorption capacity (mg/g) [% Dye removal]	%Photodehtadation
1.	Control (Pure CR)	-	3.44
2.	SZ	26.79 [96.18]	98.09
3.	SZ1	26.16 [93.89]	96.18
4.	SZ2	27.22 [97.70]	100
5.	SZ3	22.44 [80.53]	97.70
6.	ZIF-8	25.52 [91.60]	95.80

5B.3.9. Plausible Degradation Mechanism

AgNPs@ZIF-8 composite degrades MB and CR dye under UV-visible light irradiation (50 Watt halogen lamp) which is shown in Fig. 5B.17. As a result of HOMO to LUMO charge transfer in ZIF-8 [18], e^- moves easily from valence band (VB) to conduction band (CB). Further, metallic AgNPs act as e^- scavenger facilitating the transfer of photogenerated ZIF-8 conduction band e^- due to SPR [7]. Hence, photo-induced e^- and h^+ due to synergistic effect of AgNPs and ZIF-8 can easily react with oxygenated water and it can produce reactive oxidative species (ROS) such as H^+, $OH^{\bullet}$ which are probably responsible for photocatalytic degradation of both dye molecules. The ROS plays a key role for photocatalytic degradation of both the dye molecules which is proved by scavenger analysis with other catalysts (AgNPs@ZIF-11 in previous Section 5A.3.8.5) using MB dye.

5B.3.10. GC-MS Analysis

The degraded by-products of MB and CR were analyzed by GC-MS analysis. The plausible degradation path of MB is already shown in previous Chapter three (Scheme 3.2) while the degradation path of CR is depicted in Scheme 5B. 3. The mass spectra of degraded MB and CR are provided in Fig. 5B.18 and Fig. 5B.19, respectively. The dye molecules break down into smaller molecules and after long irradiation time the organic molecules completely may mineralize into inorganic ions [30].

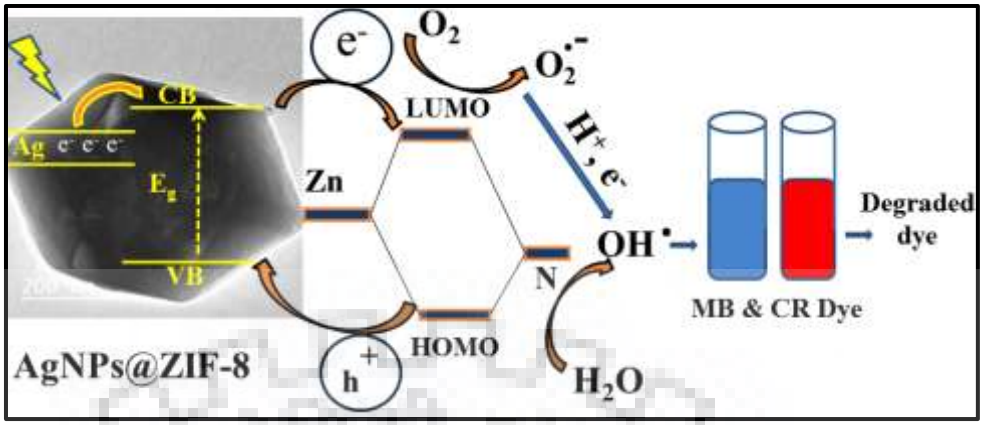

Fig. 5B.17. Illustration of proposed mechanism for MB and CR dye degradation using AgNPs@ZIF-8 composite under UV-visible light.

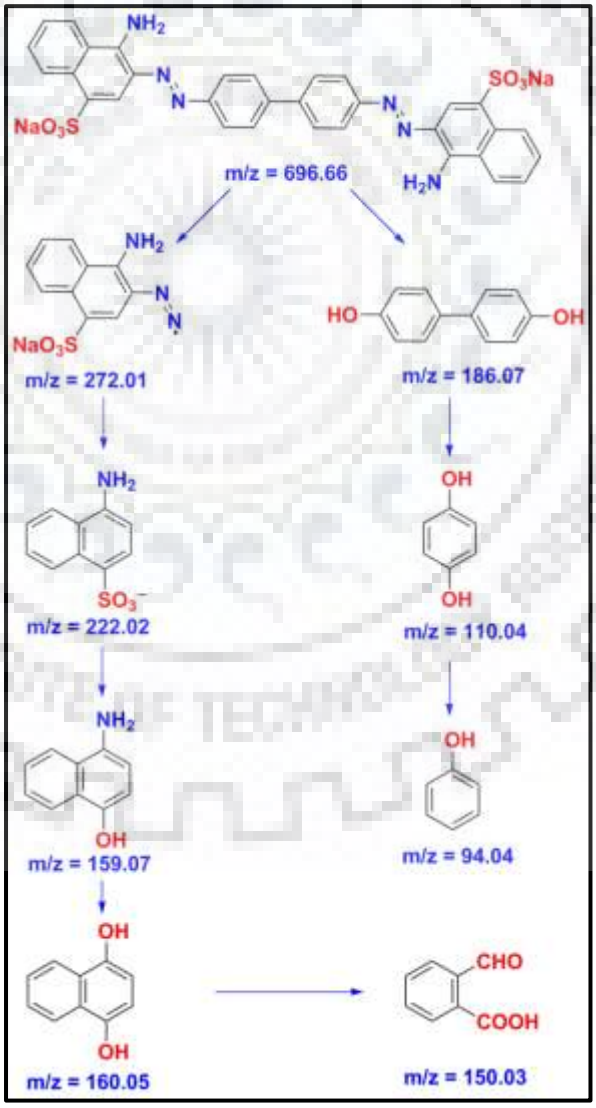

Scheme 5B.3. Proposed photocatalytic degradation pathway of CR dye using SZ2 composite.

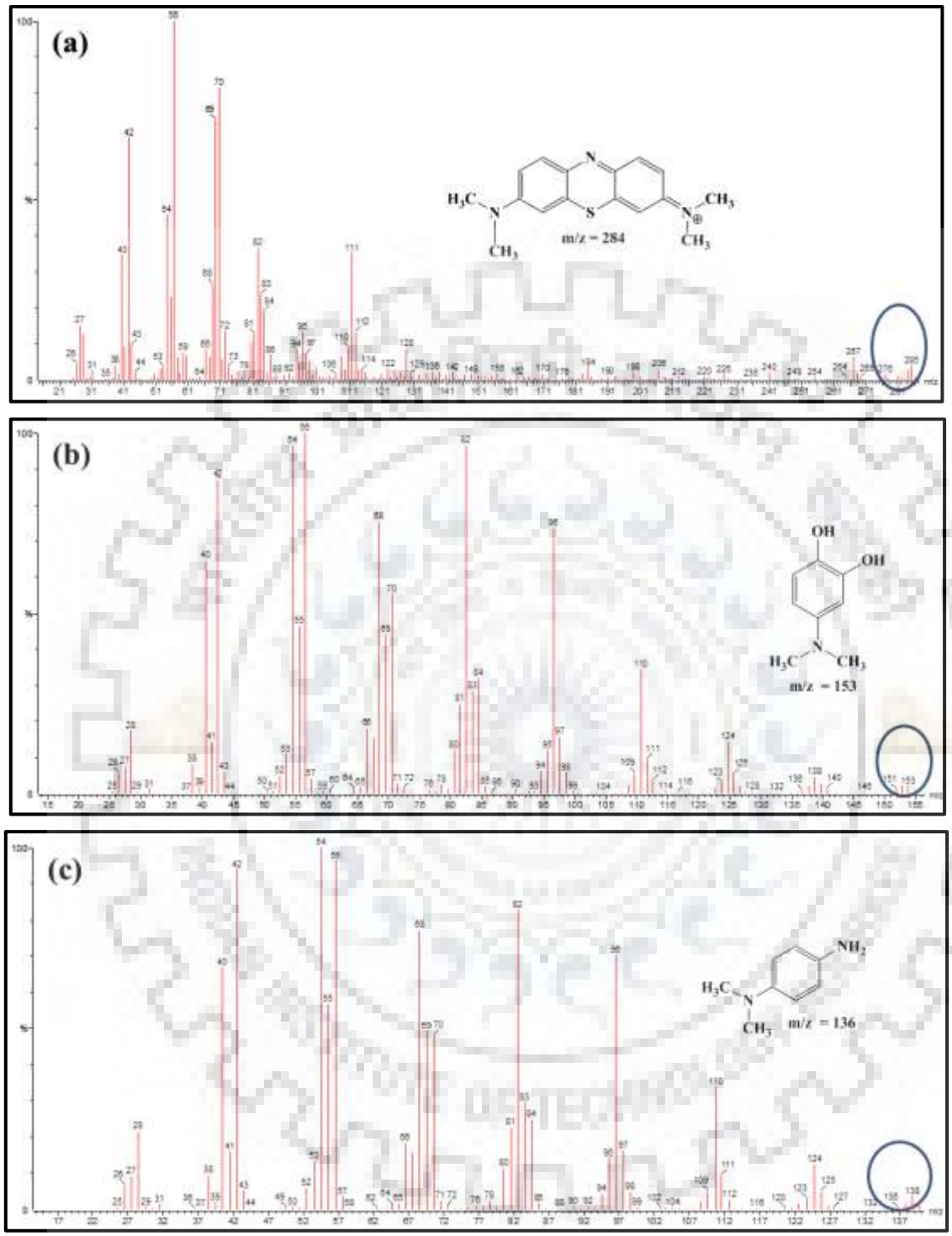

Fig. 5B.18. (a-c) GC-MS spectra of plausible fragments of MB degraded by-products.

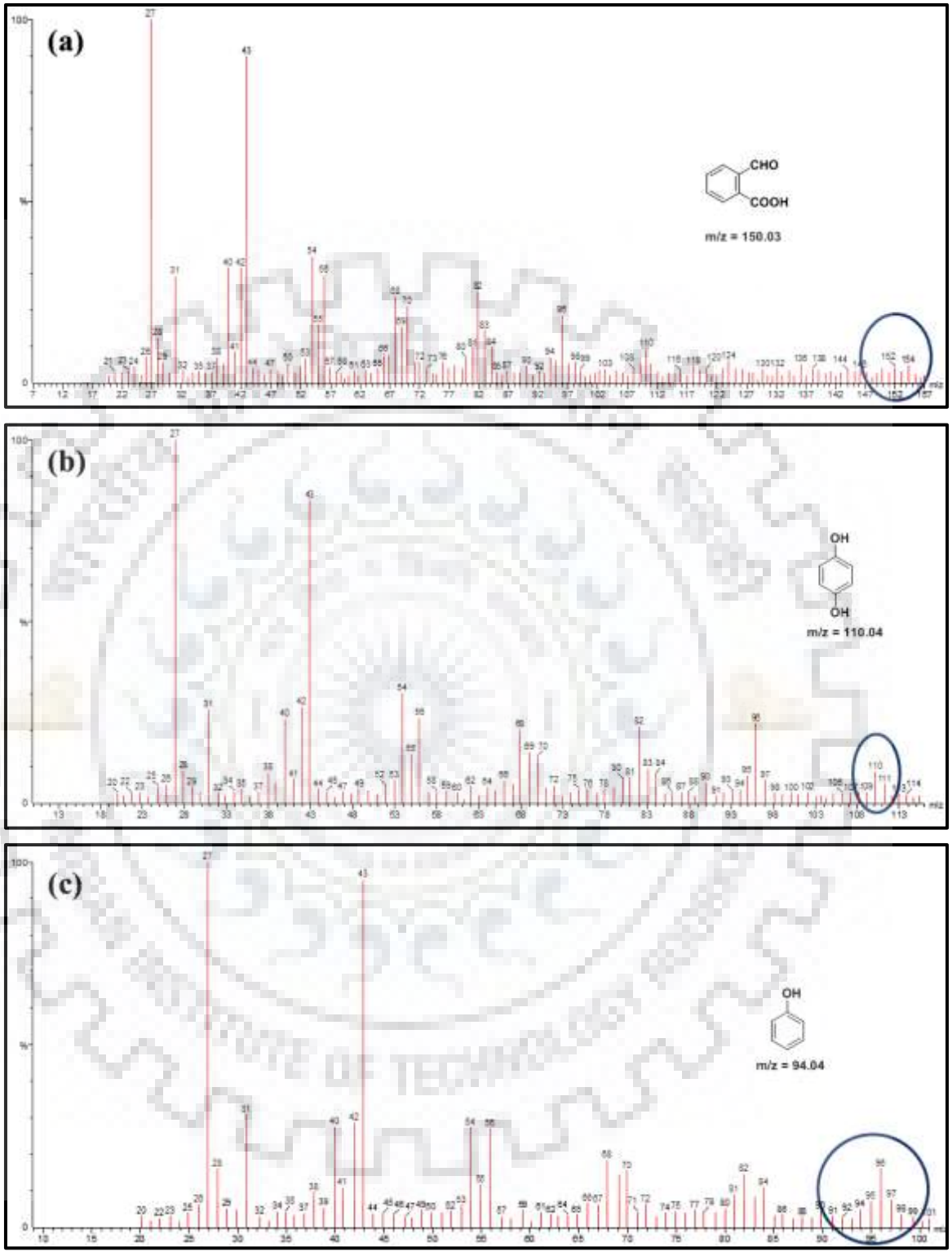

Fig. 5B.19. (a-c) GC-MS spectra of plausible fragments of CR degraded by-products.

5B.4. CONCLUSION

In summary, AgNPs@ZIF-8 composites (SZ, SZ1, SZ2 and SZ3) have been synthesized successfully and utilized as photocatalysts for the removal of industrial pollutants such as MB and CR. The SZ2 composite was found to exhibit more degradation efficiency towards MB and CR. Further, SZ2 composite also displays excellent adsorbent capacity for CR adsorption.

NOTE: The work of this Chapter is under communication in peer reviewed journal as given below.

1. R. Chandra, and M. Nath, "Toluene Assisted Synthesis of ZIF-11 and Multi-Core-Shell AgNPs@ZIF-11 composite with rho Topology: As an Effective Photocatalysts for Industrial Pollutants" under communication.
2. R. Chandra and M. Nath, "Controlled Synthesis of AgNPs@ZIF-8 Composite for Enhanced Photocatalytic degradation of Methylene Blue and Congo Red" under communication.

5.5. REFERENCES

(1) Morris, W.; He, N.; Ray, K. G.; Klonowski, P.; Furukawa, H.; Daniels, I. N.; Houndonougbo, Y. A.; Asta, M.; Yaghi, O. M.; Laird, B. B. A Combined Experimental-Computational Study on the Effect of Topology on Carbon Dioxide Adsorption in Zeolitic Imidazolate Frameworks. *J. Phys. Chem. C* **2012**, *116* (45), 24084-24090.

(2) Assfour, B.; Leoni, S.; Seifert, G. Hydrogen Adsorption Sites in Zeolite Imidazolate Frameworks ZIF-8 and ZIF-11. *J. Phys. Chem. C* **2010**, *114* (31), 13381-13384.

(3) Sánchez-Laínez, J.; Zornoza, B.; Mayoral, Á.; Berenguer-Murcia, Á.; Cazorla-Amorós, D.; Téllez, C.; Coronas, J. Beyond the H_2/CO_2 Upper Bound: One-step Crystallization and Separation of Nano-sized ZIF-11 by Centrifugation and its Application in Mixed Matrix Membranes. *J. Mater. Chem. A* **2015**, *3* (12), 6549-6556.

(4) Sánchez-Laínez, J.; Zornoza, B.; Téllez, C.; Coronas, J. On the Chemical Filler-Polymer Interaction of Nano and Micro-sized ZIF-11 in PBI Mixed Matrix Membranes and Their Application for H_2/CO_2 Separation. *J. Mater. Chem. A* **2016**, *4* (37), 14334-14341.

(5) Ehsani, A.; Pakizeh, M. Synthesis, Characterization and Gas Permeation Study of ZIF-11/Pebax® 2533 Mixed Matrix Membranes. *J. Taiwan Inst. Chem. E.* **2016**, *66*, 414-423.

(6) Boroglu, M. S.; Yumru, A. B. Gas Separation Performance of 6FDA-DAM-ZIF-11 Mixed-Matrix Membranes for H_2/CH_4 and CO_2/CH_4 Separation. *Sep. Purif. Technol.* **2017**, *173*, 269-279.

(7) Grabowska, E.; Zaleska, A.; Sorgues, S.; Kunst, M.; Etcheberry, A.; Colbeau-Justin, C.; Remita, H. Modification of Titanium (IV) Dioxide with Small Silver Nanoparticles: Application in Photocatalysis. *J. Phys. Chem. C* **2013**, *117* (4), 1955-1962.

(8) Tian, Y.; Tatsuma, T. Mechanisms and Applications of Plasmon-induced Charge Separation at TiO_2 Films Loaded with Gold Nanoparticles. *J. Am. Chem. Soc*. **2005**, *127* (20), 7632-7637.

(9) Kowalska, E.; Abe, R.; Ohtani, B. Visible Light-Induced Photocatalytic Reaction of Gold-modified Titanium (IV) Oxide Particles: Action Spectrum Analysis. *Chem. Commun.* **2009**, (2), 241-243.

(10) Kominami, H.; Tanaka, A.; Hashimoto, K. Mineralization of Organic Acids in Aqueous Suspensions of Gold Nanoparticles Supported on Cerium (IV) Oxide Powder under Visible Light Irradiation. *Chem. Commun.* **2010**, *46* (8), 1287-1289.

(11) Kominami, H.; Tanaka, A.; Hashimoto, K. Gold Nanoparticles Supported on Cerium (IV) Oxide Powder for Mineralization of Organic Acids in Aqueous Suspensions under Irradiation of Visible Light of λ= 530 nm. *Appl. Catal. A: Gen.* **2011**, *397* (1-2), 121-126.

(12) Dong, X.; Ji, X.; Jing, J.; Li, M.; Li, J.; Yang, W. Synthesis of Triangular Silver Nanoprisms by Stepwise Reduction of Sodium Borohydride and Trisodium Citrate. *J. Phys. Chem. C* **2010**, *114* (5), 2070-2074.

(13) He, M.; Yao, J.; Liu, Q.; Zhong, Z.; Wang, H. Toluene-assisted Synthesis of RHO-type Zeolitic Imidazolate Frameworks: Synthesis and Formation Mechanism of ZIF-11 and ZIF-12. *Dalton Trans.* **2013**, *42* (47), 16608-16613.

(14) Hu, Y.; Kazemian, H.; Rohani, S.; Huang, Y.; Song, Y. *In situ* High Pressure Study of ZIF-8 by FTIR Spectroscopy. *Chem. Commun.* **2011**, *47* (47), 12694-12696.

(15) Tauc, J.; Grigorovici, R.; Vancu, A. Optical Properties and Electronic Structure of Amorphous Germanium. *Phys. Status Solidi B* **1966**, *15* (2), 627-637.

(16) Xie, K.; Sun, L.; Wang, C.; Lai, Y.; Wang, M.; Chen, H.; Lin, C. Photoelectrocatalytic Properties of Ag Nanoparticles Loaded TiO_2 Nanotube Arrays Prepared by Pulse Current Deposition. *Electrochim. Acta* **2010**, *55* (24), 7211-7218.

(17) Zhao, M.; Cao, Y.; Liu, X.; Deng, J.; Li, D.; Gu, H. Effect of Nitrogen Atomic Percentage on N^+-bombarded MWCNTs in Cytocompatibility and Hemocompatibility. *Nanoscale Res. Lett.* **2014**, *9* (1), 142.

(18) Jing, H. P.; Wang, C. C.; Zhang, Y. W.; Wang, P.; Li, R. Photocatalytic Degradation of Methylene Blue in ZIF-8. *RSC Adv.* **2014**, *4* (97), 54454-54462.

(19) Saravanan, R.; Manoj, D.; Qin, J.; Naushad, M.; Gracia, F.; Lee, A. F.; Khan, M. M.; Gracia-Pinilla, M. Mechanothermal Synthesis of Ag/TiO_2 for Photocatalytic Methyl Orange Degradation and Hydrogen Production. *Process Saf. Environ.* **2018**, *120*, 339-347.

(20) Yin, K.; Shao, M.; Zhang, Z.; Lin, Z. A Single-source Precursor Route to Ag/SnO2 Heterogeneous Nanomaterials and its Photocatalysis in Degradation of Conco Red. *Mater. Res. Bull.* **2012**, *47* (11), 3704-3708.

(21) Rashid, J.; Barakat, M.; Salah, N.; Habib, S. S. Ag/ZnO Nanoparticles Thin Films as Visible Light Photocatalysts. *RSC Adv.* **2014**, *4* (100), 56892-56899.

(22) Ai, L.; Zeng, C.; Wang, Q. One-step Solvothermal Synthesis of Ag-Fe_3O_4 Composite as a Magnetically Recyclable Catalyst for Reduction of Rhodamine B. *Catal. Commun.* **2011**, *14* (1), 68-73.

(23) Sun, L.; Wu, W.; Yang, S.; Zhou, J.; Hong, M.; Xiao, X.; Ren, F.; Jiang, C. Template and Silica Interlayer Tailorable Synthesis of Spindle-like Multilayer α-Fe_2O_3/Ag/SnO_2 Ternary Hybrid Architectures and Their Enhanced Photocatalytic Activity. *ACS Appl. Mater. Interfaces* **2014**, *6* (2), 1113-1124.

(24) Grabowska, E.; Zaleska, A.; Sorgues, S.; Kunst, M.; Etcheberry, A.; Colbeau-Justin, C.; Remita, H. Modification of Titanium (IV) Dioxide with Small Silver Nanoparticles: Application in Photocatalysis. *J. Phy. Chem. C* **2013**, *117* (4), 1955-1962.

(25) Jiang, H. L.; Akita, T.; Ishida, T.; Haruta, M.; Xu, Q. Synergistic Catalysis of Au@ Ag Core-shell Nanoparticles Stabilized on Metal-Organic Frameworks. *J. Am. Chem. Soc.* **2011**, *133* (5), 1304-1306.

(26) Dai, H.; Xia, B.; Wen, L.; Du, C.; Su, J.; Luo, W.; Cheng, G. Synergistic Catalysis of AgPd@ZIF-8 on Dehydrogenation of Formic Acid. *Appl. Catal. B: Environ.* **2015**, *165*, 57-62.

(27) Liu, X.; He, L.; Zheng, J.; Guo, J.; Bi, F.; Ma, X.; Zhao, K.; Liu, Y.; Song, R.; Tang, Z. Solar-light-driven Renewable Butanol Separation by Core-shell Ag@ZIF-8 Nanowires. *Adv. Mater.* **2015**, *27* (21), 3273-3277.

(28) Guo, Y. F.; Fang, W. J.; Fu, J. R.; Wu, Y.; Zheng, J.; Gao, G. Q.; Chen, C.; Yan, R. W.; Huang, S. G.; Wang, C. C. Facile Synthesis of Ag@ ZIF-8 Core-shell Heterostructure Nanowires for Improved Antibacterial Activities. *Appl. Surf. Sci.* **2018**, *435*, 149-155.

(29) Zhang, M.; Yang, Y.; Li, C.; Liu, Q.; Williams, C. T.; Liang, C. PVP-Pd@ZIF-8 as Highly Efficient and Stable Catalysts for Selective Hydrogenation of 1, 4-butynediol. *Catal. Sci. Technol.* **2014**, *4*, 329-332.

(30) Houas, A.; Lachheb, H.; Ksibi, M.; Elaloui, E.; Guillard, C.; Herrmann, J. M. Photocatalytic Degradation Pathway of Methylene Blue in Water. *Appl. Catal. B: Environ.* **2001**, *31* (2), 145-157.

Chapter Six

Synthesis of ZnO-SnO_2 Nanocomposite Decorated ZIF-8 Composite: A Potential Photocatalyst

"Live as if you were to die tomorrow. Learn as if you were to live forever."

Mahatma Gandhi

This chapter contains two sections. **Section-A** deals with the detailed synthesis and characterization of ZnO-SnO_2 nanocomposite while **Section-B** describes the synthesis of ZnO-SnO_2 nanocomposite decorated ZIF-8 composites and their photocatalytic application.

SECTION A

6A.1. INTRODUCTION

Over past two decades, mixed metal oxide nanoparticles or hetero-nanostructures have been extensively studied owing to their fascinating properties such as nanoscale dimension, high sensitivity, low production cast, ease of fabrication and potent applications in the various fields. Thus, TiO_2-ZnO [1], TiO_2-SnO_2 [2], TiO_2-Fe_3O_4 [3], TiO_2-WO_3 [4], ZnO-WO_3 [5] and ZnO-SnO_2 [6] nanostructures have been synthesized for their widespread applications in various fields such as sensing, electrochemical analysis, photovoltaic conversion and photocatalysis. Among them, SnO_2 nanoparticles based mixed metal oxides have much attention for the photocatalysis due to better electron acceptor properties of SnO_2NPs as compared to TiO_2NPs and ZnONPs [6]. Nonetheless, bare metal oxides were also used as photocatalysts but in that case there are some limitations for e.g. fast recombination of photogenerated electron and hole (e^- and h^+) pair. Hence, many efforts have been dedicated to minimize the recombination of e^- and h^+ pair, *viz.*, various metal oxides were fabricated and obtained as hetero-nanostructures or core-shell structures. Literature overview of synthesis methods, characterization and applications of ZnO-SnO_2 nanocomposites/hetero-nanostructures are compiled in Table 6A.1. Among semiconducting metal oxide nanoparticles (NPs), ZnONPs are found suitable and efficient photocatalysts [1(a)] and SnO_2 is well-known large band gap multifunction material with good electron acceptor properties, [6] that's why it is envisioned to synthesize ZnO-SnO_2 nanocomposite.

This section describes synthesis of ZnO-SnO_2 nanocomposites *via* sol-gel and grinding method and characterization by various spectroscopic methods. From the literature overview, it has been found that grinding method is not reported for synthesis of ZnO-SnO_2 nanocomposites so far. Further, it has been found that ZnO-SnO_2 nanocomposites show efficient photocatalytic activity towards MB degradation.

Table 6A.1: Literature overview on ZnO-SnO_2 nanocomposites [6-19].

Materials	Synthesis methods	Applications	Ref.
SnO_2-ZnO Heterojunction	Hydrothermal	Photocatalysis	**6**
Lanthanum doped ZnO/SnO_2 thin film	Spray pyrolysis	Ethanol sensitivity	**7**
Indium substituted ZnO/SnO_2	Solid-state reaction	Electrochemical analysis	**8**
ZnO/SnO_2 Nano-structure	Co-precipitation	Photocatalysis	**9(a),(b),(c)**
ZnO/SnO_2 Composite	Electrochemical deposition	Dye sensitized solar cell (DSSC)	**10(a),(b)**
T-ZnO/SnO_2 Core-shell heterostrucure	Electro-spray deposition	Optical properties	**11**
ZnO-SnO_2 Nanocomposites	Micro-emulsion method	Sensing	**12(a), (b)**
ZnO-SnO_2 Hierarchical structure	Hydrothermal	Luminescence properties	**13**
SnO_2/ZnO Heterojunction Nano-catalysts	Solvothermal	Photocatalysis	**14**
Electrospun nanofibers of ZnO-SnO_2 Heterojunction	Sol-gel and Electrospinning Technology	Photocatalysis	**15**
SnO_2 Nanoparticles/ ZnO Nanotetrapods composite	Ultrasonic treatment	Dye sensitized solar cell (DSSC)	**16**
ZnO-SnO_2 Core-shell nanowires	Ultrasonic treatment	Gas Sensing	**17**
ZnO/SnO_2 Nanocomposites thin film	Sol-gel and dip coating method	Antibacterial activity	**18**
ZnO- core /SnO_2-shell nanorods	Thermal evaporation and deposition method	Optical properties	**19**

6A.2. EXPERIMENTAL SECTION

6A.2.1. Synthesis of ZnONPs

ZnONPs were synthesized by using a reported method [20] with slight modifications. 1 mM zinc acetate dihydrate ($Zn(CH_3COO)_2.2H_2O$; (0.21951 g)) was dissolved into 20 mL methanol and kept on refluxing with constant stirring at 80 °C for 3 h. After that NH_4OH

solution was added into the above resultant solution and maintained the pH ≥ 8. The resultant reaction mixture was aged for 12 h. The white residue was collected by centrifugation and washed it with deionized water (DI H_2O) and methanol to remove the unreacted species. Finally, the white powder was obtained after the calcination at 500 °C for 5 h.

6A.2.2. Synthesis of SnO_2NPs

SnO_2NPs was synthesized by grinding method which is already explained in the previous Chapter four.

6A.2.3. Synthesis of ZnO-SnO_2 Nanocomposites

Following two methods have been employed for synthesis of ZnO-SnO_2 nanocomposites.

6A.2.3.1. Sol-Gel Method

Synthesis of ZnO-SnO_2 nanocomposites by sol-gel method is depicted in scheme 6A.1. According to this method, 1 mM of zinc acetate dihydrate ($Zn(CH_3COO)_2.2H_2O$; (0.21951 g)) was dissolved into 20 mL methanol and kept on refluxing with constant stirring at 80 °C for 3 h. To this was added 1 mM of tintetrachloridepentahydrate ($SnCl_4.5H_2O$; (0.350 g)) and kept on stirring for another 3 h. The pH of resultant reaction mixture was maintained at 8 with the addition of NH_4OH solution. The above reaction mixture was aged for 12 h to yield creamy-white gel. The creamy-white precipitate was collected by centrifugation, washed with methanol and dried at *ca.* 100 °C. Resultant, creamy-white powder was calcined at 800 °C for 6 h. The molar ratio of Zn:Sn has been varied and synthesized five ZnO-SnO_2 nanocomposites having Zn:Sn ratio of 1:1, 2:8, 4:6, 6:4 and 8:2 which are abbreviated as ZS-11, ZS-28, ZS-46, ZS-64 and ZS-82, respectively.

6A.2.3.2. Grinding Method

ZnO-SnO_2 nanocomposite was synthesized by grinding method [21] with slight modifications which is illustrated in scheme 6A.2. 1 mM of anhydrous zinc chloride ($ZnCl_2$; (0.136 g)) and 1 mM of tintetrachloridepentahydrate ($SnCl_4.5H_2O$; (0.350 g)) were ground for 30 min using pestles and mortar. After that, 4 mM potassium hydroxide (KOH; 0.224 g) was added into the reaction mixture and ground for another 30 min at room temperature. The resultant reaction mixture was transferred into a round bottom flask (250 mL RB) with 100 mL

DI H_2O and kept on stirring for 3 h. The product was washed with DI H_2O and the precipitate was collected by centrifugation. Creamy-white precipitate was calcined at 800°C for 6 h. The similar method has been adopted for the synthesis of ZnO-SnO_2 nanocomposite with molar ratio of Zn:Sn 1:1, 2:8, 4:6, 6:4 and 8:2 which are represented as ZS-A, ZS-B, ZS-C, ZS-D and ZS-E, respectively.

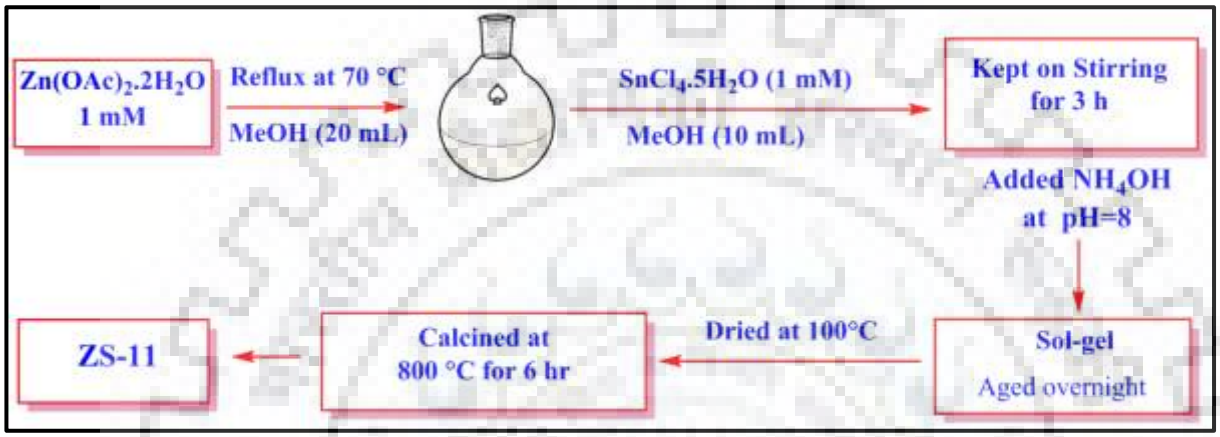

Scheme 6A.1. ZnO-SnO_2 (1:1) nanocomposite synthesized by using sol-gel method.

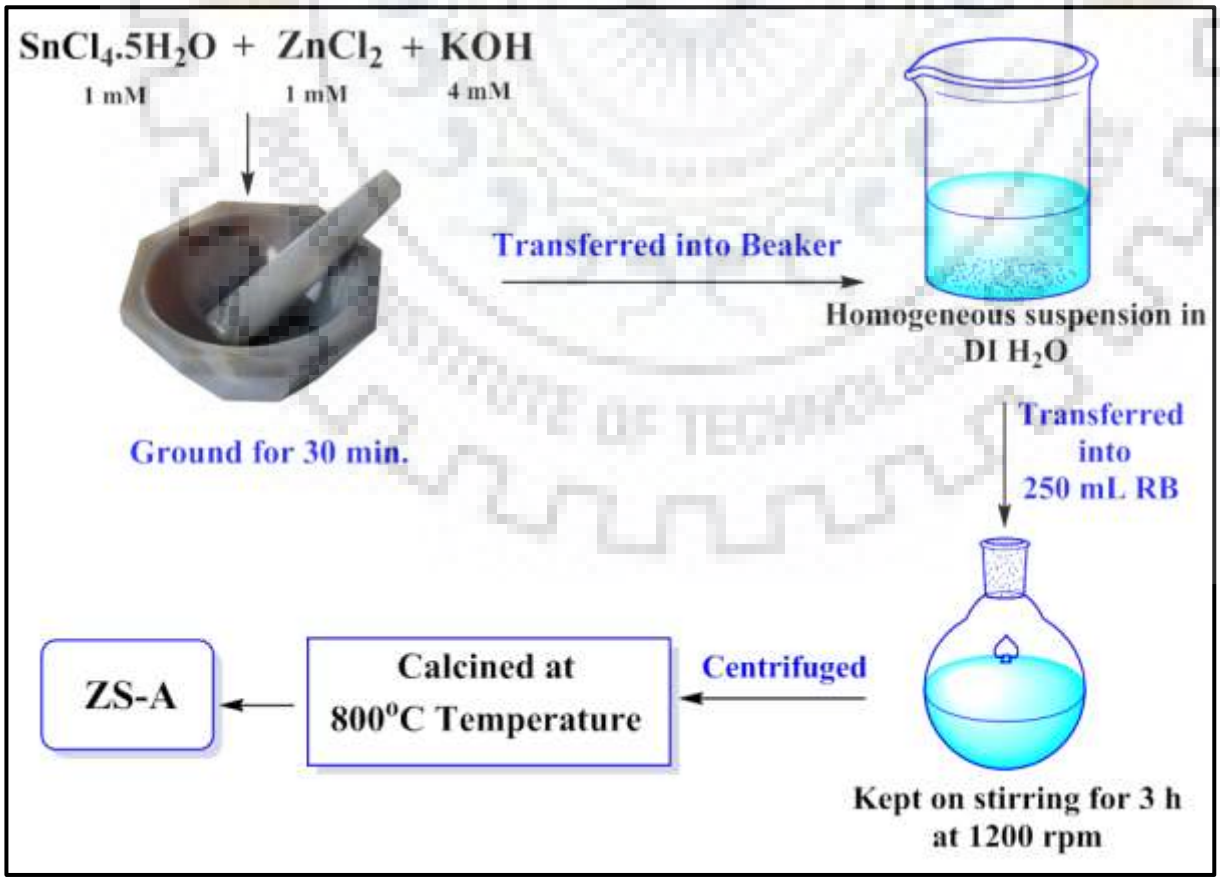

Scheme 6A.2. ZnO-SnO_2 (1:1) nanocomposite synthesized by using grinding method.

6A.3. RESULTS AND DISCUSSION

ZnO-SnO_2 nanocomposites have been synthesized by employing sol-gel and grinding methods with different molar ratio *i.e.*1:1, 2:8, 4:6, 6:4 and 8:2. Hence, 10 nanocomposites were obtained and characterized by various spectroscopic techniques.

6A.3.1. PXRD Analysis

Fig. 6A.1 shows powder X-ray diffraction (PXRD) patterns of synthesized ZnONPs, SnO_2NPs and their ZnO-SnO_2 nanocomposites. PXRD pattern of ZnONPs and SnO_2NPs are indexed with JCPDC No. 00-005-0664 and 01-072-1147, respectively.

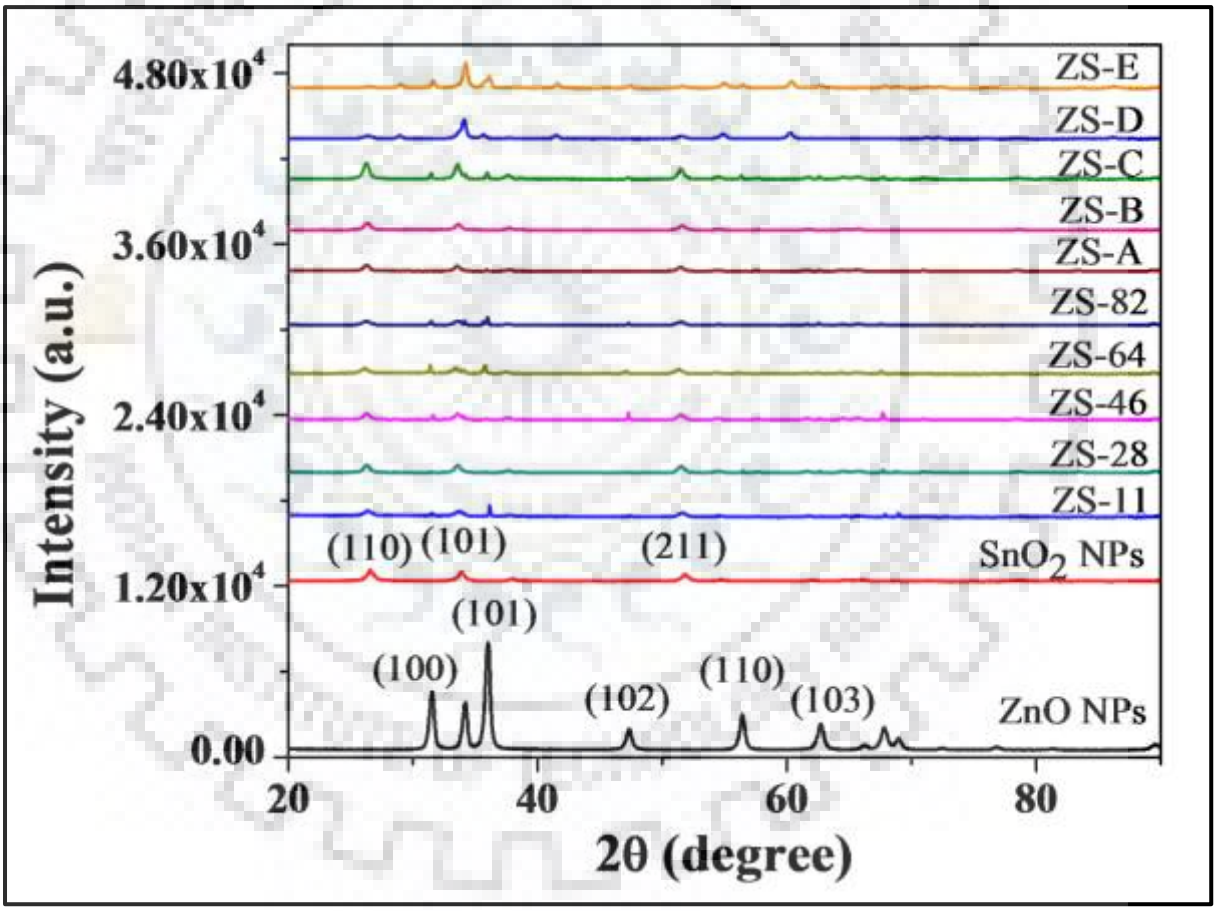

Fig. 6A.1. PXRD pattern of ZnONPs, SnO_2NPs and their ZnO-SnO_2 nanocomposites.

PXRD peaks of ZnONPs at 31.751°, 34.440°, 36.252°, 47.543°, 56.555°, 62.870°, and 67.917° correspond to the planes (100), (002), (101), (102), (110), (103) and (112), respectively, and PXRD peaks of SnO_2NPs at 26.591°, 33.888°, 37.959° and 51.787° correspond to the planes

(110), (101), (200) and (211), respectively. PXRD peaks of ZnONPs and SnO_2NPs at 34.440° and 33.888°, are merged in the composites.

6A.3.2. FT-IR Spectroscopic Studies

The FT-IR studies of ZnO-SnO_2 nanocomposites synthesized by both the methods have been performed in the range of 4000-400 cm^{-1}. The FT-IR spectra of synthesized ZnO-SnO_2 nanocomposites are illustrated in Fig. 6A.2. A broad and intense peak appears at 3443 cm^{-1} attributable to OH stretching vibrational frequency while a sharp peak at 1635 cm^{-1} corresponds to H-O-H bending vibration mode in each sample [6]. A broad peak observed at 689-624 cm^{-1} is due to Sn-O and Sn-O-Sn stretching vibration mode while peak at 484 cm^{-1} is assigned to Zn-O stretching vibration mode [22].

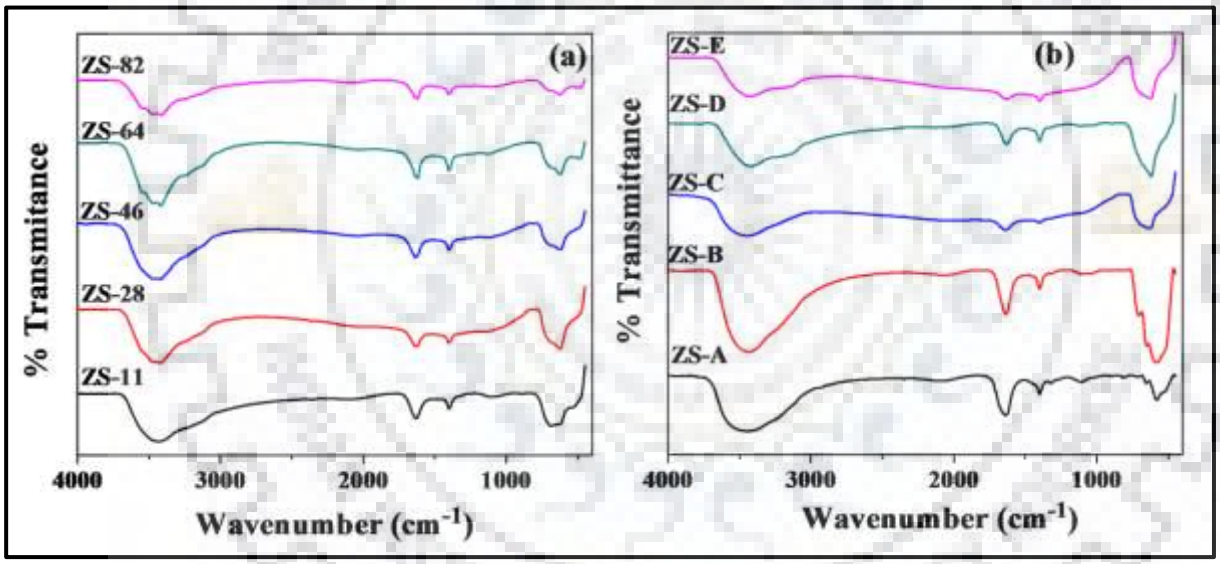

Fig. 6A.2. FT-IR spectra of synthesized ZnO-SnO_2 nanocomposites using (a) sol-gel and (b) grinding method.

6A.3.2. FE-SEM and HR-TEM Analysis

Morphology of ZnONPs, SnO_2NPs and their composites were ascertained by SEM analysis which is illustrated in Fig. 6A.3. ZnONPs have flower like morphology (Fig. 6A.3(a)) and SnO_2NPs appears as spherical dots (Fig. 6A.3(b)), while all the composites have spherical hetro-nanostructures (Fig. 6A.3(c-l)). Spherical dot hetero-nanostructures of ZnO-SnO_2 composites were also ensured by HR-TEM analysis. Fig. 6A.4 shows TEM images and SEAD patterns of ZnO-SnO_2 nanocomposites synthesized by using sol-gel method.

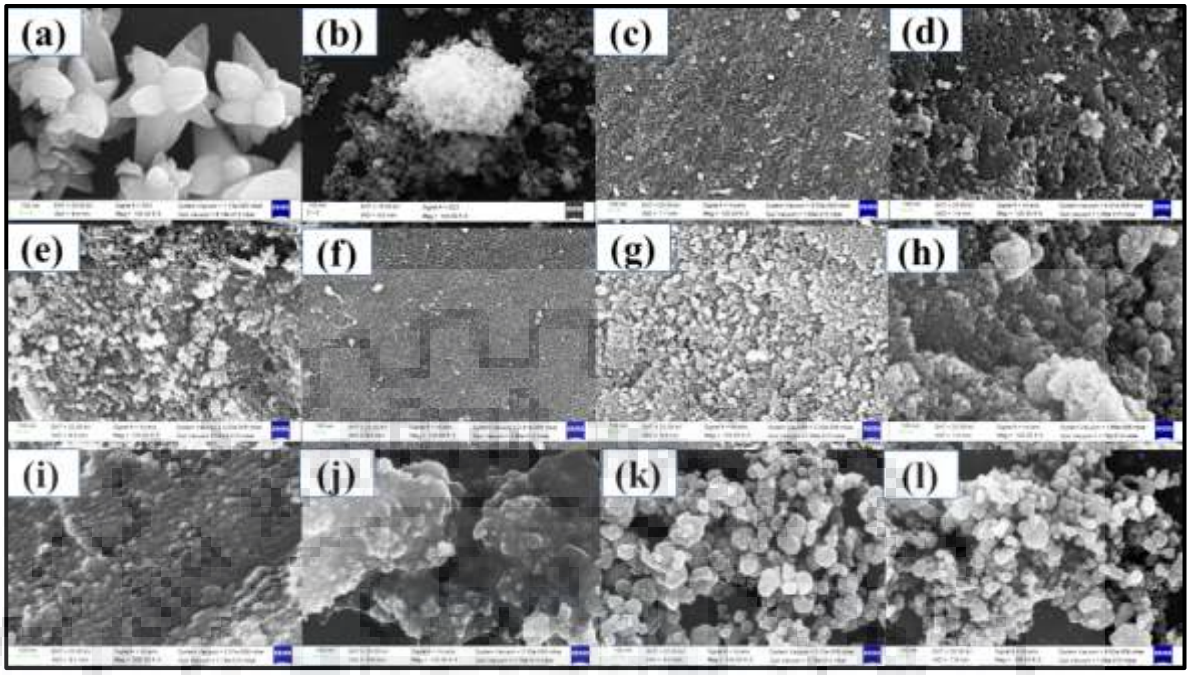

Fig. 6A.3. (a-l) SEM images of ZnONPs, SnO_2NPs, ZS-11, ZS-28, ZS-46, ZS-64, ZS-82, ZS-A, ZS-B, ZS-C, ZS-D and ZS-E nanocomposites, respectively.

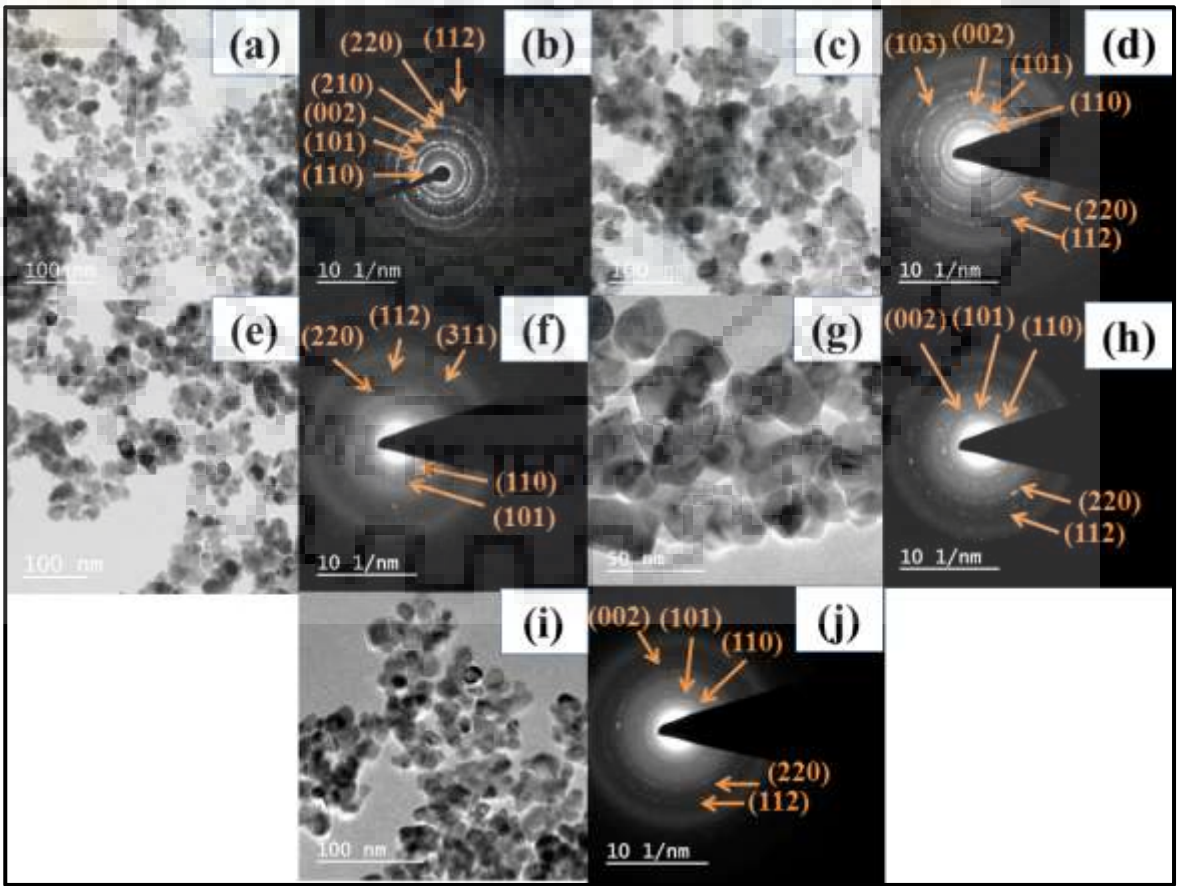

Fig. 6A.4. TEM images and their corresponding SEAD patters of (a, b) ZS-11, (c, d) ZS-28, (e, f) ZS-46, (g, h) ZS-64 and (i, j) ZS-82 nanocomposites.

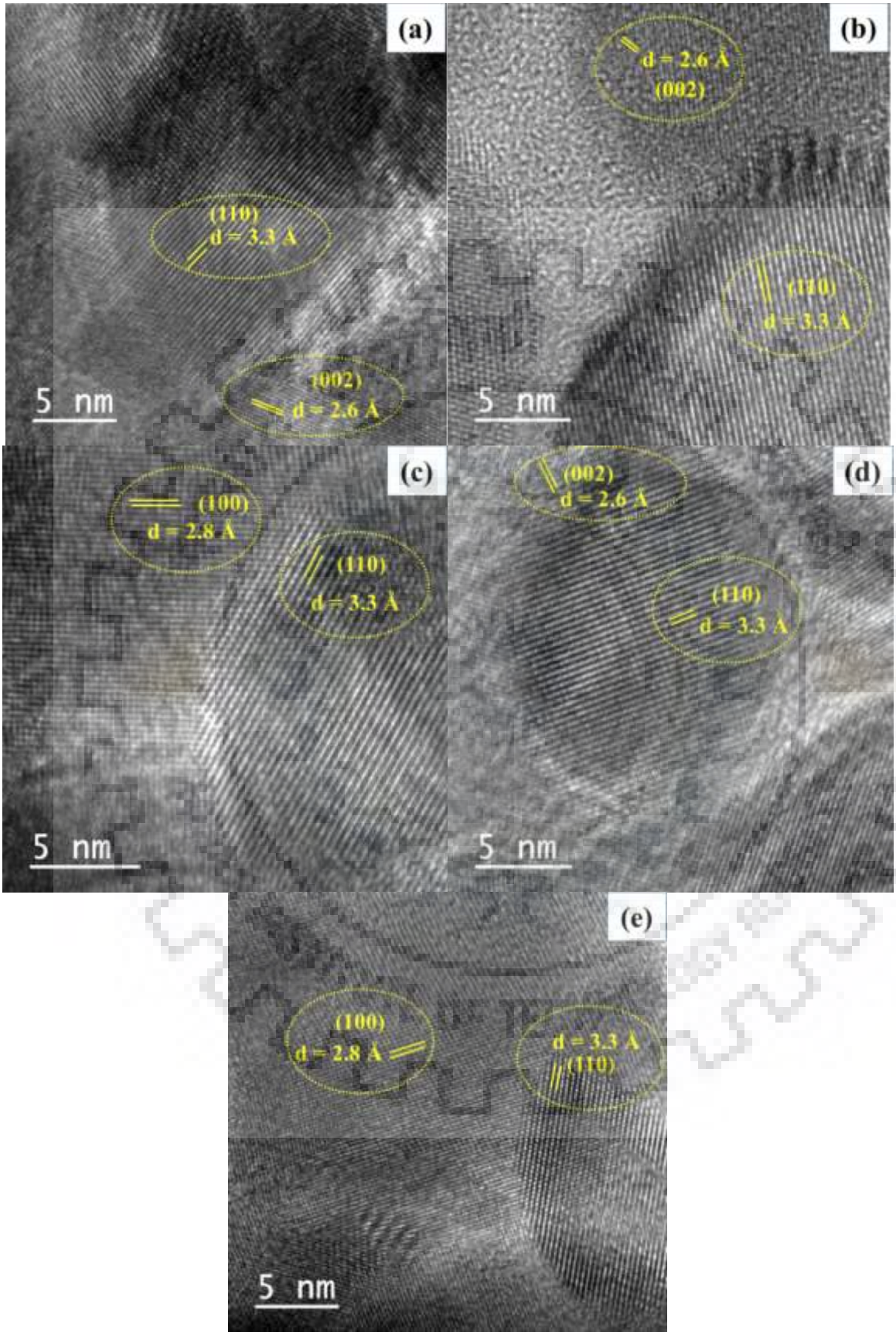

Fig. 6A.5. (a-e) HR-TEM images of ZS-11, ZS-28, ZS-46, ZS-64 and ZS-82 nanocomposites, respectively, showing interplanar spacings.

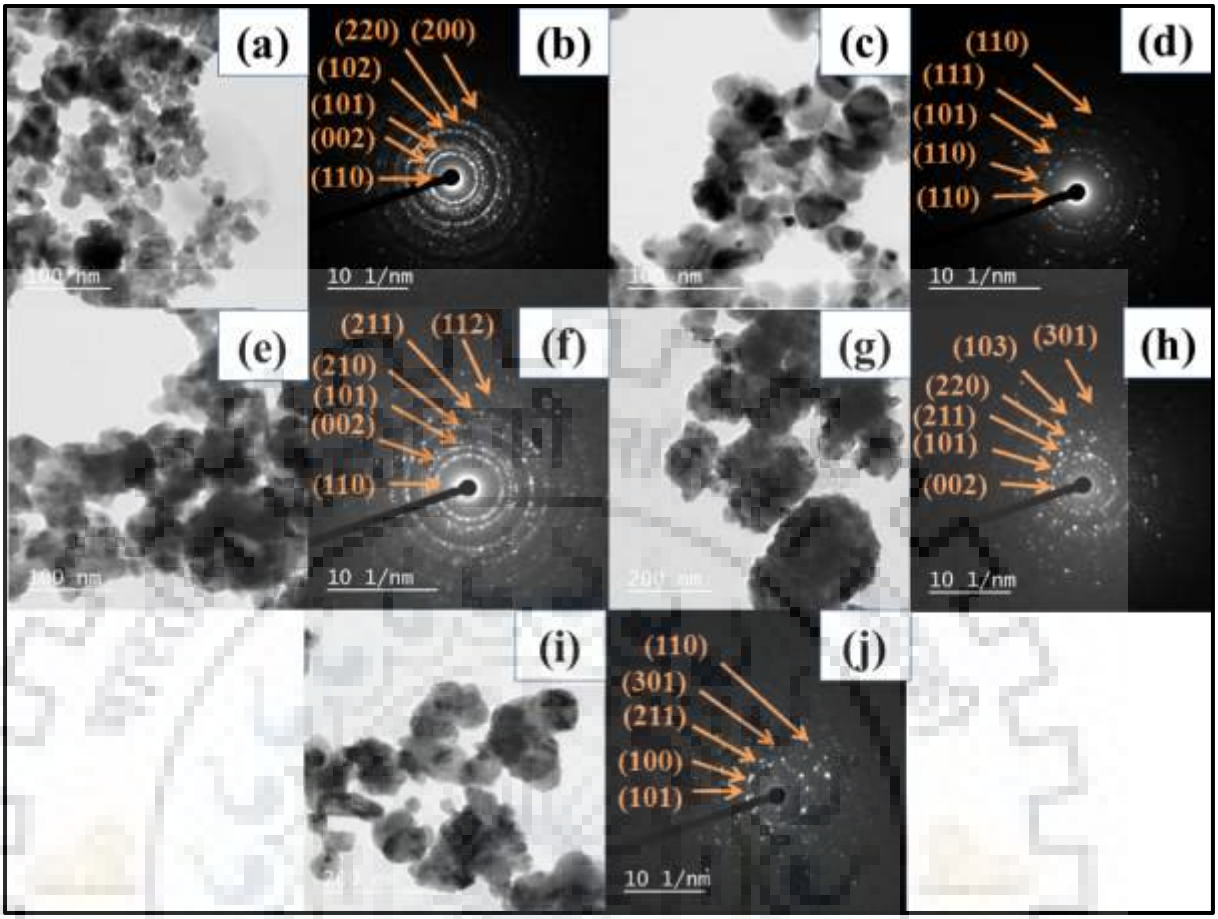

Fig. 6A.6. TEM images and their corresponding SEAD patterns of (a, b) ZS-A, (c, d) ZS-B, (e, f) ZS-C, (g, h) ZS-D and (i, j) ZS-E nanocomposites.

Moreover, HR-TEM micrographs of ZnO-SnO_2 nanocomposites (ZS-11, ZS-28, ZS-46, ZS-64 and ZS-82) also confirmed the crystallinity of ZnONPs and SnO_2NPs which is depicted in Fig. 6A.5. Similarly, ZnO-SnO_2 nanocomposites (ZS-A, ZS-B, ZS-C, ZS-D and ZS-E) synthesized by grinding method have also similar spherical uniform shape/morphology (Fig. 6A.6). The crystalline nature of ZnO-SnO_2 nanocomposites ZS-A, ZS-B, ZS-C, ZS-D and ZS-E and interplanar spacings are illustrated in Fig. 6A.7. The average particles size of synthesized ZnO-SnO_2 nanocomposite using both the methods were calculated by distribution plots using *ImageJ* software with the help of TEM images and the results are depicted in Fig. 6A.8 and Fig. 6A.9. It has been found that ZnO-SnO_2 nanocomposites have an average particle size in the rage of 15-20 nm.

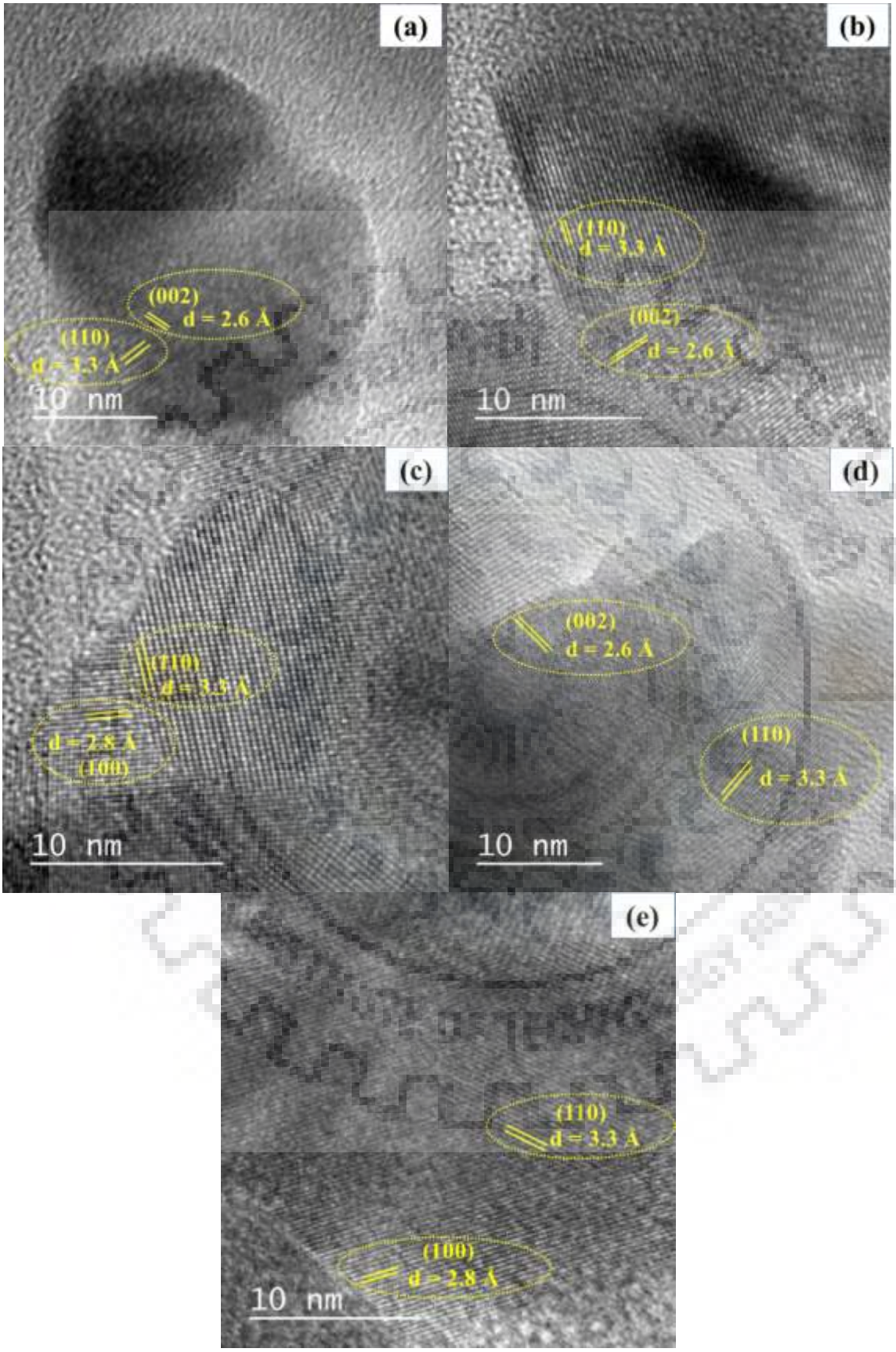

Fig. 6A.7. (a-e) HR-TEM analysis of ZS-A, ZS-B, ZS-C, ZS-D and ZS-E nanocomposites, respectively, showing interplanar spacings.

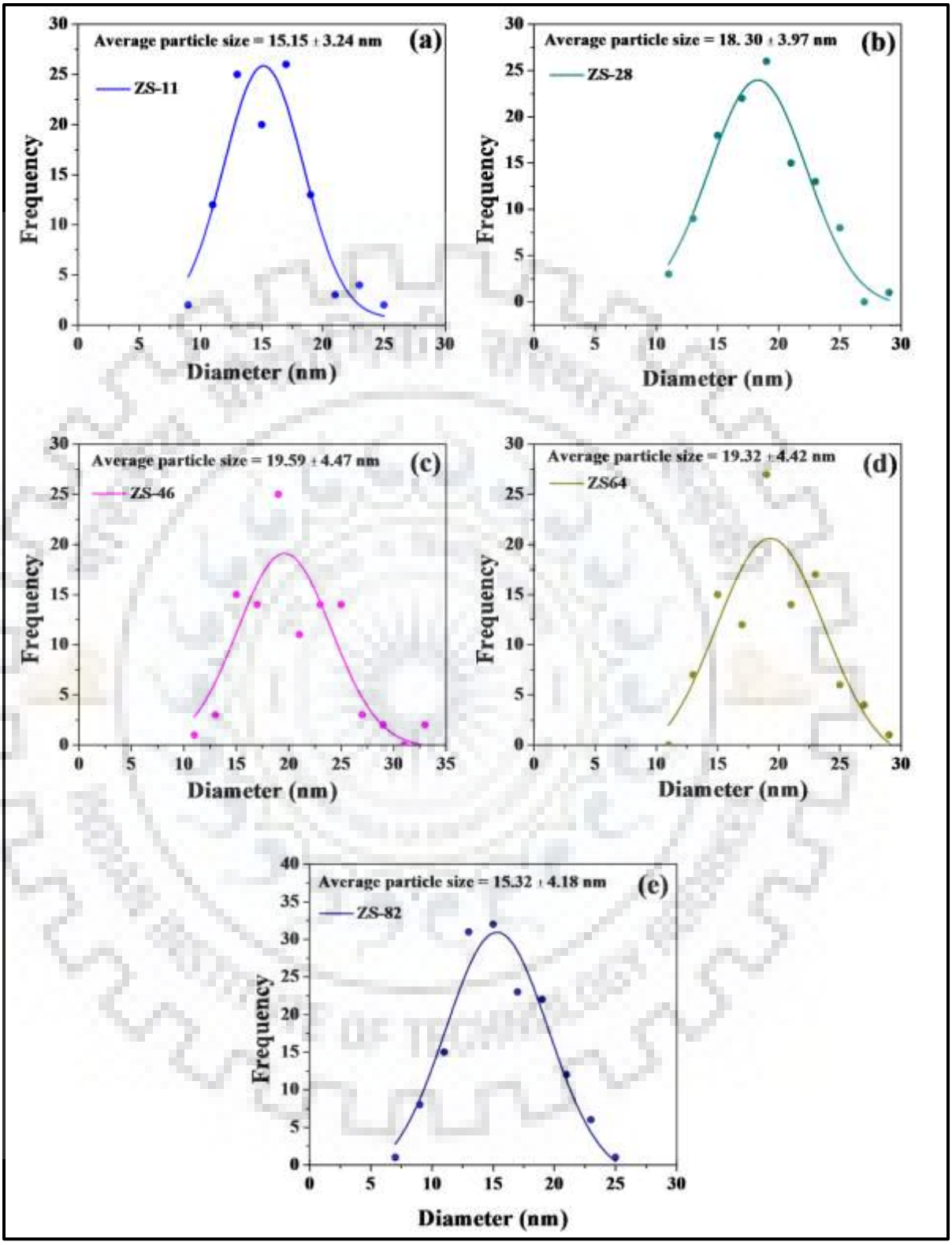

Fig. 6A.8. (a-e) Particle size distribution plots of ZS-11, ZS-28, ZS-46, ZS-64 and ZS-82 nanocomposites, respectively.

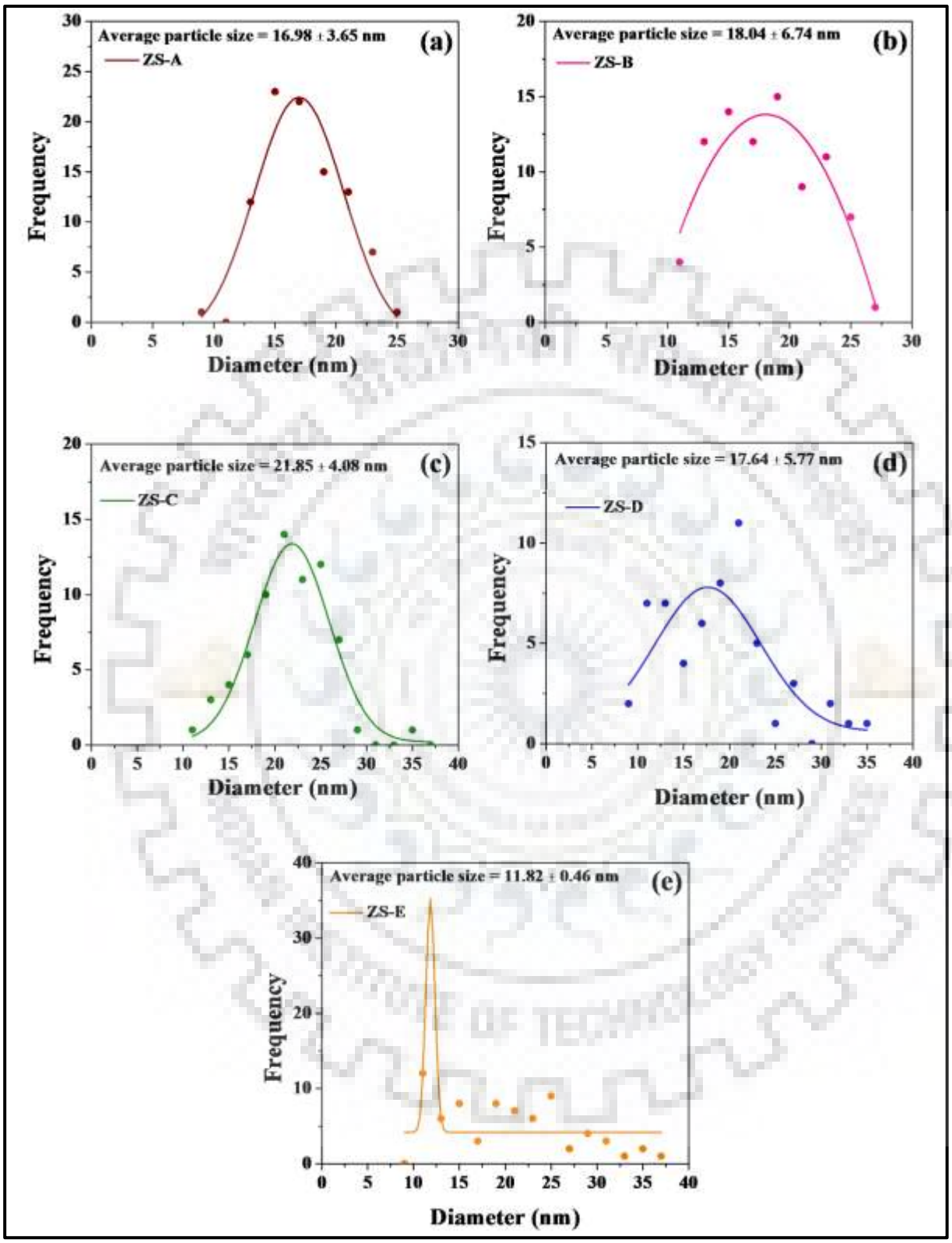

Fig. 6A.9. (a-e) Particle size distribution plots of ZS-A, ZS-B, ZS-C, ZS-D and ZS-E nanocomposites, respectively.

6A.3.4. UV-DRS Studies

The optical properties of synthesized ZnO-SnO_2 nanocomposites were examined by UV-DRS studies. Tauc method [23] has been employed for the calculation of band gap and the spectra were plotted by using direct and indirect transitions. The UV-DRS spectra are given in Fig. 6A.10 and the results are compiled in Table 6A.2. It is found that ZnO-SnO_2 nanocomposites synthesized by 1:1 molar ratio of Zn:Sn i.e. ZS-11 and ZS-A exhibits the lowest binding energies for indirect transition i.e. 3.17 eV and 3.0 eV, respectively while for the direct transition, the binding energies were estimated 4.01 eV and 3.98 eV, respectively.

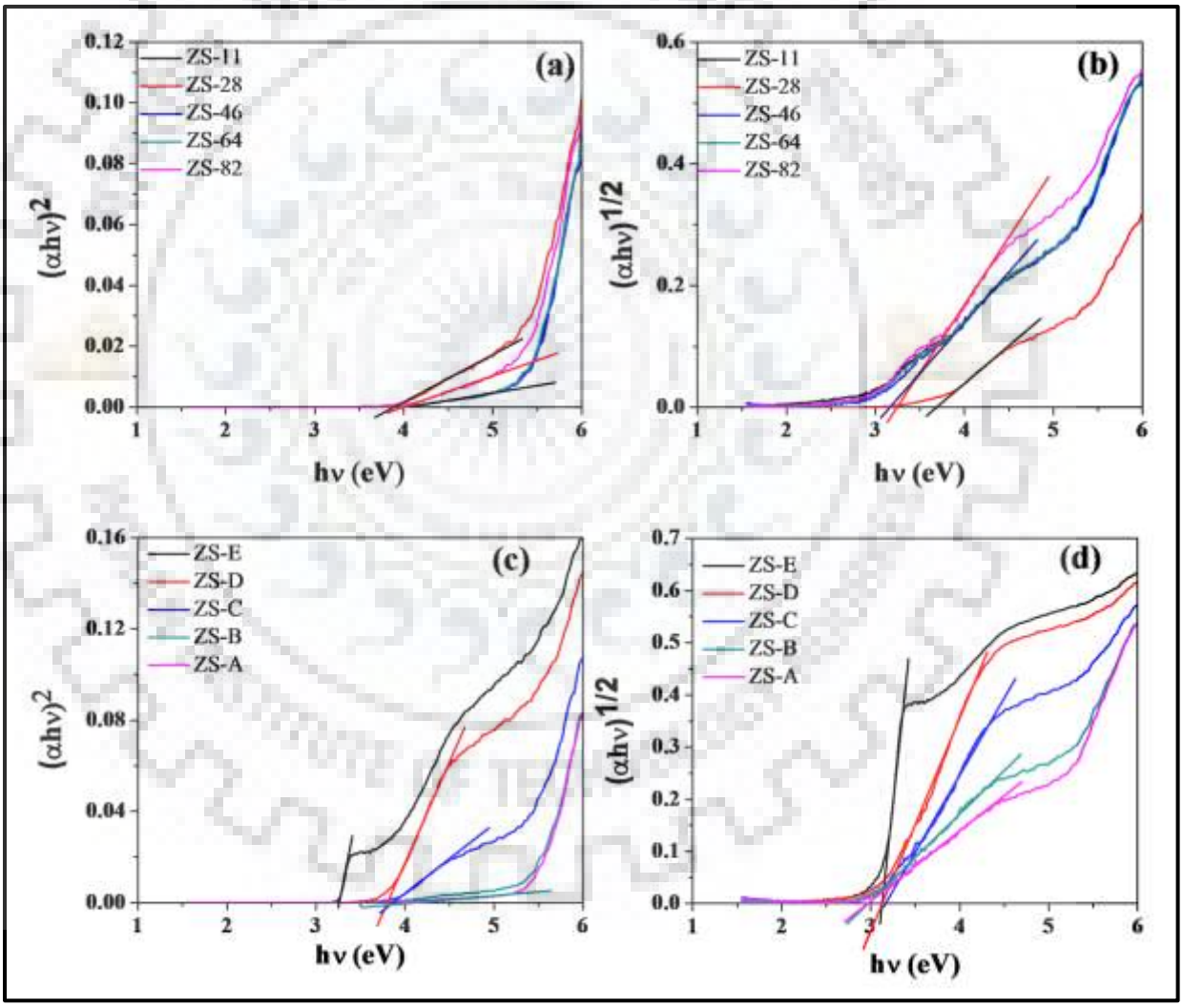

Fig. 6A.10. Typical Tauc plots of ZnO-SnO_2 nanocomposites by direct and indirect method synthesized by using sol-gel (a, b) and grinding method (c, d), respectively.

Table. 6A.2. UV-DRS analysis of ZnO-SnO_2 nanocomposites.

S.N.	Materials	Direct band gap (eV)	Indirect band gap (eV)
1.	ZS-11	4.01	3.17
2.	ZS-28	3.89	3.67
3.	ZS-46	4.01	3.17
4.	ZS-64	4.01	3.17
5.	ZS-82	3.98	3.25
6.	ZS-A	3.98	3.00
7.	ZS-B	3.91	3.00
8.	ZS-C	3.81	3.17
9.	ZS-D	3.78	3.12
10.	ZS-E	3.26	3.12

6A.3.5. BET Surface Area Analysis

The porosity of ZnO-SnO_2 nanocomposites (synthesized by both the methods) was studied by employing Brunauer-Emmett-Teller (BET) adsorption-desorption isotherms using N_2 gas at 77K and the adsorption-desorption isotherms of ZnO-SnO_2 nanocomposites are given in Fig. 6A.11 and Fig. 6A.12. BET surface area, pore volume and average pore radius of ZnO-SnO_2 nanocomposites (ZS-11, ZS-28, ZS-46, ZS-64, ZS-82, ZS-A, ZS-B, ZS-C, ZS-D and ZS-E) have been listed in Table 6A.3. BET results indicate the mesoporous nature of ZnO-SnO_2 nanocomposites having average pore radius *ca.* 20-25 Å.

Table. 6A.3. BET surface area analysis of ZnO-SnO_2 nanocomposites.

S.N.	Materials	S_{BET} (m^2g^{-1})	Pore Vol. (ccg^{-1})	Average pore radius (Å)
1.	ZS-11	21	2.61×10^{-2}	25.06
2.	ZS-28	19	2.10×10^{-2}	21.72
3.	ZS-46	21	2.31×10^{-2}	21.81
4.	ZS-64	19	1.81×10^{-2}	19.50
5.	ZS-82	26	2.74×10^{-2}	20.80
6.	ZS-A	18	2.04×10^{-2}	23.28
7.	ZS-B	13	1.53×10^{-2}	22.86
8.	ZS-C	16	1.85×10^{-2}	23.41
9.	ZS-D	11	1.33×10^{-2}	23.51
10.	ZS-E	11	1.26×10^{-2}	23.52

* S_{BET} (Brunauer-Emmett-Teller surface area in meter square per gram); * Pore Vol. (Pore volume in cubic centimeter per gram)

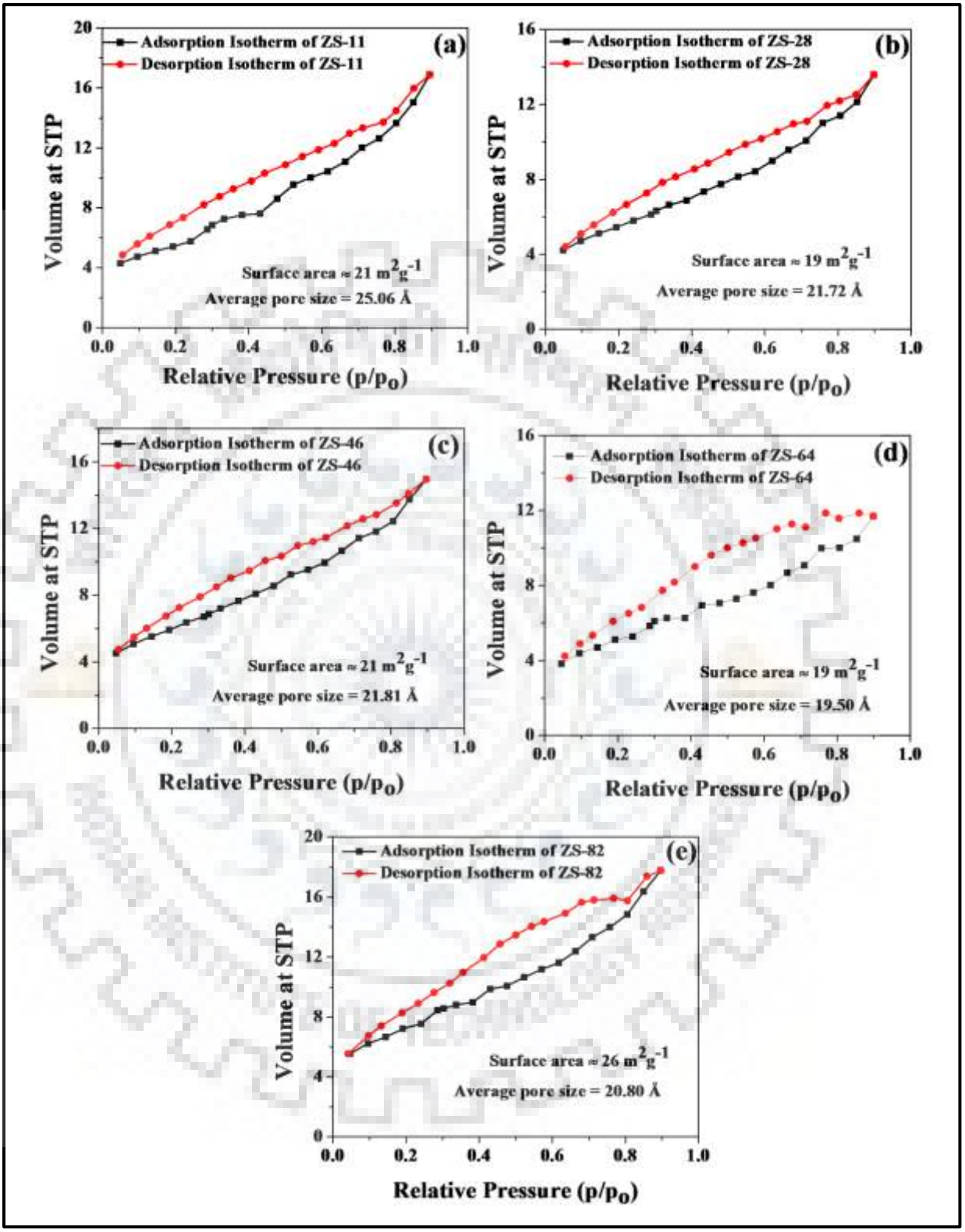

Fig. 6A.11. (a-e) BET adsorption-desorption isotherms of ZS-11, ZS-28, ZS-46, ZS-64 and ZS-82 nanocomposites, respectively.

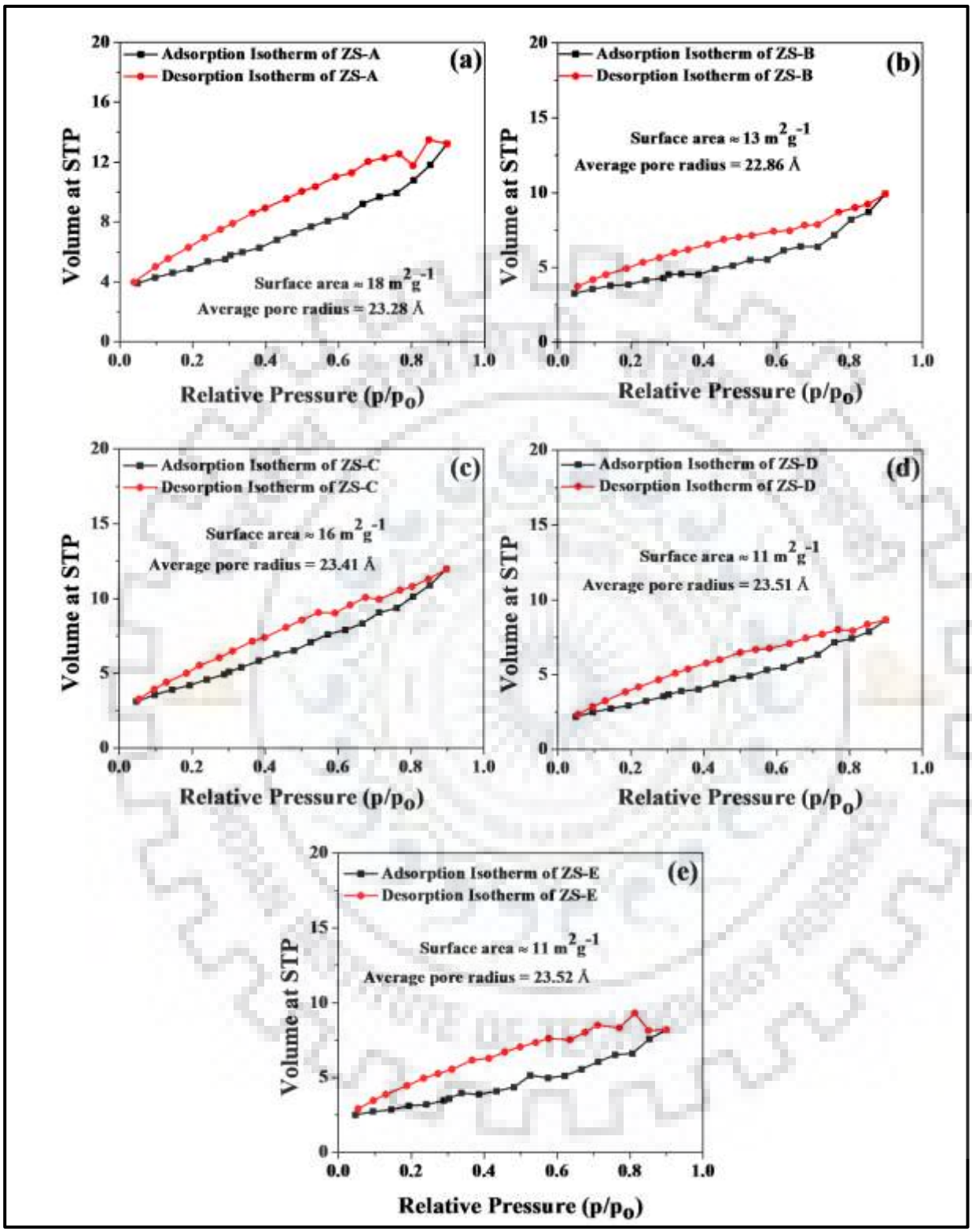

Fig. 6A.12. (a-e) BET adsorption-desorption isotherms of ZS-A, ZS-B, ZS-C, ZS-D and ZS-E nanocomposites, respectively.

6A.3.6. XPS Analysis

The surface profile of synthesized ZnO-SnO_2 nanocomposites has been analyzed by X-ray photoelectron spectroscopic (XPS) studies.

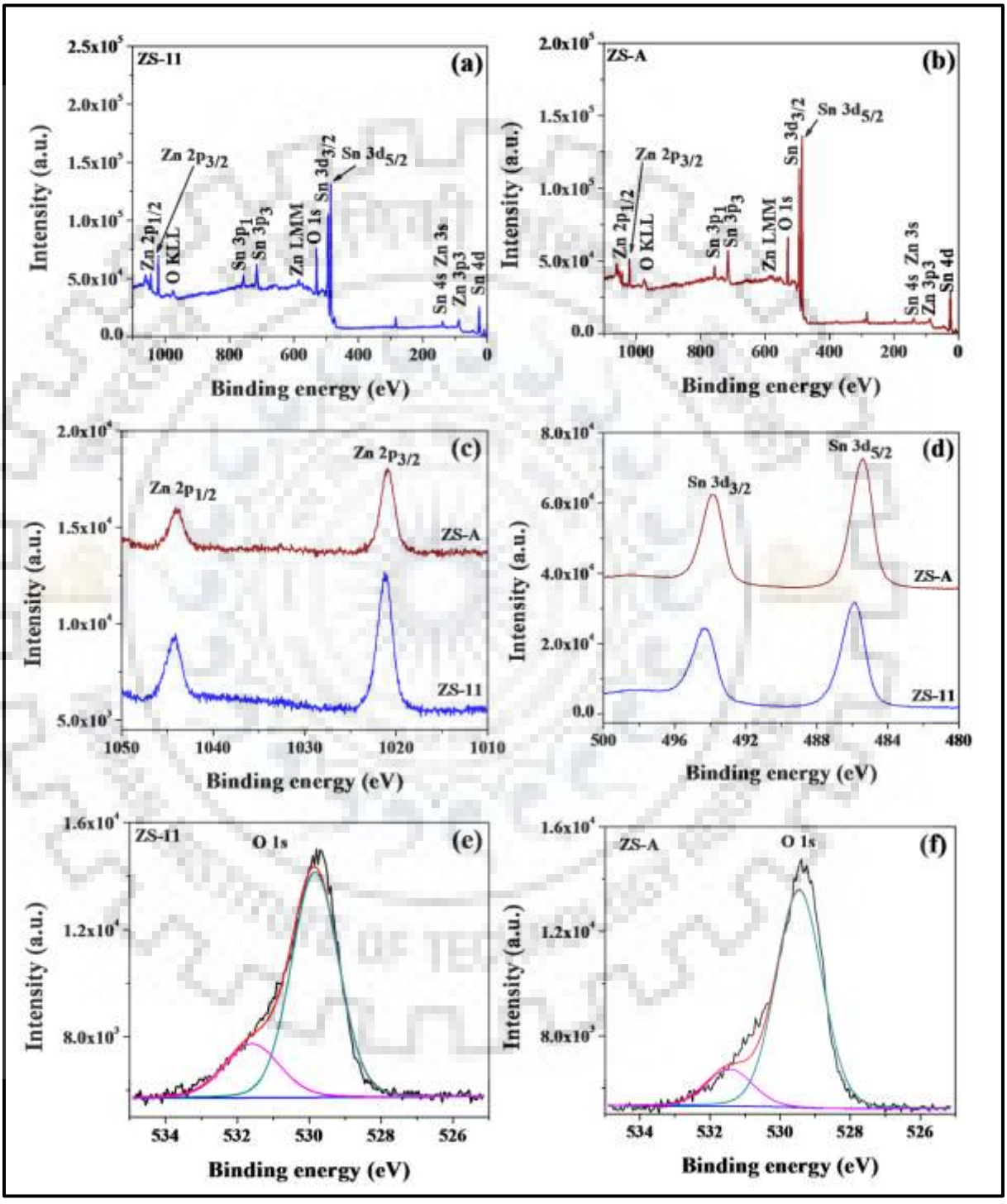

Fig. 6A.13. (a, b) The survey scan of ZS-11 and ZS-A, respectively. Their expanded XPS spectra for Zn 2p and Sn 3d are shown in (c) and (d), respectively, and the deconvoluted O 1s XPS spectra of ZS-11 and ZS-A, are shown in (e) and (f), respectively.

Full survey scan of ZS-11 and ZS-A nanocomposites are shown in Fig. 6A.13(a-b), respectively, while the expended XPS spectra of the close fitting of the metals (Zn and Sn) with their orbital position are illustrated in Fig. 6A.13(c-d), respectively. Intense peaks of Zn $2p_{1/2}$ and $2p_{3/2}$ of ZS-11 and ZS-A have binding energy 1044.27 eV and 1021.15 eV, respectively. Sn 3d orbital in ZS-11 appears as sharp peaks with binding energy of 494.31 eV and 485.92 eV while ZS-A shows the corresponding peaks at 493.89 eV and 485.44 eV which are due to $3d_{3/2}$ and $3d_{5/2}$, respectively. Fig. 6A.13(e-f) depict the expanded O 1s close fitting of ZS-11 and ZS-A, respectively. The deconvoluted XPS spectra of O 1s of both the composites (ZS-11/ZS-A) involves two peaks; at higher binding energy 531.59 eV/531.44 attributable to oxygen of SnO_2 while at lower binding energy 529.83/529.47 eV attributable to oxygen of ZnO [6].

6A.3.7. Adsorption and Photocatalytic Studies of Methylene Blue (MB) Dye using ZnO-SnO_2 Nanocomposites

To investigate the adsorption and photodegradation study of MB dye, 10 mg of ZnO-SnO_2 nanocomposites (ZS-11, ZS-28, ZS-46, ZS-64, ZS-82, ZS-A, ZS-B, ZS-C, ZS-D and ZS-E) was added into 20 mL MB (0.5×10^{-5} M) dye solution and sonicated for 30 min. MB dye suspensions with ZnO-SnO_2 nanocomposites were kept for 2 h for the adsorption studies. After the adsorption study, the dye solutions were exposed under constant UV-visible irradiations using 50 Watt halogen lamp as energy source for 2 h at room temperature and the UV-visible absorbance spectra were recorded at certain interval. The remaining dye concentration was calculated from the absorbance at 663 nm using equation 3.1 which is given in Chapter three. The results of adsorption and photodegradation are compiled in Table 6A.4 and C/C_0 *vs* time plot is shown in Fig. 6A.14. It has been found that 8:2 molar ratio of ZnO-SnO_2 nanocomposite ZS-82 and ZS-E exhibit the maximum photodegradation of 0.5×10^{-5} M MB dye as compared to others i.e. 49.5% and 58.68%, respectively, while removal% or maximum adsorption% were found 30.43% and 22.06%, respectively, at pH 7.89.

6A.3.8. Plausible Degradation Mechanism

Fig. 6A.15 describes the charge separation photo induced e^- and h^+ pair in the conduction band (CB) and valance band (VB) of semiconductor metal oxides. The electron (e^-) moves toward lower edge of CB from higher edge of CB and simultaneously hole (h^+) moves towards higher edge of VB from lower edge of VB. Thus, it increases the charge separation and

reduces the recombination rate of e^- and h^+ pair. As a consequence, e^- and h^+ pair can easily react with dye molecules, thereby enhancing the degradation efficiency of composite materials.

Table. 6A.4. Adsorption and photodegradation activity of ZnO-SnO_2 nanocomposites, amount of composite materials = 10 mg; [MB] = 1.6 mg L^{-1}; at pH = 7.89.

S.N.	Materials	Adsorption capacity (mg/g) [% removal]	% Photodegradation
1.	Pure MB	-	23.75
2.	ZS-11	0.90 [28.37]	44.75
3.	ZS-28	0.81 [25.31]	44.06
4.	ZS-46	0.89 [28.00]	47.50
5.	ZS-64	0.88 [27.68]	49.50
6.	ZS-82	0.97 [30.43]	49.50
7.	ZS-A	0.84 [26.25]	41.37
8.	ZS-B	0.81 [25.31]	40.50
9.	ZS-C	1.31 [41.12]	54.81
10.	ZS-D	1.00 [31.25]	46.43
11.	ZS-E	0.70 [22.06]	58.68

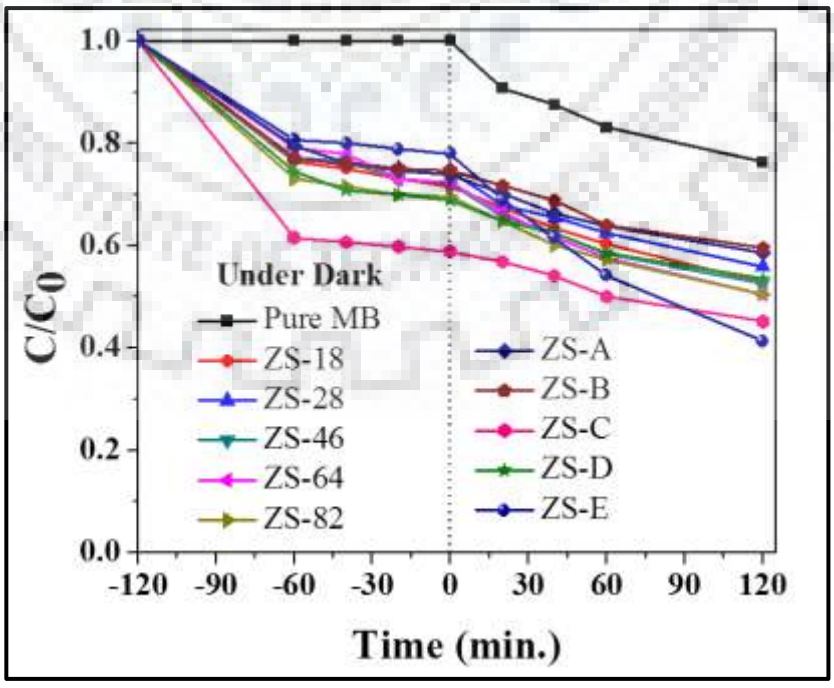

Fig.6A.14. MB Adsorption and photodegradation with ZnO-SnO_2 nanocomposites.

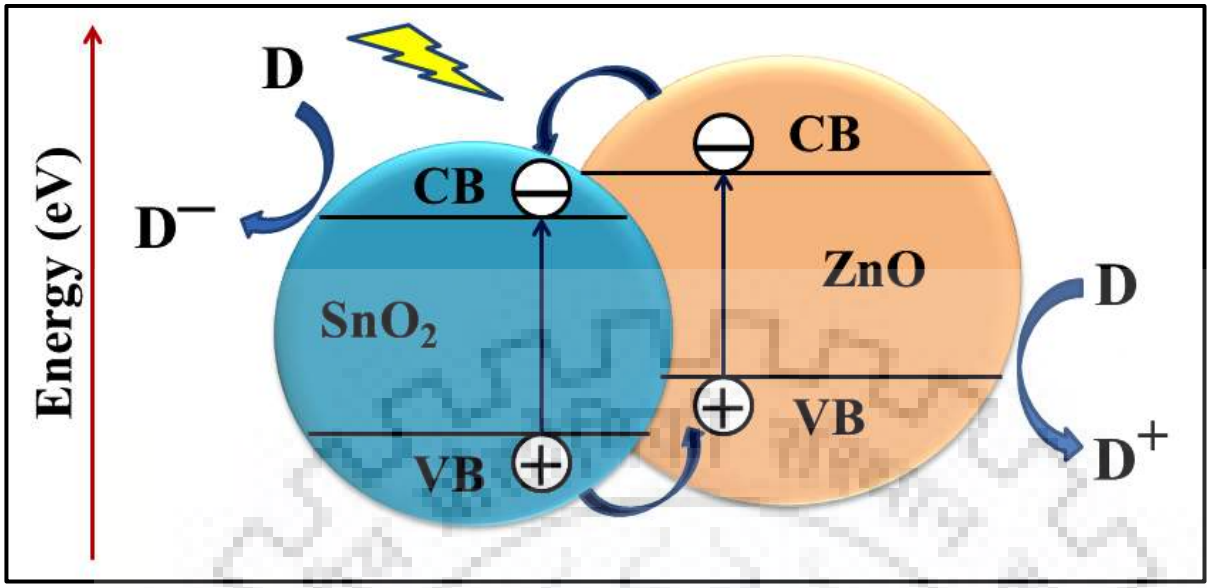

Fig.6A.15. General mechanism of photocatalytic activity of ZnO-SnO_2 nanocomposite.

6A.4. CONCLUSION

This section describes synthesis of ZnO-SnO_2 nanocomposites in various molar ratio of Zn and Sn using sol-gel and grinding method and detailed characterization using various spectroscopic techniques. In order to study their photocatalytic application, adsorption and photodegradation efficiency has been examined using model dye, *for instance*, methylene blue (MB). It has been found that ZS-E nanocomposite exhibits maximum photodegradation efficiency (58.68%). Further, ZS-E nanocomposite has been chosen for the encapsulation within ZIF-8 matrix due to its maximum photocatalytic response at pH = 7.89 which is described in next section.

.

This Section describes the synthesis of ZnO-SnO_2 nanocomposite decorated ZIF-8 composites *via* solvothermal and bench method and its photocatalytic application.

SECTION B

6B.1. INTRODUCTION

ZIF-8 has been utilized in the various field and fabricated with various metal oxides (TiO_2, ZnO, Fe_3O_4 and SnO_2 etc.) and novel metal nanoparticles (Ag, Au, Pt and Cu etc.). Despite, ZIF-8 is not fabricated with mixed metal oxide nanocomposite such as TiO_2-ZnO, TiO_2-SnO_2, TiO_2-Fe_3O_4, TiO_2-WO_3, ZnO-WO_3 and ZnO-SnO_2 so far. Therefore, this section describes ZIF-8 fabricated with ZnO-SnO_2 nanocomposite.

6B.2. EXPERIMENTAL SECTION

6B.2.1. Synthesis of ZnO-SnO_2@ZIF-8 Composites

As mentioned in section-A, ZnO-SnO_2 nanocomposites were synthesized by grinding method using 8:2 molar ratios of Zn and Sn named as ZS-E. Because of its highest photocatalytic activity, it has been selected for encapsulation within ZIF-8. ZnO-SnO_2@ZIF-8 composites were synthesized by using solvothermal and bench method.

6B.2.1.1. Solvothermal Method

0.232 g of ZnO-SnO_2 nanocomposite (ZS-E) was dispersed in (10 mL) methanol and kept on sonication for 30 min. 10 mmol (0.821 g in 10 mL methanol) of 2-methylimidazole solution was added dropwise into above reaction mixture with constant stirring. After 30 min, the resultant reaction mixture was placed into 50 mL Teflon autoclave and kept it in a controlled oven at 120 °C for 6 h for as shown in Scheme 6B.1. Finally, a white powder was collected by centrifugation and dried it at 60 °C for 6 h, stored in closed vessels and named as ZS@Z.

6B.2.1.2. Bench Method

ZnO-SnO_2@ZIF-8 composites were prepared by *in situ* encapsulation of different amounts of ZnO-SnO_2 nanocomposites in ZIF-8 (Scheme 6B.2). 20 mg ZnO-SnO_2 (ZS-E) nanocomposite was dispersed in (10 mL) methanol and sonicated for 1 h. During the synthesis of ZIF-8 as described in Chapter three, 150 µL /300 µL /500 µL methanol suspensions of ZnO-

SnO_2 nanocomposite were added at certain time interval. The reaction mixture was kept for 24 h at room temperature undisturbed as much as possible. A white powder was collected *via* centrifugation, dried it at 60 °C for 6 h, stored in closed vessels and named as ZS@Z1, ZS@Z2 and ZS@Z3, respectively.

Scheme 6B.1. Schematic illustration of synthesis of ZS@Z.

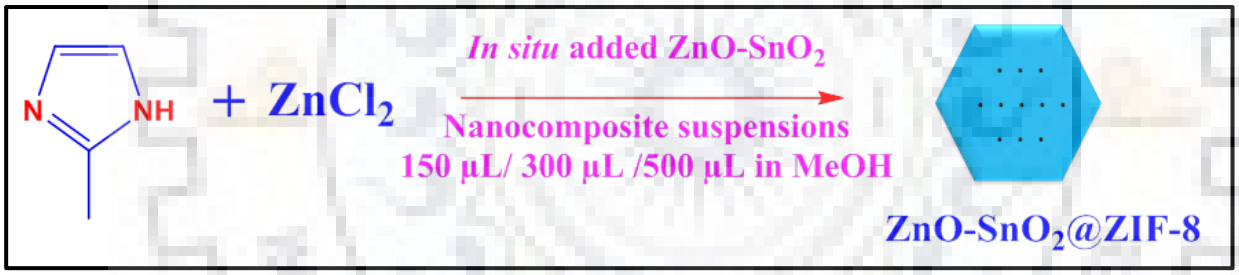

Scheme 6B.2. Schematic illustration of synthesis of ZnO-SnO_2@ZIF-8.

6A.3. RESULTS AND DISCUSSION

ZnO-SnO_2 nanocomposite was anchored on ZIF-8 surface by solvothermal method (ZS@Z), whereas encapsulation of 150 µL /300 µL /500 µL methanol suspensions of ZnO-SnO_2 (ZS-E) nanocomposite within ZIF-8 frameworks were done *in situ* yielding ZS@Z1, ZS@Z2 and ZS@Z3. All the four composite materials were characterized by employing various spectroscopic techniques.

6B.3.1. PXRD Analysis

PXRD pattern of ZS@Z, ZS@Z1, ZS@Z2 and ZS@Z3 composite are illustrated in Fig. 6B.1. Fig. 6B.1(a) shows the PXRD analysis of ZS@Z composite, the major and prominent peaks at 2θ values 7.16°, 10.26°, 12.57° and 17.88° correspond to the planes (011), (002), (122) and (222), respectively, which are characteristic peaks of ZIF-8, whereas those at 2θ values

34.44°, 36.49°, 42.19°, 61.20°, 73.29°, 77.13° correspond to the planes (002), (101), (200), (220), (311) and (222), respectively, represents the PXRD pattern of ZnONPs which is indexed with JCPDS No. 01-077-0191 and 005-0664. PXRD peaks of SnO_2NPs at 2θ values 26.59°, 33.88°, 52.18°, 57.25° and 86.66° correspond to the planes (110), (101), (211), (002) and (330), respectively, are indexed with JCPDS No. 01-072-1147. PXRD of ZS@Z composites firmly proves that ZnO-SnO_2 nanocomposite was successfully anchored on the ZIF-8 surface. PXRD pattern of ZS@Z1, ZS@Z2 and ZS@Z3 composites are illustrated in Fig. 6B.1(b-d), respectively. The major PXRD pattern of ZIF-8 appears in each spectrum (ZS@Z1, ZS@Z2 and ZS@Z3) but no significant peaks of ZnO-SnO_2 are detected indicating ZnO-SnO_2 nanocomposite was successfully encapsulated within the cavity of ZIF-8 matrix.

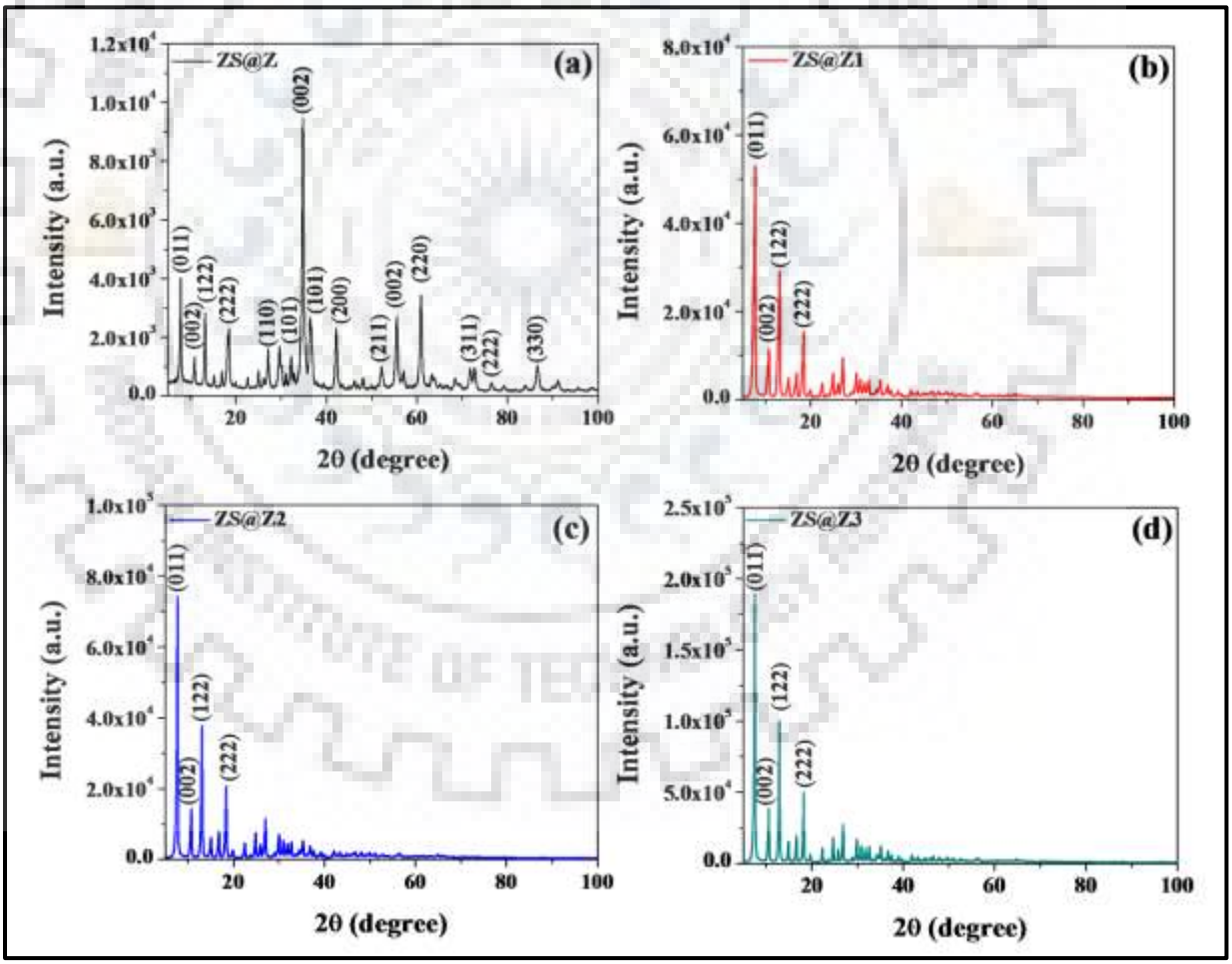

Fig. 6B.1 (a-d) PXRD analysis of ZS@Z, ZS@Z1 ZS@Z2 and ZS@Z3 composites, respectively.

6B.3.2. FT-IR Spectroscopic Studies

FT-IR spectra of synthesized SZ@Z, SZ@Z1, SZ@Z2 and SZ@Z3 are illustrated in Fig. 6B.2. A broad and intense peak appears at 3488 cm^{-1} attributable OH stretching vibrational mode and the peaks at 3165 and 2809 cm^{-1} correspond to aromatic and aliphatic C-H stretching mode [25]. A sharp peak at 1633 cm^{-1} is due to H-O-H bending vibration in each sample [6] while the peaks at 1407, 1310, 1148 997 and 760 cm^{-1} correspond to the imidazole ring [26]. The broad peaks observed at 695-620 cm^{-1} is due to Sn-O and Sn-O-Sn stretching while peak at 512 cm^{-1} is assigned to Zn-O stretching mode [22].

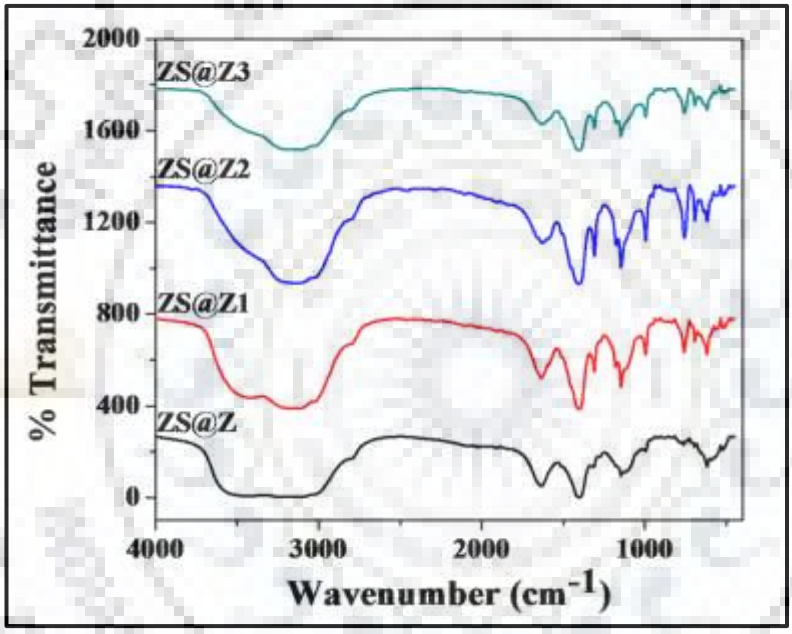

Fig. 6B.2. FT-IR spectra of ZS@Z, ZS@Z1 ZS@Z2 and ZS@Z3 composites, respectively.

6A.3.2. FE-SEM and HR-TEM Analysis

ZS-E was successfully anchored on the surface of ZIF-8 as shown in Fig. 6B.3(a), while Fig. 6B.3(b-d) exhibit hexagonal morphology of ZS@Z1 ZS@Z2 and ZS@Z3, respectively, which indicates proper encapsulation of ZnO-SnO_2 nanocomposite in ZIF-8 and ZnO-SnO_2 nanocomposite does not affect the textural properties of ZIF-8. EDX analysis of ZS@Z exhibits higher atomic percentage of Zn and Sn indicating the presence of larger amount of ZS-E on the surface of ZIF-8. On the other hand, ZS@Z1 ZS@Z2 and ZS@Z3 show the increasing trend of Zn and Sn atomic percentage with increasing the dosing amount of encapsulated ZS-E.

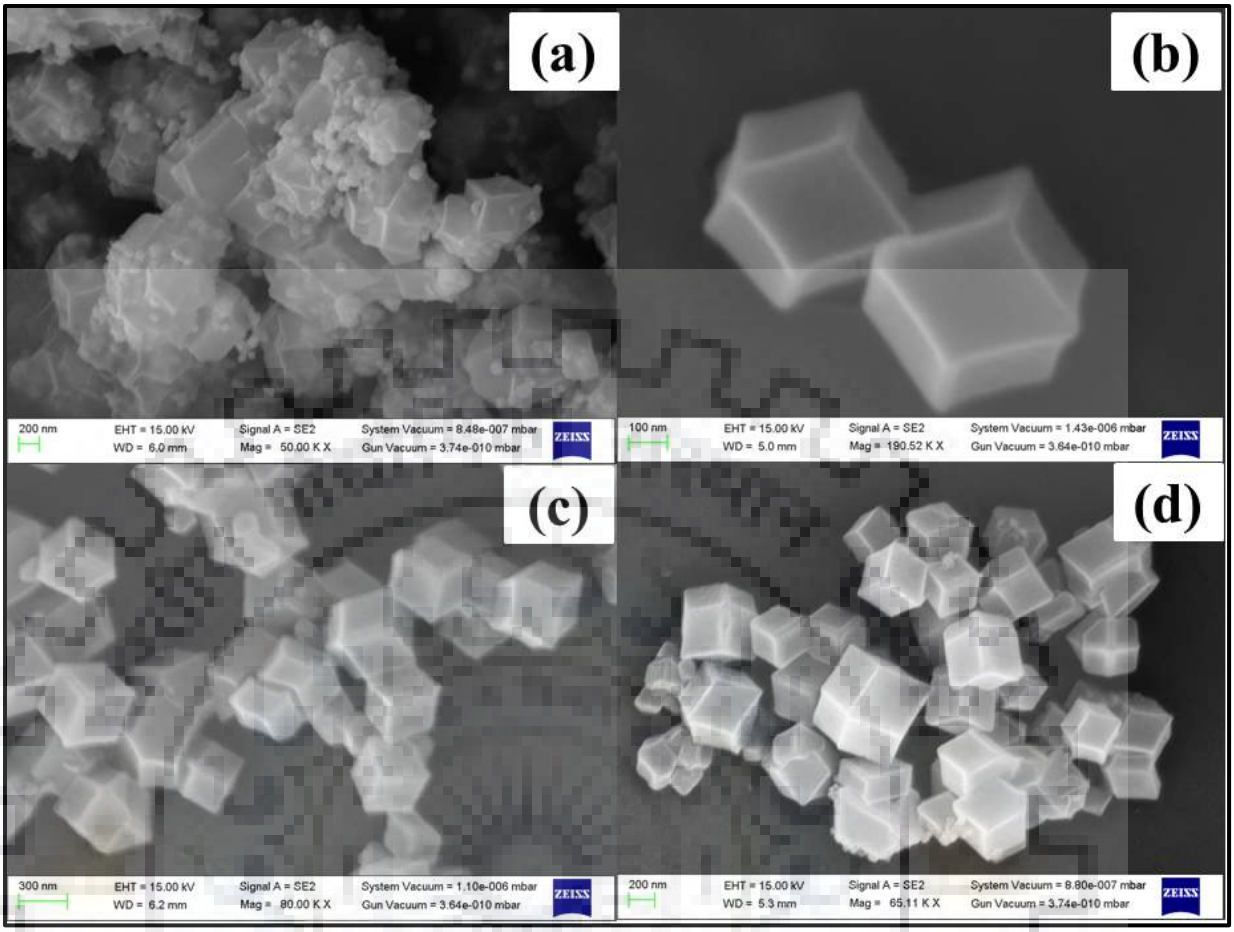

Fig. 6B.3. (a-d) SEM analysis of ZS@Z, ZS@Z1 ZS@Z2 and ZS@Z3 composites, respectively.

Table 6B.1. EDX analysis of ZS@Z, ZS@Z1 ZS@Z2 and ZS@Z3 composites.

S.N.	Materials	Atomic %				
		C	N	O	Zn	Sn
1.	ZS@Z	44.80	17.78	20.64	12.70	4.09
2.	ZS@Z1	29.38	18.58	47.11	4.68	0.24
3.	ZS@Z2	24.84	14.20	55.34	5.28	0.34
4.	ZS@Z3	28.46	17.36	48.43	5.49	0.26

The deposition of ZnO-SnO_2 nanocomposites on the surface of ZIF-8 was confirmed by TEM analysis. Fig. 6B.5(a, b) show that ZS-3 has been successfully anchored on the surface of ZIF-8. The SEAD pattern (Fig. 6B.5(c)) also ensures the presence of ZnO-SnO_2 nanocomposite. The TEM images of ZS@Z3 composite reveal the definite encapsulation of ZnO-SnO_2

nanocomposites within ZIF-8 matrix which is shown in 6B.5(d, e). The SEAD pattern of SZ@Z3 composite also (Fig. 6B.5(f)) indicates the crystalline nature of SZ@Z3 composite.

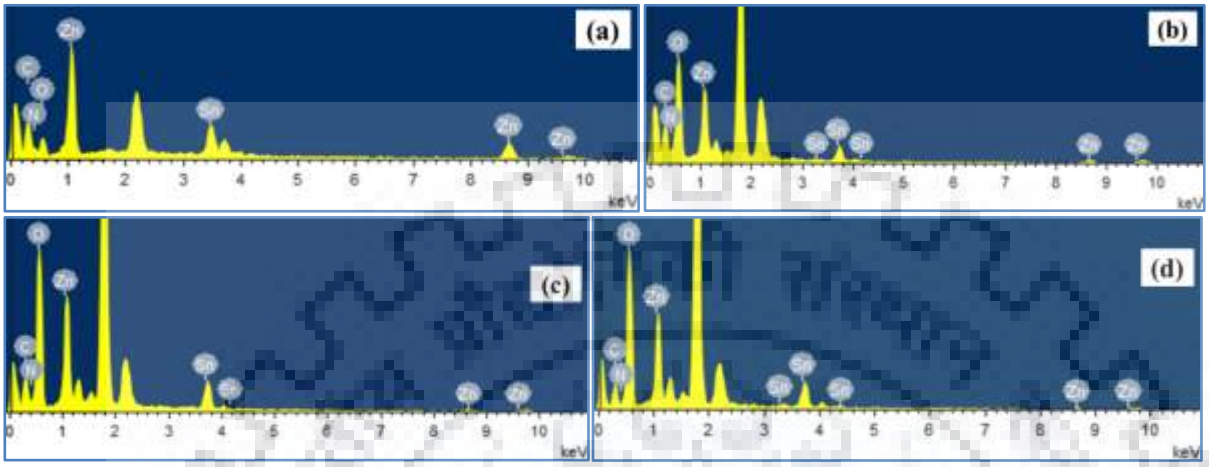

Fig. 6B.4. (a-d) EDX spectra of ZS@Z, ZS@Z1 ZS@Z2 and ZS@Z3 composites, respectively.

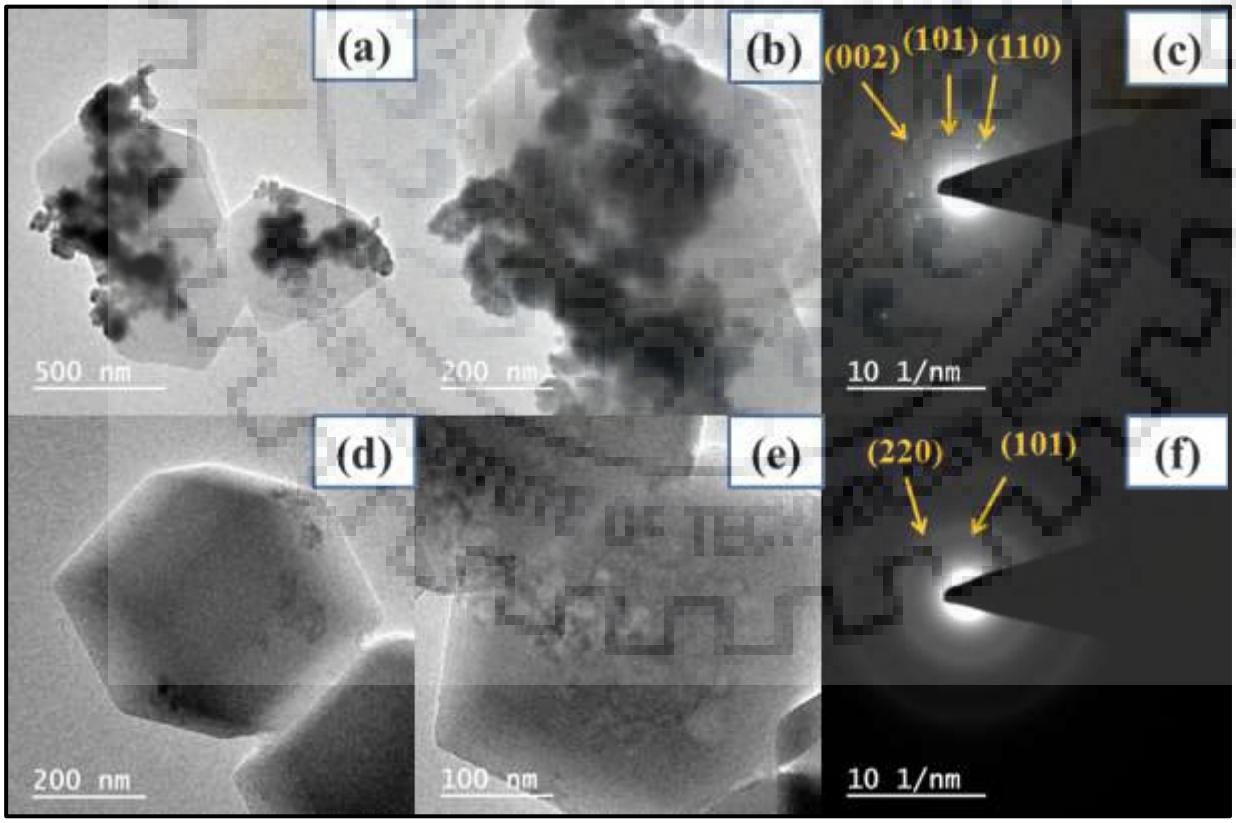

Fig. 6B.5. TEM images of (a, b) ZS@Z composite and (d, e) ZS@Z3 composite in order of increasing magnification, and (c, f) their SEAD pattern, respectively.

The particle size of anchored ZnO-SnO_2 nanocomposites are found to be 59.36 ± 5.66 nm, while encapsulated ZnO-SnO_2 nanocomposite are found to be 12.04 ± 2.85 nm which is determined by distribution plots of ZS@Z and ZS@Z3 composites using *ImageJ software* on HR-TEM images. The particle size of ZnO-SnO_2 nanocomposite is increased in SZ@Z composite due to agglomeration while in case of ZS@Z3 composite; agglomeration of ZnO-SnO_2 nanocomposites are immobilized. The distribution plots of ZnO-SnO_2 nanocomposite anchored (SZ@Z) and encapsulated (SZ@Z3) within ZIF-8 are shown in Fig. 6B.7.

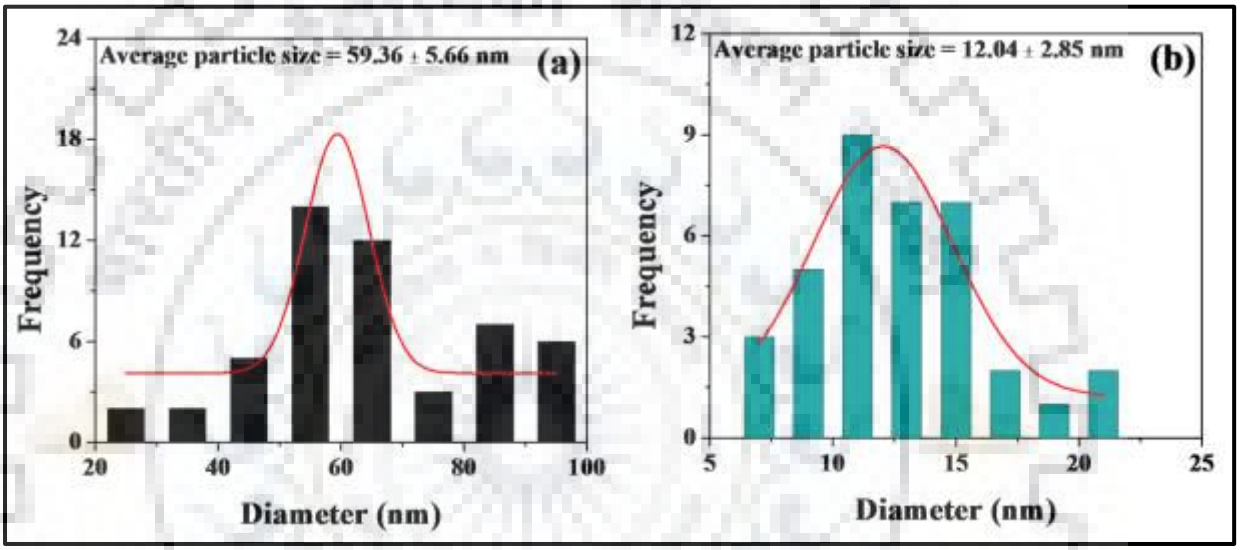

Fig. 6B.7. Particle size distribution plots of ZnO-SnO_2 nanocomposite (a) anchored (ZS@Z) and (b) encapsulated (ZS@Z3) within ZIF-8.

6B.3.4. UV-DRS Studies

The optical properties of ZS@Z, ZS@Z1 ZS@Z2 and ZS@Z3 composites have been studied with the help of ultra-violet defuse reflectance spectroscopic (UV-DRS) studies. The typical Tauc plots are shown in Fig. 6B.8(a, b), which represent for the direct and indirect transitions, respectively, while Fig. 6B.8(c) exhibits the absorbance spectra of all four composites. ZS@Z composite exhibits two bands at 3.25 eV and 3.79 eV due to ZnO and SnO_2 of anchored ZnO-SnO_2 nanocomposite for direct transitions while the bands appeared at 3.12 eV and 2.99 eV for indirect transitions. These bands do not appear in ZS@Z1, ZS@Z2 and ZS@Z3 composites due to less amount of encapsulated ZnO-SnO_2 nanocomposite in cavity of ZIF-8. In case of ZS@Z1 ZS@Z2 and ZS@Z3 composites, only one band appears at 5.28 eV for direct transitions and at 5.13 eV for indirect transitions. The UV-DRS results of all four composites are compiled in Table 6B.2.

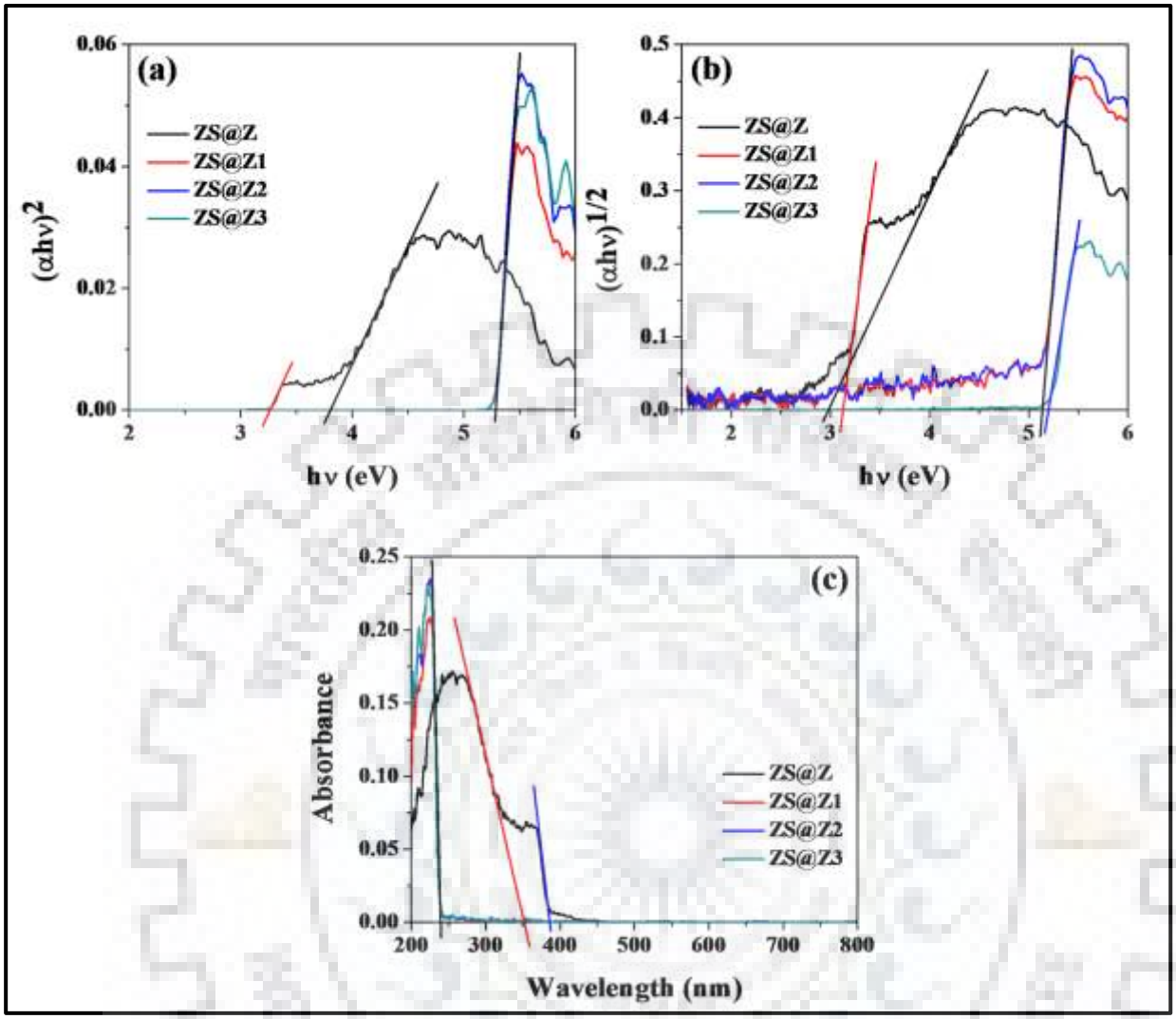

Fig. 6B.8. (a, b) Typical Tauc plots of ZS@Z, ZS@Z1, ZS@Z2 and ZS@Z3 composites are illustrated by direct transition and indirect transitions, respectively, while (c) exhibits absorbance spectra of ZS@Z, ZS@Z1, ZS@Z2 and ZS@Z3 composites.

Table. 6B.2. UV-DRS analysis of ZnO-SnO_2@ZIF-8 composites.

S.N.	Materials	Direct band gap (eV)	Indirect band gap (eV)
1.	ZS@Z	3.25/3.79	3.12/2.99
2.	ZS@Z1	5.28	5.13
3.	ZS@Z2	5.28	5.13
4.	ZS@Z3	5.28	5.19

6B.3.5. BET Surface Area Analysis

Porosity and adsorption-desorption isotherms of synthesized ZnO-SnO_2@ZIF-8 composites have been studied by employing BET (Brunauer-Emmett-Teller) model using N_2 sorption isotherms at 77K. Adsorption-desorption isotherms and pore size distribution plots of ZnO-SnO_2@ZIF-8 composites are given in Fig. 6B.9 and Fig. 6B.10. However, the results are compiled in Table 6B.3. It was found that on increasing the dosing amount of ZnO-SnO_2 nanocomposite BET surface area decreases except ZS@Z2 while ZS@Z exhibits minimum surface area *i.e.* ≈ 547 m^2 g^{-1} as compared to other composites due to ZIF-8 is wrapped by anchored ZnO-SnO_2 nanocomposite.

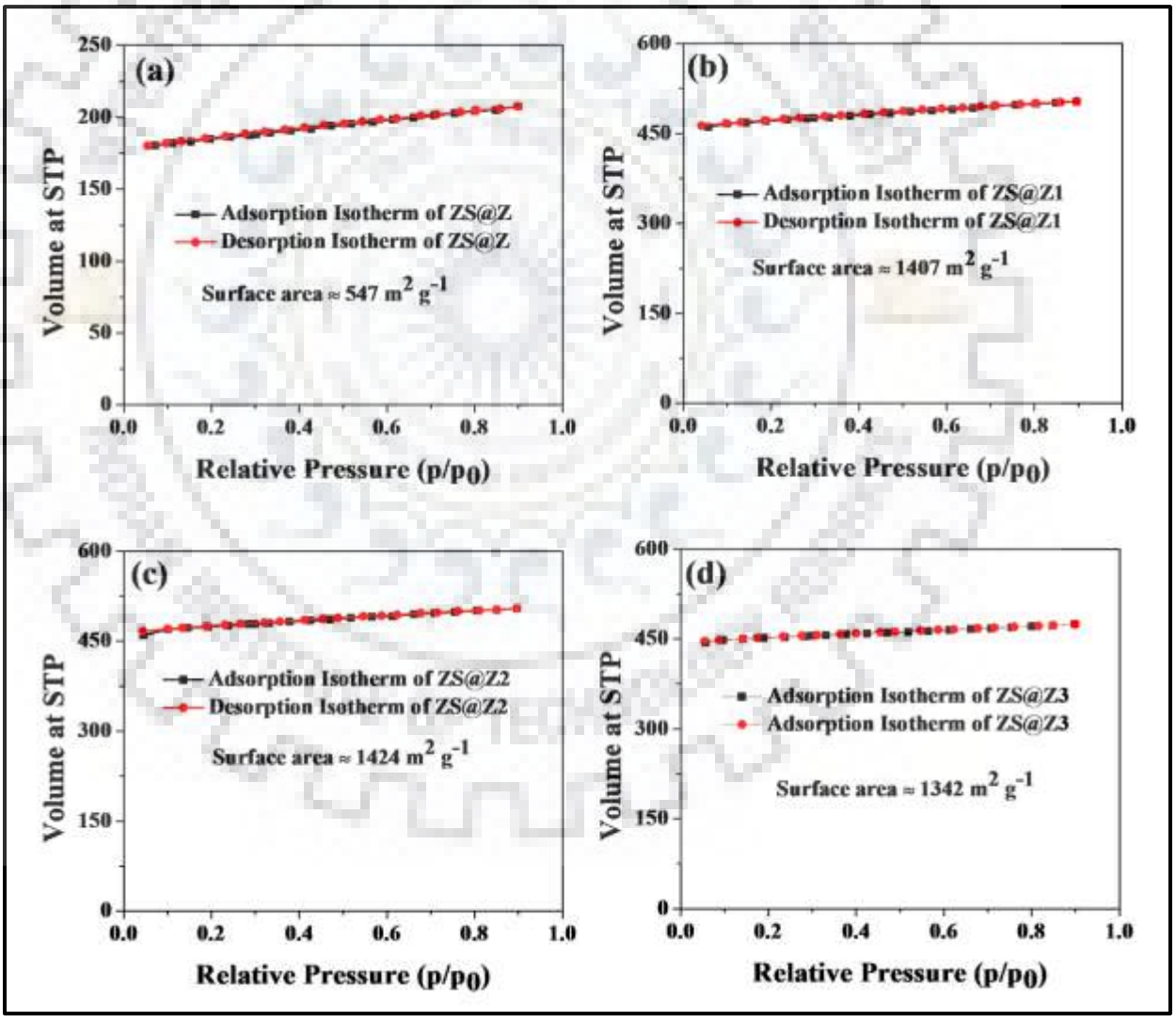

Fig. 6B.9. (a-d) BET adsorption-desorption isotherm plots of ZS@Z, ZS@Z1, ZS@Z2 and ZS@Z3 composites, respectively.

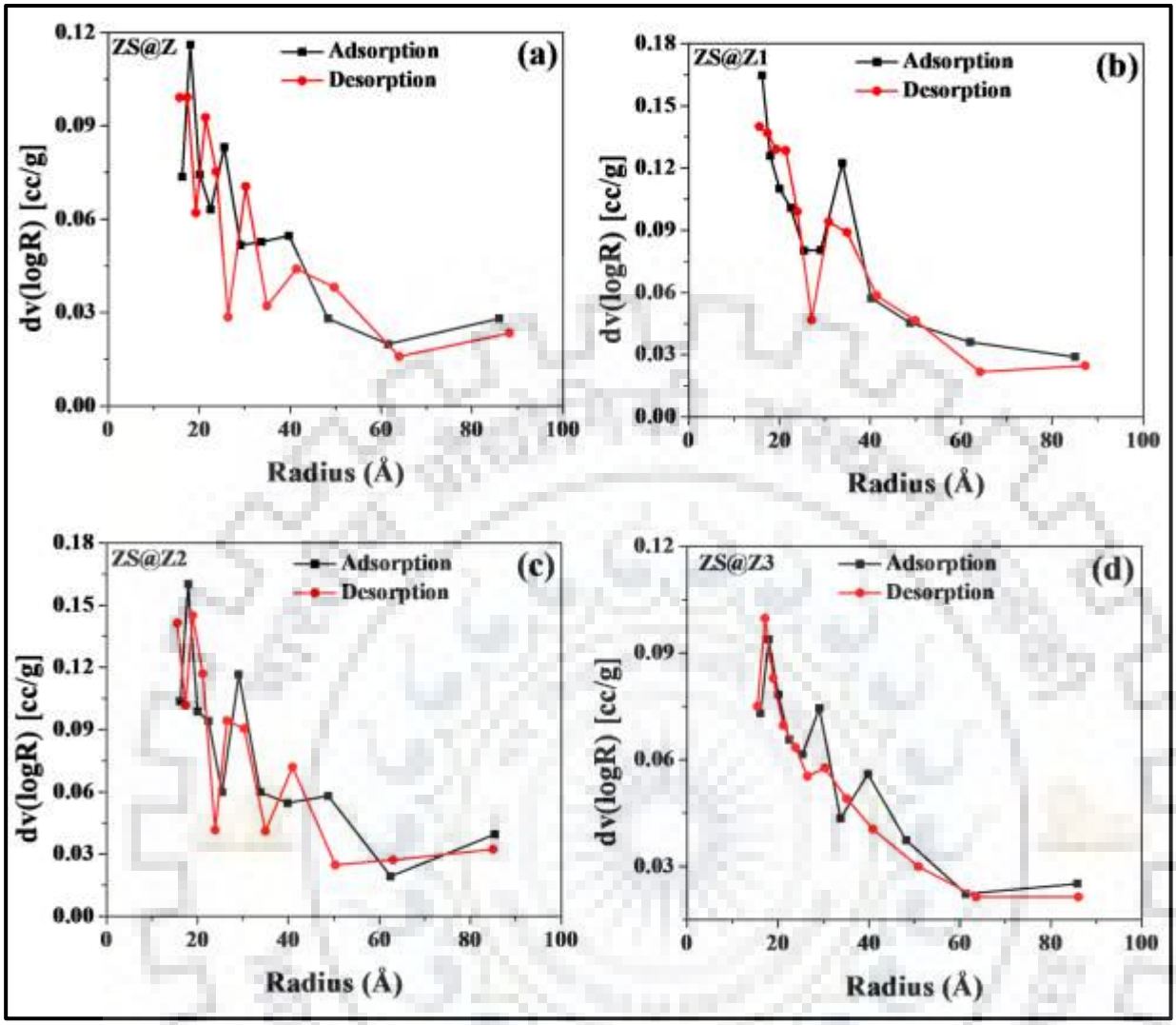

Fig. 6B.10. (a-d) BET pore size distribution plots of ZS@Z, ZS@Z1, ZS@Z2 and ZS@Z3 composites, respectively.

Table 6B.3. BET surface area analysis of ZS@Z, ZS@Z1, ZS@Z2 and ZS@Z3 composites.

S.N.	Materials	S_{BET} (m^2g^{-1})	Pore Vol. (ccg^{-1})	Average pore radius (Å)
1.	ZS@Z	547	3.209×10^{-1}	36.36
2.	ZS@Z1	1407	7.789×10^{-1}	35.78
3.	ZS@Z2	1424	7.811×10^{-1}	35.65
4.	ZS@Z3	1342	7.336×10^{-2}	35.75

6B.3.6. XPS Analysis

The survey scan and expanded XPS spectra of ZS@Z, ZS@Z1, ZS@Z2 and ZS@Z3 composites are shown in Fig. 6B.11, Fig. 6B.12, Fig. 6B.13 and Fig. 6B.14, respectively. Zn 2p of ZS@Z composite exhibits two sharp peaks with binding energy 1043.73 eV and 1020.57 eV correspond to $2p_{1/2}$ and $2p_{3/2}$, respectively (Fig. 6B.11(b)). Similar patterns of Zn 2p are observed in SZ@Z1, SZ@Z2 and SZ@Z3 composites (Fig. 6B.12(b), Fig. 6B.13(b) and Fig. 6B.14(b)) and the corresponding binding energies are compiled in Table 6B.4. Sn 3d orbital of SZ@Z composite shows two sharp peaks with binding energy 493.88 eV and 485.25 eV, attributable to $3d_{3/2}$ and $3d_{5/2}$, respectively (Fig. 6B.11(c)). Interestingly, a broad peak of Sn $3d_{3/2}$ (ZS@Z) was observed at 497.67 eV due to short interaction of ligand moiety of ZIF-8, which is also observed in all the composites with slight deviation (Fig. 6B.12(c), Fig. 6B.13(c) and Fig. 6B.14(c)). The deconvoluted XPS spectra of C 1s of ZS@Z composite contain two peaks (Fig. 6B.11(d)) at 285.46 eV and 283.84 eV due to sp^2C-N and sp^2C-C interaction, respectively [27]. The XPS spectra of O 1s (Fig. 6B.11(e)) and N 1s (Fig. 6B.11(f)) of ZS@Z composite appear at 529.68 eV and 397.76 eV, respectively, and the similar patterns of C 1s, N 1s and O 1s are also observed in all the three composites (SZ@Z1, SZ@Z2 and SZ@Z3) which indicates the similar environment of oxygen and nitrogen in composites (Table 6B.4).

6B.3.7. Thermal Analysis

The thermal gravimetric analysis (TGA) plots of synthesized ZS@Z, ZS@Z1, ZS@Z2 and ZS@Z3 composites are shown in Fig. 6B.15. It has been observed that ZS@Z exhibits high thermal stability (remaining weight% *ca.* 73.50 and 72.86 at 1000 °C) under both environments (air and N_2) while remaining weight% increases on increasing the dosing amount of ZnO-SnO_2 composite within ZIF-8 matrix. ZS@Z1, ZS@Z2 and ZS@Z3 composites exhibit remaining weight% *ca.* 35.15, 36.06 and 37.15% under areal atmosphere and 34.97, 35.60 and 36.81% under N_2 atmosphere, respectively, at 1000 °C.

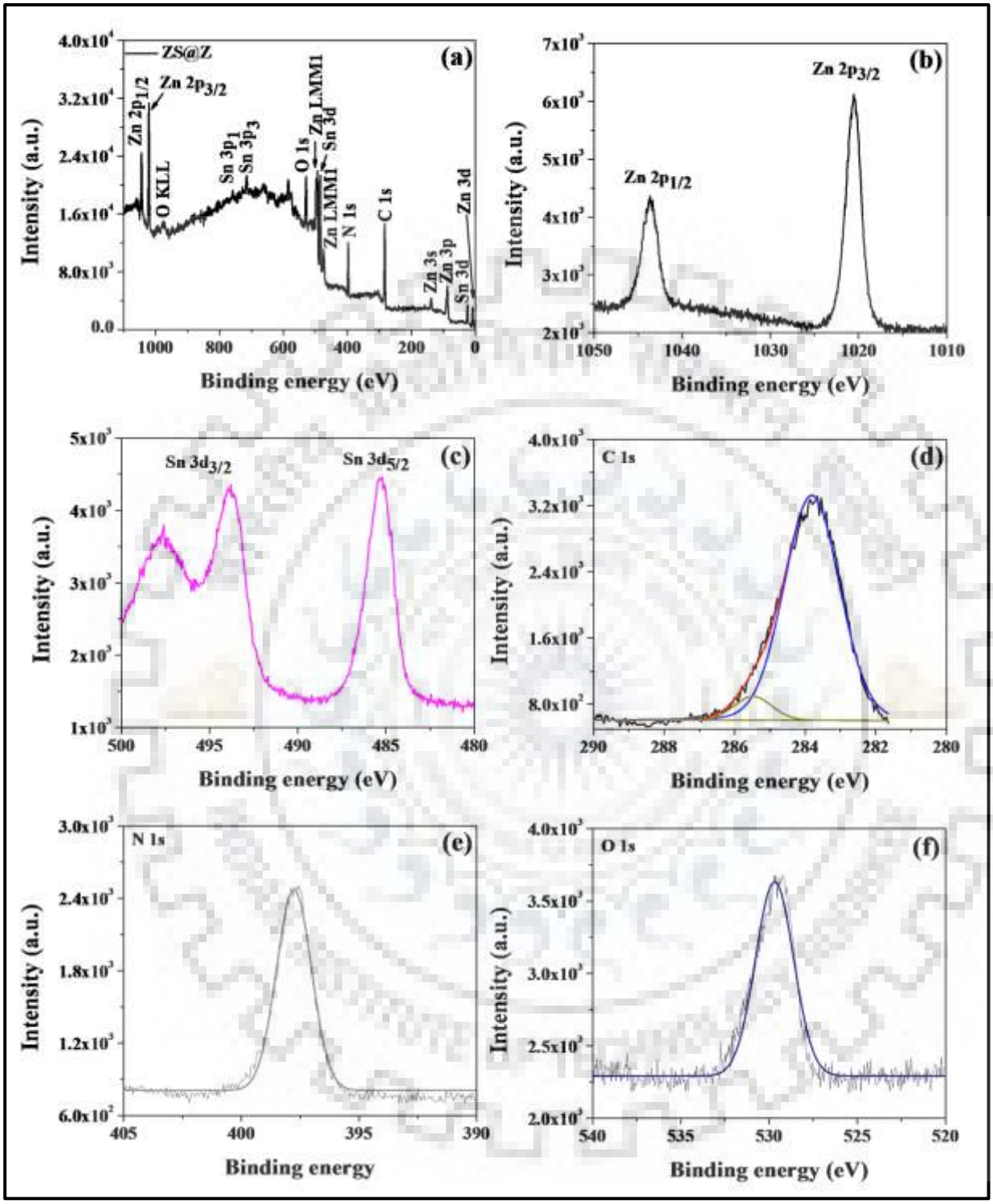

Fig. 6B.11. (a-f) Survey scan and expanded XPS spectra of Zn 2p, Sn 3d, C 1s, N 1s and O 1s of ZS@Z are shown as (a), (b), (c), (d), (e) and (f), respectively.

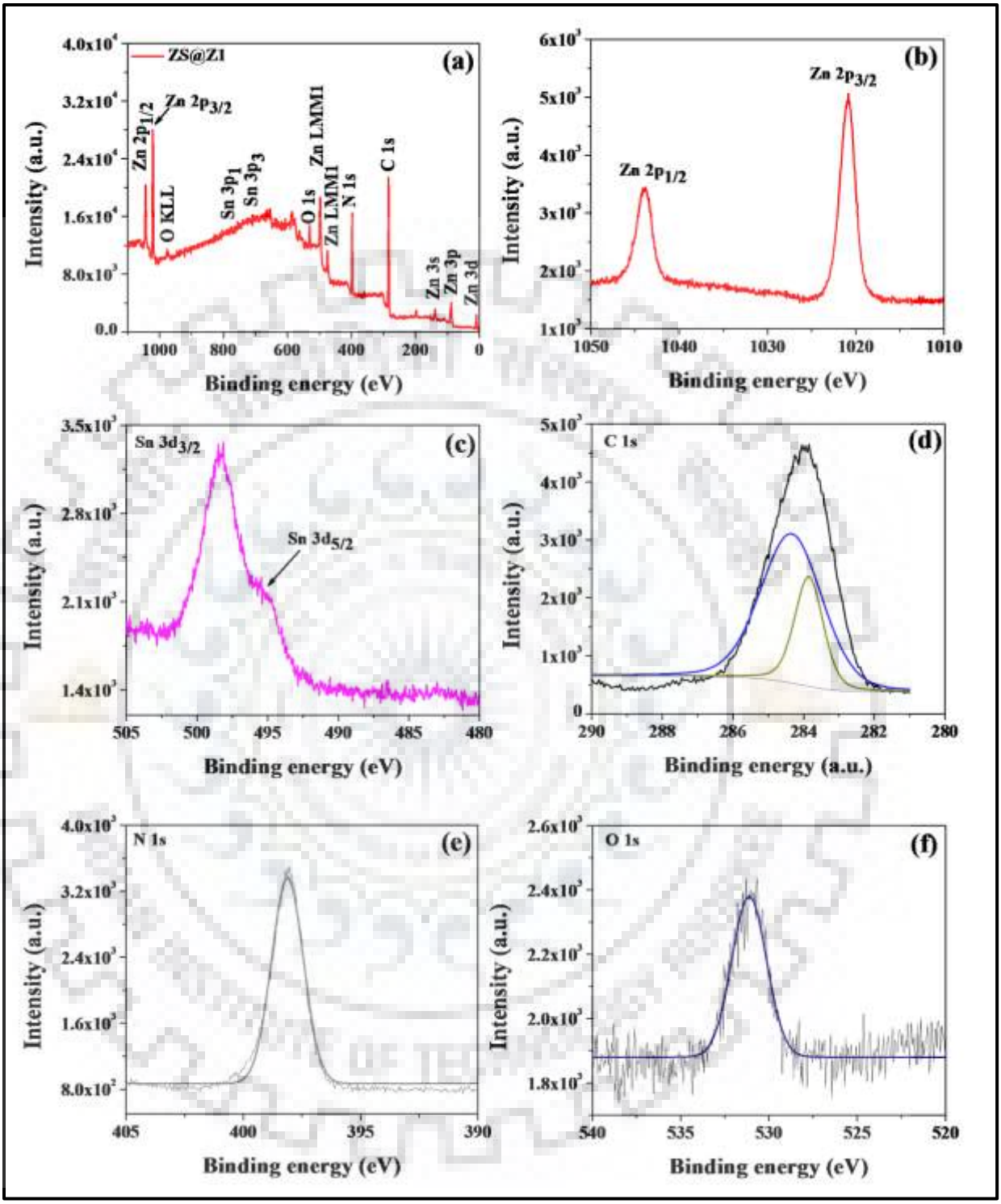

Fig. 6B.12. (a-f) Survey scan and expanded XPS spectra of Zn 2p, Sn 3d, C 1s, N 1s and O 1s of ZS@Z1 are shown as (a), (b), (c), (d), (e) and (f), respectively.

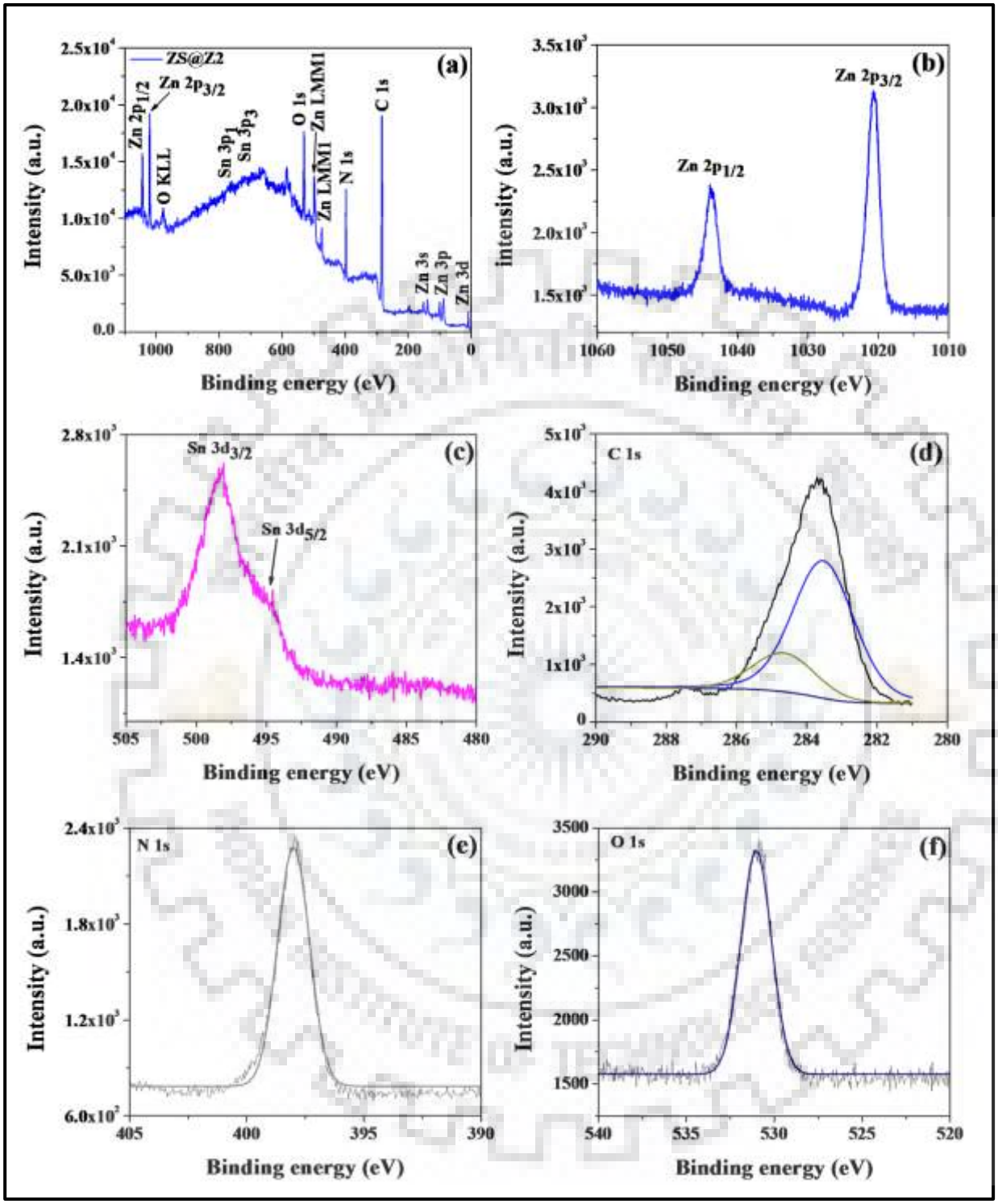

Fig. 6B.13. (a-f) Survey scan and expanded XPS spectra of Zn 2p, Sn 3d, C 1s, N 1s and O 1s of ZS@Z2 are shown as (a), (b), (c), (d), (e) and (f), respectively.

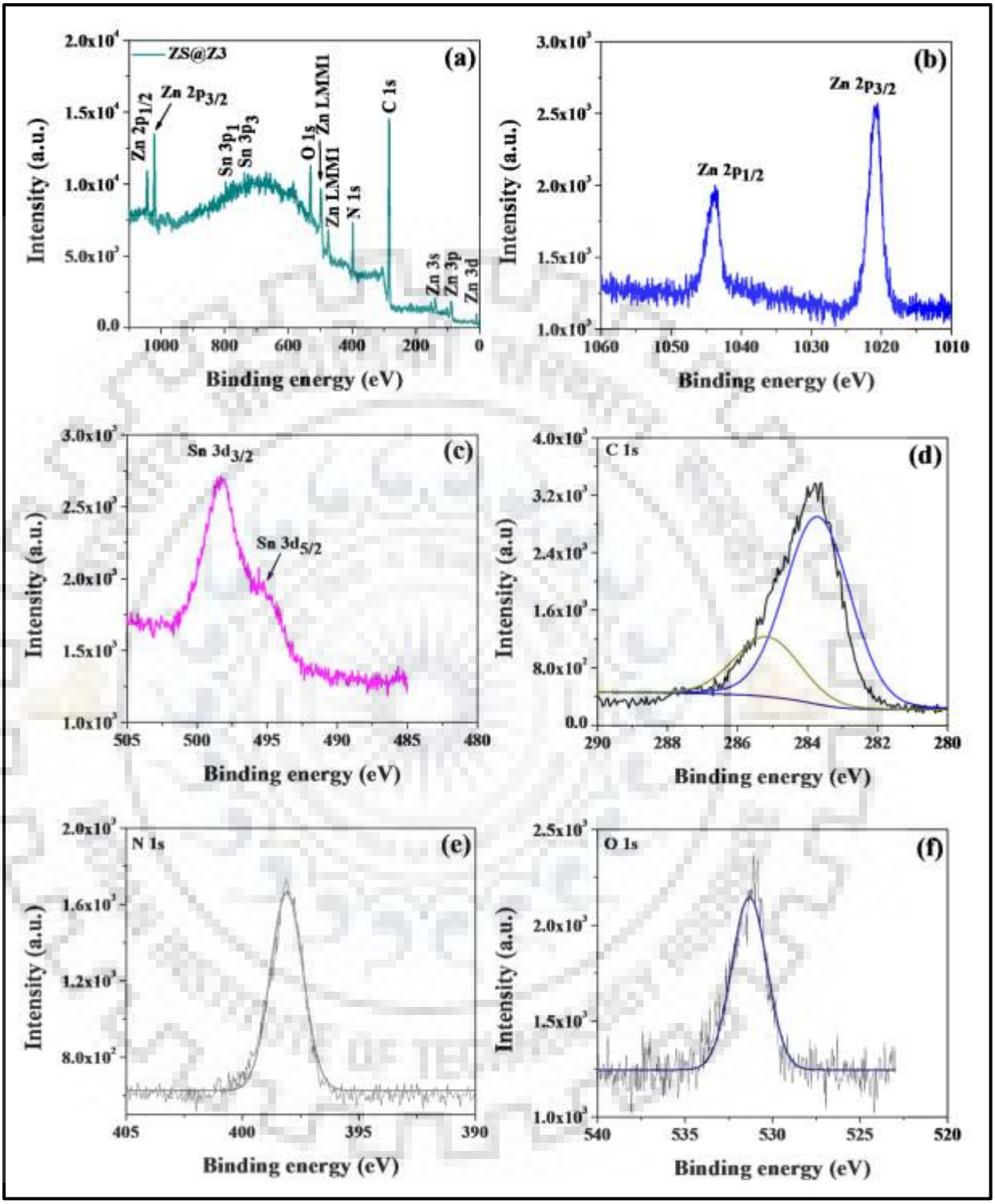

Fig. 6B.14. (a-f) Survey scan and expanded XPS spectra of Zn 2p, Sn 3d, C 1s, N 1s and O 1s of ZS@Z3 are shown as (a), (b), (c), (d), (e) and (f), respectively.

Table 6B.4. XPS analysis of ZS@Z, ZS@Z1, ZS@Z2 and ZS@Z3 composites.

S.N.	Materials	Atom/Element	State/Term	Binding energy (eV)
1.	ZS@Z	Zn	$2p_{1/2}$	1043.71
			$2p_{3/2}$	1020.57
		Sn	$3d_{3/2}$	497.67/493.88
			$3d_{5/2}$	485.29
		C	1s	285.46
				283.84
		N	1s	397.76
		O	1s	529.68
2.	ZS@Z1	Zn	$2p_{1/2}$	1043.87
			$2p_{3/2}$	1020.80
		Sn	$3d_{3/2}$	498.34
			$3d_{5/2}$	495.25
		C	1s	284.36
				283.86
		N	1s	398.11
		O	1s	531.12
3.	ZS@Z2	Zn	$2p_{1/2}$	1043.75
			$2p_{3/2}$	1020.61
		Sn	$3d_{3/2}$	498.37
			$3d_{5/2}$	495.01
		C	1s	284.72
				283.60
		N	1s	398.01
		O	1s	531.02

Continued

		Zn	$2p_{1/2}$	1043.94
			$2p_{3/2}$	1020.80
		Sn	$3d_{3/2}$	498.28
4.	ZS@Z3		$3d_{5/2}$	495.33
		C	1s	285.19
				283.73
		N	1s	398.10
		O	1s	531.32

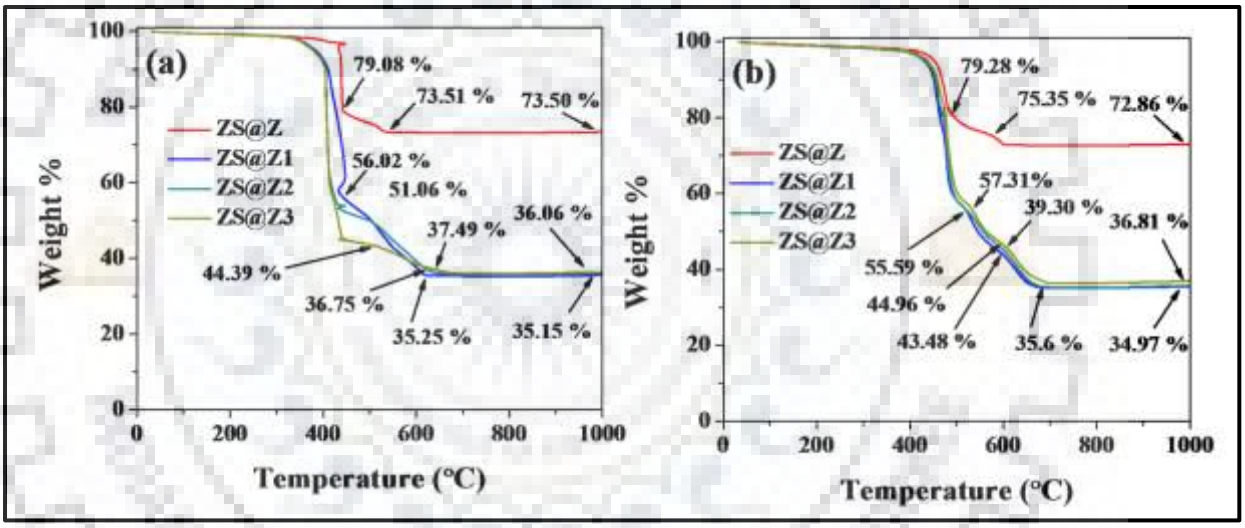

Fig. 6B.15. (a, b) TGA plots of ZS@Z, ZS@Z1, ZS@Z2 and ZS@Z3 composites under air and N_2 atmosphere, respectively.

6B.3.8. Adsorption and Photodegradation Studies of Methylene Blue (MB) Dye using ZS@Z, ZS@Z1, ZS@Z2 and ZS@Z3 Composites

Adsorption and photocatalytic degradation activity of synthesized ZS@Z, ZS@Z1, ZS@Z2 and ZS@Z3 composites were studied using MB as model dye according to the similar procedure as employed in previous Chapter five (Section B). Prior the photocatalytic activity, the adsorption capacity of composites has been examined. It was found that ZS@Z, ZS@Z1, ZS@Z2 and ZS@Z3 composites can remove 28.68%, 36.06%, 36.06% and 33.12% MB dye solution, respectively, while ZIF-8 can remove only 8.06% MB dye solution at pH = 7.89. In case of photodegradation, ZS@Z, ZS@Z1, ZS@Z2 and ZS@Z3 composites can degrade off

100%, 93.43%, 97.43% and 91.93% MB dye solution at pH = 7.89 which is quit better as compared to ZIF-8 which can degrade only 84.18% MB dye solution at same pH = 7.89. The results are tabulated in Table 6B.5 and C/C_0 *vs* time plots are illustrated in Fig. 6B.16, wherein the results of adsorption and degradation of MB dye using ZIF-8 and degradation of MB dye itself are already mentioned in previous Chapter five (Section B).

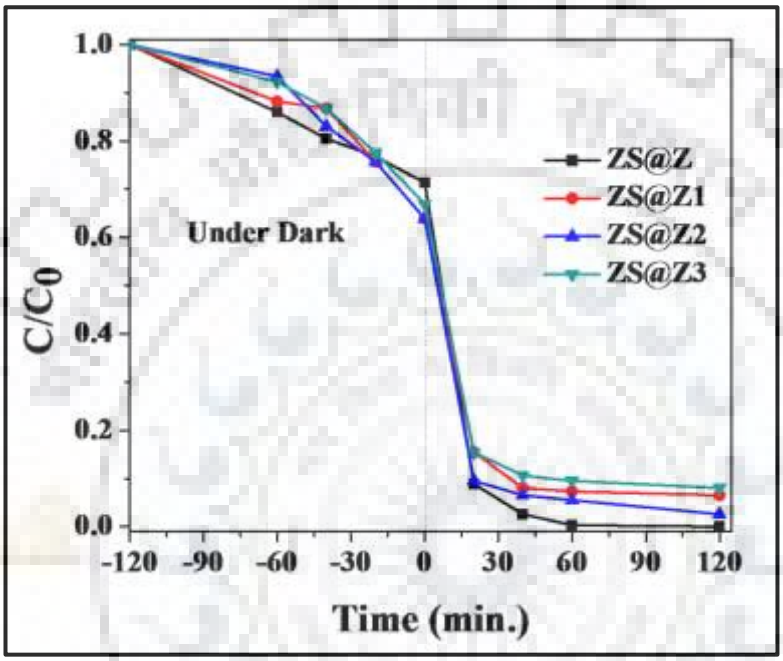

Fig. 6B.16. Concentration (C/C_0) *vs* time plot of MB employing ZS@Z, ZS@Z1, ZS@Z2 and ZS@Z3 composites.

Table 6B.5 Adsorption and photodegradation of [MB] = 0.5×10^{-5} M or 1.6 mg L^{-1}, catalysts amount = 10 mg, pH = 7.89 and time length for adsorption/photodegradation = 120 min.

S.N.	Materials	Adsorption capacity (mg/g) [% Dye removal]	%Photodegradation
1.	*MB	-	22.0
2.	*ZIF-8	0.26 [8.06]	84.18
3.	ZS@Z	0.91 [28.68]	100
4.	ZS@Z1	1.15 [36.06]	93.43
5.	ZS@Z2	1.15 [36.06]	97.43
6.	ZS@Z3	1.06 [33.12]	91.93

*Results are already given in previous Chapter five (Section B).

6B.3.9. Plausible Degradation Mechanism

The band gap of ZIF-8 was reduced due anchored mixed metal oxides (ZnO-SnO_2 nanocomposite) which are illustrated in Fig. 6B.17 wherein, yellow solid line indicates the band gap of ZIF-8 (*ca.* 5.2 eV) while white dashed line indicate the reduced band of ZS@Z composites. Photo induced e^- and h^+ pair generated in the conduction band (CB) and valance band (VB) of ZnO-SnO_2 nanocomposite, the electron (e^-) moves on the surface of ZIF-8 from lower edge of CB simultaneously hole (h^+) also moves. Thus e^- and h^+ pair are easily separated and react to dissolved oxygen and water. As a consequence, reactive oxidizing species (ROS) are produced such as such as O-O^{2-}, O-OH^-, $OH^\bullet$, etc. Among them $OH^\bullet$ plays the key role for the degradation of MB which is already proved with other composites.

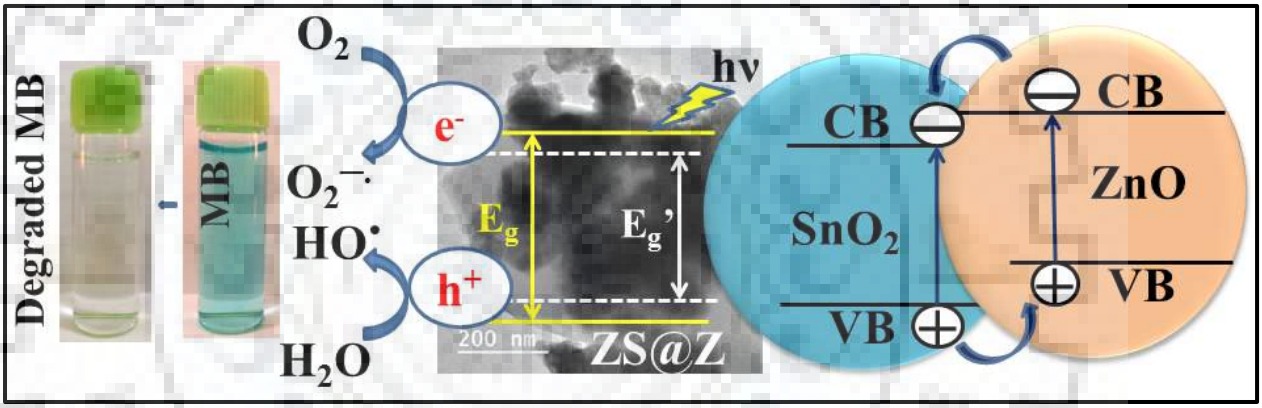

Fig. 6B.17. Plausible mechanism for MB degradation using ZS@Z composite under UV-visible light.

6B.4. CONCLUSION

In nutshell, ZnO-SnO_2 nanocomposite has been anchored (ZS@Z) and encapsulated (ZS@Z1, ZS@Z2 and ZS@Z3) within ZIF-8 framework successfully by employing solvothermal and bench method. The synthesized composites were also exploited as photocatalysts for the removal of organic pollutants such as MB. Further, it has been found that ZnO-SnO_2 nanocomposite anchored on ZIF-8 composite (ZS@Z) exhibits 100% degradation of [MB] = 1.6 mg L^{-1} dye solution at pH = 7.89.

6.5. REFERENCES

(1) (a) Jiang, Y.; Sun, Y.; Liu, H.; Zhu, F.; Yin, H. Solar Photocatalytic Decolorization of C.I. Basic Blue 41 in an Aqueous Suspension of TiO_2-ZnO. *Dyes Pig.* **2008**, *78*, 77-83. (b) Liao, D. L.; Badour, C. A.; Liao, B. Q. Preparation of Nanosized TiO_2/ZnO Composite Catalyst and its Photocatalytic Activity for Degradation of Methyl Orange. *Photochem. Photobiol. A: Chem.* **2008**, *194*, 11-19. (c) Liu, R.; Ye, H.; Xiong, X.; Liu, H. *Mater. Chem. Phys.* **2010**, *121*, 432-439. (d) Wang, M.; Cui, L.; Li, S.; Li, Z.; Ma, T.; Luan, G.; Liu, W.; Zhang, F. Facile Fabrication Hybrids of TiO_2@ZnO Tubes with Enhanced Photocatalytic Properties. *RSC Adv*. **2016**, *6*, 58452-58457.

(2) (a) Zhang, L.; Yu, W.; Han, C.; Guo, J.; Zhang, Q.; Xie, H.; Shao, Q.; Sun, Z.; Guo, Z. Large Scaled Synthesis of Heterostructured Electrospun TiO_2/SnO_2 Nanofibers with an Enhanced Photocatalytic Activity. *J. Electrochem. Soc*. **2017**, *164 (9)*, H651-H656. (b) Zhang, L.; Lv, F.; Zhang, W.; Li, R.; Zhong, H.; Zhao, Y.; Zhanga, Yu.; Wang, Xin. Photo Degradation of Methyl Orange by Attapulgite-SnO_2-TiO_2 Nanocomposites. *J. Hazard. Mater*. **2009**, *171*, 294–300.

(3) (a) Xin, T.; Ma, M.; Zhang, H.; Gu, J.; Wang, S.; Liu, M.; Zhang, Q. A Facile Approach for the Synthesis of Magnetic Separable Fe_3O_4@TiO_2, Core-shell Nanocomposites as Highly Recyclable Photocatalysts. *Appl. Surf. Sci.* **2014**, *288*, 51-59. (b) Shabani, A.; Nabiyouni, G.; Saffari, J.; Ghanbari, D. Photocatalyst Fe_3O_4/TiO_2 Nanocomposites: Green Synthesis and Investigation of Magnetic Nanoparticles Coated on Cotton. *J Mater Sci: Mater Electron* **2016**, *27*, 8661-8669.

(4) (a) Leghari, S. A. K.; Sajjad, S.; Zhanga, J. Large Mesoporous Micro-Spheres of WO_3/TiO_2 Composite with Enhanced Visible Light Photo Activity. *RSC Adv.*, **2013**, *3*, 15354-15361. (b) Kwon, Y. T.; Song, K. Y.; Lee, W. I.; Choi, G. J.; Do, Y. R. Photocatalytic Behavior of WO_3-Loaded TiO_2 in an Oxidation Reaction. *J. Catal*. **2000**, *191*, 192-199.

(5) Adhikari, S.; Sarkar, D.; Madras, G. Highly Efficient WO_3-ZnO Mixed Oxides for photocatalysis. *RSC Adv.* **2015**, *5*, 11895-11904.

(6) Uddin, M. T.; Nicolas, Y.; Olivier, C.;́Toupance, T.; Servant, L.; Müller, M. M.; Kleebe, H. J.; Ziegler, J.; Jaegermann, W. Nanostructured SnO_2-ZnO Heterojunction Photocatalysts Showing Enhanced Photocatalytic Activity for the Degradation of Organic Dyes. *Inorg. Chem.* **2012**, *51*, 7764-7773.

(7) (a) Stambolova, I.; Konstantinov, K.; Vassilev, S.; Peshev, P.; Tsacheva, T. Lanthanum doped SnO_2 and ZnO thin films sensitive to ethanol and humidity. *Mater. Chem. Phy.* **2000**, *63*, 104-108. (b) Ambrosini, A.; Palmer, G. B.; Maignan, A.; Poeppelmeier, K. R.; Lane, M. A.; Brazis, P.; Kannewurf, C. R.; Hogan, T.; Mason, T. O. Variable-Temperature Electrical Measurements of Zinc Oxide/Tin Oxide-cosubstituted Indium Oxide, *Chem. Mater.* **2002**, *14*, 52-57.

(8) Cun, W.; Jincai, Z.; Xinming, W.; Bixian, M.; Guoying, S.; Pingan, P.; Jiamo, F. Preparation, Characterization and Photocatalytic Activity of Nano-sized ZnO/SnO_2 Coupled Photocatalysts. *Applied Catal. B: Environ.* **2002**, *39*, 269–279.

(9) (a) Zhang, M.; An, T.; Hu, X.; Wang, C.; Sheng, G.; Fu, J. Preparation and Photocatalytic Properties of a Nanometer ZnO-SnO_2 Coupled Oxide. *Appl. Catal., A* **2004**, *260*, 215-222. (b) Wang, C.; Wang, X.; Xu, B. Q.; Zhao, J.; Mai, B.; Peng, P.; Sheng, G.; Fu, J. Enhanced Photocatalytic Performance of Nanosized Coupled ZnO/SnO_2 Photocatalysts for Methyl Orange Degradation, *J. Photochem. Photobiol. A* **2004**, *168*, 47-52. (c) Zhang, M.; Sheng, G.; Fu, J.; An, T.; Wang, X.; Hu, X. Novel Preparation of Nanosized ZnO–SnO_2 with High Photocatalytic Activity by Homogeneous Co-precipitation Method. *Mater. Lett.* **2005**, *59*, 3641-3644.

(10) (a) Ito, S.; Makari, Y.; Kitamura, T.; Wada, Y.; Yanagida, S. Fabrication and Characterization of Mesoporous SnO_2/ZnO Composite Electrodes for Efficient Dye Solar Cells. *J. Mater. Chem.* **2004**, *14*, 385-390. (b) Park, N. G.; Kang, M. G.; Kim, K. M.; Ryu, K. S.; Chang, S. H. Morphological and Photoelectrochemical Characterization of Core-shell Nanoparticle Films for Dye-Sensitized Solar Cells: Zn-O Type Shell on SnO_2 and TiO_2 Cores. *Langmuir* **2004**, *20*, 4246-4253.

(11) Kuang, Q.; Jiang, Z. Y.; Xie, Z. X.; Lin, S. C.; Lin, Z. W.; Xie, S. Y.; Huang, R. B.; Zheng, L. S. Tailoring the Optical Property by a Three-Dimensional Epitaxial Heterostructure: A Case of ZnO/SnO_2. *J. Am. Chem. Soc.* **2005**, *127*, 11777-11784.

(12) (a) Liangyuan, C.; Shouli, B.; Guojun, Z.; Dianqing, L.; Aifan, C.; Liu, C. C. Synthesis of ZnO-SnO_2 Nanocomposites by Microemulsion and Sensing Properties for NO_2. *Sens. Actuator B* **2008**, *134*, 360–366. (b) Zhang, W. H.; Zhang, W. D. Fabrication of SnO_2-ZnO Nanocomposite Sensor for Selective Sensing of Trimethylamine and the Freshness of Fishes. *Sens. Actuator B* **2008**, *134*, 403-408.

(13) Cheng, C.; Liu, B.; Yang, H.; Zhou, W.; Sun, L.; Chen, R.; Yu, S. F.; Zhang, J.; Gong, H.; Sun, H.; Fan, H. J. Hierarchical Assembly of ZnO Nanostructures on SnO_2

Backbone Nanowires Low-temperature Hydrothermal Preparation and Optical Properties. *ACS Nano* **2009**, *3*, 3069-3076.

(14) Zheng, L.; Zheng, Y.; Chen, C.; Zhan, Y.; Lin, X.; Zheng, Q.; Wei, K.; Zhu, J. Network Structured SnO_2/ZnO Heterojunction Nanocatalyst with High Photocatalytic Activity. *Inorg. Chem.* **2009**, *48*, 1819-1825.

(15) Zhang, Z.; Shao, C.; Li, X.; Zhang, L.; Xue, H.; Wang, C.; Liu, Y. Electrospun Nanofibers of ZnO-SnO_2 Heterojunction with High Photocatalytic Activity. *J. Phys. Chem. C* **2010**, *114*, 7920-7925.

(16) Chen, W.; Qiu, Y.; Yang, S. A New ZnO Nanotetrapods/SnO_2 Nanoparticles Composite Photoanode for high Efficiency Flexible Dye Sensitized Solar Cells. *Phys. Chem. Chem. Phys.* **2010**, *12*, 9494-9501.

(17) Hwang, I. S.; Kim, S. J.; Choi, J. K.; Choi, J.; Ji, H.; Kim, G. T.; Cao, G.; Lee, J. H. Synthesis and Gas Sensing Characteristics of Highly Crystalline ZnO-SnO_2 Core-Shell Nanowires. *Sens. Actuator B* **2010**, *148*, 595-600.

(18) Talebian, N.; Nilforoushan, M. R.; Zargar, E. B. Enhanced Antibacterial Performance of Hybrid Semiconductor Nanomaterials: ZnO/SnO_2 Nanocomposite Thin Films. *Appl. Surf. Sci.* **2011**, *258*, 547-555.

(19) Jin, C.; Kim, H.; Ryu, H. Y.; Kim, H. W.; Lee, C. Subwavelength Optical Resonant Cavity-Induced Enhancement of the Near-band-edge Emission from ZnO-core/SnO_2-shell Nanorods. *J. Phys. Chem. C* **2011**, *115*, 8513-8518.

(20) Misra, M.; Kapur, P.; Nayak, M. K.; Singla, M. L. Synthesis and Visible Photocatalytic Activities of a Au@Ag@ZnO Triple Layer Core-shell Nanostructure. *New J. Chem.* **2014**, *38*, 4197-4203.

(21) Li, F.; Xu, J.; Yu, X.; Chen, L.; Zhu, J.; Yang, Z.; Xin, X. One-step Solid-State Reaction Synthesis and Gas Sensing Property of Tin Oxide Nanoparticles, *Sens. Actuator B-Chem.* **2002**, *81*, 165-169.

(22) Khorami, H. A.; Keyanpour-Rad, M.; Vaezi, M. R. Synthesis of SnO_2/ZnO Composite Nanofibers by Electrospinning Method and Study of its Ethanol Sensing Properties. *Appl. Surf. Sci.* **2011**, *257*, 7988-7992.

(23) Tauc, J.; Grigorovici, R.; Vancu, A. Optical Properties and Electronic Structure of Amorphous Germanium. *Phys. Status Solidi B* **1966**, *15* (2), 627-637.

(24) Wang, X.; Liu, J.; Leong, S.; Lin, X.; Wei, J.; Kong, B.; Xu, Y.; Low, Z-X.; Yao, J.; Wang, H. Rapid Construction of ZnO@ZIF‑8 Heterostructures with Size-Selective Photocatalysis Properties. *ACS Appl. Mater. Interfaces* **2016**, *8*, 9080-9087.

(25) Hu, Y.; Kazemian, H.; Rohani, S.; Huang, Y.; Song, Y. *In Situ* High Pressure Study of ZIF-8 by FTIR Spectroscopy. *Chem. Commun.* **2011**, *47*, 12694-12696.

(26) Lin, L.; Zhang, T.; Liu, H.; Qiu, J.; Zhang, X. *In Situ* Fabrication of a Perfect Pd/ZnO@ZIF-8 Core-shell Microsphere as an Efficient Catalyst by a ZnO Support-induced ZIF-8 Growth Strategy. *Nanoscale* **2015**, *7*, 7615-7623.

(27) Zhao, M.; Cao, Y.; Liu, X.; Deng, J.; Li, D.; Gu, H. Effect of Nitrogen Atomic Percentage on N^+-bombarded MWCNTs in Cytocompatibility and Hemocompatibility. *Nanoscale Res. Lett.* **2014**, *9* (1), 142.

Chapter Seven

Conclusion & Future Prospects

"Education is the most powerful weapon which you can use to change the world."

Nelson Mandela

7.1. CONCLUSION

Multi-core-shell TiO_2NPs@ZIF-8 and SnO_2NPs@ZIF-8 composites have been synthesized by *in situ* encapsulation of TiO_2NPs and SnO_2NPs within ZIF-8 matrix. TiO_2NPs@ZIF-8 composites were applied as photocatalyst for the photodegradation of MB and RB by considering the various factors such as dosing amount of TiO_2NPs, amount of catalysts (ZIF-8 and TiO_2NPs@ZIF-8), pH and concentration of dye solutions. Similarly, SnO_2NPs@ZIF-8 composites were also employed as photocatalysts for MB degradation. Both (TiO_2NPs@ZIF-8 and SnO_2NPs@ZIF-8) composites exhibit maximum photodegradation efficiency toward MB dye degradation. For the first time, SnO_2NPs, ZIF-8 and SnO_2NPs@ZIF-8 composite were analyzed for anti-viral activity against *Chikungunya virus*.

Ag metal nanoparticles have been synthesized and encapsulated within ZIF-11 and ZIF-8 (AgNPs@ZIF-11 and AgNPs@ZIF-8) for the environmental remediation. AgNPs@ZIF-11 (AZ1) composite exhibits excellent photodegradation efficiency at 1×10^{-5} M (3.19 mg L^{-1}) *i.e.* 100% and at 2×10^{-5} M (6.38 mg L^{-1}) concentration, it can degrade off 80.79% MB dye solution. Moreover, AZ1 composite has been reused for the photocatalytic degradation of MB up to third cycle with 100% efficiency at 0.5×10^{-5} M (1.6 mg L^{-1}) MB dye solution. Additionally, AZ1 composite was used as photocatalyst for the 4-NP reduction into 4-AP. Further, AgNPs@ZIF-8 composites (SZ, SZ1, SZ2 and SZ3) were exploited as adsorbent and photocatalysts for the removal/degradation of MB and CR dye. AgNPs@ZIF-8 (SZ2) composite exhibits good degradation efficiency for the dyes *i.e.* 97.25% for [MB] = 0.5×10^{-5} M and 100% for [CR] = 2×10^{-5} M.

ZnO-SnO_2 nanocomposites were synthesized in various molar ratio of Zn and Sn *i.e.* 1:1, 2:8, 4:6, 6:4 and 8:2, using sol-gel (ZS-11, ZS-28, ZS-46, ZS-64 and ZS-82) and grinding (ZS-A, ZS-B, ZS-C, ZS-D and ZS-E) method and characterized by using various spectroscopic techniques. It has been found that ZS-E nanocomposite exhibits maximum photodegradation efficiency (58.68%) for [MB] = 1.6 mg L^{-1} dye solution at pH = 7.89. Further, ZIF-8 is fabricated with ZS-E nanocomposite and synthesized ZnO-SnO_2@ZIF-8 composites *via* solvothermal (ZS@Z) and bench method (ZS@Z1, ZS@Z2 and ZS@Z3) for enhancement of photodegradation efficiency of ZIF-8 as well as ZnO-SnO_2 nanocomposite. It has been found that ZS@Z composite exhibits 100% degradation of [MB] = 1.6 mg L^{-1} dye solution at pH = 7.89.

Among all of synthesized and studied composites, AZ1 and ZS@Z composites exhibit remarkable and excellent photodegradation efficiency which can degrade off 100% [MB] = 1.6 mg L^{-1} dye solution within 40 min and 120 min, respectively.

7.2. FUTURE PROSPECTS

- The synthesized hybrid materials (TiO_2NPs@ZIF-8, SnO_2NPs@ZIF-8, AgNPs@ZIF-8, AgNPs@ZIF-11 and ZnO-SnO_2@ZIF-8 composite) have been well characterized and utilized as photocatalysts for the environmental remediation. Further, these materials can be explored as anti-bacterial, anti-fungal and anti-viral agents while Ag nanowire@ZIF-8 composite material is already reported as potential candidate for anti-bacterial activity.
- AgNPs exhibits excellent catalytic activity in various organic conversion reactions. So, AgNPs encapsulated ZIFs materials also can be employed as heterogeneous catalyst for controlled and selective catalysis for the organic conversion reactions.
- ZnO-SnO_2@ZIF-8 composites (ZS@Z, ZS@Z1, ZS@Z2 and ZS@Z3) show excellent photodegradation efficiency for MB dye degradation. Hence, mixed metal oxides such as TiO_2-ZnO, TiO_2-SnO_2, TiO_2-Fe_3O_4, TiO_2-WO_3 and ZnO-WO_3 nanocomposites encapsulated MOFs can also be used as photocatalysts, supercapacitors and in biomedical applications.